



**HAL**  
open science

# Multilayer diffraction gratings with broadband efficiency in the extreme ultraviolet

Amr Hisham K. Mahmoud

► **To cite this version:**

Amr Hisham K. Mahmoud. Multilayer diffraction gratings with broadband efficiency in the extreme ultraviolet. Optics [physics.optics]. Université Paris-Saclay, 2023. English. NNT : 2023UPASP091 . tel-04545710

**HAL Id: tel-04545710**

**<https://hal.science/tel-04545710v1>**

Submitted on 1 Nov 2024

**HAL** is a multi-disciplinary open access archive for the deposit and dissemination of scientific research documents, whether they are published or not. The documents may come from teaching and research institutions in France or abroad, or from public or private research centers.

L'archive ouverte pluridisciplinaire **HAL**, est destinée au dépôt et à la diffusion de documents scientifiques de niveau recherche, publiés ou non, émanant des établissements d'enseignement et de recherche français ou étrangers, des laboratoires publics ou privés.

# Multilayer diffraction gratings with broadband efficiency in the extreme ultraviolet

*Réseaux de diffraction multicouches efficaces sur une large bande passante dans l'extrême ultraviolet*

**Thèse de doctorat de l'Université Paris-Saclay**

École doctorale n°572 ONDES ET MATIÈRE (EDOM)  
Spécialité de doctorat: Physique

Graduate school: Physique, Référent: Institut d'Optique

Thèse préparée dans l'unité de recherche Université Paris-Saclay, Institut d'Optique Graduate School, CNRS, Laboratoire Charles Fabry, 91127, Palaiseau, France, sous la direction de **Franck DELMOTTE** (Professeur des universités, Institut d'Optique Graduate School - Université Paris-Saclay), et le co-encadrement de **Sébastien DE ROSSI** (Maître de conférences, Institut d'Optique Graduate School - Université Paris-Saclay).

**Thèse soutenue à Paris-Saclay, le 25 September 2023, par**

**Amr Hisham Khalaf MAHMOUD**

## Composition du Jury

Membres du jury avec voix délibérative

**Frédéric AUCHÈRE**

Astronome, Institut d'Astrophysique Spatiale - Université Paris-Saclay      Président et Examineur

**Maria Guglielmina PELIZZO**

Professeure associée, Università degli Studi di Padova      Examinatrice et Rapporteuse

**Philippe JONNARD**

Directeur de recherche, Laboratoire de Chimie Physique, Matière et Rayonnement - Sorbonne Université      Examineur et Rapporteur

**Regina SOUFLI**

Chercheuse principale, Lawrence Livermore National Laboratory      Examinatrice

Membres du jury sans voix délibérative

**Franck DELMOTTE**

Professeur des universités, Institut d'Optique Graduate School - Université Paris-Saclay      Directeur de thèse, Examineur

**Sébastien DE ROSSI**

Maître de conférences, Institut d'Optique Graduate School - Université Paris-Saclay      Co-Encadrant de thèse, Examineur

*"The seeker of truth is not the one who studies the writings of the ancients as they are and places his trust in them. Instead, he is the one who questions his faith in them and wonders what he has gained from them. He is the one who seeks evidence and does not rely on the words of a person, whose nature is filled with all kinds of deficiencies and shortcomings. Therefore, it is the duty of anyone who investigates the writings of scholars, if the pursuit of truth is his goal, to criticize everything he reads and to use his mind to its fullest extent to examine those ideas from every angle. He should also doubt the results of his own study, in order to avoid falling into any bias or complacency."*

*— Ibn al-Haytham*





# Acknowledgements

This document provides a summary of the work I conducted during my thesis at the XUV Optics Group of Laboratoire Charles Fabry (Institute of Optics Graduate School, Paris-Saclay University). Over the course of three years for my doctorate and six months of internship in a master's program, I gained significant scientific knowledge and expertise in the area of thin film technology.

I would like to express my gratitude to the "L'École Doctorale Ondes et Matière – EDOM" at the University of Paris-Saclay for providing funding for my doctoral thesis and giving me the opportunity to participate in this research project.

I would like to express my sincere gratitude to all the individuals who played a role in making this work possible. Without their support and contributions, this project would not have been successful.

- I would like to extend my heartfelt thanks to my thesis director, Prof. Franck Delmotte, for his unwavering support and guidance throughout this project. Franck's proposal of an excellent research topic and his continuous encouragement, valuable insights, and extensive discussions have been instrumental in the successful completion of this work. Throughout the duration of my thesis, Franck taught me immensely, and I am grateful for his trust and confidence in my abilities. His advices, always offered with great patience and good humor, have been invaluable. I also extend my sincere appreciation for his careful review of the manuscript.
- I would like to express my gratitude to Sébastien de Rossi, my co-supervisor, for his invaluable assistance throughout this project. Sébastien played a crucial role in helping me understand the Rigorous coupled-wave analysis method and in revising my work, including checking results and preparing documents. His patience and dedication have been greatly appreciated, and I am thankful for his guidance in keeping me on the right track when I veered off course.
- I would like to extend my acknowledgment to Patrick Georges for his welcoming me to the institute, attentive listening during my annual presentations, and encouraging me to participate in international conferences.

I would also like to extend my sincere thanks to the entire XUV team for their support and contributions to my thesis project. In particular, I would like to thank:

- I would like to thank Evgueni Meltchakov for his valuable support and guidance during my research work. He provided me with hands-on training on the magnetron sputtering deposition technique using MP800 and helped me in cutting the silicon wafer samples for preparation and cleaning the samples. His expertise and knowledge have been invaluable in my research work, and I am grateful for his help.
- I would like to express my gratitude to Blandine Capitanio for her support and guidance during my research work. She taught me how to characterize the samples using an X-ray reflectometer (Bruker Discover D8 diffractometer) and helped me with the measurements of monochromatic synchrotron radiation on the XUV Metrology beamline at the SOLEIL Synchrotron. Her expertise and knowledge have been invaluable in my research work, and I am grateful for her help.
- I am profoundly thankful to Eirini PAPAGIANNOULI for her invaluable involvement in conducting certain technical measurements and providing a thorough review of one of the articles. Her expertise and insights greatly contributed to the scientific rigor of this thesis. I am sincerely grateful for her willingness to share her experience and provide valuable feedback throughout the development of this research.
- I would like to express my sincere gratitude to Anne-Lise COUTROT for her invaluable contributions to fabricating custom silicon gratings and for providing us with comprehensive information regarding the fabrication process. Furthermore, I am deeply grateful to her for readily providing me with all the information I requested.
- I extend my heartfelt appreciation to Arnaud JEROME for his invaluable assistance in enhancing my understanding of the mechanism of Ion Beam Sputtering. I am truly grateful to him for generously providing me with all the necessary information I required.
- I would like to express my sincere gratitude to Muriel THOMASSET and Maxime VALLET for their invaluable support in providing me with the necessary information and guidance regarding atomic force microscopy and transmission electron microscopy. Their assistance has been instrumental in reviewing the sections of my thesis related to these tools. I am truly thankful for their expertise and contribution.
- I extend my gratitude to the thesis reviewers for their valuable comments and suggestions, which have significantly elevated the text's quality and facilitated reader comprehension.

I would like to express my gratitude to Pascal Mercere, who provided technical support and valuable advice during the synchrotron measurements at SOLEIL Synchrotron.

# Contents

<b>1</b>	<b>Context of the PhD</b>	<b>27</b>
1.1	PhD Objectives . . . . .	27
1.2	Abstract . . . . .	28
1.3	Keywords . . . . .	29
<b>2</b>	<b>Introduction</b>	<b>31</b>
2.1	Extreme ultraviolet and X-ray regions . . . . .	32
2.2	Thin film optics . . . . .	33
2.2.1	Deposition Techniques for Thin Film and Coating. . . . .	33
2.2.2	Material response at EUV range . . . . .	34
2.3	Multilayer Physics . . . . .	37
2.3.1	Multilayer mirror . . . . .	37
2.3.2	Multilayer Synthesis . . . . .	39
2.3.3	Quality of interfaces . . . . .	41
2.3.3.1	Interfacial roughness . . . . .	41
2.3.3.2	Interdiffusion and interlayer formation . . . . .	41
2.3.3.3	Examples . . . . .	41
2.4	Physics of the Gratings . . . . .	43
2.4.1	Classical Grating Diffraction . . . . .	44
2.4.2	Conical Grating Diffraction . . . . .	46
2.5	Multilayer Gratings . . . . .	47
2.5.1	State of the art multilayer gratings . . . . .	48
2.6	EUV domain for astrophysics . . . . .	50
2.6.1	The Sun: the EUV rays of its corona . . . . .	51
2.6.2	History of solar observation missions in the EUV . . . . .	52
2.6.3	Solar-C -Mission . . . . .	54



2.7	Summary . . . . .	58
<b>3</b>	<b>Methods and Metrology</b>	<b>59</b>
3.1	Experimental Tools . . . . .	59
3.1.1	Magnetron sputtering deposition . . . . .	60
3.1.1.1	Principle of operation . . . . .	60
3.1.1.2	Sputtering machine at Laboratory Charles Fabry (LCF) – Plassys MP800S . . . . .	61
3.1.2	X-ray reflectometry . . . . .	64
3.1.3	Atomic Force Microscopy (AFM) . . . . .	67
3.1.4	Extreme ultraviolet reflectometry on synchrotron facility. . . . .	70
3.1.4.1	Direct Beam Comparison . . . . .	74
3.1.4.2	Dark Current . . . . .	74
3.1.4.3	Diode Uniformity . . . . .	75
3.1.4.4	Measuring the efficiency of the beamline . . . . .	76
3.1.4.5	Estimating the polarization factor of the beamline . . . . .	77
3.1.5	Transmission Electron Microscopy (TEM) . . . . .	78
3.1.5.1	Physics of Transmission Electron Microscopy . . . . .	78
3.1.5.2	Operation of Transmission Electron Microscopy . . . . .	79
3.1.5.3	Imaging modes . . . . .	80
3.1.5.3.1	High Angle Annular Dark Field Imaging: . . . . .	80
3.1.5.3.2	Bright Field Imaging: . . . . .	80
3.1.5.3.3	Energy-Dispersive X-ray Imaging: . . . . .	80
3.1.5.4	Focused Ion Beam preparation for TEM . . . . .	81
3.2	SIMULATIONS TOOLS . . . . .	83
3.2.1	Fresnel Equations Multilayer . . . . .	83
3.2.1.1	Optimization by IMD . . . . .	83
3.2.1.2	Fitting by IMD . . . . .	84
3.2.1.3	Simulation by custom MATLAB code . . . . .	85
3.2.2	Rigorous Coupled-Wave Analysis (RCWA) . . . . .	85
3.2.3	Materials optical constants. . . . .	87
3.3	Methodology used to develop EUV multilayer gratings. . . . .	88

3.4	Summary. . . . .	91
<b>4</b>	<b>Study of The Grating Substrates</b>	<b>93</b>
4.1	The Gratings (from Zeiss Report). . . . .	93
4.1.1	Fabrication process and Characterization. . . . .	93
4.2	Atomic Force Microscopy measurements . . . . .	95
4.2.1	Mechanical layout . . . . .	95
4.2.2	Measurements parameters . . . . .	96
4.2.3	AFM surface morphology and profile. . . . .	96
4.2.3.1	AFM analysis for surface morphology. . . . .	97
4.2.3.2	AFM analysis for surface profiles. . . . .	97
4.2.3.3	AFM analysis for all the sets of the gratings. . . . .	97
4.2.3.3.1	Roughness . . . . .	97
4.2.3.3.2	grating depth (d) . . . . .	97
4.2.3.3.3	Slope angle ( $\alpha$ ) . . . . .	97
4.2.3.3.4	fill factor ( $f.f$ ) . . . . .	100
4.2.3.3.5	$X_{part}$ . . . . .	101
4.2.3.4	AFM conclusion . . . . .	101
4.3	X ray reflectivity analysis. . . . .	103
4.3.1	GIXR measurements of the grating substrates. . . . .	103
4.3.2	Grating Models. . . . .	103
4.4	Effect of grating parameters on EUV efficiency . . . . .	106
4.4.1	Grating depth's influence. . . . .	106
4.4.2	Grating fill factor effect. . . . .	108
4.4.3	Grating slope impact. . . . .	109
4.4.4	The grating groove alignment's consequence. . . . .	110
4.5	Effect of the grating parameters on x-ray angular reflectance spectra. . . . .	111
4.5.1	The effect of the grating depth. . . . .	111
4.5.2	The effect of the grating fill factor. . . . .	112
4.5.3	The effect of the grating slope. . . . .	112
4.5.4	The effect of grooves grating alignment. . . . .	112
4.6	Summary. . . . .	113
<b>5</b>	<b>Study of the interference coating</b>	<b>115</b>
5.1	Choosing optical materials . . . . .	115

5.2	From broadband to very broadband. . . . .	117
5.3	Multilayer optimization. . . . .	119
5.3.1	Periodic multilayer for set#1. . . . .	120
5.3.2	Aperiodic multilayer for set#1. . . . .	121
5.3.3	Periodic multilayer for set#3. . . . .	122
5.3.4	Aperiodic multilayer for set#3. . . . .	123
5.3.5	Periodic multilayer for set#2. . . . .	124
5.3.6	Aperiodic multilayer for set#2. . . . .	124
5.4	Multilayer sensitivity to the thickness changes. . . . .	125
5.4.1	Sensitivity of the ML periodic design. . . . .	125
5.4.2	Effect of adding a cap of SiC. . . . .	127
5.5	Characterization multilayers deposition on a silicon substrate. . . . .	128
5.6	Final multilayers for the deposition process. . . . .	136
5.7	summary. . . . .	137
<b>6</b>	<b>Investigating the Impact of Multilayer Deposition on High-Density Silica Gratings</b>	<b>139</b>
6.1	Multilayer on the gratings : state of the art. . . . .	139
6.2	Multilayer on the gratings : simulations . . . . .	140
6.2.1	Influence of depth and wavelength on periodic multilayer grating efficiency orders. . . . .	141
6.2.2	Effect of depth and fill factor on periodic and aperiodic multilayers gratings . . . . .	143
6.2.3	Impact of depth and grating slope on periodic and aperiodic multilayer gratings . . . . .	144
6.3	Multilayer on the gratings: experimental results . . . . .	146
6.3.1	Surface profile evolution . . . . .	146
6.3.2	Characterization and modeling . . . . .	153
6.4	Three sets of multilayer gratings fulfilling Solar C mission requirements . . . . .	159
6.4.1	Comparative Analysis with Previous Literature (Solar B mission) . . . . .	159
6.4.2	Recommendations . . . . .	161
6.5	Summary . . . . .	162
<b>7</b>	<b>Additional studies and observations for multilayer gratings</b>	<b>165</b>
7.1	Angular Performance of Multilayer Gratings . . . . .	166
7.2	Conical and Classical measurements at EUV . . . . .	171
7.2.1	Multilayer gratings sensitivity to EUV . . . . .	174
7.3	Summary . . . . .	176

<b>8</b>	<b>Conclusions and Future Work</b>	<b>177</b>
8.1	Conclusions . . . . .	177
8.2	Future Work . . . . .	178
<b>A</b>	<b>Deposition on Custom Silicon Grating.</b>	<b>181</b>
A.1	Etched Silicon Arrays Fabrication Process . . . . .	181
A.2	Custom silicon gratings sample 1 . . . . .	182
A.2.1	Characterization before deposition. . . . .	182
A.2.2	Initial deposition. . . . .	183
A.2.3	Characterization after deposition by X-ray reflectometry. . . . .	183
A.2.4	Optical microscope. . . . .	185
A.2.5	Characterization after deposition by TEM. . . . .	185
A.3	Custom silicon gratings sample 2 . . . . .	187
A.3.1	Initial AFM Profile of Custom Silicon Gratings Sample 2 . . . . .	187
A.3.2	Optimized multilayer structure . . . . .	188
A.3.3	Analysis of Multilayer on Custom Silicon Gratings Sample 2 . . . . .	188
A.3.4	AFM Profile of Custom Silicon Gratings Sample 2 Following Deposition . . . . .	191
A.4	Layer growth model . . . . .	191
A.5	Summary . . . . .	193
<b>B</b>	<b>Appendix Tables</b>	<b>195</b>
<b>C</b>	<b>Appendix Figures</b>	<b>199</b>
<b>D</b>	<b>Compendium of Deposition Specifications for Multilayer Coatings on Silica Gratings</b>	<b>207</b>

# List of Figures

2.1	EUV Electromagnetic spectrum [1]. . . . .	32
2.2	variation of attenuation length with wavelength for different materials [2]. . . . .	35
2.3	representation of the reflection and transmission of an electromagnetic wave at the interface between their medium indices $n_1$ and $n_2$ ( $n_1 > n_2$ ). . . . .	36
2.4	The reflectivity as a function of the normalized grazing angle can be represented by a stepwise change in reflection for low absorption ( $\beta$ ), while for higher absorption, a more gradual enhancement becomes evident. [3]. . . . .	37
2.5	(a) The diagram below illustrates the X-ray reflection at a 2-periods multilayer mirror, and (b) The right graph shows the reflectance at $\theta=5^\circ$ of an optimized 2-periods, and 20-periods multilayer mirror consisting of a-Si (7.45nm) and Mo (6.23nm) over a Si substrate, without taking into account the roughness. . . . .	38
2.6	Illustrations of four simulated scenarios at $\theta=5^\circ$ : (a) presence of roughness between layers, (b) inter-diffusion occurring between layers, (c) formation of oxidation at the top, and (d) development of an interface layer between layers. . . . .	42
2.7	Transmission electron microscopy image of the Al/Mo/SiC multilayer sample studied by Ahmed Ziani (2010) [4]. . . . .	43
2.8	(a) refraction phenomena through the prism (b) diffraction phenomena in classical configuration [5] . . . . .	43
2.9	schematic diagram of classical position (left), and conical position (right). . . . .	44
2.10	The 0-order diffraction photons are reflected directly from diffraction, while the other parts of the incident light will be diffracted to $1^{st}, 2^{nd}$ , and extra orders depending on the wavelength. . . . .	45
2.11	different grating profiles (a) lamellar gratings, (b) trapezoidal gratings, and (c)blazed gratings. . . . .	46
2.12	Diagram of the structure of the Sun to scale [6]. . . . .	51
2.13	Solar spectrum shown here is obtained from the MEGS-A channel measuring the spectrum from 7 to 37 nm [7]. . . . .	52
2.14	Comparison of reflectivities acquired using EUVI for the STEREO mission and EIT for the SOHO test samples [8], with the visualization image captured by the EUVI sensor in 2016 [9] at various wavelengths: (a) $\lambda=17.1\text{nm}$ , (b) $\lambda=19.5\text{nm}$ , (c) $\lambda=28.4\text{nm}$ , and (d) $\lambda=30.4\text{nm}$ . . . . .	54

2.15 The Full Sun Imager on board the ESA/NASA Solar Orbiter spacecraft captured a giant solar eruption at $\lambda=30.4\text{nm}$ on 15 February 2022 [10]. . . . .	55
2.16 The optical configuration of the EUVST instrument with international contributions. [11]. . . . .	56
2.17 The optical arrangement of the EUVST instrument. . . . .	57
2.18 Data obtained from Seely et al. [12] for the +1 order at nearly normal incidence. . . . .	58
3.1 Schematic diagram of DC and RF magnetron sputtering. . . . .	61
3.2 Photograph of DC and RF magnetron sputtering (a) external, and (b) internal. . . . .	62
3.3 Photograph of the sample holder. . . . .	63
3.4 Setup of X-ray Reflectometry [13]. . . . .	64
3.5 Simulation of reflectivity spectra at 8keV of a silica substrate, Mo thin film, and a periodic $[\text{Al}/\text{Mo}/\text{SiC}]_{10}$ multilayer. . . . .	65
3.6 Photograph of the rotation stage. . . . .	66
3.7 Schematic diagram of AFM [14]. . . . .	67
3.8 The AFM surface morphology of the grating is depicted in the following figures: (a) presents the original AFM image, (b) displays the image after vertically aligning the grating grooves, (c) shows a zoomed-in view of the grating grooves, and (d) illustrates the profile of the grooves in the grating. . . . .	69
3.9 AFM measurements were conducted using two different modes to examine the profile of the grating. . . . .	70
3.10 schematic diagram of Soleil Synchrotron [15]. . . . .	70
3.11 Illustration depicting the XUV branch of the Metrology beamline [16]. . . . .	71
3.12 Photography of (a) an external view of a reflectometer. (b) an internal view of a reflectometer. (c) Close-up images of the diodes within the reflectometer. (d) the alignment of the multilayer gratings samples within the reflectometer. . . . .	72
3.13 The schematic diagram illustrates the principle of synchrotron beamline measurements, showcasing (a) the acquisition of a measurement and (b) the acquisition of a direct beam. . . . .	73
3.14 Variation of the current with Energy for a diode with the slit at different measurements on different days. . . . .	74
3.15 Variation of the photons flux current as a function of the rotation position for the (a) diode with slit, and (b) diode without slit. . . . .	75
3.16 Variation of all orders efficiency with diode angle for multilayer grating at near normal incidence. . . . .	76
3.17 Variation of +1 orders current intensity with diode angle on multilayer grating for different energies at near normal incidence ( $\theta = 5^\circ$ ). . . . .	77
3.18 Simulation of the +1 orders of a 6-period Al/Mo/SiC multilayer grating Set#1 for different values of the polarization factor at (a) $\theta = 5^\circ$ near-normal incidence and (b) $\theta = 45^\circ$ . . . . .	77

3.19 Photograph of Transmission electron microscopy at CentraleSupélec, ENS Paris-Saclay, Université Paris-Saclay. . . . .	79
3.20 Photograph of different processes of Scanning electron microscopy to prepare the sample for transmission electron microscopy measurement. . . . .	81
3.21 The optimization criteria differ for (a) periodic multilayers, and (b) aperiodic multilayers. . . . .	84
3.22 The data obtained includes fitted data using IMD and measured data obtained through GIXR for the following scenarios: (a) a thin film of SiC deposited on a flat Si substrate, and (b) 10-period of Al/Mo/SiC deposited on a flat Si substrate. . . . .	85
3.23 schematic diagram of (a) the trapezoidal grating profile before deposition and (b) the multilayer coating (N=6) deposited on the trapezoidal grating. . . . .	86
3.24 Schematic diagram illustrating the structure of multilayer trapezoidal gratings with periodic multilayers ( $N = 2$ ) in both symmetric (a) and asymmetric (b) configurations. . . . .	86
3.25 optical index of different materials in the EUV [2] (a) $\delta$ , and (b) $\beta$ . . . . .	87
3.26 Simulation and Experimental strategy for multilayer gratings. . . . .	89
4.1 Schematic diagram for the gratings of different groove depths. . . . .	94
4.2 Photograph of the final gratings of the second batch with dimensions $20 \times 20 \times 6 \text{ mm}^3$ after the fabrication process by Zeiss. . . . .	94
4.3 Schematic diagram of (a) the grating (b) the positions of points on the top of the grating. . . . .	96
4.4 Photograph of the preparation of the gratings for AFM measurements. . . . .	96
4.5 The $2\mu\text{m} \times 2\mu\text{m}$ AFM surface morphology at different substrates and different positions of the trapezoidal grating without multilayers for set#1. . . . .	98
4.6 The $2\mu\text{m} \times 2\mu\text{m}$ AFM surface morphology at different substrates and different positions of the trapezoidal grating without multilayers for set#2. . . . .	98
4.7 The $2\mu\text{m} \times 2\mu\text{m}$ AFM surface morphology at different substrates and different positions of the trapezoidal grating without multilayers for set#3. . . . .	98
4.8 AFM groove profiles at different substrates and different positions of the trapezoidal grating without multilayers for set#1. . . . .	99
4.9 AFM groove profiles at different substrates and different positions of the trapezoidal grating without multilayers for set#2. . . . .	99
4.10 AFM groove profiles at different substrates and different positions of the trapezoidal grating without multilayers for set#3. . . . .	99
4.11 A bar chart displaying the fluctuations in roughness observed on the upper surface of the grating substrate. . . . .	100

4.12 A bar chart depicting the fluctuation in roughness on the bottom surface of the grating substrate. . . .	100
4.13 Bar chart depicting the fluctuation in grating depth across the grating substrate . . . . .	101
4.14 A bar chart illustrating the changes in the slope of the trapezoidal shape of the grating across the substrate. . . . .	101
4.15 An illustrated bar chart showcasing the variations in grating fill factor (FWHM) observed across the grating substrate. . . . .	102
4.16 A visually represented bar chart displaying the observed variations in $X_{part}$ grating across the substrate.	102
4.17 GIXR measurements for gratings (a) Set#1 substrate#1, (b) Set#2 substrate#4, and (c) Set#3 substrate#4 in classical, and conical configurations. . . . .	103
4.18 The schematic illustrates three physical structures (a) lamellar gratings, (b) the EMA model, and the RCWA model. . . . .	104
4.19 EMA model for GIXR measurements for gratings Set#1 substrate#1 in classical position. . . . .	105
4.20 EMA model for GIXR measurements for gratings Set#2 substrate#4 in classical position. . . . .	105
4.21 EMA model for GIXR measurements for gratings Set#3 substrate#4 in classical position. . . . .	106
4.22 RCWA simulation for grating depth as a function of grating efficiency for gratings without multilayers. .	107
4.23 RCWA simulation for transverse electric grating efficiency +1 <sup>st</sup> order as a function of wavelength and depth for lamellar gratings substrate. . . . .	108
4.24 RCWA simulation for wavelength as a function of grating efficiency and fill factor for a lamellar grating substrate. . . . .	109
4.25 RCWA simulation for wavelength as a function of grating efficiency and alpha for gratings substrate. .	109
4.26 RCWA simulation for wavelength as a function of grating efficiency (+1-order) and omega for lamellar gratings substrate. . . . .	110
4.27 RCWA simulation for wavelength as a function of grating efficiency (-1-order) and omega for lamellar gratings substrate. . . . .	110
4.28 RCWA simulation for grazing angle as a function of reflectance logarithm and depth for lamellar gratings substrate. . . . .	111
4.29 RCWA simulation for grazing angle as a function of reflectance logarithm and fill factor for lamellar gratings substrate. . . . .	112
4.30 RCWA simulation for grazing angle as a function of reflectance logarithm and alpha for gratings substrate.	113
4.31 RCWA simulation for grazing angle as a function of reflectance logarithm and $\omega$ for lamellar gratings substrate. . . . .	113



5.1	Theoretical calculated maximum reflectance of Si/Mo, Al/Mo, Al/SiC, and Al/Mo/SiC multilayer structures under normal incidence, spanning wavelengths from 15 to 40 nm. These calculations assume ideal structures (no surface roughness) comprising 50 periods. [17]. . . . .	116
5.2	The EUV peak reflectances of certain Al/Mo/SiC and Al/Mo/B4C multilayers were assessed based on (a) their ability to achieve a high peak reflectance and (b) their capacity to maintain high stability throughout the period from April 2009 to February 2013. [18]. . . . .	117
5.3	TE simulated reflectance of the optimized periodic Al/Mo/SiC multilayer as a function of wavelength and the number of periods (N) at $\theta = 5^\circ$ for set#1. . . . .	120
5.4	TE simulated reflectance of the optimized periodic Al/Mo/SiC multilayer N=6 as a function of wavelength and incidence ( $\theta$ ) for set#1. . . . .	121
5.5	The simulated reflectance of the optimized aperiodic (12-layers) and periodic ( $N = 6$ ) Al/Mo/SiC multilayers as a function of wavelength at $\theta = 5^\circ$ . . . . .	121
5.6	TE simulated reflectance of the optimized periodic Al/Mo/SiC multilayer as a function of wavelength and the number of periods (N) at $\theta = 5^\circ$ for set#3. . . . .	122
5.7	TE simulated reflectance of the optimized periodic Al/Mo/SiC multilayer N=6 as a function of wavelength and incidence ( $\theta$ ) for set#3. . . . .	123
5.8	The reflectance simulation results are presented in this caption, showcasing the optimized performance of two aperiodic designs with 18 and 24 layers, along with the periodic ( $N = 6$ ) Al/Mo/SiC multilayers. The reflectance is plotted as a function of wavelength at an incidence angle of $\theta = 5^\circ$ . . . . .	123
5.9	The reflectance simulations of the optimized periodic ( $N = 6$ ) Al/Mo/SiC multilayers and two aperiodic designs (consisting of 18 layers and 24 layers) are presented as a function of wavelength at an incidence angle of $\theta = 5^\circ$ . . . . .	124
5.10	The schematic of 2 periods Al/Mo/SiC multilayers on a Si substrate illustrates the relative thickness variation between the Mo and SiC layers, while the thickness of the Al layer remains constant. . . . .	125
5.11	Relative thickness changes between SiC and Mo of TE simulated reflectance of optimized periodic Al/Mo/SiC multilayer design for Set#1 as a function of wavelength at $\theta = 5^\circ$ . . . . .	126
5.12	Relative thickness changes between SiC and Mo of TE simulated reflectance of optimized periodic Al/Mo/SiC multilayer design for set#2 as a function of wavelength at $\theta = 5^\circ$ . . . . .	126
5.13	The relative thickness changes between SiC and Mo of TE simulated reflectance of the optimized periodic Al/Mo/SiC multilayer design for Set #3 as a function of wavelength at $\theta = 5^\circ$ . . . . .	127
5.14	TE simulated reflectance variation due to adding SiC cap layer at the top of optimized multilayers for ML Set#2 at $\theta = 5^\circ$ . . . . .	127
5.15	TE simulated reflectance variation due to adding SiC cap layer at the top of optimized multilayers for ML Set#3 at $\theta = 5^\circ$ . . . . .	128

5.16	TEM analyses of sample MP20065: (a) HAADF (b) EDX images and (c) profile of the atom concentration, in arbitrary units (a.u.), as a function of the position. . . . .	129
5.17	GIXR measured and fitted curves at $\lambda=0.154$ nm for the 10-periods Al/Mo/SiC multilayer (sample MP20065) and the 12 layers aperiodic Al/Mo/SiC multilayer (sample MP20070). . . . .	130
5.18	Reflectance of SXR measured and fitted spectra at $\theta=5^\circ$ for the 10-periods Al/Mo/SiC multilayer (sample MP20065) and the 12 layers aperiodic Al/Mo/SiC multilayer (sample MP20070). . . . .	131
5.19	Reflectance of SXR measured and fitted spectra at $\theta=45^\circ$ for the 10-periods Al/Mo/SiC multilayer (sample MP20065) and the 12 layers aperiodic Al/Mo/SiC multilayer (sample MP20070). . . . .	132
5.20	The measured and fitted curves for the 10-period Al/Mo/SiC multilayer (sample MP21074), the 18-layer aperiodic Al/Mo/SiC multilayer (sample MP21077), and the 24-layer aperiodic Al/Mo/SiC multilayer (sample MP21083) at GIXR at $\lambda=0.154$ nm . . . . .	133
5.21	The measured and fitted curves for the 10-period Al/Mo/SiC multilayer (sample MP21075), the 18-layer aperiodic Al/Mo/SiC multilayer (sample MP21077), and the 24-layer aperiodic Al/Mo/SiC multilayer (sample MP21083) for SXR at $\theta=5^\circ$ (a) reflectance-wavelength, and (b) reflectance logarithm-wavelength. . . . .	133
5.22	The measured and fitted curves for the 10-period Al/Mo/SiC multilayer (sample MP21074), the 18-layer aperiodic Al/Mo/SiC multilayer (sample MP21076), and the 24-layer aperiodic Al/Mo/SiC multilayer (sample MP21082) at GIXR at $\lambda=0.154$ nm . . . . .	134
5.23	The measured and fitted curves for the 10-period Al/Mo/SiC multilayer (sample MP21074), the 18-layer aperiodic Al/Mo/SiC multilayer (sample MP21076), and the 24-layer aperiodic Al/Mo/SiC multilayer (sample MP21082) for SXR at $\theta=5^\circ$ (a) reflectance-wavelength, and (b) reflectance logarithm-wavelength. . . . .	135
5.24	Simulated reflectance of optimized periodic Al/Mo/SiC multilayer with different numbers of periods and aperiodic Al/Mo/SiC multilayer as a function of wavelength for ML Set#1 at $\theta= 5^\circ$ . . . . .	136
5.25	Simulated reflectance of optimized periodic Al/Mo/SiC multilayer with different numbers of periods and aperiodic Al/Mo/SiC multilayer as a function of wavelength for ML Set#2 at $\theta= 5^\circ$ . . . . .	137
5.26	Simulated reflectance of optimized periodic Al/Mo/SiC multilayer with different numbers of periods and aperiodic Al/Mo/SiC multilayer as a function of wavelength for ML Set#3 at $\theta= 5^\circ$ . . . . .	137
6.1	+1-Order simulation for wavelength as a function of grating efficiency and grating depth for multilayers on lamellar gratings with $N = 6$ periods multilayers for gratings set#1. . . . .	141
6.2	+1-Order simulation for wavelength as a function of grating efficiency and grating depth for multilayers on lamellar gratings with $N = 6$ periods multilayers for gratings set#3. . . . .	142
6.3	+1-Order simulation for wavelength as a function of grating efficiency and grating depth for multilayers on lamellar gratings with $N = 6$ periods multilayers for gratings set#2. . . . .	142

6.4	Calculated 0-order (a) and +1-order (b) grating efficiency in transverse electric mode at $\lambda=27\text{nm}$ as a function of fill factor and grating depth. The parameters for the simulation are $\theta=5^\circ$ , $N = 6$ , $\alpha=90^\circ$ (lamellar), and $P=277.8 \text{ nm}$ . The grating efficiency for the aperiodic multilayer with the same grating parameters is plotted in (c) 0-order and (d) +1-order. . . . .	143
6.5	Calculated 0-order (a) and +1-order (b) grating efficiency in transverse electric mode at $\lambda=27\text{nm}$ as a function of $\alpha$ and grating depth. The parameters for the simulation are $\theta=5^\circ$ , $N = 6$ , $f.f=0.5$ , and $P=277.8\text{nm}$ . The grating efficiency for the aperiodic multilayer with the same grating parameters is plotted in (c) 0-order and (d) +1-order. . . . .	144
6.6	TE +1-order grating efficiency calculated at $\lambda=19\text{nm}$ as a function of $\alpha$ and grating depth. The simulation parameters used are $\theta=5^\circ$ , $N=6$ , $f.f=0.5$ , and $P=250\text{nm}$ . . . . .	145
6.7	The $2\mu\text{m} \times 2\mu\text{m}$ AFM surface morphology of trapezoidal grating substrate Set#1 before deposition (a), and after deposition of Al/Mo/SiC multilayer with (b) $N = 6$ , (c) $N = 8$ , (d) $N = 16$ . (e) Average groove profiles as a function of the number of periods; every profile is shifted by 30nm in the Z-Scale. $N = 0$ corresponds to the measurement $N = 6$ before deposition. . . . .	147
6.8	variation of the trapeze angle $\alpha$ with the number of periods deposited on the grating Set#1. . . . .	148
6.9	(a) Average groove profiles before (on black) and after (on colored) the deposition of Al/Mo/SiC for grating Set#2 as a function of the number of periods; every profile is shifted by 20.0nm in Z-Scale, and The $2\mu\text{m} \times 2\mu\text{m}$ AFM surface morphology of trapezoidal grating substrate before, and after the deposition of Al/Mo/SiC multilayer with (b) $N = 4$ , and (C) $N = 10$ . . . . .	149
6.10	(a) Average groove profiles before (on black) and after (on colored) the deposition of Al/Mo/SiC for grating Set#3 as a function of the number of periods; every profile is shifted by 8.0nm in Z-Scale, and The $2\mu\text{m} \times 2\mu\text{m}$ AFM surface morphology of trapezoidal grating substrate before, and after the deposition of Al/Mo/SiC multilayer with (b) $N = 4$ , and (C) $N = 10$ . . . . .	150
6.11	TEM analyses of periodic multilayer grating ( $N = 16$ ) for grating Set#1: (a) HAADF, and EDX images for (b) Al, (c) Mo, (d) Si, (e) O, and (f) Al/Mo/Si. . . . .	151
6.12	TEM analyses of periodic multilayer grating (12 layers) for grating Set#1: (a) HAADF, and EDX images for (b) Al, (c) Mo, (d) Si, (e) O, and (f) Al/Mo/Si. . . . .	152
6.13	TEM analyses of periodic multilayer grating ( $N = 10$ ) for grating Set#2: (a) HAADF, and EDX images for (b) Al, (c) Mo, (d) Si, (e) O, and (f) Al/Mo/Si. . . . .	153
6.14	TEM analyses of periodic multilayer grating ( $N = 10$ ) for grating Set#3: (a) HAADF, and EDX images for (b) Al, (c) Mo, (d) Si, (e) O, and (f) Al/Mo/Si. . . . .	154
6.15	Measured and modeled +1 order diffraction efficiency of the multilayer gratings Set#1 at $\theta=5^\circ$ : (a) $N = 2$ , (b) $N = 4$ , (c) $N = 6$ , (d) $N = 8$ , (e) $N = 16$ , and (f) aperiodic. . . . .	155

6.16 Measured and modeled +1 order diffraction efficiency of the multilayer gratings Set#1 at $\theta=45^\circ$ : (a) $N = 2$ , (b) $N = 4$ , (c) $N = 6$ , (d) $N = 8$ , (e) $N = 16$ , and (f) aperiodic. . . . .	156
6.17 +1 order maximum efficiency and bandwidth for SXR at (a) $\theta=5^\circ$ and (a) $\theta=45^\circ$ . . . . .	157
6.18 Measured and modeled +1 order diffraction efficiency of the multilayer grating set#2 at $\theta=5^\circ$ : (a) $N = 4$ , (b) $N = 6$ , (c) $N = 8$ , (d) $N = 10$ , (e) 18-layers aperiodic, and (f) 24-layers aperiodic. . . . .	158
6.19 Measured and modeled +1 order diffraction efficiency of the multilayer grating set#3 at $\theta=5^\circ$ : (a) $N = 4$ , (b) $N = 6$ , (c) $N = 8$ , (d) $N = 10$ , (e) 18-layers aperiodic, and (f) 24-layers aperiodic. . . . .	160
6.20 Parameters of +1 order achieved for grating Set#2 and Set#3 as a function of multilayer period $N$ for SXR at near normal incidence ( $\theta = 5^\circ$ ): (a) Peak efficiency, and (b) Bandwidth. . . . .	161
6.21 : +1 order efficiency measurement at $\theta=5^\circ$ for the gratings for $N=4$ , $N=6$ , and aperiodic coatings. Experimental data from Seely et al.[12; 19] are also plotted for comparison. . . . .	161
6.22 +1 order efficiency measurement at $\theta=5^\circ$ for the grating set#2 for $N=6$ , 24 layers of aperiodic coatings, and for the grating set#3 for $N=8$ , 24 layers of aperiodic coatings. Experimental data from Seely et al.[12; 19] are also plotted for comparison. . . . .	162
7.1 Schematic diagram for the gratings with periodic multilayers ( $N = 4$ ) at two different configurations, i.e., (a) classical and (b) conical. . . . .	166
7.2 Alignment of the conical multilayer grating set#1 with $N = 8$ layers using a rocking curve within the GIXR set up at an angle of $\omega = 6^\circ$ . . . . .	166
7.3 Estimation results of GIXR: Variation of diffraction angle for the $0^{th}$ , $+1^{st}$ , and $-1^{st}$ orders with grazing angle for (a) classical configuration, and (b) conical configuration. . . . .	167
7.4 GIXR simulations and measurements for gratings Set#1. (a) GIXR simulation without multilayers ( $N = 0$ ), (b) and (c) GIXR simulations with periodic multilayers at $N = 2$ and $N = 8$ , respectively. (d) GIXR measurements without multilayers ( $N = 0$ ) in both conical and classical configurations, (e) and (f) GIXR measurements with multilayers at $N = 2$ and $N = 8$ in both conical and classical configurations, respectively. . . . .	168
7.5 GIXR measurements using a rotation stage for different angles of $\omega$ with grazing angle, and reflectance in the color bar for the behavior of multilayer gratings Set#1 with multilayer periods of (a) $N = 2$ and (b) $N = 8$ . Zoom-in GIXR simulations with periodic multilayers at (c) $N = 2$ and (d) $N = 8$ . . . . .	169
7.6 RCWA Model for GIXR measurements for multilayers on gratings set#1 (a) periodic ( $N = 2$ ), (b) periodic ( $N = 4$ ), (c) periodic ( $N = 6$ ), (d) periodic ( $N = 8$ ), (e) periodic ( $N = 16$ ) and (f) aperiodic (12 – layers). . . . .	170

7.7	(a) TEM HAADF images of three sets of multilayer gratings, along with our estimation method used to compute the slope, (b) Slope calculation for each $N$ in periodic multilayer (where $N = 16$ ) of Grating Set #1, (c) Slope calculation for each $N$ in periodic multilayer (where $N = 10$ ) of Grating Set #2, and (d) Slope calculation for each $N$ in periodic multilayer (where $N = 10$ ) of Grating Set #3. . . . .	172
7.8	HAADF STEM images of different multilayer gratings: (a) Periodic Set#1 ( $N = 16$ ), (b) Aperiodic Set#1 (12 Layers), (c) Periodic Set#2 ( $N = 10$ ), and (d) Periodic Set#3 ( $N = 10$ ). . . . .	172
7.9	SXR measurements and models for periodic multilayer gratings Set#1 $N=6$ at (a) a classical position and (b) conical position, and for aperiodic multilayers gratings Set#1 at (c) classical position and (d) conical position. . . . .	173
7.10	(a) +1-order simulation of the variation of $\omega$ angle with wavelength, and efficiency for periodic $N = 6$ at an incident angle $45^\circ$ , and (b) SXR grating efficiencies measurements for conical position and inverse conical position (rotation $180^\circ$ ). . . . .	174
7.11	(a) Schematic diagram of the top x-y plan of the gratings showing the positions where the SXR beam interacts with multilayer gratings in classical position. (b) Three measurements of the 0-order at near-normal incidence ( $\theta = 5^\circ$ ). (c) Three measurements of the +1-order at near-normal incidence ( $\theta = 5^\circ$ ). (d) Three measurements of the 0-order at incidence ( $\theta = 45^\circ$ ). (e) Three measurements of the +1-order at incidence ( $\theta = 45^\circ$ ). (f) Three measurements of the +1-order at incidence ( $\theta = 45^\circ$ ). . . . .	175
8.1	A comparison between our findings and the previous work on the Solar B mission, which focused on a 20-period Mo/Si multilayer presented by Seely [12]. Our study demonstrates improvements in (a) the +1-order measurements for the 8-periodic and 24-layer aperiodic Al/Mo/SiC multilayer of gratings set 3 at a central wavelength of 19 nm, and (b) the +1-order measurements for the 6-periodic and 12-layer aperiodic Al/Mo/SiC multilayer of gratings set 1 at a central wavelength of 27 nm. . . . .	179
A.1	(a) The $5\mu\text{m} \times 5\mu\text{m}$ AFM surface morphology, and (b) the groove profiles after making rotation to the grooves to have a perpendicular alignment of the grooves. . . . .	183
A.2	GIXR measured and fitted curves at $\lambda=0.154\text{nm}$ for the 20-periods Al/Mo/SiC multilayer (sample MP22055).184	
A.3	GIXR measured for multilayer on Si reference sample (red line) multilayer on Si grating sample (blue line), and multilayer on Si grating sample after rotating it $90^\circ$ with respect to $\omega$ (black line) at $\lambda=0.154\text{nm}$ for the 20-periods Al/Mo/SiC multilayer. . . . .	184
A.4	Optical telescope photography for test grating sample before and after deposition. . . . .	185
A.5	TEM analyses of sample MP22055: (a) HAADF, and EDX images (b) Al, (c) Mo, (d) Si, (e) O, and (f) 20-periods three materials Al/Mo/Si. . . . .	186
A.6	surface profile growth model of multilayer grating [20]. . . . .	187

A.7	Surface morphology of custom Si grating sample 2 at different scales: (a) $2\mu m \times 2\mu m$ , (b) $5\mu m \times 5\mu m$ , and (c) $10\mu m \times 10\mu m$ . Additionally, (d) displays the groove profile of the sample at a scale of $5\mu m \times 5\mu m$ .	188
A.8	GIXR measurements conducted on a Si grating sample with multilayer compositions of $N = 10$ , including Si/Mo/B4C (green line), Mo/Si (blue line), and Si/B4C (red line).	189
A.9	GIXR measurements were performed on a Si grating sample containing multilayer Mo/Si compositions with $N = 10$ . The data is presented as the measured results (blue line) and the corresponding modeled data (red dashed line).	190
A.10	Surface morphology of a custom Si grating sample 2 at different deposition stages: (a) without deposition, (b) after 10 periods of Mo/Si deposition, and (c) after 10 periods of Al/Mo/B4C deposition. Additionally, (d) presents the groove profile of the undeposited sample in blue, the profile after 10 periods of Mo/Si deposition in red with a Y-axis shift of 20 nm, and the profile after 10 periods of Mo/Si/B4C deposition in green with a Y-axis shift of 40 nm.	190
A.11	Profile model of multilayer gratings from Set#1 shown for different numbers of periods: (a) $N = 2$ , (b) $N = 4$ , (c) $N = 6$ , and (d) $N = 8$ . The red dot curve represents the AFM profile of the grating before deposition, while the blue dot curve represents the AFM profile of the grating after deposition.	192
C.1	Photography of TEM sample holder.	199
C.2	TE simulated reflectance of the optimized periodic Al/Mo/SiC multilayer as a function of wavelength and the number of periods (N) at $\theta = 5^\circ$ for set#2.	199
C.3	TE simulated reflectance of the optimized periodic Al/Mo/SiC multilayer N=6 as a function of wavelength and incidence ( $\theta$ ) for set#2.	200
C.4	Logarithme reflectance of SXR measured and fitted spectra at $\theta = 5^\circ$ for the 10-periods Al/Mo/SiC multilayer (sample MP20065) and the 12 layers aperiodic Al/Mo/SiC multilayer (sample MP20070)	200
C.5	Logarithme reflectance of SXR measured and fitted spectra at $\theta = 45^\circ$ for the 10-periods Al/Mo/SiC multilayer (sample MP20065) and the 12 layers aperiodic Al/Mo/SiC multilayer (sample MP20070)	200
C.6	0-Order simulation for wavelength as a function of grating efficiency logarithm and grating depth for multilayers on lamellar gratings with N=6 periods multilayers for gratings set#1.	201
C.7	0-Order simulation for wavelength as a function of grating efficiency logarithm and grating depth for multilayers on lamellar gratings with N=6 periods multilayers for gratings set#3.	201
C.8	0-Order simulation for wavelength as a function of grating efficiency logarithm and grating depth for multilayers on lamellar gratings with N=6 periods multilayers for gratings set#2.	201
C.9	Measured and modeled logarithm +1 order diffraction efficiency of the multilayer gratings at $\theta = 5^\circ$ : (a) N=2, (b) N=4, (c) N=6, (d) N=8, (e) N=16, and (f) aperiodic.	202

C.10 Measured and modeled logarithm +1 order diffraction efficiency of the multilayer gratings at $\theta=45^\circ$ : (a) N=2, (b) N=4, (c) N=6, (d) N=8, (e) N=16, and (f) aperiodic. . . . .	202
C.11 Classical and Conical GIXR measurements for multilayers on gratings set#2 (a) periodic ( $N = 4$ ), (b) periodic ( $N = 6$ ), (c) periodic ( $N = 8$ ), (d) periodic ( $N = 10$ ), (e) aperiodic (18 – layers) and (f) aperiodic (24 – layers). . . . .	203
C.12 Classical and Conical GIXR measurements for multilayers on gratings set#3 (a) periodic ( $N = 4$ ), (b) periodic ( $N = 6$ ), (c) periodic ( $N = 8$ ), (d) periodic ( $N = 10$ ), (e) aperiodic (18 – layers) and (f) aperiodic (24 – layers). . . . .	204
C.13 Measured three orders results for all depositions at $\theta=45^\circ$ for gratings set#1. . . . .	205
C.14 Measured zero-order results for all depositions at $\theta=5^\circ$ for gratings set#1. . . . .	205
C.15 Measured zero-order results for all depositions at $\theta=5^\circ$ for gratings set#2. . . . .	206
C.16 Measured zero-order results for all depositions at $\theta=5^\circ$ for gratings set#3. . . . .	206

# List of Tables

2.1	comparison between conventional multilayer and a multilayer grating. . . . .	48
2.2	Overview of the achieved efficiency of different multilayer gratings in various applications. Table adapted and updated from original source [21]. . . . .	49
2.3	EUV spectral lines are emitted by the solar corona according to the CHIANTI database [22]. . . . .	53
2.4	Involvement of Our XUV Optics Group in Past EUV Missions. . . . .	54
2.5	Essential criteria for EUVST instrument performance and design specifications [11]. . . . .	56
3.1	Comparison of the different modes of Atomic Force Microscopy (AFM) - non-contact mode, tapping mode, and contact mode. . . . .	68
3.2	Mean and standard deviation of the dark current. . . . .	75
3.3	Comparison of TEM and STEM. . . . .	78
3.4	Diverse material optical densities and their optical constants at $\lambda = 0.154$ nm. [2]. . . . .	87
4.1	Zeiss's description of the grating before deposition. . . . .	94
4.2	schematic diagram of set#1. . . . .	95
4.3	schematic diagram of set#2 and set#3. . . . .	95
4.4	Average gratings parameters. . . . .	102
4.5	The thickness (T) and density ( $\rho$ ) of the effective layer obtained by the EMA model. . . . .	104
4.6	The grating depth (d), grating slope ( $\alpha$ ), and fill factor ( $f.f$ ) of the effective layer obtained by the RCWA model. . . . .	105
4.7	The grating parameters. . . . .	106
4.8	The choice of a wavelength range depends on the depth of grating grooves. . . . .	108
4.9	The grating parameters. . . . .	111
5.1	Different multilayer designs. . . . .	118
5.2	Layer thickness and interfacial roughness for the optimized periodic Al/Mo/SiC for set#1 on the SiO <sub>2</sub> substrate. . . . .	120



5.3	Comparison of maximum reflectance and broadband for periodic ( $N = 6$ ) and aperiodic (Design 1) multilayer designs for Set#1 . . . . .	121
5.4	Layer thicknesses and interfacial roughness for the optimized periodic Al/Mo/SiC structure for Set#2 on the SiO <sub>2</sub> substrate. . . . .	122
5.5	Comparison of maximum reflectance and broadband for periodic ( $N = 6$ ), aperiodic Design 4, and aperiodic Design 5 of multilayer designs for Set#3 . . . . .	123
5.6	Layer thickness and interfacial roughness for the optimized periodic Al/Mo/SiC for Set#2 on the SiO <sub>2</sub> substrate. . . . .	124
5.7	Comparison of maximum reflectance and broadband for periodic ( $N = 6$ ), aperiodic Design 2, and aperiodic Design 3 of multilayer designs for Set#2 . . . . .	125
5.8	Layer thickness and interfacial roughness used to model the periodic Al/Mo/SiC coating (sample MP20065) on Si substrate. . . . .	130
5.9	Interfacial roughness used to model the aperiodic Al/Mo/SiC coating (sample MP20070) on Si substrate.	132
5.10	Layer thickness and interfacial roughness were used to model the periodic Al/Mo/SiC coating (sample MP20075) on Si substrate. . . . .	134
5.11	Layer thickness and interfacial roughness were used to model the periodic Al/Mo/SiC coating (sample MP20074) on Si substrate. . . . .	135
6.1	RMS roughness of the surface assessed by AFM before and after deposition for multilayer grating Set#1.	147
6.2	RMS roughness of the surface before and after deposition measured by AFM for grating Set#2. . . . .	149
6.3	RMS roughness of the surface before and after deposition measured by AFM for grating Set#3. . . . .	150
6.4	Grating Set#1 parameters used to simulate +1 order efficiencies in Fig.6.15 and Fig.6.16. . . . .	156
6.5	Grating Set#2 parameters used to simulate +1 order efficiencies in Fig.6.18. . . . .	157
6.6	Grating Set#3 parameters used to simulate +1 order efficiencies in Fig.6.19. . . . .	159
7.1	RCWA models parameters for modeling asymmetric trapezoidal multilayer grating. . . . .	173
A.1	The average grating parameters computed from Fig.A.1.(b). . . . .	183
A.2	The proposed multilayers parameters for the gratings. . . . .	183
A.3	Layer thickness and interfacial roughness for the analyzed periodic Al/Mo/SiC of $N = 20$ on the Si substrate. . . . .	184
A.4	Comparative of three distinct optimized multilayer structures, showcasing the layer thicknesses acquired through the optimization process. . . . .	189
A.5	Layer thickness and interfacial roughness for the analyzed periodic Mo/Si of $N = 20$ on the Si substrate.	189
A.6	Multilayer Period and Corresponding Damping Parameters . . . . .	192

B.1	Comparison of DC and RF Magnetron Sputtering . . . . .	195
B.2	the model design thickness for aperiodic design for grating set#1. . . . .	196
B.3	the model design thickness for aperiodic design for grating set#2. . . . .	197
B.4	the model design thickness for aperiodic design for grating set#3. . . . .	198
D.1	Multilayer deposition by magnetron sputtering deposition on the grating set#1 samples. . . . .	207
D.2	Multilayer deposition by magnetron sputtering deposition on the grating set#2 samples. . . . .	208
D.3	Multilayer deposition by magnetron sputtering deposition on the grating set#3 samples. . . . .	209

# List of Publications

## Journals Article

- **Amr Hisham K. Mahmoud**, Sébastien de Rossi, Evgueni Meltchakov, Blandine Capitanio, Muriel Thomasset, Maxime Vallet, Eva Hériprié, and Franck Delmotte, "Al/Mo/SiC multilayer diffraction gratings with broadband efficiency in the extreme ultraviolet," Opt. Express 30, 38319-38338 (2022).

## Conference Paper

- **A. H. K. Mahmoud**, S. de Rossi, E. Meltchakov, E. Papagiannouli, B. Capitanio, M. Thomasset, A. Philippon, F. Auchère, and F. Delmotte "Development of multilayer gratings for Solar-C EUV spectro-imager", Proc. SPIE 12576, EUV and X-ray Optics: Synergy between Laboratory and Space VIII, 1257608 (7 June 2023).



# List of Formations

## List of Conferences

- 317th PTB seminar on VUV and EUV metrology (19 octobre 2021 - 20 octobre 2021) Berlin -Germany
- INTERNATIONAL SCHOOL ON SPACE OPTICS (25 octobre 2021) ESA Conference Bureau / ATPI Corporate Events  
PO Box 299 2200 AG Noordwijk The Netherlands
- Journée Couches Minces Optiques (12 mai 2022) Institut Fresnel-Toulouse
- SPIE Optics + Optoelectronics 2023 (24–27 April 2023) Prague, Czech Republic



# List of Abbreviations

<b>Symbol</b>	<b>Description</b>
$\lambda$	wavelength
$E$	energy
$h$	Planck's constant
$c$	speed of light in vacuum
$n$	refractive index
$f_1$	real part of the atomic scattering factor
$f_2$	imaginary part of the atomic scattering factor
$r_e$	classical electron radius
$N_A$	electron density
$1-\delta$	real refractive index
$\beta$	imaginary refractive index
$\theta$	normal incidence angle
$\psi$	grazing incidence angle
$l_{\text{atten}}$	attenuation length
$\Phi$	phase of the peak
$t$	thickness of illuminated multilayer period
$\lambda_0$	central wavelength
$L$	coherence length
$\phi$	angle of diffraction
$N$	Number of illuminated multilayer periods or Number of iteration
$N_T$	Total number of multilayer periods
$\lambda/\Delta\lambda$	Spectral resolution
$R$	Reflectance
$I$	Intensity
$\mu$	Mean

<b>Symbol</b>	<b>Description</b>
$S$	Standard deviation
$d$	Grating depth
$\alpha$	Trapeze angle
$f.f$	Fill factor
$\rho$	Density
$T$	Thickness of one layer
$m$	Order of diffraction
$\alpha_1$	Right slope angle of asymmetric trapezoidal gratings
$\alpha_2$	Left slope angle of asymmetric trapezoidal gratings
$X_{part}$	Projection of grating slope
$P$	Periodicity of the gratings
$\omega$	Angle between incidence angle and grooves alignment

# Résumé

En combinant le phénomène d'interférences à ondes multiples (pour une grande efficacité) et la diffraction sur une structure périodique (pour une haute résolution spectrale), les réseaux multicouches présentent un grand potentiel pour l'instrumentation dans l'extrême ultraviolet (EUV). Notre étude marque la première investigation expérimentale des réseaux multicouches EUV visant à atteindre une efficacité large bande. Plus précisément, nous avons obtenu une largeur de bande sans précédent en utilisant des réseaux multicouches aperiodiques tout en maintenant un niveau raisonnable d'efficacité. Les simulations numériques réalisées se sont révélées efficaces pour optimiser de nouveaux composants. Ces découvertes ouvrent la voie à la conception d'instruments dotés de capacités accrues dans les applications de spectrométrie haute résolution EUV et de spectro-imagerie.

## Objectifs du doctorat

Avant de commencer mon doctorat, j'ai eu le privilège d'effectuer un stage de six mois au sein du groupe Optique XUV du Laboratoire Charles Fabry. Le titre de mon stage était "propriétés optiques et optimisation de matériaux à films minces pour les applications aux rayons X." Les recherches menées au cours de mon doctorat sont une extension directe du travail initié pendant ce stage. Tout au long de mon stage et de mon doctorat, l'objectif principal était de concevoir et d'optimiser un composant optique à revêtement multicouche pour les applications dans le domaine de l'extrême ultraviolet. Initialement, notre plan pour le stage impliquait la réalisation de travaux expérimentaux. Cependant, en raison de la pandémie de COVID-19, nous avons dû adapter notre approche et orienter nos travaux vers la modélisation. En revanche, pendant mon doctorat, j'ai eu l'opportunité d'effectuer des travaux expérimentaux et des mesures de caractérisation. Pour atteindre nos objectifs de recherche, nous avons utilisé le logiciel IMD pour résoudre les équations de Fresnel et comparé nos simulations avec le code MATLAB utilisant l'analyse rigoureuse des ondes couplées pour résoudre numériquement les équations de Maxwell. De plus, j'ai reçu une formation sur le diffractomètre Bruker Discover D8 et le logiciel LEPTOS, qui intègre un algorithme génétique pour l'ajustement des mesures. Cependant, au cours de mon doctorat, l'accent s'est déplacé vers l'utilisation du logiciel IMD pour l'optimisation et les ajustements. Le cœur de notre recherche a porté sur la caractérisation des réseaux à l'aide de la réflectométrie aux rayons X pour optimiser le réseau multicouche pour le projet de spectro-imagerie de la mission Solar-C. Nous avons reçu trois ensembles de réseaux de silice à haute densité avec des profondeurs de

rainure variables, allant de 5 nm à 22 nm. Ces réseaux ont été fabriqués par la société Zeiss spécifiquement comme échantillons de test pour le miroir multicouche réel qui sera utilisé dans l'instrument Solar C. Solar C est un projet spatial impliquant la NASA, l'ESA, la JAXA, des instituts européens et américains. Son objectif principal est d'observer et de détecter les températures dans la plage EUV de la chromosphère, de la couronne solaire en utilisant un nombre minimal d'éléments optiques, à savoir un réseau de diffraction et un miroir primaire. Le projet vise à maximiser la collecte du rayonnement solaire UV, visant à atteindre des efficacités dix à trente fois plus grandes que les instruments précédents, tout en assurant une résolution spatiale et temporelle extrême. Contribuant de manière significative à la mission Solar C, le Laboratoire Charles Fabry a joué un rôle clé dans le développement et la production du réseau pour le Spectro-imageur, qui opère à des longueurs d'onde entre 17 nm et 21 nm. Notre activité de recherche était dédiée à la caractérisation et à la modélisation du réseau nu tout en optimisant les revêtements multicouches périodiques et aperiodiques. Par la suite, nous avons utilisé la technique de dépôt par pulvérisation magnétron pour déposer la multicouche sur les réseaux de silice, suivie d'une caractérisation à l'aide de divers outils tels que la Microscopie à Force Atomique (AFM), la Réflectométrie aux Rayons X en Incidence Rasante (GIXR) et la métrologie EUV. Notre objectif était d'atteindre une efficacité de diffraction de l'ordre +1 en large bande supérieure à celle obtenue dans les travaux précédents pour la mission Solar B. Le travail a présenté plusieurs défis, notamment l'évolution de la multicouche sur les rainures du réseau, la rugosité en haut et en bas des rainures, et la haute densité des rainures. Ces facteurs ont contribué à des altérations dans la forme du profil des rainures principales après le dépôt de la multicouche, ayant un impact négatif sur l'efficacité maximale de la diffraction de l'ordre utile. De plus, le choix de la composition appropriée pour la multicouche a posé des défis, de même que les problèmes liés au dépôt de la multicouche, tels que la rugosité, l'interdiffusion, la formation de couches d'interface et l'oxydation.

## Résumé de thèse

Dans cette thèse, nous présentons des résultats expérimentaux et des modèles de réseaux multicouches développés pour le spectromètre-imageur EUV du projet de mission spatiale Solar-C. Des multicouches périodiques Al/Mo/SiC ont été optimisées et déposées par pulvérisation magnétron sur des réseaux trapézoïdaux à haute densité de rainures avec des profondeurs variables. La caractérisation de tous les échantillons de réseaux a été réalisée à l'aide d'un microscope AFM et d'un réflectomètre à 8,05 keV, avant et après le dépôt des multicouches. L'évolution du profil de surface avec l'augmentation du nombre de couches déposées a été observée grâce aux mesures AFM, ce qui a été confirmé par une analyse en coupe au microscope électronique à transmission. L'efficacité de diffraction EUV des réseaux multicouches a été évaluée en utilisant un rayonnement synchrotron monochromatique sur la ligne de métrologie du synchrotron SOLEIL. Les résultats obtenus concordent bien avec les simulations obtenues par l'analyse rigoureuse des ondes couplées (RCWA), en intégrant les paramètres structuraux déterminés par l'AFM et le GIXR. L'efficacité du premier ordre mesurée à incidence quasi-normale atteint un maximum d'environ 9,27%, 6,54% et 7,18% pour des longueurs d'onde de 27,3 nm, 21,4 nm et 19,4 nm, respectivement. La thèse est rédigée en



anglais et elle se compose de huit chapitres accompagnés de quatre annexes.

- Dans le **chapitre 2**, nous fournissons une vue d'ensemble de l'optique des rayons X, comprenant des discussions sur l'interaction des matériaux, les réseaux, et les réseaux multicouches. Nous explorons également l'histoire et l'importance des missions d'observation solaire et du projet Solar C.
- Dans le **chapitre 3**, nous expliquons la physique et le fonctionnement des outils utilisés pour le dépôt, la caractérisation et la simulation de multicouches sur des réseaux. Nous discutons des critères de mesure des spectres angulaires et normaux, analysons les données de l'AFM et du TEM, et explorons des outils de simulation tels que IMD et RCWA.
- Dans le **chapitre 4**, nous caractérisons les réseaux de la société Zeiss, en comparant les paramètres à l'aide d'un graphique à barres. Nous analysons les spectres angulaires, distinguons les caractéristiques entre les positions classiques et coniques, et extrayons les paramètres absolus à l'aide de deux modèles. De plus, nous étudions l'impact des paramètres du réseau sur l'efficacité.
- Dans le **chapitre 5**, nous optimisons les revêtements multicouches périodiques et aperiodiques sur des substrats en silicium plat à l'aide du logiciel IMD. Nous mettons en évidence les avantages de la combinaison de matériaux Al/Mo/SiC et discutons de la sensibilité de la multicouche. Nous examinons les effets d'une couche de protection sur la réflectance et la largeur de bande, déposons avec succès la multicouche optimisée, et utilisons diverses techniques de caractérisation pour l'analyse.
- Dans le **chapitre 6**, nous avons étudié l'impact des paramètres du réseau sur l'efficacité de diffraction de l'ordre +1. Les réseaux multicouches ont été caractérisés à l'aide de l'AFM, du TEM et d'une ligne de métrologie. L'évolution de la multicouche a été documentée. Notre modèle incorpore l'équation de Debye-Waller. Les résultats ont été comparés aux études précédentes de la mission Solar B.
- Dans le **chapitre 7**, nous avons modélisé les spectres angulaires des réseaux multicouches en position classique et conique. Les alignements absolus des rainures ont été déterminés à l'aide de spectres angulaires coniques. Nous avons mesuré la diffraction conique à l'incidence quasi-normale et amélioré la modélisation avec des réseaux trapézoïdaux asymétriques.
- Dans le **chapitre 8**, nous avons présenté la conclusion de la thèse et discuté des orientations futures de ces travaux de recherche.

## Mots-clés.

Multicouches, Approximations de Milieu Effectif, Réflectométrie aux Rayons X, Optique des Rayons X, et Films Minces.

# Chapter 1

## Context of the PhD

The PhD program was completed at the Laboratoire Charles Fabry, Optique XUV group of the Institute d'optique graduate school. This research group focuses on developing original ideas for the manipulation and utilization of XUV radiation, with wavelengths ranging from 100 nm to 0.1 nm. Various fields such as solar imaging and attosecond physics rely on this XUV radiation and require the development of optical components and systems at the limits of technological expertise and metrology. The group activities revolve around the following research areas.

1. Material study, design, and fabrication of coatings
2. Design and implementation of advanced optical systems
3. Digital processing for attosecond metrology

### 1.1 PhD Objectives

Prior to starting my PhD, I had the privilege of completing a six-month internship with the Optique XUV group at Laboratoire Charles Fabry. The title of my internship was "Optical Properties and Optimization of Thin-Film Materials for X-ray Applications." The research undertaken during my doctorate is a direct extension of the work initiated during this internship.

Throughout both my internship and doctorate, our primary objective was to design and optimize a multilayer mirror component for X-ray applications. Initially, our plan for the internship involved conducting experimental work. However, due to the COVID-19 pandemic, we had to adapt our approach and shift our focus towards modeling. In contrast, during my doctorate, I had the opportunity to perform experimental work and characterization measurements.

To accomplish our research goals, we employed IMD software to solve Fresnel equations and compared our simulations with MATLAB code that utilized Rigorous coupled-wave analysis for numerically solving the Maxwell

equation. Additionally, I received training on the Bruker Discover D8 diffractometer and LEPTOS software, which incorporated a genetic algorithm for fitting measurements. However, during my PhD, the emphasis shifted towards utilizing IMD software for optimization and fittings.

The core of our research revolved around characterizing gratings using x-ray reflectometry to optimize the multilayer grating for the Spectro imaging project within the Solar-C mission. We were provided with three sets of high-density silica gratings with varying groove depths, ranging from 5 nm to 22 nm. These gratings were fabricated by Zeiss company specifically as test samples for the actual multilayer grating mirror that will be used in the "EUV High-Throughput Spectroscopic Telescope" for the Solar C project.

The Solar C project is a collaborative endeavor involving NASA, ESA, JAXA, European institutes, and the United States. Its primary objective is to observe and detect temperatures in the EUV range from the chromosphere, corona, and flare plasmas using minimal optical elements, namely a diffraction grating and a primary mirror. The project strives to maximize the collection of solar UV radiation, aiming to achieve effective areas 10-30 times larger than previous instruments, while ensuring extreme spatial and temporal resolution.

Significantly contributing to the Solar C mission, the Laboratoire Charles Fabry played a pivotal role in the development and production of the grating component for the Spectro-imager EUVST, which operates at wavelengths around 19 nm and 27 nm. Our research group was dedicated to characterizing and modeling the uncoated grating while optimizing periodic and aperiodic multilayer coatings. Subsequently, we employed magnetron sputtering deposition to deposit the multilayer onto the silica gratings, followed by characterization using various tools such as Atomic Force Microscopy (AFM), Grazing Incidence X-ray Reflectometry (GIXR), and EUV metrology.

Our objective in PhD involved achieving higher broadband +1-order diffraction efficiency compared to the +1-order diffraction efficiency achieved in previous work for the Solar B mission.

The work presented several challenges, including the evolution of the multilayer on the grating grooves, roughness at the top and bottom of the grooves, and the high groove density. These factors contributed to alterations in the profile shape of the primary grooves after the multilayer deposition, negatively impacting the peak efficiency of the +1-order diffraction. Additionally, selecting the appropriate material composition for the multilayer posed challenges, as did issues related to multilayer deposition, such as roughness, interdiffusion, interface layer formation, and oxidation.

## 1.2 Abstract

In this thesis, we present experimental results and modeling of multilayer gratings developed for the EUV spectro-imager aboard Solar-C mission. Periodic Al/Mo/SiC multilayers were optimized and deposited by magnetron sputtering on high groove density trapezoidal gratings with varying depths. AFM and GIXR at 8.05 keV were used to characterize all grating samples before and after multilayer deposition. The evolution of the surface profile with an

increasing number of deposited layers was observed through AFM measurements, which was further confirmed by a transmission electron microscope cross-section analysis. The EUV diffraction efficiency of the multilayer gratings was evaluated using monochromatic synchrotron radiation on the XUV Metrology beamline at SOLEIL Synchrotron. The obtained results agree well with the model simulated by rigorous coupled-wave analysis, incorporating structural parameters determined by AFM and GIXR. The measured first-order efficiency at near-normal incidence reaches a maximum of approximately 9.27%, 6.54%, and 7.18% for wavelengths of 27.3 nm, 21.4 nm, and 19.4 nm, respectively.

The thesis is divided into eight chapters and four appendices.

- In **Chapter-2**, we provide an overview of x-ray optics, including discussions on materials' interaction, gratings, and multilayer gratings. We also explore the history and significance of solar observation missions and the Solar C project.
- In **Chapter-3**, we explain the physics and operation of tools used for depositing, characterizing, and simulating multilayers on gratings. We discuss criteria for measuring angular and normal spectra, analyze data from AFM and TEM, and explore simulation tools like IMD and RCWA.
- In **Chapter-4**, we characterize gratings from Zeiss Company, comparing parameters using a bar chart. We analyze angular spectra, distinguish characteristics between classical and conical positions, and extract absolute parameters using two models. Additionally, we investigate the impact of grating parameters on efficiency.
- In **Chapter-5**, we optimize periodic and aperiodic multilayer coatings on flat silicon substrates using IMD software. We highlight the advantages of the Al/Mo/SiC materials combination and discuss the sensitivity of the multilayer. We examine the effects of a cap layer on reflectance and bandwidth, successfully deposit the optimized multilayer, and employ various characterization techniques for analysis.
- In **Chapter-6**, we studied the impact of grating parameters on +1-order diffraction efficiency. Multilayer gratings were characterized using AFM, TEM, and a metrology beamline. The multilayer evolution was documented. Our model, incorporating the Debye-Waller equation, simulated the efficiency. Results were compared with previous Solar B mission studies.
- In **Chapter-7**, we modeled the angular spectra of multilayer gratings in the classical position. Absolute groove alignments were determined using conical angular spectra. We measured conical diffraction at the near-normal incidence and improved modeling with asymmetric trapezoidal gratings.
- In **Chapter-8**, we provided the thesis conclusion and discussed future research directions.

### 1.3 Keywords

Multilayer, Effective Medium Approximations, X-Ray Reflectometry, X-Ray Optics, and Thin Film.



## Chapter 2

# Introduction

Over the last few years, there has been notable progress in the advancement of extreme ultraviolet and soft X-ray (XUV) multilayer optics. A significant focus has been placed on manipulating the spectral properties of light for various advanced applications such as EUV photolithography, space observation, and accelerator- or lab-based XUV experiments. Both planar and grating multilayer structures have been developed to precisely control the spectral response across a wide range of wavelengths. In the case of planar multilayer optics, diverse layered configurations have been investigated, including stacks of periodic multilayers and capping layers. These configurations have successfully achieved either the reflection of multiple channels or the suppression of reflective properties.

Ongoing research endeavors are dedicated to investigating diverse multilayer grating configurations with the aim of achieving high-resolution and high-efficiency XUV spectrometers/monochromators. These configurations include multilayer-coated gratings, sliced multilayer gratings, and lamellar multilayer gratings, each presenting their own set of advantages and disadvantages in terms of performance. Additionally, advancements have been made in developing multilayer diffraction optics to enhance spectral purity. A comprehensive review has also been conducted on emerging structures such as gratings, zone plates, and pyramids, which exhibit pronounced capabilities in effectively suppressing unwanted radiation and exhibiting exceptional XUV reflectance.

This chapter will provide an introduction to various topics related to Extreme Ultraviolet (EUV) and X-ray physics. It will cover the fundamentals of Thin Film Optics, including the behavior of materials in the EUV range. The physics of multilayer structures and gratings will also be discussed, exploring their underlying principles and properties. Furthermore, the chapter will delve into the physics of multilayer optics, examining their unique characteristics. Lastly, the Solar C project will be introduced as a specific area of study within the context of this thesis.

## 2.1 Extreme ultraviolet and X-ray regions

X-ray is electromagnetic radiation with wavelengths ranging from approximately 0.01 nm to 10 nm (roughly 100 keV to 100 eV), as depicted in Figure 2.1. The energy of X-ray photons is significantly higher than that of visible light photons. These rays were first discovered by the German physicist Wilhelm RÖNTGEN in 1895 [23], and possess intriguing properties for material analysis, as their energy is near the binding energy of the internal electronic shells of an atom (of the order of keV). The distinction between soft-X and hard-X radiation is not universal and varies among scientific communities, but many consider the boundary to range from  $E = 5\text{eV}$  to  $E = 10\text{KeV}$ . Electromagnetic wave units are expressed either in wavelength (in nanometers [nm]) or in energy  $E$  (in electron volts [eV]), depending on the scientific community. The relationship between wavelength and photon energy is defined as follows:

$$E = h \cdot \nu = \frac{h \times c}{\lambda} = 1239.8[\text{nm} \cdot \text{eV}] \frac{1}{\lambda} \quad (2.1)$$

where:  $h = 6,626 \times 10^{-34} \text{ J} \cdot \text{s}$  ( $= 4,135 \times 10^{-15} \text{ eV} \cdot \text{s}$ ) is Planck's constant,  $c = 2,998 \times 10^8 \text{ m/s}$  is the speed of light in vacuum.

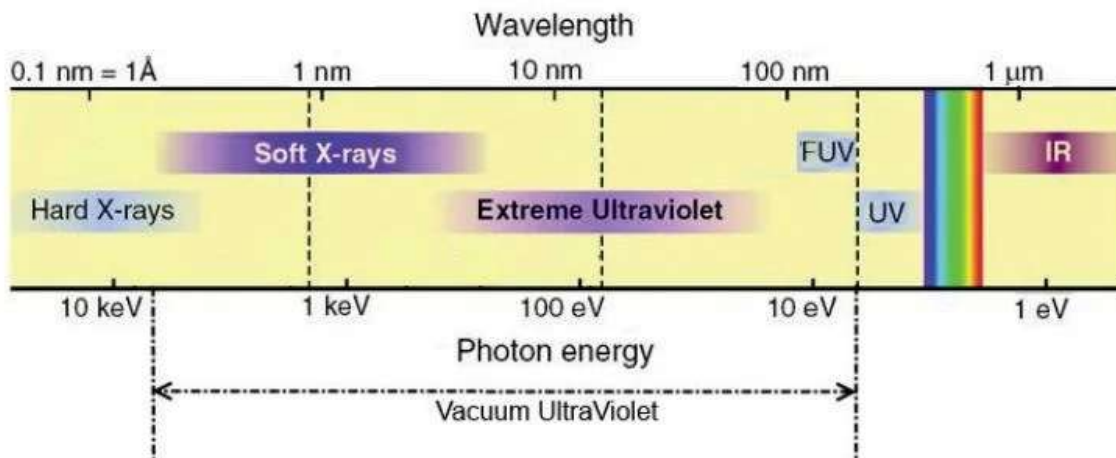


Figure 2.1: EUV Electromagnetic spectrum [1].

Extreme ultraviolet (EUV) is a segment of the electromagnetic spectrum, illustrated in Figure 2.1, ranging approximately from 30 eV ( $\lambda=40 \text{ nm}$ ) to 250 eV ( $\lambda=5 \text{ nm}$ ) [24]. The spectral region has two distinct characteristics.

1. The resolution of any optical system can be approximated as  $\Delta \approx \lambda/NA$ , where  $\lambda$  and  $NA$  represent the wavelength and the numerical aperture, respectively. This approximation holds true because, in the EUV region, the wavelengths are incredibly short. As a result, EUV and soft X-ray microscopy have the potential to visualize small structures.

2. The EUV and X-ray regions encompass absorption edges for both low and high atomic numbers, as well as atomic resonances, enabling the chemical and physical identification of materials. Numerous techniques rely on these scientific properties, including emission spectroscopy and absorption spectroscopy.

## **2.2 Thin film optics**

The phenomenon of light interference can be used to improve the optical response of a surface, making thin film technology an important aspect of modern optics [25]. Thin film coatings can optimize the spectral characteristics of a surface for a desired range of wavelengths [25]. This technology has a wide range of applications in research and industry, such as environmental monitoring, anti-counterfeiting devices, clean energy, solar cells, lasers, telecommunications, astronomy, aerospace, smart windows, and light-emitting diodes [26; 27; 28]. For example, an anti-reflective coating with only a few layers can suppress the Fresnel reflection of a lens over a broad range of wavelengths [29]. Optical coatings can also provide high reflectance values, up to 99.99%, for a specific wavelength range using a layer stack with low and high refractive materials. Additionally, thin film technology enables the production of spectral filters with a broad range of characteristics that are required in modern optics and laser technology. The current progress in thin film technology allows for combining the necessary optical properties with other significant features, such as the mechanical, thermal, or chemical stability of a surface.

Thin-film optics have revolutionized the fields of EUV and soft X-ray microscopy by enabling high-performance optics for these spectral ranges. Conventional lens optics cannot be used in these ranges due to the extreme opacity of materials for these radiation bands. Additionally, the wavelengths of these radiations are not small enough to approach Bragg reflection conditions for most crystals in X-ray diffraction, nor are they extensively reflected by standard mirrors at normal incidence. However, the development of highly reflective multilayer interference mirrors has changed the situation completely [30]. Now, many areas of science and technology, including microscopy, material science, lithography, biology, and molecular chemistry, can be improved by employing EUV and soft X-rays.

### **2.2.1 Deposition Techniques for Thin Film and Coating.**

In recent years, advanced techniques for depositing thin films and coatings have emerged, allowing for precise control over layer thickness and composition [31]. One of these techniques is atomic layer deposition (ALD)[31], which involves the cyclical deposition of two or more precursor chemicals to create extremely thin layers with accurate material composition control. Another technique, molecular beam epitaxy (MBE)[31], is ideal for the growth of semiconductor materials and uses a high-vacuum environment and molecular or atomic beams to deposit thin films with exceptional control over layer thickness and composition, resulting in high-quality films with few defects. Physical vapor deposition (PVD)[31] is another widely used technique that employs methods such as sputtering or



evaporation to deposit material in a high-vacuum environment for applications ranging from decorative coatings to semiconductor fabrication. Additionally, emerging deposition methods such as pulsed laser deposition (PLD)[31], which uses a laser to vaporize a target material and chemical vapor deposition (CVD)[31], which deposits thin films through the reaction of precursor gases on a heated substrate, show promise for the growth of thin films and coatings. In summary, advanced deposition techniques offer enhanced precision and control over the growth of thin films and coatings, enabling the development of high-performance materials for various applications.

In this thesis, the sputtering technique was employed due to its widespread usage in EUV multilayers. This technique offers several advantages, including the ability to achieve smooth interfaces and precise control over layer thickness.

## 2.2.2 Material response at EUV range

The fundamental hypothesis in the X-ray domain is that condensed matter can be modeled by atoms without interaction (“atom-like behavior”). This hypothesis is generally good for energies far enough from the absorption thresholds of the material considered. In the regions of threshold, the specific chemical state influences the interaction of the x-ray with the matter, and experimental measurements of the optical indices are required. The material index ( $n$ ) can be written depending on the atomic scattering factor  $f$  ( $f = f_1 + i f_2$ ). The imaginary part  $f_2$  characterizes the whole attenuation processes in the medium, which can be measured by photo absorption and the real part  $f_1$  corresponds to the number of free electrons participating in the diffusion of the electromagnetic wave.  $f_1$  and  $f_2$  are related by the relations of Kramers-Kronig [32]. In consequence, one can calculate  $f_1$  by using the experimental values of  $f_2$ . Henke *et al.* [33] established a data table grouping the experimental and theoretical values of  $f_1$  and  $f_2$  for a wide range of energy (10 eV - 30 keV). The optical index  $n$  is written in the following form for a simple element:

$$n(E) = 1 - \frac{N_A r_e \lambda^2}{2\pi} (f_1(E) + i f_2(E)) \quad (2.2)$$

Where  $r_e$  is the classic electron beam ( $\approx 2.82 \times 10^{-15}$  m),  $N_A$  is the number of atoms per unit volume. In the case of a body consisting of several materials, it can be written as

$$n(E) = 1 - \frac{r_e \lambda^2}{2\pi} \sum_i N_i (f_1(E) + i f_2(E)) \quad (2.3)$$

$N_i$  is the number of atoms of species  $i$  per unit volume. In practice, we utilize the coefficient  $\delta$  and  $\beta$  defined by the following equation

$$n(E) = 1 - \delta(E) - i\beta(E) \quad (2.4)$$

where,

$$\delta(E) = \frac{N_A r_e \lambda^2}{2\pi} f_1(E) \quad (2.5)$$

$$\beta(E) = \frac{N_A r_e \lambda^2}{2\pi} f_2(E) \quad (2.6)$$

The index's real part ( $1-\delta$ ) is slightly lower than one, indicating low refraction, which behaves differently from the typical crossing of a diopter by visible radiation. In this case, the angle of incidence ( $\theta_1$ ) is greater than the refracted angle of the middle ( $\theta_2$ ), whereas, in the visible range,  $\theta_1$  is less than  $\theta_2$ . Although the absorption of radiation is minimal, it cannot be ignored. The attenuation length ( $l_{atten}$ ), which is determined by the following equation, is used to measure absorption.

$$l_{atten} = \frac{\lambda}{4\pi\beta} \quad (2.7)$$

The attenuation length is expressed as the distance into a material where the beam flux has fallen to  $\approx 37\%$  ( $1/e$ ) of its incident flux.

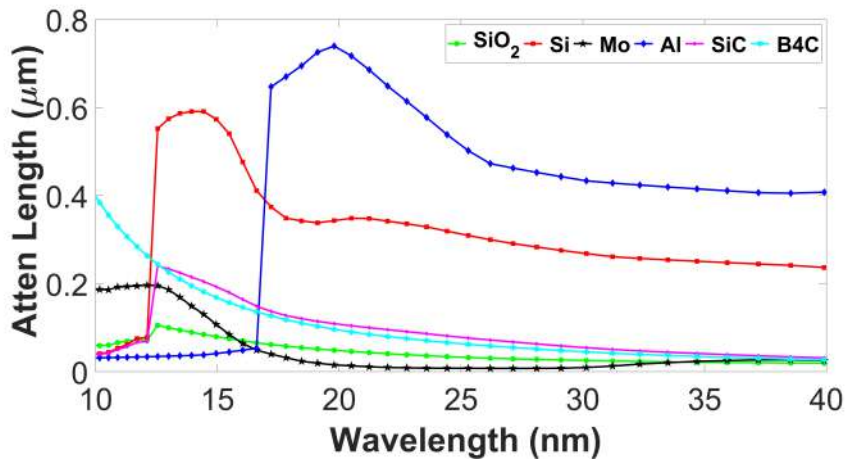


Figure 2.2: variation of attenuation length with wavelength for different materials [2].

In this thesis, the material amorphous silica ( $a - SiO_2$ ) is employed, as depicted in Fig.2.2 [2]. Figure 2.2 demonstrates that the attenuation length in the EUV x-ray domain is below 1 micron across the desired range. Among the materials investigated, molybdenum (Mo) exhibits the lowest attenuation length, measuring slightly less than 0.2 microns. For silicon carbide (SiC) and boron carbide (B4C), the attenuation length falls below 0.2 microns after a wavelength of 15 nm. Despite silicon (Si) having a higher attenuation length compared to Mo and  $a - SiO_2$ , it decreases to less than 0.5 microns after 17 nm. On the other hand, aluminum (Al) exhibits the highest attenuation length among all the materials in Fig.2.2. At 20 nm wavelengths, its attenuation length is  $0.7\mu m$ , which gradually decreases to 0.5 microns at 40 nm wavelength.

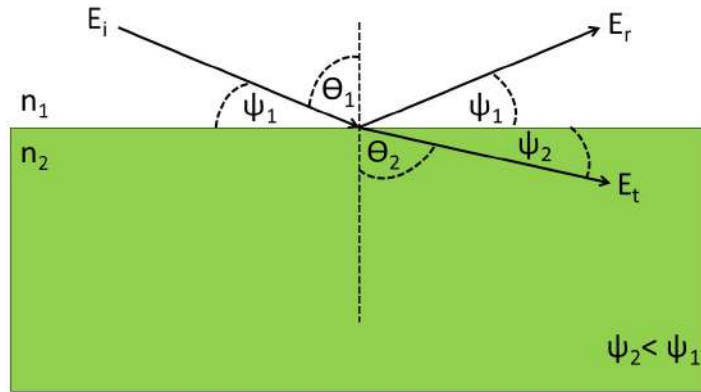


Figure 2.3: representation of the reflection and transmission of an electromagnetic wave at the interface between their medium indices  $n_1$  and  $n_2$  ( $n_1 > n_2$ ).

The total reflection is one of the ways to reflect X-rays: this phenomenon is produced only [2; 34] for very small grazing angles ( $\theta_1 < \theta_c$ , where  $\theta_c$  is the critical angle), according to Snell's law, at the interface between two media  $n_1$  and  $n_2$  (Fig.2.3). If we assume negligible absorption ( $\beta = 0$ ),

$$n_1 \sin(\theta_1) = n_2 \sin(\theta_2) \quad (2.8)$$

With  $\theta_1$  the angle of incidence and  $\theta_2$  the angle of refraction. In case of working with the grazing angles such as  $\psi_1 = \frac{\pi}{2} - \theta_1$  and  $\psi_2 = \frac{\pi}{2} - \theta_2$ , the equation (1.8) will be modified to

$$n_1 \cos(\psi_1) = n_2 \cos(\psi_2) \quad (2.9)$$

In addition, if  $n_1=1$  (vacuum index) and if  $n_2=n$  (media index), and we are at the total external reflection, we will find the critical angle (limit of  $\theta_1$  for which  $\theta_2=0$ ) will be equal to

$$\cos(\psi_c) = n \quad (2.10)$$

The critical angle is valid in the approximation of weekly absorbent materials ( $\beta \rightarrow 0$  and therefore  $n=1-\delta$ )

$$\psi_c = \arccos(1 - \delta) \quad (2.11)$$

Which becomes for  $\delta \ll 1$  and after a limited development of arcs ( $1-\delta$ ) to order 1

$$\psi_c \approx \sqrt{2\delta} \quad (2.12)$$

The critical angle for total external reflection, typically falling within the range of approximately  $0.2^\circ$  to  $1^\circ$  for a

wavelength of around 0.1 nm, is known for its small magnitude. Interferences originating from thin films primarily occur within a narrow range near the critical angle, assuming a single layer on the substrate.

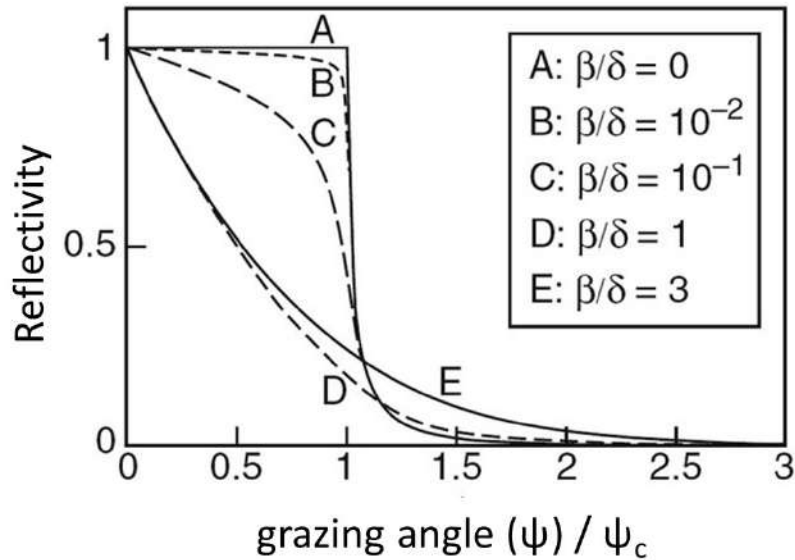


Figure 2.4: The reflectivity as a function of the normalized grazing angle can be represented by a stepwise change in reflection for low absorption ( $\beta$ ), while for higher absorption, a more gradual enhancement becomes evident. [3].

Reflectometry, a technique highly responsive to electron density and absorption, demonstrates independence from factors such as crystallinity and crystal texture. The reflectivity can be precisely determined using established Fresnel equations [35]. Figure.2.4 depicts the reflection behavior for different ratios of  $\beta/\delta$ , demonstrating the sensitivity of such measurements to chemical composition [3].

## 2.3 Multilayer Physics

### 2.3.1 Multilayer mirror

Multilayer mirrors are commonly used to achieve high optical reflectivity. Typically, they consist of two or three different materials [12; 17] that are stacked on top of each other to achieve maximum reflectivity within a particular wavelength range.

A basic multilayer is a periodic stack made of a periodic combination of nm-scale bi-layers (see Figure.2.5(a)) or tri-layers. The material with lower density (low  $Z \Rightarrow$  low  $\delta$  & low  $\beta \Rightarrow$  high  $n$ ) is the spacer while the one with higher density (high  $Z \Rightarrow$  high  $\delta$  & high  $\beta \Rightarrow$  low  $n$ ) is the absorber. The selection of materials is usually based on their significant differences in refraction coefficients and low absorption coefficients.

The reflectance peak at a target wavelength, usually called “the central wavelength,” is achieved by optimizing the layer thicknesses in order to add all reflected components at each interface in phase. Although the precise

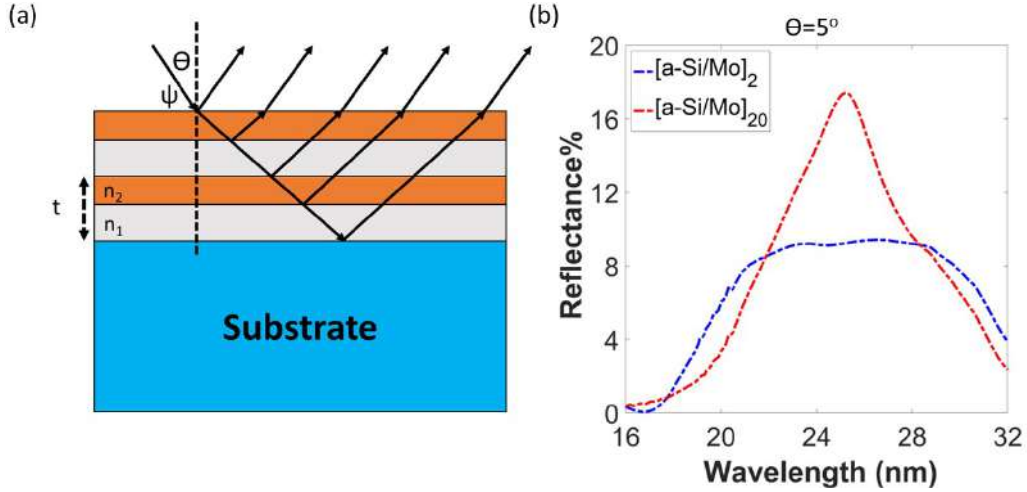


Figure 2.5: (a) The diagram below illustrates the X-ray reflection at a 2-periods multilayer mirror, and (b) The right graph shows the reflectance at  $\theta=5^\circ$  of an optimized 2-periods, and 20-periods multilayer mirror consisting of a-Si (7.45nm) and Mo (6.23nm) over a Si substrate, without taking into account the roughness.

calculation of multilayer optical performance requires the recursive application of the Fresnel coefficients at each interface, it is possible to use an approximate relationship. By neglecting the small effects of the refraction occurring within each layer, the phase difference between the radiation reflected by two consecutive multilayers is given by:

$$\Delta\Phi = \frac{2\pi}{\lambda_o} 2t \cos \theta \quad (2.13)$$

In the provided equation,  $t$  represents the total thickness period of the multilayers,  $\theta$  signifies the incidence angle measured with respect to the surface normal direction, and  $\lambda_o$  corresponds to the target or central wavelength. Constructive interference occurs when the phase difference is an integer multiple of  $2\pi$ . The  $\psi$  in Fig.2.5(a) represents the angle of grazing incidence, which denotes the angle between the incident beam and the surface of the multilayer, where  $\psi+\theta=90^\circ$ . In the case of EUV multilayers, it is customary to introduce a phase delay of exactly  $2\pi$  to satisfy the following condition:

$$N\lambda_o = 2t \cos \theta = 2t \sin \psi \quad (2.14)$$

Here,  $N$  is an integer that represents the order of the interference. Equation 2.14, known as Bragg's law [36], describes the reflectance behavior of multilayer mirrors. By selecting the period of the bi-layer or tri-layer structure in accordance with eqn.2.14, constructive interference of the reflected beam can be achieved.

Furthermore, the design of these coatings involves finding a balance between different mirror properties, including power reflectivity, spectral selectivity, phase, and polarization. These properties are closely tied to the specific application requirements and thus require careful consideration during the design process.

It is important to note that for EUV wavelengths and near-normal incidence, the period of multilayers is approx-

imately half the wavelength, as stated in eqn.2.14 and reference [30]. This explains why each layer's thickness is extremely thin, typically in the nanometer range. At these wavelengths, interactions with matter are weak, resulting in a refractive index ( $n$ ) that is close to unity for X-rays. Therefore, eqn.2.4 is used to calculate the X-ray refractive index.

In order to enhance the performance of a multilayer mirror, it is crucial to optimize the characteristics of the absorber and spacer layers. The absorber layer should possess a high value of  $\delta$  and a low value of  $\beta$ , while the spacer layer should have low values for both  $\delta$  and  $\beta$ . This ensures efficient reflection and minimal absorption of the incident light, leading to improved mirror performance.

In addition, The presence of a multilayer stack enables a significant increase in reflectance within a spectral band centered on the desired wavelength. For an approximate estimation of the bandwidth, the temporal coherence exhibited by the multilayer stack can be taken into account. In particular, it is essential to ensure the coherent addition of the waves reflected by the inner layers with those originating from the top surface. This coherence criterion implies that the overall optical thickness of the multilayer should be proportionate to the coherence length of the stack. As a result, we derive the following relationship:

$$L = \frac{\lambda_o^2}{\Delta\lambda} \propto 2N_T t \Rightarrow \Delta\lambda \propto \frac{1}{N_T} \quad (2.15)$$

The spectral band, denoted as  $\Delta\lambda$ , represents the "full width at half maximum" (FWHM). Equation.(2.15) indicates that a narrow-band response can be achieved by increasing the number of multilayers in the stack. However, the absorption characteristics of the materials used in the multilayer stack impose a maximum penetration depth, limiting the interaction of the impinging radiation with certain multilayer periods.  $N_T$  denotes the total number of multilayer periods.

Consequently, for a periodic multilayer utilizing specific materials, there exists a lower limit for the bandwidth that cannot be surpassed by increasing the multilayer periods. Conversely, it is common practice to broaden the spectral response by reducing the number of layers. However, this approach also results in a reduction in peak reflectance. Fig.2.5(b) presents a clear illustration of the phenomenon discussed. It depicts a simulation showcasing the optimization of reflectance in a-Si/Mo multilayers. Specifically, two and twenty periods are compared. The results indicate that while the 20-period configuration exhibits a higher maximum reflectance, it demonstrates lower broadband reflectance when compared to the 2-period configuration.

### 2.3.2 Multilayer Synthesis

The performance of a multilayer mirror is highly dependent on the choice of materials, particularly in the range of  $6\text{nm} < \lambda < 35\text{nm}$ , as noted in reference [37].

Spacer and absorber layers within multilayer systems play a crucial role in the control and manipulation of optical

properties.

**Spacer layers** serve to regulate the optical path length between two interfaces, offering control over interference effects that can either amplify or diminish specific light wavelengths. The thickness of the spacer layer can be precisely adjusted to achieve this effect. It is advisable to craft these spacer layers from materials that resist hydrogen diffusion and blistering, such as nitrides and carbides. Moreover, the spacer layers are preferably grown in an amorphous structure to function effectively as barriers against hydrogen diffusion. In some cases, certain materials exhibit microcrystalline growth in thin layers, making hydrogen diffusion more manageable along grain boundaries within crystalline layers. Hence, amorphously grown layers with minimal defect densities are favored as hydrogen barriers. Carbides, borides, and nitrides are highly regarded for their ability to impede hydrogen diffusion effectively. Additionally, it is preferable for spacer layers to consist of materials that are relatively inert and do not readily react with hydrogen. For instance, silicon carbide (SiC) is a suitable choice because it features fully saturated bonds between silicon and carbon, making it less susceptible to blistering. For spacer materials, an ideal choice would be a material with an absorption edge below the desired wavelength range. Previous studies have shown that materials such as magnesium (Mg), Al, Si, beryllium (Be), yttrium (Y), and boron (B) exhibit good spacer materials for EUV multilayer applications [37].

**An absorber layer** functions by selectively capturing specific light wavelengths, commonly utilized to obstruct or weaken particular spectral regions while allowing the transmission or reflection of others. In scenarios involving interference filters, for instance, an absorber layer can be employed to minimize undesirable spectral bands. It is ideal for absorber layers to be crafted from appropriate oxide or metal materials capable of impeding the penetration of incident ions. In essence, the absorber layer material should possess a relatively high ability to halt the progress of hydrogen ions, indicating a preferred large stopping cross-section. Ideally, hydrogen ions with energy around 100 eV should not be able to penetrate the material beyond a few nanometers. Zirconium dioxide (ZrO<sub>2</sub>) serves as an example of such a material. Regarding metals, molybdenum is a favored choice, and for specific applications, molybdenum carbide (Mo<sub>2</sub>C) emerges as the preferred "metal" material due to its nearly equivalent extreme ultraviolet (EUV) reflectance to molybdenum, coupled with superior growth characteristics and enhanced resistance to hydrogen diffusion.

In addition to material selection, the physical and chemical properties of the multilayer material are also crucial parameters affecting optical properties. These properties include low chemical reactivity, low inter-diffusivity, and stability, as highlighted in reference [37].

There are various techniques for depositing multilayers, including magnetron sputtering deposition [17] and ion beam deposition [8]. These techniques enable precise control of layer growth at a specific temperature with high stability. In recent literature, a wide range of multilayer combinations have been employed, such as Mo/Si [8; 38], Mo/Be [39], Sc/Si [40], Mg/Sc/SiC [41], Al/Mo/SiC [17; 42], and Al/Sc/SiC [43]. These combinations are designed to maximize reflectance at specific wavelength ranges. However, it should be noted that these multilayers are typically

designed for wavelength ranges greater than 0.84 nm, where imperfections at the interface layer will not significantly impact reflectance.

### **2.3.3 Quality of interfaces**

In order to meet the specific requirements of various applications, thin-film structures are typically designed by selecting appropriate layer materials, thicknesses, and stacking order through calculations. Despite these efforts, the performance of nanoscale thin structures is often hindered by various issues related to layer growth characteristics. These issues include clustering or island formation, phase segregation, intermixing between consecutive layers, roughness buildup, and porous growth. These limitations can negatively impact the functionality of the thin-film structures, making it crucial to address these challenges during the design and fabrication process. The Fig.2.6 example was employed to represent various scenarios resulting from imperfections in the multilayer coating. In all four scenarios, the reflectance peak was diminished, but the presence of an oxide layer caused a shift in the peak.

#### **2.3.3.1 Interfacial roughness**

There is roughness at each layer interfaces between two layers or substrate with a layer at the surface. This roughness is generated mainly due to three reasons:

1. The particles arriving in the deposition machine onto the surface possess high energy and may potentially induce ballistic intermixing.
2. Insufficient energy of incoming particles hinders the mobility of adatoms, resulting in the formation of clusters instead of a homogeneous distribution of atoms throughout the layer.
3. The growth of layers in most materials exhibits a polycrystalline nature (see an example in TEM Fig.2.7).

#### **2.3.3.2 Interdiffusion and interlayer formation**

The reflectance of multilayers can be impacted by interdiffusion or the formation of an interfacial layer resulting from a chemical reaction between two deposited layers. Specifically, the presence of the interfacial layer alters the effective periodicity of the multilayer, leading to a reduction in reflectance, particularly for larger periods.

#### **2.3.3.3 Examples**

By considering the example depicted in Fig.2.5(b) consisting of 20 periods, we successfully demonstrated the impact of roughness in Fig.2.6(a), interdiffusion in Fig.2.6(b), oxidation in Fig.2.6(c), and the significance of interface layers in Fig.2.6(d). It is important to note that each phenomenon has been studied separately.



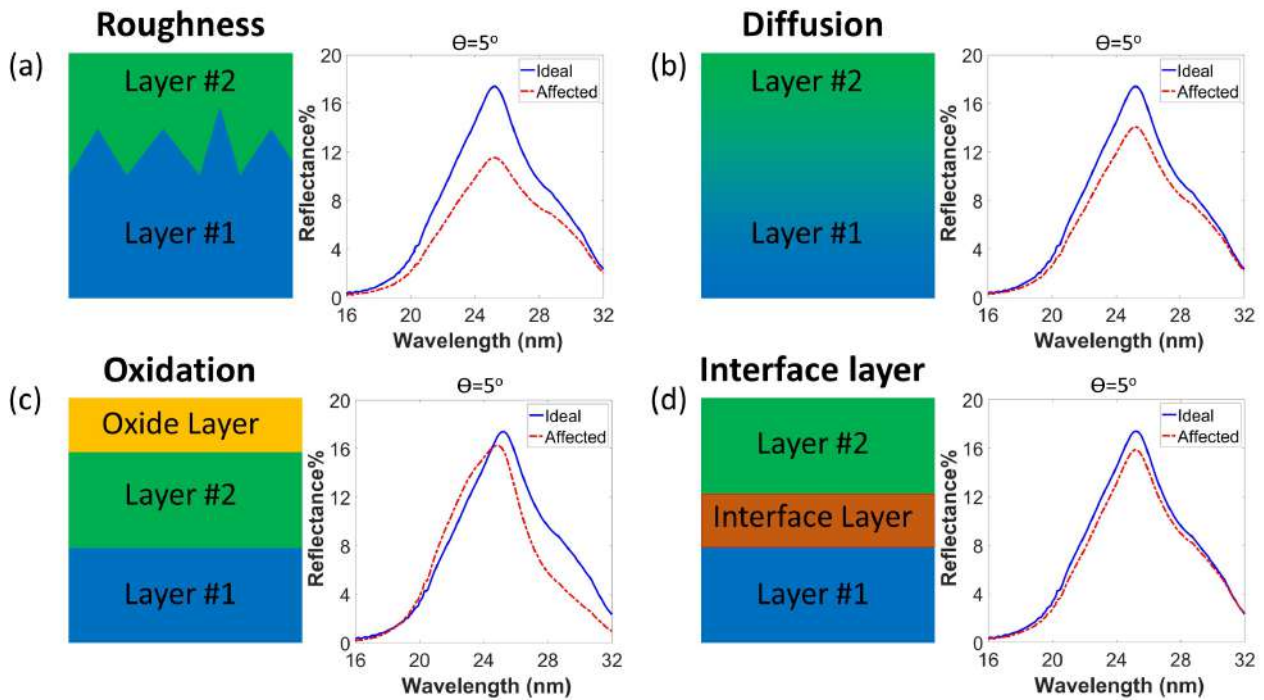


Figure 2.6: Illustrations of four simulated scenarios at  $\theta=5^\circ$ : (a) presence of roughness between layers, (b) interdiffusion occurring between layers, (c) formation of oxidation at the top, and (d) development of an interface layer between layers.

In Fig.2.6(a), we utilized the "power spectral density" function from the IMD software, which is described in the forthcoming section.3.2.1 of Chapter.3. In this analysis, we defined the roughness sigma ( $\sigma_r$ ) between a-Si and Mo to be 1nm. It is evident from Fig.2.6(a) that roughness has a noticeable impact on reducing peak reflectance.

In Fig.2.6(b), we once again employed the "power spectral density" function from the IMD software. For this analysis, we defined the diffusion sigma ( $\sigma_d$ ) between a-Si and Mo to be 1nm. It is evident from Fig.2.6(b) that diffusion significantly reduces peak reflectance, thereby impacting the bandwidth.

In Fig.2.6(c), we introduced a 2nm SiO<sub>2</sub> layer on top of the multilayer to simulate oxidation. As anticipated, the presence of the oxidation layer decreases both the peak reflectance and the bandwidth. However, an intriguing observation is that the peak reflectance shifts towards lower wavelengths.

In Fig.2.6(d), we introduced a 2nm layer of MoSi<sub>2</sub> between a-Si and Mo. The multilayer period was kept constant at 13.68nm, while the thickness of a-Si and Mo were 6.45nm and 5.23nm, respectively. The presence of the interface layer has a detrimental effect on the ideal peak, resulting in a reduction in both peak reflectance and bandwidth.

The TEM analysis (Figure 2.7) revealed a previously deposited periodic multilayer structure of Al/Mo/SiC, comprising 25 periods. Each period consisted of layers with thicknesses of 6.4 nm of Al, 1.4 nm of Mo, and 1.1 nm of SiC. The TEM images depicted a darker layer corresponding to Mo, a thin amorphous layer of SiC observed at the Al-on-Mo interface, and a brighter layer identified as Al. Notably, distinctive patterns were observed within the Al layers, indicating their crystallization and the presence of well-defined crystalline features.

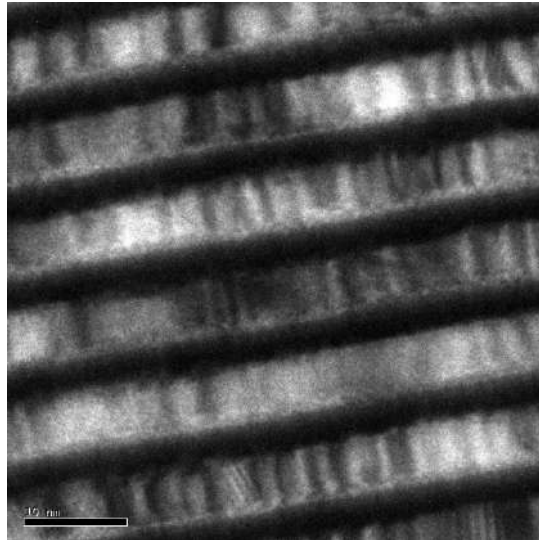


Figure 2.7: Transmission electron microscopy image of the Al/Mo/SiC multilayer sample studied by Ahmed Ziani (2010) [4].

## 2.4 Physics of the Gratings

Diffraction gratings are widely used in various applications, including analytical instruments, monochromators, spectrometers, and laser systems. These gratings typically feature a periodic microscopic groove structure that directs photons of varying wavelengths in different directions. While the dispersion prisms separate wavelengths based on refraction, as illustrated in Fig. 2.8, the diffraction grating performs a similar function.

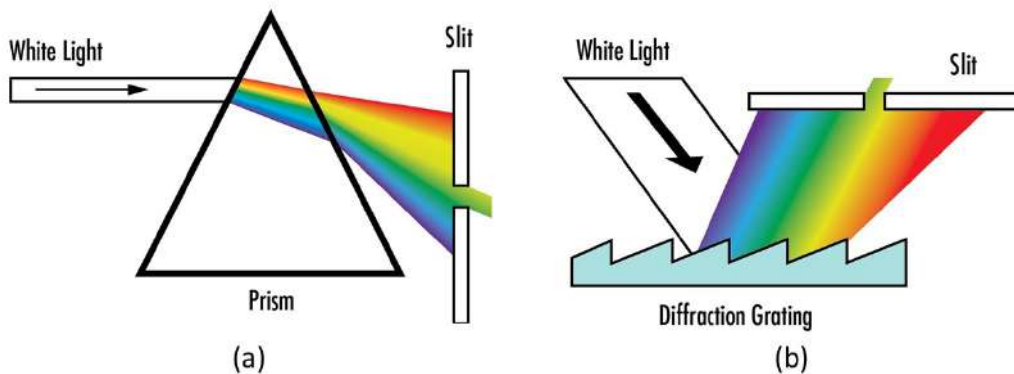


Figure 2.8: (a) refraction phenomena through the prism (b) diffraction phenomena in classical configuration [5]

Figure 2.9 illustrates two distinct ways in which incident beams can be diffracted by a grating. The Conical configuration Fig. 2.9 (right) and the classical configuration Fig. 2.9 (left) grating diffraction pertain to distinct patterns of diffraction generated by gratings.

The primary distinction between classical and conical grating diffraction resides in the degree of approximation and accuracy within the mathematical models employed to elucidate the diffraction phenomenon. Classical grating diffraction presents a simplified yet reasonably accurate depiction of diffraction effects for numerous practical

applications. Conversely, conical grating diffraction presents a more rigorous and comprehensive analysis that incorporates additional factors, including non-paraxial angles, curved gratings, and the vectorial nature of light.

In the upcoming subsections, the author will provide a thorough explanation of both configurations, highlighting their respective characteristics. Toward the end of this section, the author will summarize the key distinctions between these configurations.

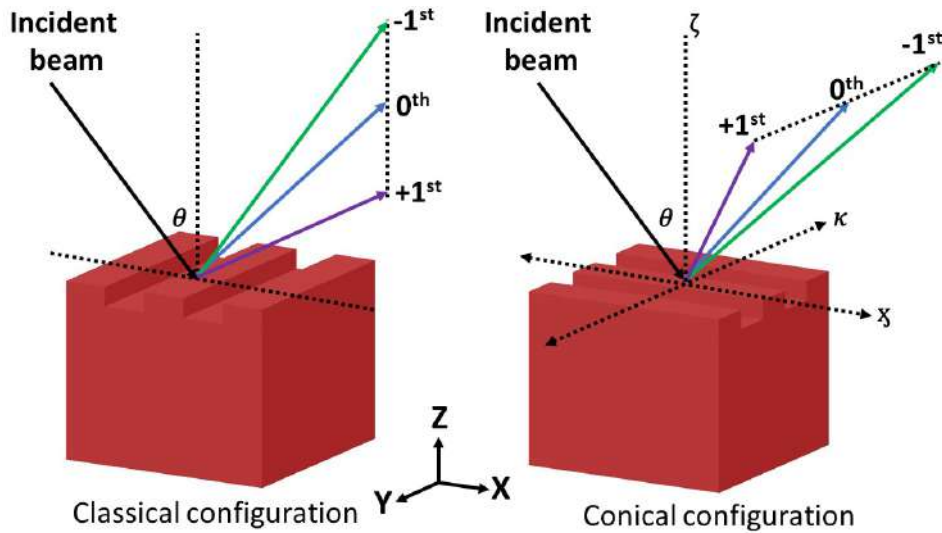


Figure 2.9: schematic diagram of classical position (left), and conical position (right).

## 2.4.1 Classical Grating Diffraction

Classical grating diffraction, referred to as planar or scalar grating diffraction, represents the prevalent and extensively researched type of diffraction. It arises when a coherent light wave traverses a periodic structure known as a grating, which comprises evenly spaced parallel slits or lines etched or deposited onto a surface. As light interacts with the grating, it undergoes diffraction, resulting in the formation of an interference pattern characterized by alternating bright and dark regions. In the classical diffraction theory, the grating is treated as a thin and flat structure.

The incident light undergoes diffraction upon encountering the gratings in a classical configuration, governed by the grating equation.2.16.

$$m\lambda = P(\sin \theta + \sin \phi) \quad (2.16)$$

where  $m$ ,  $P$ ,  $\theta$ , and  $\phi$  are values illustrating the integer diffraction order, grating period, incident angle of light, and diffracted angle of light exiting the grating respectively. Constructive interference occurs when multiple diffractive wavefronts align at integer multiples of the wavelength. The term  $m$  is presenting the diffraction orders, where  $m=1$  means "1<sup>st</sup> order" diffraction", and  $m=2$  signifies "2<sup>nd</sup> order diffraction" as demonstrated in Fig.2.10. If  $m=0$ , it means

the photons are directly reflected or transmitted by the grating and named “0<sup>th</sup> order” diffraction”. Normally, all the angles are determined or measured perpendicular to the grating (grating normal incidence).

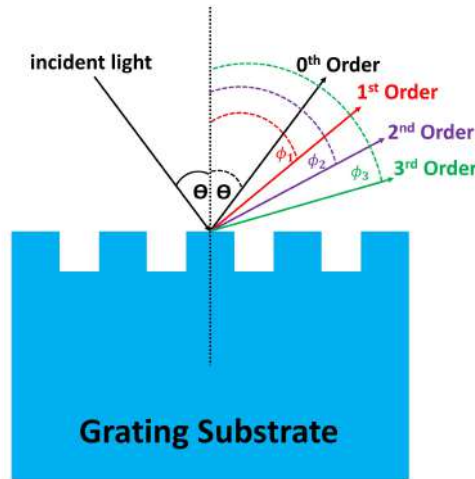


Figure 2.10: The 0-order diffraction photons are reflected directly from diffraction, while the other parts of the incident light will be diffracted to 1<sup>st</sup>, 2<sup>nd</sup>, and extra orders depending on the wavelength.

When photons interact with an irregular grating profile with length scales similar to their own wavelength, they are reflected and refracted at a microscopic level in various directions according to the law of diffraction. If the grating profile is periodic, photons will diffract from multiple periods in specific directions, causing constructive interference and resulting in the incident beam propagating in a particular direction. The grating efficiency (GE) is defined as the ratio of optical power between the output order from the gratings and the incident power on the gratings.

$$GE = \frac{P_{out}}{P_{in}} \quad (2.17)$$

In order to achieve the highest possible diffraction efficiency from gratings, it is necessary for all incident photons to diffract into a single-order diffraction pattern. This is important for minimizing losses in the overall system [44; 45]. However, achieving 100% diffraction efficiency in a single order can be challenging due to interference that allows for multiple diffracted orders. Research has shown that the most effective way to achieve single-order diffraction is through the use of small period gratings, which can eliminate all nonzero orders.

It is worth noting that the shape of the grating profile does not affect the direction of diffraction orders [44] as shown in Fig.2.11.

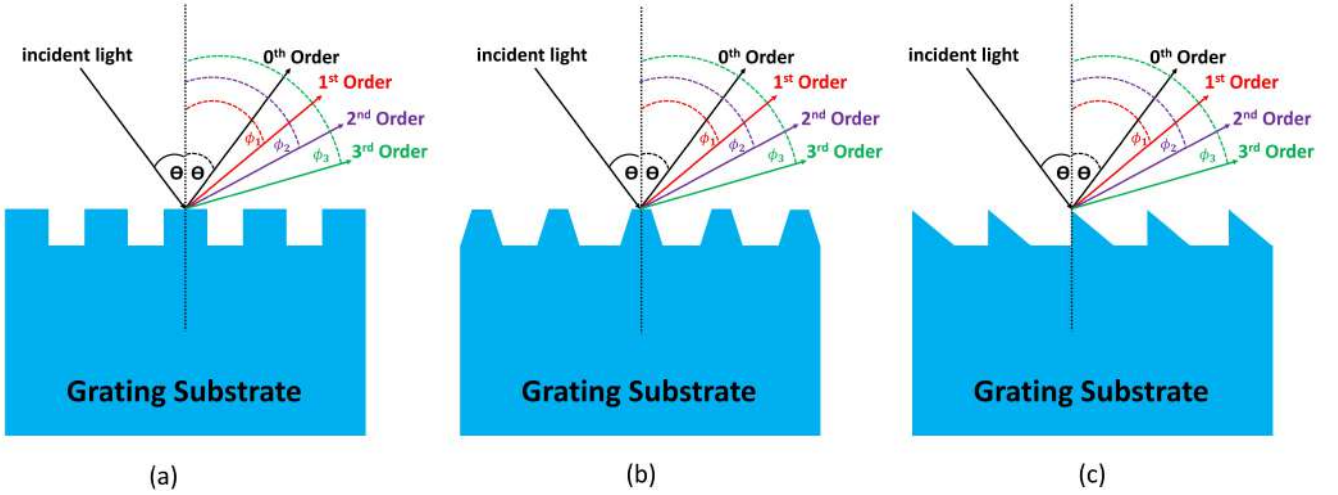


Figure 2.11: different grating profiles (a) lamellar gratings, (b) trapezoidal gratings, and (c)blazed gratings.

## 2.4.2 Conical Grating Diffraction

Conical grating diffraction, known as rigorous diffraction, vector diffraction, or non-paraxial diffraction, encompasses a more thorough examination of the diffraction process. It takes into consideration the three-dimensional characteristics of both the grating and the incident light wave. Unlike classical diffraction, conical diffraction does not treat the grating as a thin, flat structure; instead, it treats it as a thick, curved surface. This approach accounts for the vectorial properties of light and enables more precise predictions, particularly when dealing with significant diffraction angles or highly convergent or divergent incident light.

The investigation focuses on the diffraction phenomenon of conventional linear reflection grating. However, the scenario under consideration involves the incident light interacting with the grating at a significant oblique angle. This angle is represented by the direction cosines  $\kappa_i$  and  $\chi_i$ , as depicted in Fig.2.9 (right). Consequently, a distinct diffraction behavior arises, and it can be effectively described by a grating equation. This equation is formulated in terms of the direction cosines of the propagation vectors of the incident beam and the diffracted orders [46]. It should be noted that the grooves of the grating are assumed to be parallel to the  $y$ -axis as shown in Fig.2.9 (right).

$$\kappa_i + \kappa_m = \frac{m\lambda}{d} \quad (2.18)$$

$$\chi_i + \chi_m = 0 \quad (2.19)$$

If an angle  $\phi_o$  exists between the incident light and the  $x$ - $z$  plane, the following equations will be employed.

$$\kappa_m = \sin \theta_m \cos \phi_o \quad (2.20)$$

$$\kappa_i = -\sin \theta_o \cos \phi_o \quad (2.21)$$

$$\chi_i = -\sin \phi_o \quad (2.22)$$

The propagation of diffracted orders occurs on a conical surface, resulting in their intersection with the observation hemisphere in a cross-section that deviates from a perfect circle. A crucial point to consider is that the direction cosines are obtained by projecting the respective points on the hemisphere onto the aperture plane and then normalizing them to a unit radius.

In summary,

### 1. Classical diffraction for the gratings

- The incident beam falls perpendicular to the grooves of the grating as shown in Fig.2.9 (left).
- The phenomenon of diffraction is uncomplicated and can be effectively elucidated by equation.2.16.
- The occurrence of diffraction is limited to a specific plane.
- The transverse electric and transverse magnetic modes exhibit independent behavior.
- It is suitable for most practical situations

### 2. Conical diffraction for the gratings

- The incoming beam aligns parallel to the grating's grooves, as depicted in Fig.2.9 (right).
- The phenomenon of diffraction is characterized by its complexity, necessitating a comprehensive analysis that can be facilitated by the equations.(2.18-2.22).
- The previously established confinement of diffraction within a plane is no longer applicable.
- The transverse electric and transverse magnetic modes exhibit interdependence and are mutually coupled.
- It is challenging for high-precision applications

## 2.5 Multilayer Gratings

Despite these high efficiencies and a wide range of applications, one-dimensional multilayer structures suffer from a limited spectral resolution (typically  $\lambda/\Delta\lambda < 50$  in the EUV). Two-dimensional multilayer gratings have been proposed as an alternative to achieve higher spectral resolution [47; 48]. By combining multilayer interferences and

Table 2.1: comparison between conventional multilayer and a multilayer grating.

	Conventional Multilayer	Multilayer Gratings
Spectral resolution	Limited by $\lambda/\Delta\lambda \approx 20$	Enhanced by $\lambda/\Delta\lambda \approx 5000$ [11]
Limitations	Depends on illuminated periods	Depends on illuminated lines.

grating diffraction, they enable very high spectral resolution ( $\lambda/\Delta\lambda > 1000$ ) with good efficiency. Table.2.4 presented below illustrates the distinction between a conventional multilayer and a multilayer grating.

Moreover, the multilayer grating offers a highly advantageous characteristic whereby the diffraction angles of all orders except the 0-order depend on the wavelength. This property has been observed and documented in the subsequent chapter.

### 2.5.1 State of the art multilayer gratings

In the 1980s, the concept of a multilayer grating was initially introduced [49] with the purpose of developing a spectrometer for normal incidence EUV spectroscopy in astronomical applications. Multilayer gratings offer several advantages over single-layer coated gratings. These advantages encompass:

- improved spectral resolution.
- less stringent substrate requirements [50; 51].
- reduced imaging aberrations.
- significantly higher diffraction efficiency (in grazing incidences soft X-ray applications like monochromators or normal incidence applications like EUV spectrometers).

Consequently, multilayer gratings have found widespread usage in various spectroscopy experiments, including electron microscopes [52], synchrotron beamlines [53], and astronomical observations [19; 12].

The lamellar phase grating, which is coated with a multilayer, serves as an alternative form of multilayer grating. Previous research has demonstrated that the diffraction efficiency of such gratings can achieve 27% at 2.2 keV [54] and 47% at 6 keV [55]. To enhance the efficiency even further, a multilayer blazed grating has been proposed, theoretically capable of achieving a maximum groove efficiency of 100% [56; 57]. However, fabricating a flawless multilayer coating on top of sharp and smooth triangular grooves poses a significant challenge. It is important to note that the maximum groove efficiency is defined as the grating efficiency normalized by the corresponding multilayer reflectivity. To tackle this challenge, Carl Zeiss in Germany and Seely et al. fabricated a multilayer blazed grating using holographic patterning and ion etching [58]. This specific multilayer  $\text{Mo}_2\text{C}/\text{Si}$  blazed grating achieves a groove efficiency of 53% at a wavelength of 15.79 nm.

Yang et al. [45] proposed a theoretical study on aperiodic multilayer designs on a blazed grating operating in the spectral range of 17-25 nm. Their simulations, utilizing various material combinations for the multilayer, demon-

Table 2.2: Overview of the achieved efficiency of different multilayer gratings in various applications. Table adapted and updated from original source [21].

Multilayer	Grating Type	Period(nm)	$\lambda$ (nm)	order	efficiency	Reference
Mo <sub>2</sub> C/Si	Blazed	333	15.8	2	30% (53%)	Kowalski et al. [2004] [56]
Mo/Si	Blazed	190	13.1	1	44% (71%)	Voronov et al. [2012] [65]
Al/Zr	Blazed	100	17.2	1	24% (42%)	Voronov et al. [2011] [62]
Mo/Si	Blazed	396	13.4	2	52% (78%)	Voronov et al. [2014] [61]
Mo/Si	Blazed	1000	13.4	1	41% (63%)	Naulleau et al. [2004] [66]
Mo <sub>2</sub> C/B <sub>4</sub> C	Lamellar	420	0.564	1	≈ 27%	Choueikani et al. [2014] [53]
Co/SiO <sub>2</sub>	Lamellar	830	0.206	1	47%	Ishino et al. [2006] [55]
W/C	Lamellar	830	0.155	1	38%	Ishino et al. [2006] [55]
Mo/B <sub>4</sub> C	Lamellar	1000	0.83	0	7.5% (62%)	Benbalagh et al. [2005] [67]
W/Si	Lamellar	300	2.36	0	7.5% (78%)	van der Meer et al. [2013] [68]
Mo/Si	Blazed	50.7	13.2	1	51.4% (95%)	Bajt et al. [2012] [69]
Mo/Si	Blazed	36.9	13.2	1	29.7% (59%)	Prasciolu et al. [2015] [70]
SiC/W/Ir	Lamellar	833.33	70	-1	13.4%	He et al. [2011] [71]
Mo/Si	Lamellar	555.56	0.729	-1	25%	Feng et al. [2021] [72]

strated the potential to optimize diffraction efficiency across a wide spectral range using aperiodic multilayer coatings. Additionally, Yang et al. provided evidence that the grating parameters enable single-order operation, selectively exciting one diffraction wave while suppressing the diffraction waves of all other orders.

To enhance the performance of multilayer gratings, an anisotropic chemical etching process of crystalline silicon has been implemented to create blazed facets [59; 60]. This process has demonstrated improvements in high diffraction orders, achieved ultrahigh spectral resolution, increased groove density, and enhanced overall grating efficiency. Consequently, multilayer blazed gratings have proven especially valuable for advanced spectroscopy techniques with a resolving power ranging from 10,000 to 100,000 [21]. Voronov et al. [61] achieved a diffraction efficiency of 52% for the second order of diffraction using a high-groove-density Mo/Si multilayer blazed grating at a wavelength of 13.4 nm (2525 lines/mm). Moreover, a multilayer blazed grating with a groove density of 10,000 lines/mm [62] achieved an efficiency of 13.2% (at normal incidence) at a wavelength of 19.2 nm. Regrettably, the technologies employed for fabricating blazed gratings with high groove density (typically > 3000 l/mm) are incompatible with curved surface substrates [62; 63] due to the complexity and cost involved in the fabrication process [64].

Table.2.2 provides an overview of the current status of prior publications concerning multilayer gratings. The table displays information including the composition of the multilayer material, grating type, grating periodicity, wavelength, measured diffraction order, and efficiency. It's noteworthy that certain entries have dual values due to the presentation of both theoretically and experimentally obtained results within the publications.

It should be noted that the high efficiency observed for the multilayer blazed gratings, as depicted in Table.2.2, is a result of the optical properties of the blaze gratings. These properties lead to the reduction of energy in all diffracted orders while simultaneously increasing the energy in a single diffracted order [45].



## 2.6 EUV domain for astrophysics

Observing the celestial sky has been practiced since ancient times through naked-eye observation and later with the use of glasses and telescopes, limited to the visible spectrum until the 19<sup>th</sup> century. With the development of sensors, access to other energy ranges became possible, leading to a revolution in observation techniques and expanding astronomers' knowledge of our universe. Since then, progress in observation and theory has advanced hand in hand, with a particular emphasis on exploring the vastness and complexity of the universe, resulting in a race to build increasingly large instruments. This pursuit of gigantism reflects the ongoing endeavor to unlock the secrets of the forces shaping our universe.

Within this field, astrophysics is a specific discipline that focuses on comprehending the birth, evolution, and demise of stars and systems according to the laws of physics. The study of the radiation emitted by stars provides insight into their nature and interactions with our environment. The objective is to push exploration further towards the ends of the electromagnetic spectrum, such as with missions like PLANCK, which is dedicated to studying the cosmic microwave background (fossil radiation from the Big Bang) at a 2mm wavelength, or the INTEGRAL mission, which is focused on observing radiation from 15 keV to 10 MeV produced by violent events in the universe, such as novae, supernovae, and black holes absorbing stars.

Certain types of radiation, such as those in the extreme ultraviolet to gamma ray range and certain infrared spectral bands, are absorbed by the Earth's atmosphere and cannot be observed from the ground. To study high-energy phenomena that emit primarily outside the visible spectrum, observations must be conducted from space. These observations are conducted during "rocket" flights or satellite missions. Rocket flights are typically used to qualify or calibrate onboard instruments and involve a brief acquisition phase lasting a few minutes or hours before returning the instrument to Earth. In contrast, satellite missions have a scientific acquisition phase that can last several years.

Observing sunspots from the 19<sup>th</sup> century and measuring electromagnetic storms at the beginning of the 20<sup>th</sup> century were initially peripheral events for astrophysicists. However, observing the Sun in the X-ray and extreme ultraviolet (EUV) domains, in particular, has enabled researchers to make correlations between these events. In the first part, we will explore the contributions of EUV imaging to astrophysics and the origins of its emission. Then, we will provide a summary of different missions used to study the Sun in the EUV domain.

In the 1960s, sounding rockets equipped with pinhole-type instruments captured the first images of the Sun in broad "soft X" bands, with wavelengths reaching approximately 4 nm. Following these early successes, several sounding rocket missions were launched in the 1980s to observe the Sun in the extreme ultraviolet (XUV) range

using telescopes equipped with interference coatings.

The first image of an active region of the Sun was captured on October 25, 1985, by James H. Underwood and his colleagues at the Lawrence Berkeley Laboratory and Lockheed Martin at the Palo Alto Research Laboratory. They used a multilayer telescope in normal incidence during the flight of the first sounding rocket equipped with a Cassegrain-type telescope treated with a 30-layer interference coating in tungsten and carbon to image the Si XII emission line at 44.02 Å and 44.16 Å. This telescope achieved an angular resolution on the order of 5 to 10 arc seconds.

On October 23, 1987, Arthur B. C. Walker, Jr. and his team from Stanford University captured the first image of the solar disk in soft X-rays corresponding to a temperature of 1 million degrees using a Cassegrain telescope embedded in a sounding rocket. This telescope also benefited from an interference coating, which helped to improve the resolution of the images.

## 2.6.1 The Sun: the EUV rays of its corona

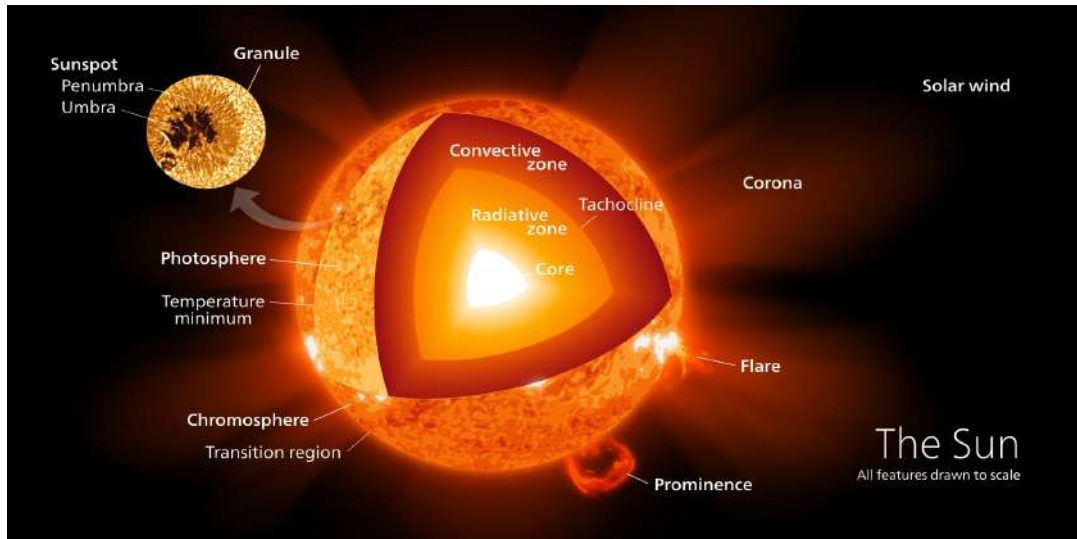


Figure 2.12: Diagram of the structure of the Sun to scale [6].

Our focus in this project is centered on the Sun and its corona, which exhibit a high level of activity. Despite being one of 250 billion ( $\pm 150$  billion) stars in the Milky Way, the Sun's close proximity to Earth makes it an ideal subject for investigation. Like other stars, it maintains hydrostatic equilibrium between the forces of fusion in its core, which produce energy from hydrogen and helium nuclei, and its gravitational forces. The solar radius is defined as the distance from the center to the photosphere, where gases are opaque, and beyond which they become transparent.

The Sun's internal structure consists of a molten core that reaches nearly 15 million Kelvins, a radiation zone, and a convection zone. The radiative zone's density is so high that it takes between 10,000 and 150,000 years for X and gamma photons produced there to reach the surface. The temperature of the radiative zone decreases to 2 million Kelvins, while the convective zone's temperature drops further to 5800 Kelvins, corresponding to the star's surface temperature. A thick boundary of about 3000 km separates the convective zone from the radiative zone, designated as the tachocline, where the magnetic field is believed to be formed through the dynamo effect.

Based on the Hertzsprung-Russell diagram shown in Figure 2.12, the Sun falls into the category of class G stars on the main sequence, with a surface temperature of 5800 K. This temperature is determined using Wien's law, which relates the wavelength  $\lambda_{max}$  corresponding to maximum emission (in meters) to the surface temperature T (in Kelvin) of an incandescent body:  $\lambda_{max} \times T = 2,89 \times 10^{-3} \text{ m.K}$ . It is therefore reasonable to apply the reduced models used to observe the Sun to other stars in the same category.

Figure.2.13 displays the EUV spectral changes observed during the C8.8 flare, and Table.2.3 provides a concise overview of the flares categorized by their X-ray class.

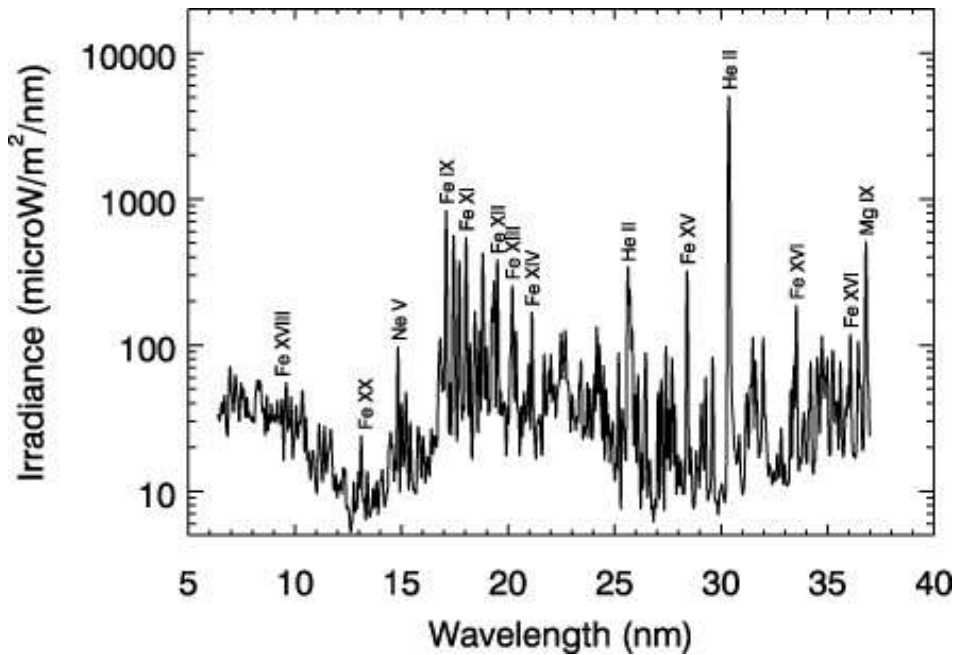


Figure 2.13: Solar spectrum shown here is obtained from the MEGS-A channel measuring the spectrum from 7 to 37 nm [7].

## 2.6.2 History of solar observation missions in the EUV

In 1995, the first satellite equipped with a EUV imaging telescope that featured multilayer coatings was launched as part of the Solar Heliophysics Observatory (SOHO) mission. The telescope was a Ritchey-Chrétien EIT (Extreme

Table 2.3: EUV spectral lines are emitted by the solar corona according to the CHIANTI database [22].

E (eV)	$\lambda$ (nm)	Emitter Ione	Log(T)	Region
132.6	9.35	Fe XVIII	6.8	Rash Area
94.6	13.1	Fe VIII	5.7	Transition Region
93.9	13.2	Fe XX	7.0-7.1	Rash Area
91.2	13.6	Fe XXII	7.1	Rash Area
72.5	17.1	Fe IX	5.9	Calm Crown, High Transition Region
70.8	17.5	Fe X	6	Calm Crown, High Transition Region
64.6	19.2	Fe XXIV	7.2	Crown and Warm Flare
63.6	19.5	FE XII	6.1-6.2	Crown and Warm Flare
58.8	21.1	Fe XIV	6.3	Active Crown Region
49.0	25.3	FE XXII	7.1	Active Region
48.6	25.5	Fe XXIV	7.2	Active Region
43.7	28.4	Fe XV	6.4	Active Region
40.8	30.4	He II	4.9	The chromosphere, Transition Region

Ultraviolet Imager Telescope) type, capable of imaging four different emission lines by dividing its primary and secondary mirrors into four quadrants. Each quadrant was coated with a periodic Mo/Si multilayer optimized to reflect a specific emission line: Fe IX/X at 17.1 nm, Fe XII at 19.5 nm, Fe XV at 28.4 nm, and He II at 30.4 nm. In 2006, the STEREO satellite, equipped with the same type of imager as SOHO, was launched. The STEREO-A and STEREO-B satellites work together to provide complementary observation points for imaging the Sun.

The ion beam sputtering technique was employed to deposit Mo/Si coatings for STEREO's Extreme UltraViolet Imager (EUVI). It has been observed that the performance of the ion-beam deposited multilayers surpasses the Mo/Si coatings previously obtained through the e-beam evaporation technique for the Extreme UV Imaging Telescope (EIT) of the SOHO mission, as depicted in Fig.2.14.

In 2010, the Solar Dynamics Observatory (SDO) mission was launched by NASA, featuring the AIA (Atmospheric Imaging Assembly) imager with three types of multilayer optical coatings: Mo/Y, Mo/Si, and SiC/Si. The AIA imager is capable of probing 7 distinct wavelengths staggered between 9.4 nm and 33.5 nm. The same year, the Japanese satellite Hinode (meaning "Sunrise" in Japanese, and previously known as Solar-B during its development) was launched with a spectrometer-imager that can probe the solar corona in the EUV in two bandwidths from 17.1 nm to 21.2 nm and from 24.6 nm to 29.2 nm. This was made possible with an interference coating in Mo/Si deposited on a suitable reflection diffraction grating. Table 2.4 provides a non-exhaustive list of solar observation missions that use multilayer coatings at normal incidence in the EUV range.

The Solar Orbiter satellite was launched on February 10, 2020, from Cape Canaveral in Florida. It carries 10 instruments, including an extreme ultraviolet EUV imager, making it the first satellite to have Al/Mo/SiC three-material interference mirrors to detect emission lines at 17.4 nm and 30.4 nm. The satellite's orbital trajectory, aided by the gravitational force of Venus, allows it to capture images of the Sun's poles for the first time in history. Figure.2.15

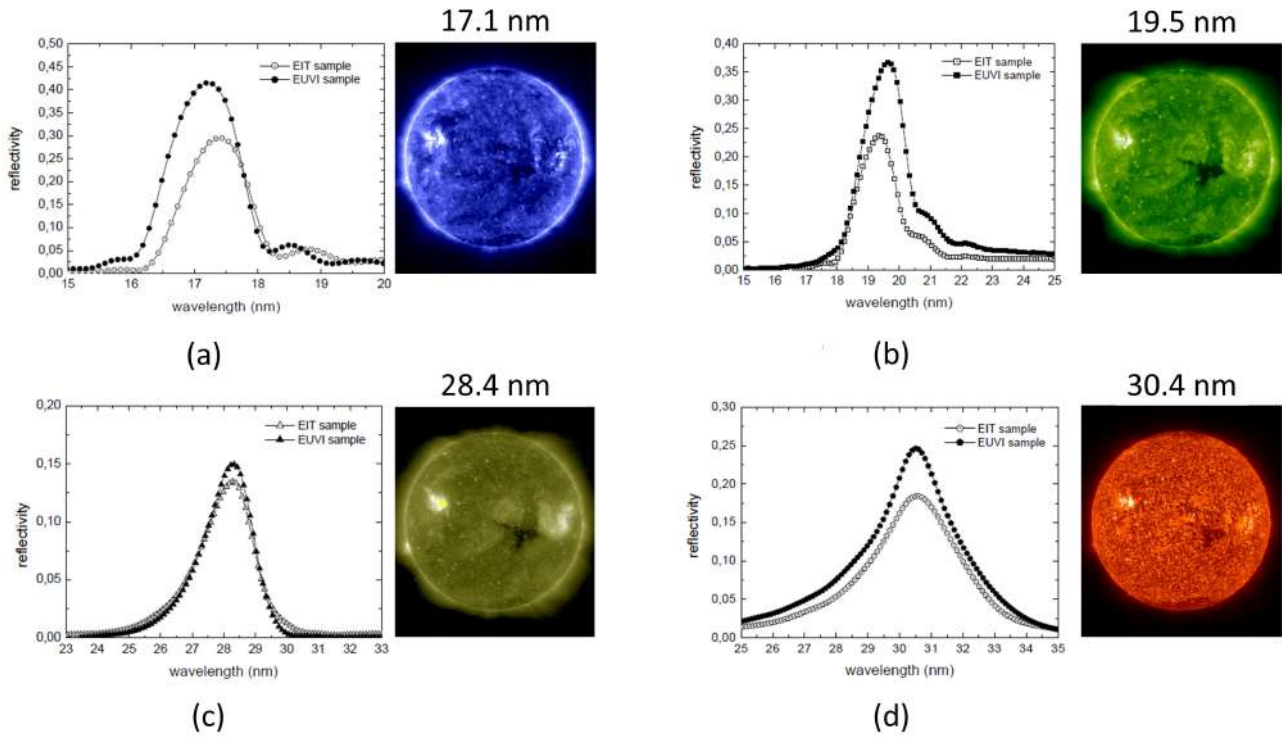


Figure 2.14: Comparison of reflectivities acquired using EUVI for the STEREO mission and EIT for the SOHO test samples [8], with the visualization image captured by the EUVI sensor in 2016 [9] at various wavelengths: (a)  $\lambda=17.1\text{nm}$ , (b)  $\lambda=19.5\text{nm}$ , (c)  $\lambda=28.4\text{nm}$ , and (d)  $\lambda=30.4\text{nm}$ .

depicts an image captured by this mission, showcasing the sun at a wavelength of  $\lambda = 30.4\text{nm}$ .

Table 2.4: Involvement of Our XUV Optics Group in Past EUV Missions.

Mission	Year	Instrument	$\lambda$ (nm)	Ion	MLS	Type
Soho [73]	1996	EIT Imager	17.1	Fe IX/X	Mo/Si	Satellite
			19.5	Fe XII		
			28.4	Fe XV		
			30.4	He II		
STEREO [74]	2006	EUVI Imager	17.1	Fe IX/X	Mo/Si	Satellite
			19.5	Fe XII		
			28.4	Fe XV		
			30.4	He II		
Solar Orbiter [75]	2020	EUI Imager	17.4	Fe IX/X	Al/Mo/SiC	Satellite
			30.4	He II		

### 2.6.3 Solar-C -Mission

The scientific objective of the Solar-C EUV High-Throughput Spectroscopic Telescope (EUVST) is to examine the dynamics and energetics of the solar atmosphere by conducting spectroscopic and imaging observations with high spatial resolution, high throughput, and high cadence. These observations will be carried out seamlessly across the

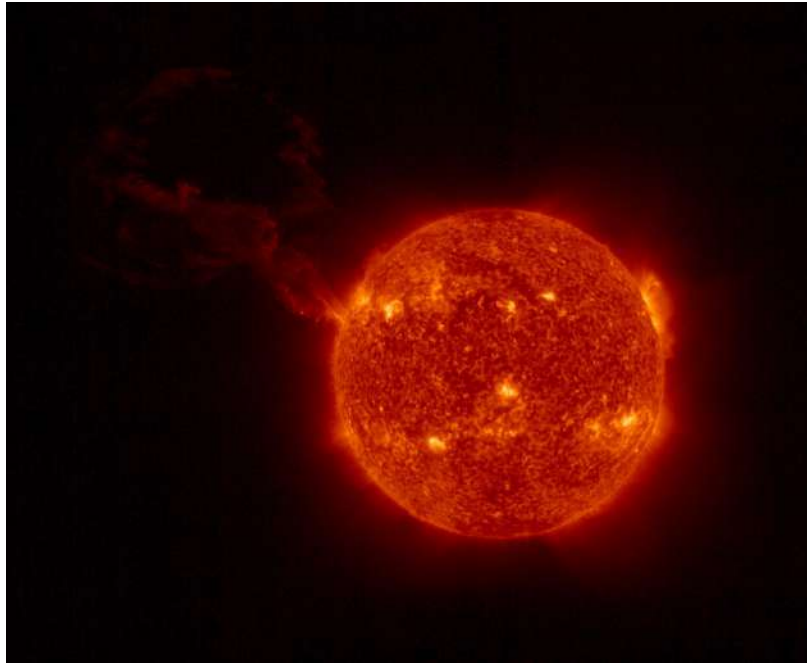


Figure 2.15: The Full Sun Imager on board the ESA/NASA Solar Orbiter spacecraft captured a giant solar eruption at  $\lambda=30.4\text{nm}$  on 15 February 2022 [10].

chromosphere to the corona. The Solar-C EUVST project has received approval from both Japan and the USA, and it is scheduled for launch in 2027-2028 [11]. This mission is based on the Large European module for solar Ultraviolet Research (LEMUR) concept and will incorporate an imaging slit spectrometer equipped with a Slitjaw Imager similar to the one used in the Interface Region Imaging Spectrograph (IRIS). To observe plasmas ranging from 0.02 to 15 MK, Solar-C requires a spectral range in the EUV of 17.0-21.0 nm and a vacuum ultraviolet (VUV) range of 46.3-53.7, 55.7-62.2, 69.0-85.0, 92.5-107.5, and 111.5-124.5 nm. Additionally, the spectral resolution needs to exceed  $\lambda/\Delta\lambda$  of 3240 in the EUV range and 7450 in the VUV range to resolve velocity structures larger than thermal velocities [76]. The EUVST's primary mirror and grating (see Fig.2.16) will employ multilayer coatings and a broadband boron carbide coating to achieve high efficiency in the longer ultraviolet (UV) wavebands and the EUV waveband of 17–21.5 nm [77].

It is worth mentioning that Solar-A and Solar-B, two Japanese missions, were subsequently renamed Yohkoh and Hinode, respectively, upon their launch [77].

The key characteristic of the EUVST telescope is its minimal number of optical elements, specifically the primary mirror and the diffraction grating, which eliminates the need for filters. This design allows the telescope to capture a maximum amount of solar UV radiation. Figure.2.16 presents the schematic configuration of the EUVST, while Table.2.5 provides an overview of the targeted spectral range of the EUVST. It is important to highlight that Table.2.5 contains dual range values for LW2 and LW3. This distinction arises from the utilization of multilayer gratings designed to cover two separate wavelength ranges, achieved by employing distinct diffraction orders.

The outcomes obtained from the multilayer blazed gratings in Table.2.2 exhibit a noteworthy level of interest

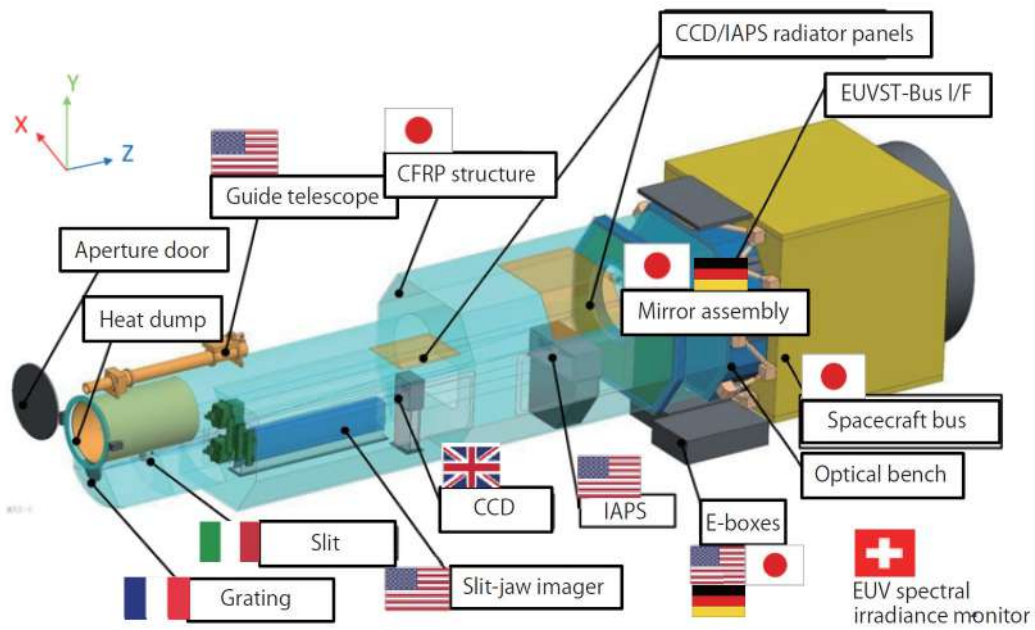


Figure 2.16: The optical configuration of the EUVST instrument with international contributions. [11].

Table 2.5: Essential criteria for EUVST instrument performance and design specifications [11].

Investigations' system requirements	Instrument design parameters	specifications
Temperature coverage: 0.02-20 MK without substantial gaps	Wavelength	17.0-21.5 nm (SW) 69.0-85.0 nm (LW1) 92.5-108.5 (46.3-54.2) nm (LW2) 111.5-127.5 (55.7-63.7) nm (LW3)
Spatial resolution $\leq 0.4$ arcsec ( $100 \times 100$ arcsec <sup>2</sup> ) $\leq 0.8$ arcsec ( $280 \times 280$ arcsec <sup>2</sup> )	Spatial resolution	$\leq 0.4$ arcsec ( $100 \times 100$ arcsec <sup>2</sup> ) $\leq 0.8$ arcsec ( $280 \times 280$ arcsec <sup>2</sup> )
Temporal resolution 0.5 sec (shortest) with spectroscopic capability	Effective area Cadence of area coverage	Higher than $0.6$ - $5.6$ cm <sup>2</sup> 0.5 sec (shortest)
Field of view $280 \times 280$ arcsec <sup>2</sup>	Field of view	$280 \times 280$ arcsec <sup>2</sup>
Velocity resolution: $V_d \sim 2$ km/s	Spectral resolution ( $\lambda/\Delta\lambda$ )	SW= 5000, LW= 13500
Image observations: chromosphere/photosphere	Slit-jaw images ( $\lambda$ )	279.6, 283.3, and 285.2 nm include the corresponding ions Mg II, continuum, Mg I

when considering the experimental and theoretical efficiency for high-density blazed gratings. However, the fabrication process for these high-density blazed gratings is done with an exceptionally long duration and exceedingly high costs, particularly in the context of their use in the Solar C mission. Specifically, the high-density grating intended for use in EUVST possesses an external toroidal design with a substantial diameter, necessitating a significantly extended manufacturing timeline. As a consequence, the decision has been made to replace the high-density blazed gratings with the high-density trapezoidal gratings.

Furthermore, Table 2.5 outlines the specifications of the EUVST instrument; nevertheless, our involvement pertains solely to the SW part. It should be considered that the Solar-C project is constituted by three phases: A, B, and



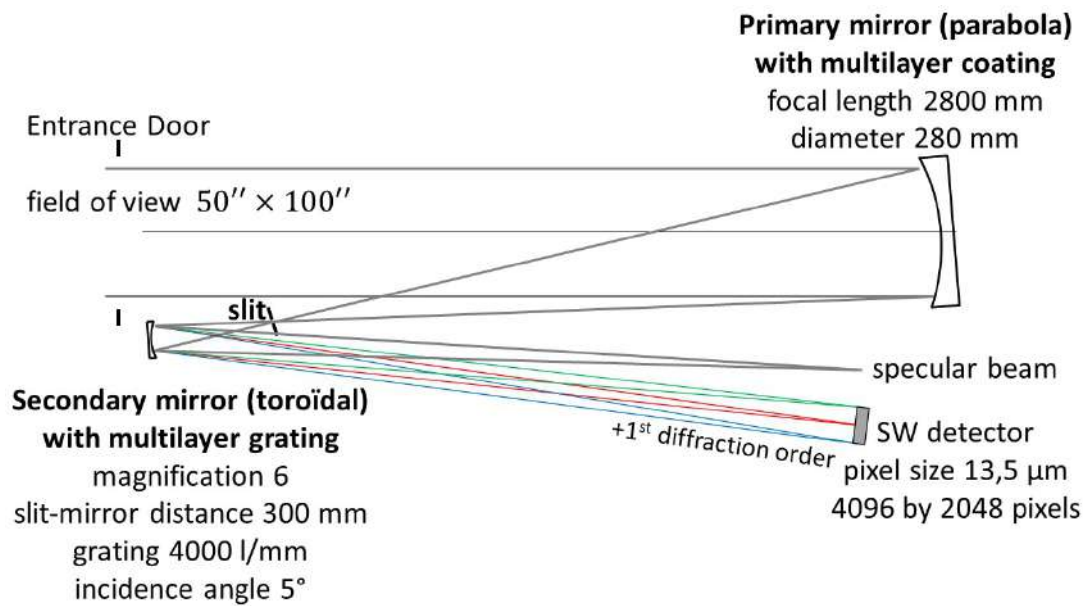


Figure 2.17: The optical arrangement of the EUVST instrument.

C, where phase C represents the launch, and there is a possibility that the specific requirements may be subject to changes.

Additional information can be found regarding the grating designated for use in the ultimate phase of the Solar C mission (phase C). This grating takes on a toroidal shape and incorporates two distinct coatings: one for longer wavelengths and another for shorter wavelengths. During the final stage, our team will engage Zeiss to manufacture this toroidal grating, featuring a 30mm diameter, intended for the application of an optimal coating that meets the criteria for short wavelengths spanning 17.0-21.5nm. Figure.2.17 provides a more comprehensive depiction of the operational principle of toroidal multilayer gratings. In this illustration, light is directed onto the toroidal multilayer gratings from the primary mirror, after which it undergoes diffraction toward the camera.

In our effort to contribute to the development of the EUVST instrument, we have submitted a request to Zeiss for the fabrication of three distinct high-density silica gratings, each with a resolution of 4,000 lines per millimeter. These gratings possess varying groove depths, as elaborated upon in the upcoming chapter.4. These fabricated gratings will function as test samples intended for assessing the performance of the ellipsoidal grating depicted by the arrow, aligned with the French flag in Fig. 2.16, which is designated for use within the EUVST instrument. Our primary objective is to achieve an efficiency level that is either on par with or exceeds the results of Seely et al. for the Solar-B mission [12; 19].

It is worth highlighting an advantage of the Solar C mission, namely, the considerably larger diameter of its primary mirror compared to the one used in the Solar B mission. This implies that in the Solar C mission, a greater number of photons will engage with the multilayer gratings as compared to the previous Solar B mission.

In the research conducted by Seely et al. [12; 19], they reported the performance of a 20-period Mo/Si-coated



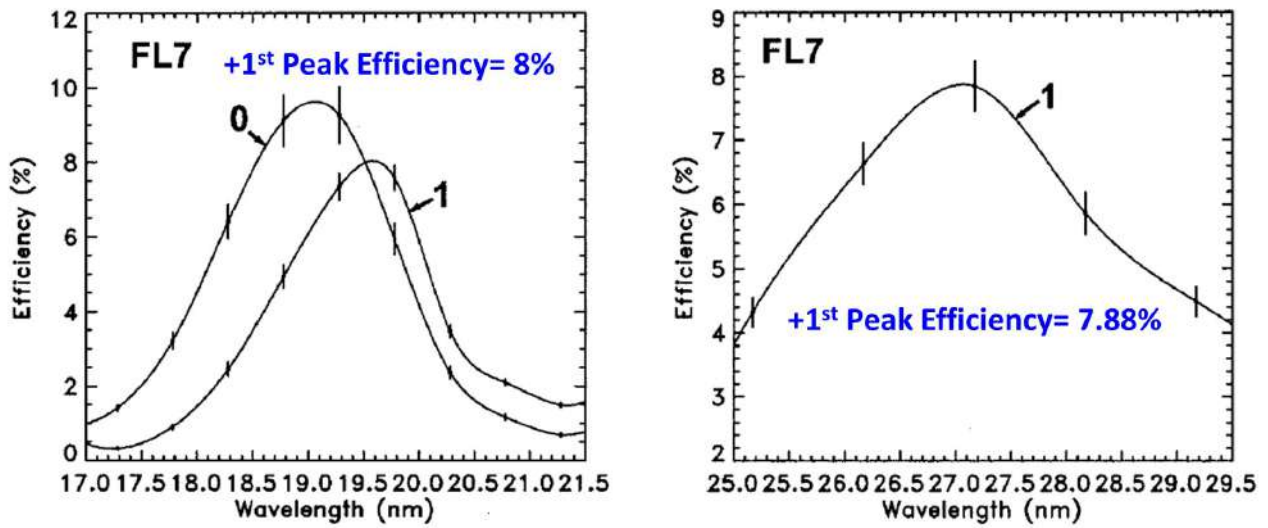


Figure 2.18: Data obtained from Seely et al. [12] for the +1 order at nearly normal incidence.

lamellar grating. They achieved a +1<sup>st</sup> peak efficiency of 8% and a bandwidth of 1.1 nm, as depicted in Fig.2.18 (right), within a wavelength range of 17.0-21.5 nm. Additionally, Seely et al. obtained a +1<sup>st</sup> peak efficiency of 7.88% with a bandwidth of 2.64 nm for wavelengths ranging from 25.0 to 29.5 nm, as shown in Fig.2.18 (left).

Therefore, the primary goal of this thesis is to achieve comparable results to those reported by Seely et al. or even improve upon them, particularly in terms of peak efficiency and bandwidth.

## 2.7 Summary

To summarize this chapter, We discussed the physics of EUV (Extreme Ultraviolet) radiation, thin film coatings, conventional multilayers, gratings, multilayer gratings, and the main challenge faced in the Solar C mission. The multilayer grating exhibits superior spectral resolution compared to conventional multilayers. However, the selection of grating types, the high cost of fabrication, the evolution of multilayer coatings on the gratings, and the material selectivity pose significant challenges, as evident from previous literature.

## Chapter 3

# Methods and Metrology

In this chapter, the tools used for experimental and simulation purposes are demonstrated. The physical principles of the experimental tools, such as magnetron sputtering deposition, x-ray reflectometry, metrology beamline reflectometry, atomic force microscopy, and transmission electron microscopy, are explained. Furthermore, a detailed account is given of how the data was analyzed to achieve high accuracy. Additionally, the simulation tools are discussed from the perspective of optimization, fitting, modeling, and analysis. Finally, the metrology of combining all those tools is discussed.

### 3.1 Experimental Tools

Producing components such as multilayer-coated mirrors necessitates working within a highly precise environment. To achieve this, the Charles Fabry Laboratory utilizes the CEMOX facility, which incorporates a class 1000 clean room that meets ISO 6 standards of the ISO 14644-1 standard. This requires maintaining an environment with less than 1000 particles of more than  $0.5 \mu\text{m}$  in diameter per cubic foot of air by maintaining slight overpressure to prevent dust from entering. In addition, the clean room's temperature and humidity levels are closely monitored and the atmosphere is frequently refreshed using filtering methods. To enable the production of multilayer coatings, several frames have been installed within the clean room, and chemical fume cupboards are used to clean samples before depositing.

There are multiple methods available for depositing multilayer coatings, which can be achieved through physical or chemical means. The physical deposition method is the most commonly used approach and can be performed by several techniques such as cathode sputtering, ion beam sputtering, assisted evaporation, and laser ablation.

In this thesis, I had the chance to work with two techniques for depositing thin films: magnetron sputtering and ion sputtering. However, only one of these methods is elaborated on in the later part of this section. This is because the deposition of multilayers on a test textured grating silicon substrate will be carried out using ion beam sputtering.

However, this work will not be accomplished within the timeframe of this thesis.

### 3.1.1 Magnetron sputtering deposition

The production of thin films can be achieved through a physical process known as sputtering. This section will cover its operating principle, as well as the sputtering deposition setup that is accessible in our laboratory.

#### 3.1.1.1 Principle of operation

All of the samples examined in the following sections were fabricated using magnetron sputtering, a physical technique for depositing thin films in a vacuum chamber that can be utilized in two modes: the DC mode and the RF mode (as depicted in Fig. 3.1 and listed in Table.B.1). The choice of mode is determined by the material that is to be deposited, with the RF mode being especially well-suited for insulating materials. In this technique, the material to be deposited is in the form of a "target."

In DC mode, the deposit process is as follows:

1. In magnetron sputtering, a negative bias voltage is applied to the material's target to be deposited (the cathode), while the enclosure walls and the substrate, which are placed above the target, are connected to the ground (anode).
2. A neutral gas, typically argon (Ar), is introduced at very low pressure into the enclosure, which is previously maintained at a residual pressure of  $\approx 10^{-5}$  mTorr ( $=1.33 \times 10^{-6}$  Pa).
3. The potential difference leads to the ionization of the gas, resulting in the formation of a plasma comprising electrons, positively charged ions ( $\text{Ar}^+$ ), and neutral atoms.
4. The plasma electrons are drawn towards the anode and sustain the discharge by colliding with neutral atoms, thereby ionizing them.
5. The target draws  $\text{Ar}^+$  ions with enough energy to physically sputter atoms and clusters of the target material, which are subsequently deposited in the enclosure and on the substrate. This results in the formation of a thin layer of target material on the substrate.

When the target material is insulating, it is not feasible to use the DC mode because the accumulation of  $\text{Ar}^+$  ions on the surface creates a space charge, which impedes the flow of current between the anode and cathode.

As a result, we opt for the RF radio frequency mode, where an alternating voltage is applied using an impedance-matching box, with a fixed frequency conventionally set at 13.56 MHz. At this frequency, the heavier ions remain nearly static while the lighter electrons oscillate in the field. Therefore, during a positive alternation, a higher number of electrons reach the target as compared to the number of ions during a negative alternation, creating a negative

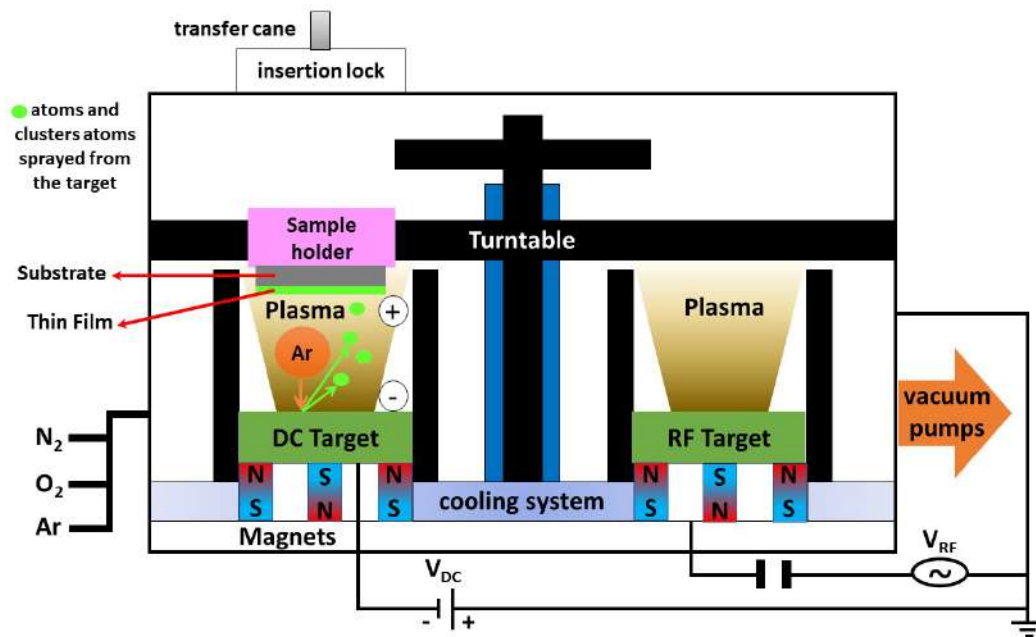


Figure 3.1: Schematic diagram of DC and RF magnetron sputtering.

static charge on the surface of the target. This results in a negative self-polarization potential that accelerates the  $\text{Ar}^+$  ions from the plasma to sputter the target material with an energy greater than or equal to 100 eV.

The efficiency of this deposition method is directly proportional to the number of collisions between electrons and neutral atoms in the plasma. To increase the deposition rate and reduce the pressure in the chamber, a magnetron device can be added. This system of magnets placed near the target creates a magnetic field that traps the electrons near the target, causing them to follow a helical trajectory along the field lines. This, in turn, increases the likelihood of electron-atom collisions and the density of  $\text{Ar}^+$  ions that are available to sputter the target material.

To modify the properties of the thin layers of materials deposited using this method, a chemically active gas such as dioxygen  $\text{O}_2$  or dinitrogen  $\text{N}_2$  can be added in addition to the neutral gas. This creates a reactive atmosphere that modifies the composition of the thin layer deposited.

### 3.1.1.2 Sputtering machine at Laboratory Charles Fabry (LCF) – Plassys MP800S

The MP800S model from Plassys® was used as the framework for the thesis work. This model includes a cylindrical enclosure with an 800 mm diameter that houses four material targets, with two slots for DC mode and two for RF mode (refer to Fig. 3.2). In DC mode, currents ranging from 50 mA to 200 mA can be applied, whereas in RF mode, the powers range from 80 W to 300 W. The targets, measuring 80 mm x 200 mm, are isolated from each other by shields to confine the plasma and prevent cross-contamination during deposition. To achieve a vacuum of approximately  $10^{-8}$  Torr (i.e.,  $1.33 \cdot 10^{-6}$  Pa), a pumping system consisting of a primary membrane pump and a cryogenic pump is used. During deposition, the working pressure increases between 0.6 mTorr and 10 mTorr (corresponding to 0.08

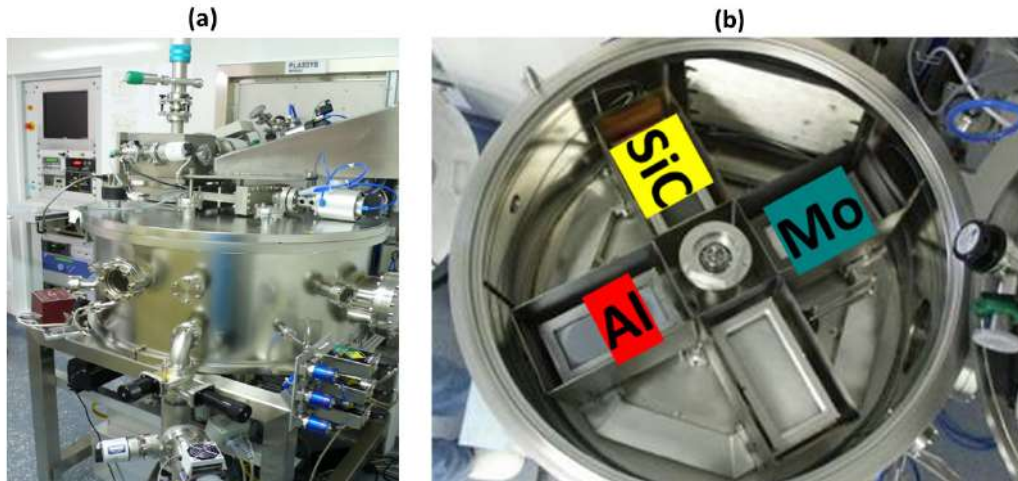


Figure 3.2: Photograph of DC and RF magnetron sputtering (a) external, and (b) internal.

Pa and 1.33 Pa, respectively) under argon. To maintain the cleanliness of the chamber under vacuum, an insertion airlock is used in which the sample holder is placed and transferred to a rotating tray in the deposition chamber using a transfer rod. The sample to be processed is located 10 cm above the targets. The speed and homogeneity of the deposit are controlled by adjusting the planetary rotation speed of the plate (rotation on itself around the central axis of the frame) and the satellite rotation speed of the sample holder (rotation around its axis). Optics up to 125 mm in diameter can be processed through the transfer airlock.

To ensure high-quality thin layers, the deposition process begins with pre-sputtering the target to remove any unwanted oxides or contaminants, without exposing the sample to be coated. As the MP800 does not have an in situ or real-time thickness characterization tool, a calibration step is necessary to establish the relationship between the deposition rate and the sample's speed over the target, with fixed plasma parameters. This involves an iterative process of manufacturing samples and measuring the thickness ex-situ using grazing X-ray reflectometry. To produce multilayer coatings, the following steps are followed:

1. **Calibration of individual thin layers:** To calibrate individual thin layers, multiple samples of a particular material are deposited at different scan velocity, and the resulting thicknesses are measured. A relationship between the scan velocity and the deposited thickness is then derived, and the process is repeated for each material used. (An illustration can be found in the forthcoming Subsection.3.2.1.2, as depicted in Fig.3.22(a).)
2. **Calibration of multilayer structures:** In addition to producing single-layer samples, we also create multilayer samples consisting of multiple materials. This is necessary because interface effects between the deposited layers could affect the accuracy of deposition rates and thicknesses determined for single layers. To address this, we vary the scan velocity of the material and characterize the multilayers using grazing X-ray reflectometry. This enables us to deduce a more precise relationship between the velocity and thickness of the multilayer coating. (A clear illustrative example is showcased in the forthcoming Subsection 3.2.1.2, Fig.3.22(b).)

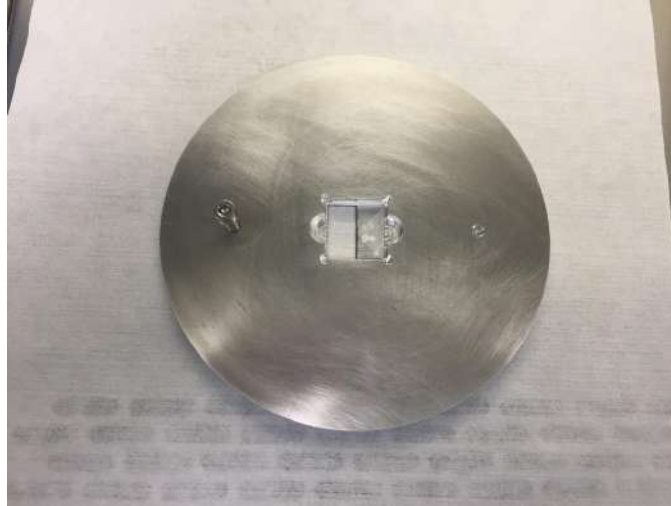


Figure 3.3: Photograph of the sample holder.

Finally, Because of the irregularities in the deposition process [78], the uniformity profile, which represents the radial thickness distribution on the sample, doesn't remain constant but takes on a parabolic shape when the sample moves steadily over the target [78]. To address this uneven thickness across the sample, the MP800 offers the option to adjust the platen's rotation scan velocity as the sample passes above the target [79]. In practical experiments, it has been noted that when dealing with a flat substrate, the thickness deposited in the center is greater than at the edges. To correct this non-uniformity, we'll increase the scan velocity when the sample's center aligns with the deposition area (in practice, velocity modification occurs as the substrate passes the shield to position above the target). Subsequently, the planetary velocity will be restored to its initial value when the sample's center reaches the opposite end of the target. A well-considered choice of the ratio between these two velocities can effectively rectify the radial uniformity profile by minimizing thickness variations on the sample.

In the present thesis, Al/Mo/SiC multilayers were fabricated in an ISO6 cleanroom using a Plassys MP800 magnetron sputtering machine, either on flat Si substrates or on substrates with a silica grating. The flat Si substrates used were  $30 \times 30 \text{ mm}^2$  or  $20 \times 20 \text{ mm}^2$  Si wafer pieces with 1 mm thickness, (100) crystal orientation, and surface microroughness in the 0.3 nm range. For the grating substrates  $20 \times 20 \text{ mm}^2$ , two different multilayer coatings were deposited on each sample half using a mask (see Fig.3.3). The sputtering machine geometry and deposition parameters have been reported in previous works [78; 17]. Pure SiC and Mo targets with a purity of 99.5% and 99.95%, respectively, and a Si-doped (1.5 wt. %) Al target with a purity of 99.99% were used. A plasma discharge was established under an Argon pressure of 2 mTorr [17]. DC-Current of 0.06 A and RF powers of 200 W and 150 W were applied to the Mo, Al, and SiC targets, respectively.

### 3.1.2 X-ray reflectometry

The fundamental principle of X-ray reflectometry stems from the interaction of electrons with a solid target, resulting in the emission of X-rays in the form of  $K\alpha$  and  $K\beta$  lines, as well as a nearly continuous spectrum of photons referred to as continuous braking radiation or Bremsstrahlung. The setup for this X-ray reflectometry involves a cathode ray tube, where a filament is powered by a 40 kV high-voltage generator, allowing a current of 40 mA to circulate through it.

After the bombardment, atoms in an excited state return to their ground state. Electrons from higher core levels and the valence band fill the resulting gaps. Copper's K emission ( $\text{Cu } K\alpha$ ) involves a transition between core levels, releasing excess energy as photons. These emitted photons have energies corresponding to the energy difference between the shells, resulting in a discrete line spectrum superimposed on the continuous bremsstrahlung radiation.

The grazing X-ray reflectometry (XRR) measurements of the grating samples were conducted at the LCF laboratory, using a device called "Discover D8" constructed by BRUKER company [80].

XRR is an interface-sensitive analytical technique used for characterizing thin films and multilayers. The method relies on measuring the intensity of X-rays reflected in the specular direction from a top flat surface. If the interface is not entirely smooth and sharp, the reflected intensity deviates from what is expected by the law of Fresnel reflectivity [81].

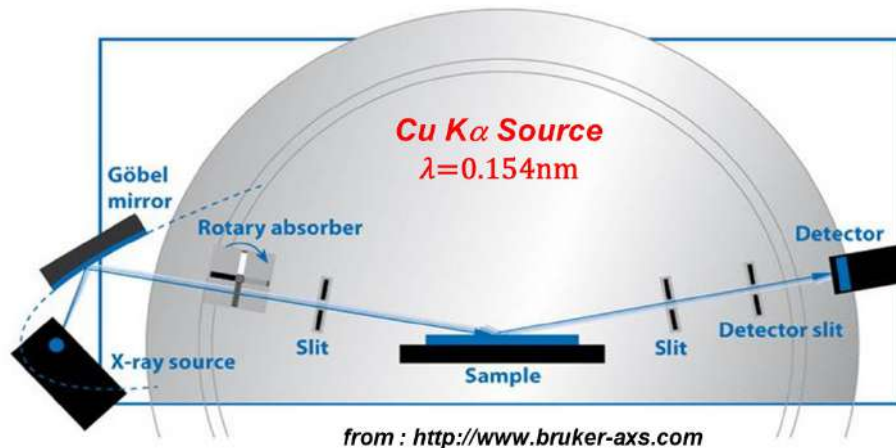


Figure 3.4: Setup of X-ray Reflectometry [13].

The schematic diagram of the setup is shown in Fig.3.4. The device employs a  $\text{Cu } K\alpha$  source with a wavelength of approximately 0.154nm and is equipped with several slits to control and reduce the size of the beam. It is composed of:

1. **The Göbel mirror** is positioned at the X-ray tube's exit. It is used to control and shape the X-ray beam. It consists of alternating layers of Ni/C with high- and low-density materials, respectively, carefully designed for



specific X-ray reflectivity properties. Its primary function is to collimate the X-ray beam, improving spatial resolution and reducing background scattering.

2. **The rotating absorber** is a crucial tool for precise control and accurate reflectivity measurements of thin films and multilayer structures in X-ray reflectometry. The design and material selection of the rotating absorber depends on experimental requirements, often involving alternating layers of high- and low-Z materials for efficient attenuation and a wide energy range. The primary purpose of this rotating absorber was to facilitate operation across a wide range of reflectance values, encompassing multiple orders of magnitude.
3. **Soller slits** are crucial for controlling the beam's horizontal divergence. They narrow down the X-ray beam's angle, making it more focused and parallel. This enhances measurement precision. Additionally, they reduce background noise by limiting X-ray interactions, improving the data signal-to-noise ratio. Narrowing the beam also boosts angular resolution, allowing for finer interface detail analysis.

The reflectivity curve is obtained by measuring the reflected beam while varying the grazing angle of incidence of the incident beam on the mirror (in a scanning configuration  $\theta-2\theta$ ). The angular mechanical precision is superior to  $0.01^\circ$ .

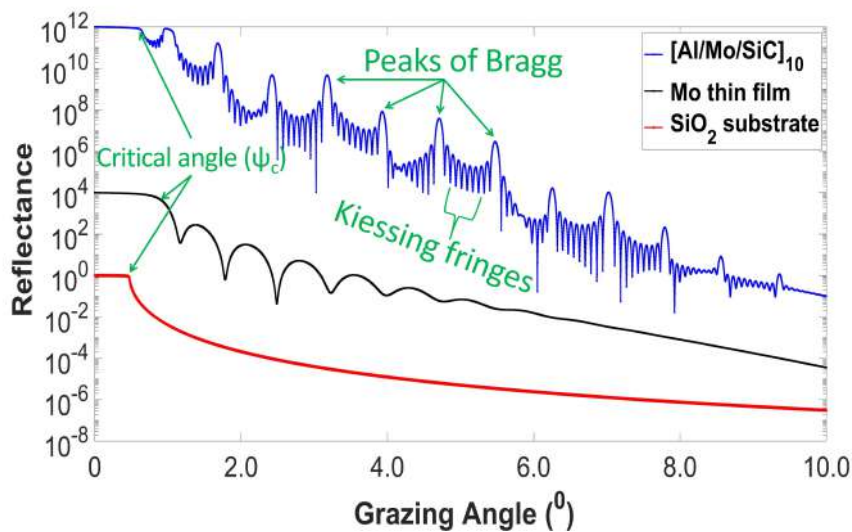


Figure 3.5: Simulation of reflectivity spectra at 8keV of a silica substrate, Mo thin film, and a periodic  $[Al/Mo/SiC]_{10}$  multilayer.

The signals obtained at 8 keV exhibit varying features depending on the type of sample. An illustration of the modeling for a bare silicon substrate, a thin layer of molybdenum (11.36 nm) on the same substrate, and a multilayer of 10 periods  $[Al (5.00 \text{ nm})/Mo (4.36 \text{ nm})/SiC (2.00 \text{ nm})]$  is shown in Fig.3.5. These curves provide significant information such as

1. **Total Reflectance:** it refers to the phenomenon where X-rays are entirely reflected when incident on a material's surface at angles smaller than the critical angle ( $\psi_C$ ). At these angles, all incoming X-rays experience total



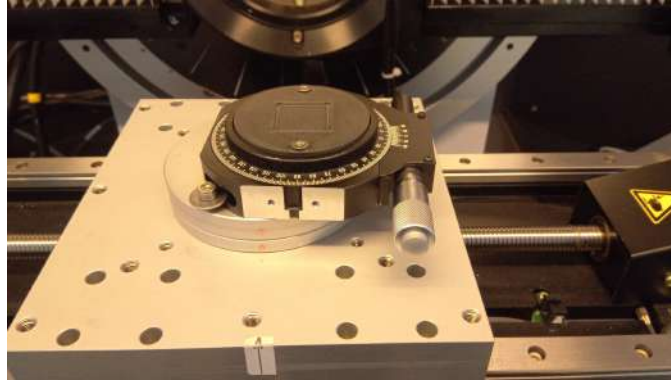


Figure 3.6: Photograph of the rotation stage.

internal reflection, and none are transmitted into the material. This is in contrast to angles near the critical angle, where partial reflectance and interference effects occur.

2. **The Critical Angle ( $\psi_C$ ):** it is the minimum angle at which X-rays must be incident on a material's surface to be completely reflected, rather than absorbed or transmitted. It plays a crucial role in GIXR experiments, where X-rays are directed at a very shallow angle to the sample. Operating near or just above the critical angle enhances sensitivity to surface and interface properties, making GIXR a valuable technique for characterizing thin films and multilayer structures by analyzing the reflected X-ray patterns. The specific critical angle depends on factors like the X-ray wavelength and the material's electron density.
3. **Bragg's peaks:** they are sharp, intense reflections that occur due to the constructive interference of X-rays scattered by the periodic layers within a multilayer sample. These peaks appear as distinct spikes in the reflected X-ray intensity and correspond to specific angles of incidence and scattering, providing valuable information about the structural characteristics of the layered material. By analyzing the positions and intensities of Bragg's peaks in GIXR spectra, we can determine parameters like layer thickness, periodicity, and crystallographic orientation, making it a powerful technique for studying the properties of thin films and multilayer structures.
4. **Kiessig fringes:** they are a series of interference fringes that appear as oscillations in the reflected X-ray intensity. These fringes are caused by the interference of X-rays reflected from the top surface of a thin film or multilayer structure with those reflected from the substrate. Kiessig fringes are particularly useful for extracting information about layer thickness, density, and interface roughness in the sample. Analyzing the spacing and shape of these fringes allows us to gain valuable insights into the structural characteristics and quality of thin films and multilayer systems.

Additionally, the roughness at the surface of each thin layer can also be determined from the contrast of the interference fringes, which decreases as the angle increases. In the case of the example presented in Fig.3.5, a roughness of 0.35 nm RMS was considered for the silicon substrate, and roughness values of 0.7 nm RMS were used

for all layers of the coating. For multilayers, a reflectivity spectrum with  $N - 2$  fringes between two Bragg peaks is obtained, where  $N$  is the number of periods.

By utilizing the rotation stage, it becomes feasible to investigate the impact of rotation on the multilayer grating. This can be achieved by adjusting the angle in both classical and conical positions. The rotation stage is illustrated in Fig.3.6.

### 3.1.3 Atomic Force Microscopy (AFM)

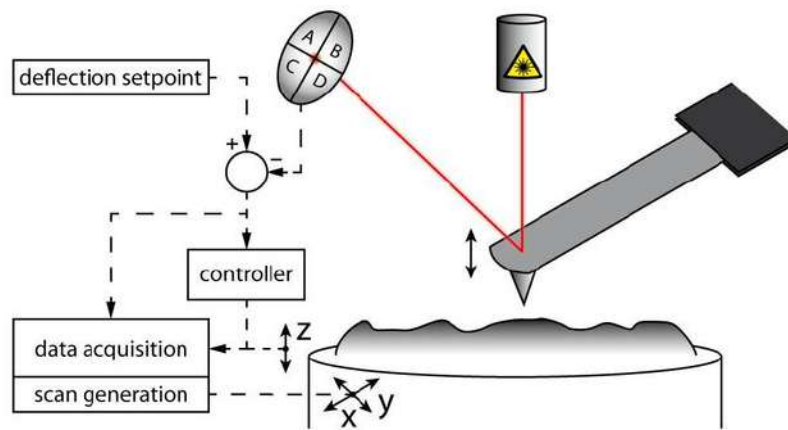



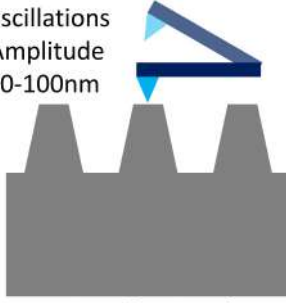
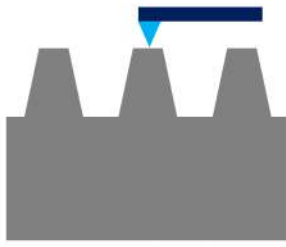
Figure 3.7: Schematic diagram of AFM [14].

Atomic force microscopy (AFM) is used to analyze sample topography and examine material properties at the nanoscale. It involves using a probing tip situated at the end of a cantilever that interacts with the sample. Different forces contribute to AFM measurements, including the Pauli exclusion principle, Van der Waals forces, electrostatic forces, magnetic forces, and capillary forces. These forces can generate attractive or repulsive forces when the sample interacts with the tip. These forces provide valuable information and specific details about topography and material properties at the nanoscale. The cantilever system serves as the force sensor in AFM. When the tip comes into contact with the sample, the attractive force causes the cantilever to deflect toward the sample. Conversely, the repulsive force causes the cantilever to deflect away from the sample. The cantilever comes in various shapes, depending on the type of measurement to be conducted. A laser beam is reflected from the cantilever's surface to detect the cantilever's position. Fig.3.7 shows a schematic diagram of the interaction between the tip and the samples.

Thus, AFM offers several modes of operation, with the most commonly used modes being non-contact mode, tapping mode, and contact mode. The key characteristics of the three distinct AFM modes have been summarized by us and presented in Table.3.1.

To analyze the AFM data with greater accuracy, we imported the ASCII-type matrix data into WSXM 5.0 software [82] for visualization and comprehensive analysis. In Fig.3.8(a), the AFM surface of one of the gratings before the

Table 3.1: Comparison of the different modes of Atomic Force Microscopy (AFM) - non-contact mode, tapping mode, and contact mode.

Non-Contact Mode	Tapping Mode	Contact Mode
 <p style="text-align: center;"><b>Non-Contact Mode</b></p>	 <p style="text-align: center;"><b>Tapping Mode</b></p>	 <p style="text-align: center;"><b>Contact Mode</b></p>
AFM tip moves close to the surface without making physical contact with the sample.	Oscillations Amplitude 20-100nm AFM tip lightly taps or intermittently makes contact with the sample surface during the scanning process.	AFM tip maintains continuous contact with the sample surface throughout the entire scanning procedure.
AFM tip operates oscillating, detecting only attractive forces, preserving tip integrity without surface contact.	AFM tip is driven at or close to its resonance frequency, resulting in gentle oscillation and interaction with the sample surface.	A constant force is applied to the surface, and the resulting deflection of the cantilever is recorded..
Well-suited for imaging delicate or soft samples that may be susceptible to damage from direct contact.	reduce lateral forces and minimal tip wear.	Suitable for imaging relatively flat and rigid samples with minimal variations in topography.
Generally provides higher imaging resolution but may exhibit less stability compared to other modes.	It is commonly employed for imaging both hard and soft samples.	High-resolution images with exceptional sensitivity to lateral forces.
It is frequently utilized for imaging samples in ambient or low-pressure environments.	lower risk of damaging delicate samples when compared to contact mode.	It can be more abrasive and has the potential to cause wear on the tip and potential damage to soft or delicate samples.

deposition is displayed, revealing that the grooves were not initially perfectly aligned horizontally or vertically, but inclined. In Fig.3.8(b), we rotate surface morphology through WSXM software manually to align the grooves vertically as closely as possible in a vertical orientation. Subsequently, Fig.3.8(c) provides a zoomed-in view of the aligned grooves after removing unnecessary elements such as crooked grooves from Fig.3.8(b). In Fig.3.8(c), three golden lines indicate the locations where we conducted profile analysis on the grating: the top, middle, and bottom positions. Fig.3.8(d) illustrates the profiles of the gratings at these three different lines, with the violet line representing the average of the three lines. Additionally, the blue line represents the average along the grooves, calculated using an averaging tool within the WSXM software.

Fig. 3.8(d) illustrates that the three lines exhibit distinct behavior in terms of roughness, groove slope, and groove depth, despite belonging to the same set of gratings. This observation suggests that the grooves within the gratings are not uniformly distributed along the vertical groove line. The average of the three lines depicted in Fig. 3.8(d) reveals lower roughness at the top and bottom of the grooves. When considering the average of all lines using the

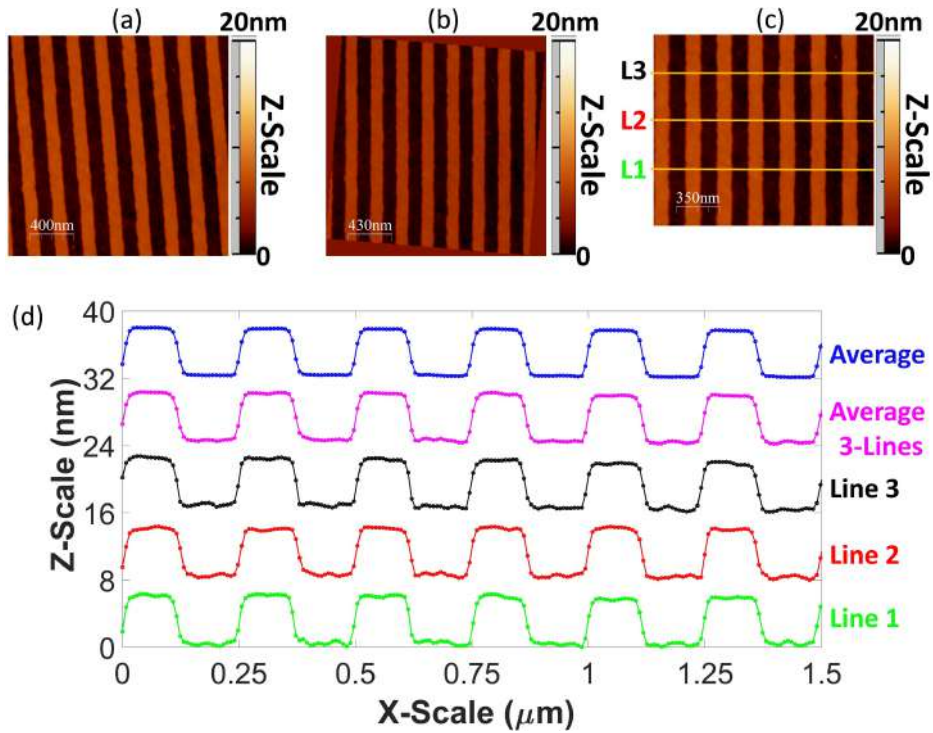


Figure 3.8: The AFM surface morphology of the grating is depicted in the following figures: (a) presents the original AFM image, (b) displays the image after vertically aligning the grating grooves, (c) shows a zoomed-in view of the grating grooves, and (d) illustrates the profile of the grooves in the grating.

averaging tool in WSXM 5.0 software, the profile indicates a more consistent roughness at the top and bottom of the grating grooves. Therefore, the authors opted to utilize the average profile generated by the tool within WSXM 5.0 software to represent the profile of the grating grooves. This average profile will be employed to extract the average slope angle of the grooves from the left and right sides of the trapezoidal grooves, as well as the average fill factor by manually placing a line close to the full-width half-maximum of the grooves.

Due to the sensitivity of the surface profile in our case, which involves a multilayer grating, we have ruled out contact mode and opted to use both tapping and non-contact modes. Although tapping mode was effective in cases where the surface had high roughness, we have chosen to use non-contact mode to prevent any damage to the multilayer evolution on the grating grooves.

Figure.3.9 presents AFM measurements of a single grating using two distinct modes: tapping and non-contact. It is important to highlight that these measurements were conducted on different days and at potentially different locations. Upon observing Fig.3.9, it becomes apparent that the depth of the grating grooves remains consistent, while the width of the grooves displays variations.

As a part of the analysis of multilayer grating coatings, an atomic force microscope can be utilized to measure the profile shape of the grating samples. This measurement can be compared to the estimated grating parameters obtained through a custom MATLAB code based on rigorous coupled wave analysis (RCWA) and RETICOLO software [83]). The comparison is made after modeling X-ray reflectivity measurements and Soleil measurements.

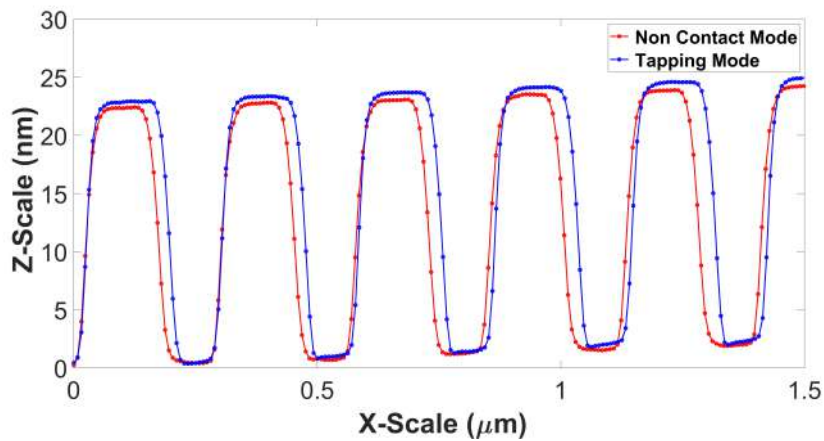


Figure 3.9: AFM measurements were conducted using two different modes to examine the profile of the grating.

In this study, the Atomic Force Microscope equipment at the SOLEIL facility (Park Company NX20) is utilized in non-contact mode, employing AC160 TS Olympus tips.

The analysis of the AFM data involves utilizing the "WSxM 5.0 Software" [82] to extract the grating parameters, including top and bottom roughness, groove depth ( $d$ ), FWHM fill factor ( $f.f$ ), and the slope of the trapeze ( $\alpha$ ).

### 3.1.4 Extreme ultraviolet reflectometry on synchrotron facility.

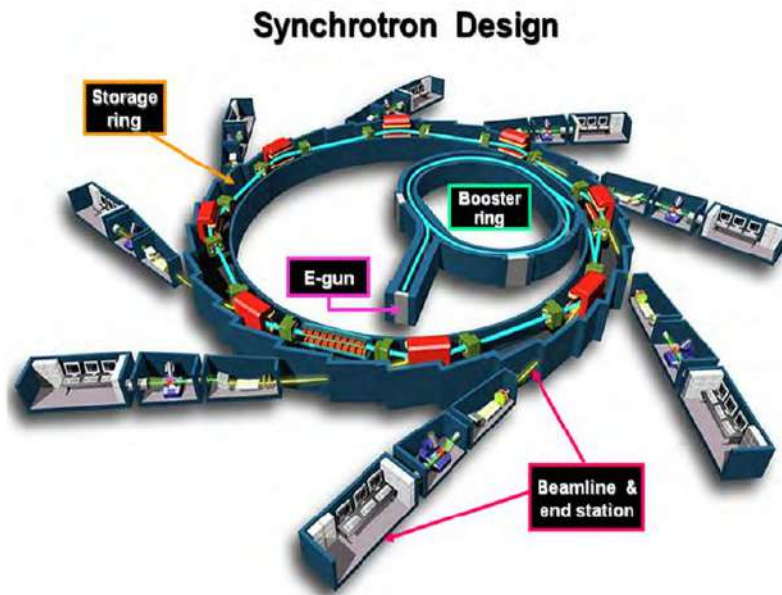


Figure 3.10: schematic diagram of Soleil Synchrotron [15].

In practical terms, a synchrotron (illustrated in Fig.3.10) comprises an electron accelerator where electrons are injected and circulated at relativistic speeds within a storage ring measuring around a hundred meters in diameter. Throughout the ring, various magnetic devices such as bending magnets, undulators, and wigglers are strategically

positioned to alter the electron trajectory, resulting in their acceleration and the generation of synchrotron radiation. The emitted light is then collected and directed into different beamlines for various applications.

The Synchrotron SOLEIL operates with electrons in its storage ring at an energy level of 2.75 GeV. This configuration enables the generation of a broad spectrum of light spanning from 1 eV (infrared) to 50 keV (hard X-rays). The radiometric performance of a synchrotron is evaluated based on its brightness, which is determined by factors such as the flux of photons per unit solid angle, cross-sectional area, and bandwidth. At the Synchrotron SOLEIL, the brightness reaches an impressive level of  $10^{20}$  photons per second, per square millimeter, per milliradian squared, per 0.1% relative bandwidth change ( $\Delta\lambda/\lambda$ ).

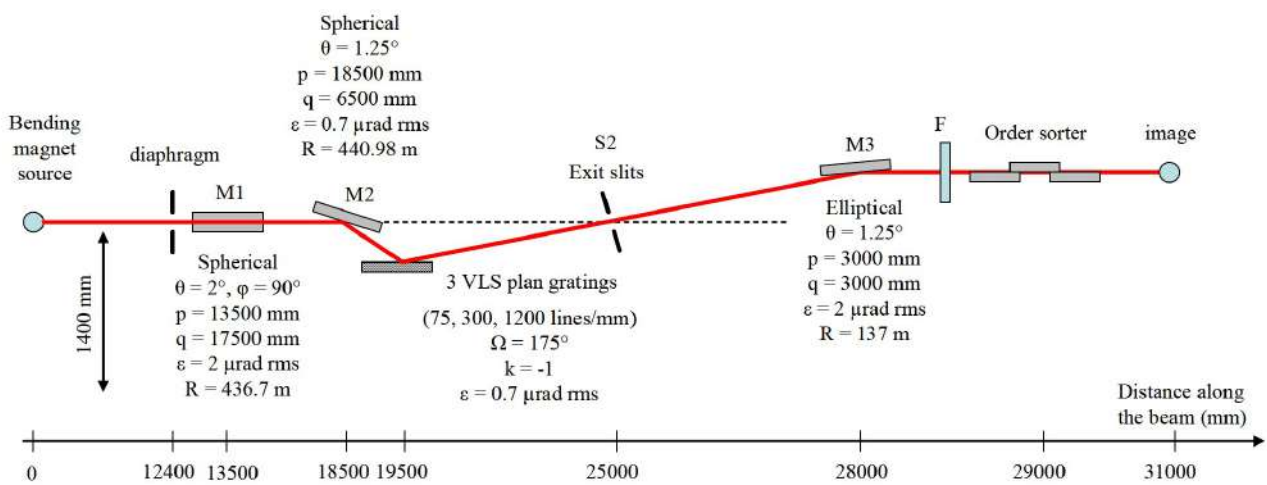


Figure 3.11: Illustration depicting the XUV branch of the Metrology beamline [16].

The XUV branch of the metrology beamline at Synchrotron SOLEIL was employed to investigate the relationship between wavelength variation and the reflectance of multilayers deposited on flat silicon substrates, as well as the efficiency of multilayer gratings. The spectral range covered by this branch extends from 30 eV to 1800 eV, as demonstrated in Fig.3.11. The metrology beamline serves as a valuable facility for developing instruments and diagnostics that are essential for the characterization of X-ray beams, such as intensity, size, degree of coherence, polarization, and so on.

The Metrology beamline is positioned on a bending magnet and incorporates several components to manipulate the XUV beam. At the beginning of the XUV branch, a diaphragm is employed to clean the beam. Subsequently, two mirrors denoted as M1 and M3 in Fig.3.11, enable horizontal and vertical focusing of the beam, respectively, in the image plane located 31 meters from the source. Between these mirrors, a monochromator is inserted, consisting of a spherical mirror, a "Variable Line Spacing" (VLS) plane grating, and an exit slit.



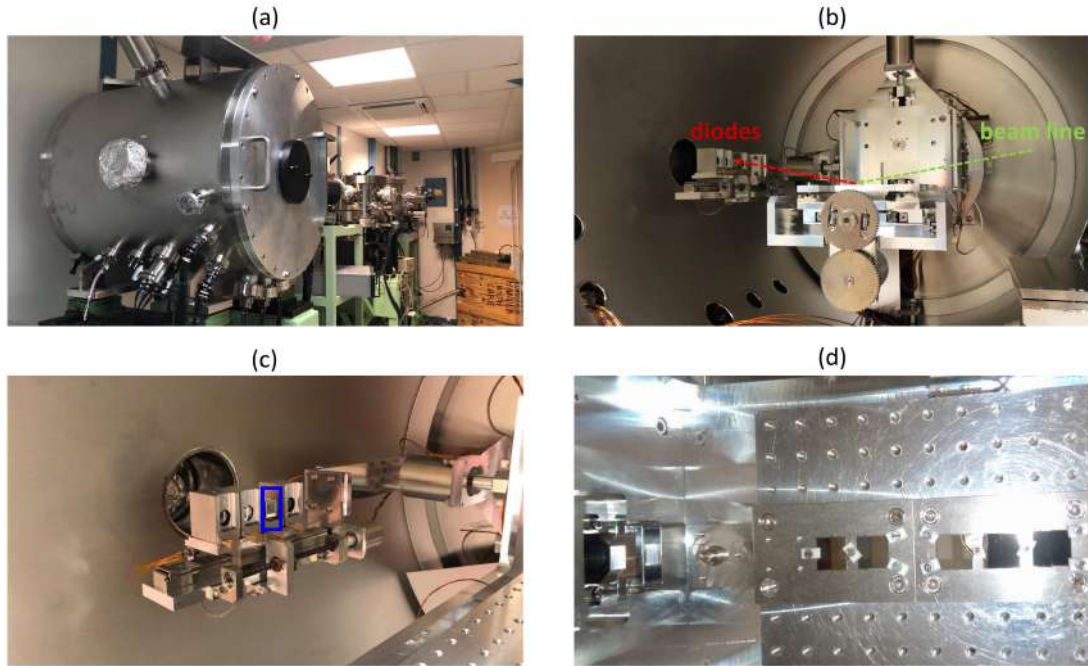


Figure 3.12: Photography of (a) an external view of a reflectometer. (b) an internal view of a reflectometer. (c) Close-up images of the diodes within the reflectometer. (d) the alignment of the multilayer gratings samples within the reflectometer.

The monochromator comprises three gratings, and the choice of the grating determines the spectral range of operation. For instance, a grating with 75 lines/mm covers the range of 45–600 eV, a grating with 300 lines/mm covers the range of 300–1600 eV, and a grating with 1200 lines/mm is used from 600 eV to 1800 eV at XUV. Following the VLS grating, the exit slit is positioned, and its width can be adjusted to control the spectral resolution: a narrower slit enhances spectral resolution but reduces the flux.

After the vertical focusing mirror, the low pass filter is utilized to eliminate high-order harmonics. The low pass filter consists of a set of transmission filters and a low-energy filter, incorporating three plane mirrors. The filter selection, mirrors angle, and mirrors coating depend on the desired working energy range.

After completing the various steps involved in spatial and spectral shaping of the beam, the reflectometer is positioned as follows: it is located within a cylindrical enclosure maintained under a high vacuum  $\approx 10^{-7}$  mbar (see Fig.3.12(a)). The reflectometer consists of a motorized sample holder stage capable of translations along the x, y, and z axes and rotation (see Fig.3.12(b)). Additionally, there is a swiveling detector arm. Users have the option to select the desired detector, which can be a bare photodiode, an aluminum-coated silicon photodiode, or a zirconium-coated silicon photodiode (see Fig.3.12(c)). The detector employed for measuring the spectra of reflectance or efficiency is situated within the blue box, as depicted in Fig.3.12(c). The photodiode's current is measured using a Keithley 6517B electrometer, as it provides the necessary information for reflectivity measurements. It is also possible to incorporate a slot in front of the selected diode if required.

Two aluminum diode has been used, one of which lacks a slit while the other contains a  $100\mu\text{m}$  slit. The diode

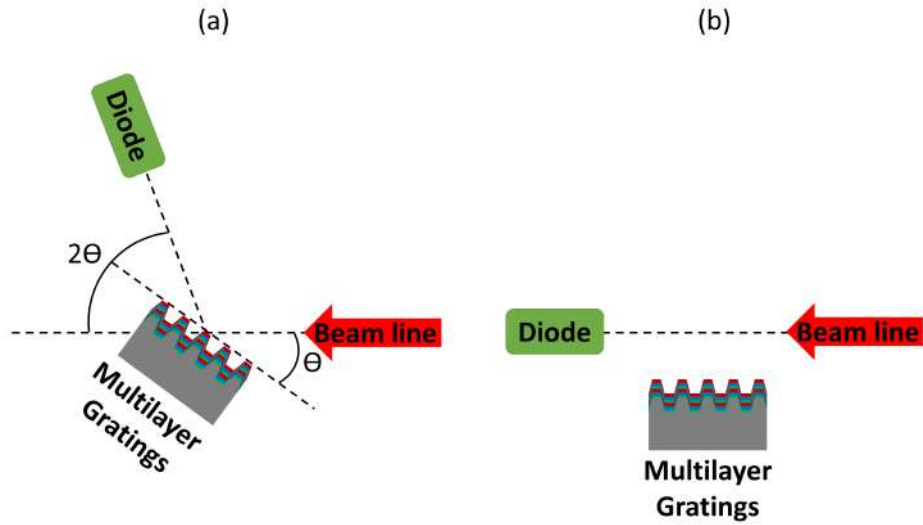


Figure 3.13: The schematic diagram illustrates the principle of synchrotron beamline measurements, showcasing (a) the acquisition of a measurement and (b) the acquisition of a direct beam.

with a slot was employed to align the sample position relative to the beamline, whereas the diode without a slot was used to detect the reflected flux from flat multilayer test samples or diffracted flux from multilayer gratings.

Achieving precise alignment of the multilayer gratings within the reflectometer is crucial (see Fig.3.12(d)). Different steps are taken to measure the efficiency for each classical or conical position. We have successfully measured the efficiency in both classical and conical positions. The alignment of the multilayer gratings is carried out in accordance with the mark etched established by Zeiss, which has been confirmed by AFM. Further discussion on this alignment process will be provided in the upcoming chapter.

Consequently, the metrology device of the XUV branch allows for mirror reflectivity measurements through  $\theta - 2\theta$  measurements. In this setup, the position of the beam is fixed. To perform the  $\theta - 2\theta$  measurement, the sample is rotated by an angle  $\theta$ , while the detector rotates by an angle  $2\theta$  (see Fig.3.13(a)).

To normalize the measurement and calculate the reflectivity of the studied sample, it is necessary to measure the current flux of the direct beam. To accomplish this, the sample is removed from the beam's path, and a diode is positioned in front of the beam (Fig.3.13(b)). This allows for the acquisition of diode current as a function of time. Since measurements in the XUV range can involve low current values, it is important to consider the noise in the reflectivity calculation as well.

Moreover, we measured the noise of both the direct beam measurement and the  $\theta - 2\theta$  measurement. This will be done using the same setup as shown in Fig.3.13(a) and Fig.3.13(b), but with the shutter closed to mask the beam and measure only the noise.

For this thesis, the XUV metrology beamline was utilized to perform measurements on the multilayer grating samples within their designated energy range from 40 eV to 72 eV.



### 3.1.4.1 Direct Beam Comparison

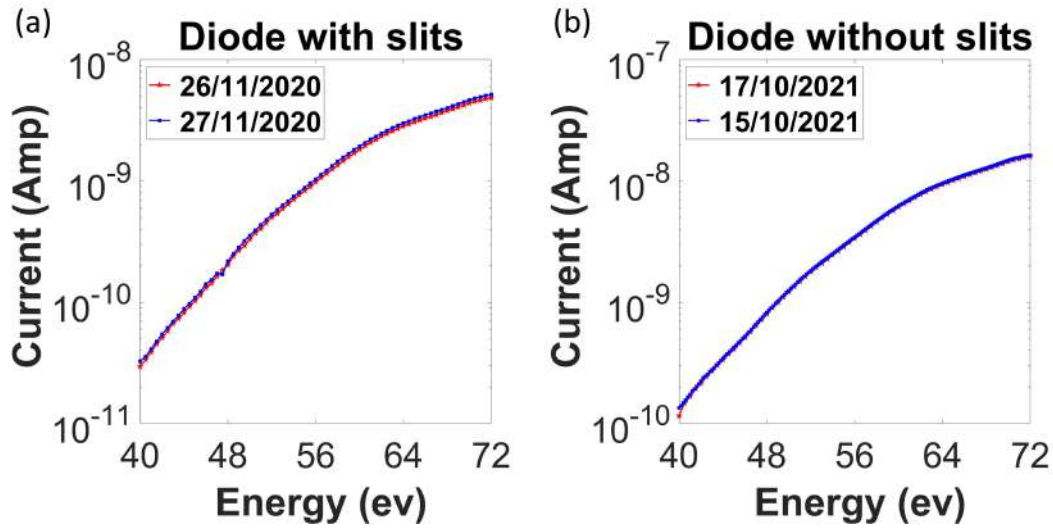


Figure 3.14: Variation of the current with Energy for a diode with the slit at different measurements on different days.

In Figure 3.14(a), we have plotted the direct beam measurements obtained with diode with the slits on different days during our initial experiment. The maximum variation in the value of the direct beam from one day to another is 40.91% at 45 eV and 11.12% at 70 eV. These values remain relatively unchanged even after excluding the dark current. Furthermore, the maximum variation in the direct beam within the same day is below 6.51%. Additionally, we performed two direct beam measurements with a diode without a slit on the same day, as shown in Figure 3.14(b). The variation between these two measurements is approximately identical.

Typically, the reflectance is calculated using the following equation:

$$R = \frac{I_{Reflected} - I_{Dark}}{I_0 - I_{Dark}} \quad (3.1)$$

Where, the terms  $I_{Reflected}$ ,  $I_0$ , and  $I_{Dark}$  denote the intensity of the reflected beam by the sample, the intensity of the original beamline, and the intensity measured by the detector in the absence of the beamline, respectively.

### 3.1.4.2 Dark Current

In this section, our objective is to examine the dark current and demonstrate its negligible impact on our measurements. Table.3.2 showcases the mean average and standard deviation of the dark current for various current ranges (20 pA, 200 pA, 2 nA). The measurements were conducted at two different incident angles (5 degrees and 45 degrees). It's worth emphasizing that the noise varies depending on the diode's position due to the cable movements within the reflectometry setup. The mean (equation.3.2) and standard deviation (equation.3.3) calculations were performed using a function available in MATLAB software. The dark current measurements were captured by

the diode without a slit, with each measurement lasting for a duration of 30 seconds.

$$\mu(I_{Dark}) = \frac{\sum_{i=1}^N I_{Dark}[i]}{N} \quad (3.2)$$

$$S(I_{Dark}) = \sqrt{\frac{\sum_{i=1}^N [I_{Dark}[i] - \mu(I_{Dark})]^2}{N - 1}} \quad (3.3)$$

Table 3.2: Mean and standard deviation of the dark current.

Dark current	Incident angle (°)	$\mu(I_{Dark})$	$S(I_{Dark})$
20 pA	5	2.0206e-12	5.4258e-14
200 pA	5	2.0263e-12	4.8451e-14
2 nA	5	2.3531e-12	1.6282e-12
20 pA	45	2.8823e-12	5.5146e-14
200 pA	45	2.9016e-12	5.2302e-14
2 nA	45	3.3676e-12	2.1897e-12

### 3.1.4.3 Diode Uniformity

Figure.3.15 illustrates the detection of the +1-order for the same multilayer grating using both a diode with a slit and a diode without a slit. When employing the diode with a slit, the detection of the +1 order appears as a shoulder peak, as shown in Fig. 3.15(a). Consequently, the efficiency is computed by selecting the maximum point of this peak and substituting it into Equation 3.1. Additionally, we observed that the calculation of the +1-order is affected by the dark current, as the intensity of the diffracted flux photons is in close proximity to the detected flux photons of the dark current.

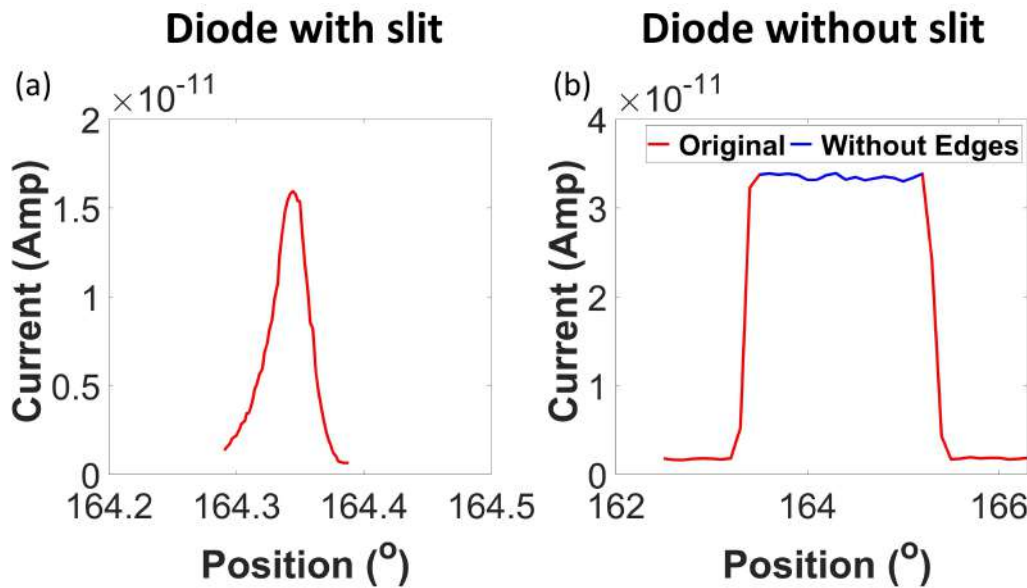


Figure 3.15: Variation of the photons flux current as a function of the rotation position for the (a) diode with slit, and (b) diode without slit.

On the other hand, when using a diode without a slit, the detection of the +1-order results in a broadband peak with a plateau at the top, as depicted in Fig. 3.15(b). The presence of this plateau enhances the accuracy of measuring the +1-order because the mean of the top points can be computed after removing the peak edges, which is then substituted into Equation 3.1. Importantly, it should be noted that we observed the computed +1-order to be largely unaffected by the dark current when employing the diode without a slit, as it detects a significantly higher number of flux photons compared to the diode with a slit.

Hence, the authors made the decision to utilize the diode without a slit in order to obtain more precise measurements and mitigate the impact of dark current on the measurements.

To evaluate the uniformity of the diode without slit for this measurement, the edge portion that corresponds to the limits of the diode was excluded. Subsequently, the peak-to-valley (PV) variation, which denotes the difference between the maximum and minimum photon flux current detected by the diode, was determined. The calculated PV variation was approximately  $4.0238 \times 10^{-10} \text{A}$ , corresponding to an error of around 12.34% relative to the average signal (see Equation 3.4).

$$Error(I_{Diffracted}) = \frac{\text{maximum}(I_{Diffracted}) - \text{minimum}(I_{Diffracted})}{\text{mean}(I_{Diffracted})} \quad (3.4)$$

#### 3.1.4.4 Measuring the efficiency of the beamline

Figure 3.16 illustrates the detection of different orders by the diode at various positions under near-normal incidence and constant energy conditions for a multilayer grating. In this arrangement, the 0<sup>th</sup> order is positioned at 170 degrees, followed by the +1<sup>st</sup> order, +2<sup>nd</sup> order, and so on.

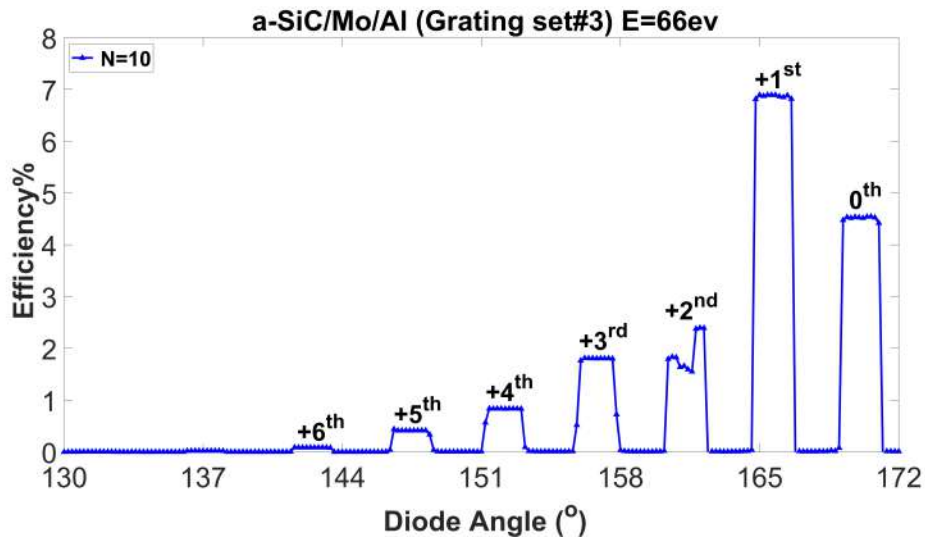


Figure 3.16: Variation of all orders efficiency with diode angle for multilayer grating at near normal incidence.

In order to achieve more precise measurements of the orders, it is customary to average the points located at

the peak plateau and subsequently divide them by the intensity associated with the same energy. The following Figure 3.17 demonstrates how the position of the peak plateau varies with the energy magnitude.

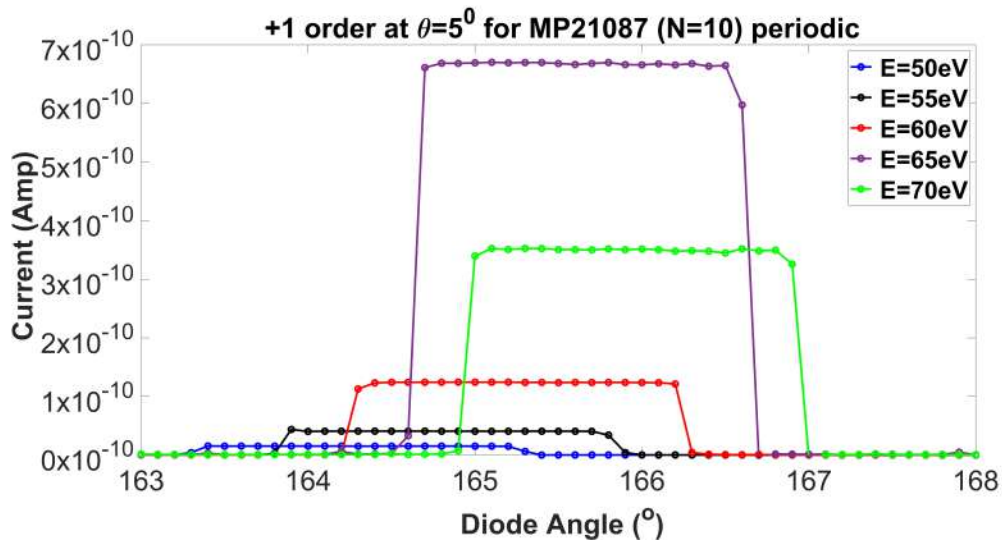


Figure 3.17: Variation of +1 orders current intensity with diode angle on multilayer grating for different energies at near normal incidence ( $\theta = 5^\circ$ ).

### 3.1.4.5 Estimating the polarization factor of the beamline

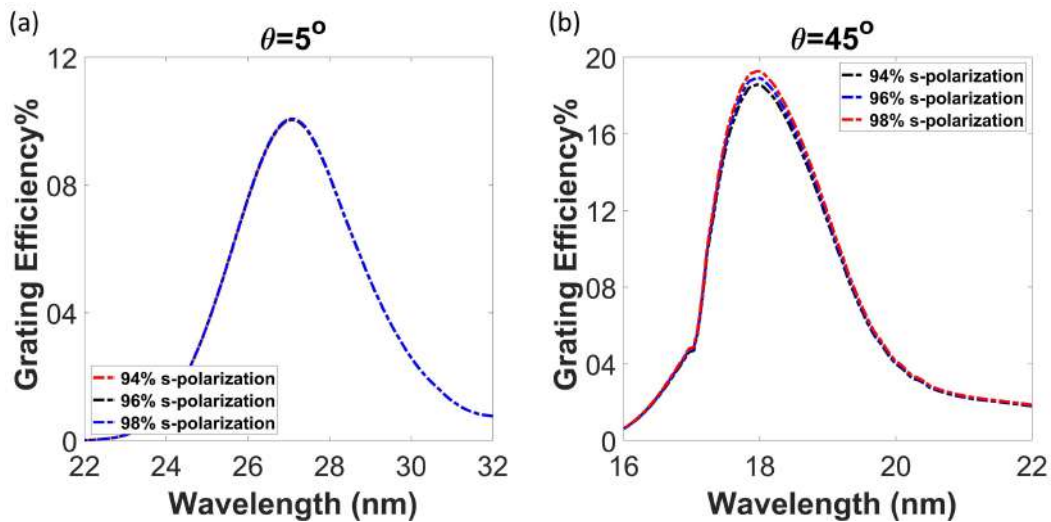


Figure 3.18: Simulation of the +1 orders of a 6-period Al/Mo/SiC multilayer grating Set#1 for different values of the polarization factor at (a)  $\theta = 5^\circ$  near-normal incidence and (b)  $\theta = 45^\circ$ .

Theoretical estimation of the polarization factor of the beamline indicates a polarization higher than 90% s-polarization. However, prior to our experiment, the polarization of this beamline had not been measured within the energy range of interest. To obtain a more accurate value, we measured the multilayer sample, named MP20065, consisting of 10 periods of Al/Mo/SiC at  $\theta = 5^\circ$  and  $\theta = 45^\circ$  angles (details provided in Section.5.5 of Chapter.5). Since reflectance at

near-normal incidence  $\theta = 5^\circ$  is nearly polarization-independent, we employed the model determined at this angle to fit the polarization factor for the  $\theta = 45^\circ$  data. The estimated polarization factor is  $0.96 \pm 0.02$ .

Additionally, we deposited a 6-period Al/Mo/SiC multilayer on one of the samples from Grating Set#1 (described in detail in Section.6.3.2 of Chapter.6). It should be noted that a variation in the polarization factor within the range of 0.94-0.98 does not significantly affect the efficiency of the +1 order of the multilayer grating in Set#1. The impact is negligible at near-normal incidence  $\theta = 5^\circ$ , and for  $\theta = 45^\circ$ , the variation in efficiency stays within  $\pm 0.70\%$ . This is illustrated in Fig.3.18(a) and Fig.3.18(b), which depict the simulation of the +1 order efficiency for  $N = 6$  with various s-polarizations. It's important to recognize that the decrease in intensity around the 17nm wavelength in Fig. 3.18(b) is attributable to the presence of the aluminum edge.

### 3.1.5 Transmission Electron Microscopy (TEM)

#### 3.1.5.1 Physics of Transmission Electron Microscopy

Electron microscopy is a microscopy technique that employs a beam of electrons to illuminate a sample and generate an image. Due to the extremely short De Broglie wavelength of electrons, electron microscopy enables the attainment of exceptionally high resolutions, surpassing those achievable with photonic microscopy. This allows for the visualization of fine details, such as individual silicon atoms. Various electron microscopy techniques are available, including transmission electron microscopy (TEM), reflection electron microscopy, and scanning transmission electron microscopy (STEM). In this thesis, both STEM and TEM techniques have been utilized, and their key distinctions are outlined in the provided Table.3.3.

Table 3.3: Comparison of TEM and STEM.

Point of Comparison	STEM	TEM
Imaging Principle	STEM uses a focused electron beam to scan the sample and collect transmitted electrons for image formation.	TEM transmits an electron beam through a thin sample to create an image based on electron interactions.
Electron Beam	STEM employs a fine electron probe that scans the sample in a raster pattern.	TEM uses a broader electron beam that illuminates the entire sample.
Imaging Modes	STEM offers various imaging modes including bright-field, dark-field, and HAADF imaging.	TEM enables bright-field imaging and can capture dark-field images.
Spatial Resolution	STEM achieves high-resolution imaging down to sub-angstrom levels.	TEM provides high-resolution imaging typically ranging from sub-nanometer to a few angstroms.
Sample Preparation	STEM requires thin samples that can transmit electrons, prepared through mechanical thinning or ion milling.	TEM also requires thin samples achieved through methods like FIB milling or ultramicrotomy.



Figure 3.19: Photograph of Transmission electron microscopy at CentraleSupélec, ENS Paris-Saclay, Université Paris-Saclay.

### 3.1.5.2 Operation of Transmission Electron Microscopy

For the study of Al/Mo/SiC multilayers carried out during this thesis, electron microscopy measurements were carried out. The TEM images were taken with a ThermoFisher TITAN3 G2 equipped with a probe aberration corrector, which provides a spatial resolution of 0.07 nm.

As part of the analysis of multilayer coatings, one may want to use electron microscopy to visualize a cross-section of the sample, and therefore observe the alternation of the layers, for example for the direct measurement of their thickness. The samples to be observed must first be prepared to obtain a section. It is necessary for these samples that the multilayer coatings have been deposited on a substrate that can be cut (typically a silicon wafer). The TEM cross-section sample has been prepared by using a focused ion beam scanning electron microscopy (FIB-SEM) Thermofisher Helios Nanolab 660. A protective layer of approximately 2  $\mu\text{m}$  of platinum was first deposited on the sample to protect the multilayers. Then TEM lamella was prepared by using the standard “lift out” method. Bright-field images were made using central diffraction order only. Besides, Energy dispersive x-ray spectrometry (EDX) was performed in scanning TEM (STEM) mode by using an FEI ThermoFisher Titan3 G2 80-300 microscopy operating at 300 kV and equipped with a Cs probe corrector as well as a Super X EDX detector.

### 3.1.5.3 Imaging modes

Utilizing both its axial detector and annular detector, this microscope facilitated the implementation of bright field imaging, and the microscope is equipped with three Dark Field detectors specifically designed for dark field imaging. Among these detectors, the High Angle Annular Dark Field (HAADF) imaging technique is one of the available options.

#### 3.1.5.3.1 High Angle Annular Dark Field Imaging:

By collecting the highly scattered electrons in a ring encircling the illuminating beam, the detector captures the essence of Rutherford scattering. This type of scattering involves electrons scattered at high angles, with the differential scattering cross-section proportional to the atomic number  $Z$  squared. Consequently, this apparatus enables the visualization of  $Z$  contrast, revealing the varying atomic numbers of the sample's elements. In contrast to TEM images, high- $Z$  materials appear bright in STEM images, while low- $Z$  materials appear dark.

#### 3.1.5.3.2 Bright Field Imaging:

The acquisition of this signal occurs when electrons pass through the sample in the microscope and are subsequently transmitted and diffused onto the axial detector. The signal primarily comprises electrons that have undergone inelastic scattering within a specific angular range. Regions containing elements with higher atomic masses tend to scatter or absorb a greater number of electrons, resulting in their appearance as dark regions in a bright field image.

#### 3.1.5.3.3 Energy-Dispersive X-ray Imaging:

EDX imaging is employed to acquire information about the distribution of elements within a sample by leveraging the principles of X-ray spectroscopy. In this technique, high-energy electrons interact with the sample, leading to the generation of characteristic X-rays.

Within TEM, a finely focused electron beam is directed through a thin sample, and as the electrons interact with the atoms, they can induce excitations and ionizations in the inner electron shells. As an electron from a higher energy level fills the resulting vacancy in the inner shell, it emits energy in the form of characteristic X-rays that are specific to the element being analyzed. These emitted X-rays possess distinct energies that correspond to the atomic structure of the elements involved.

The TEM's EDX system incorporates an X-ray detector situated in close proximity to the sample. This detector captures the energy of the X-rays emitted by the sample, enabling the identification of present elements and their relative intensities. Through a pixel-by-pixel scanning of the electron beam across the sample and concurrent acquisition of EDX spectra, an elemental map can be generated. This map visualizes the spatial distribution of elements

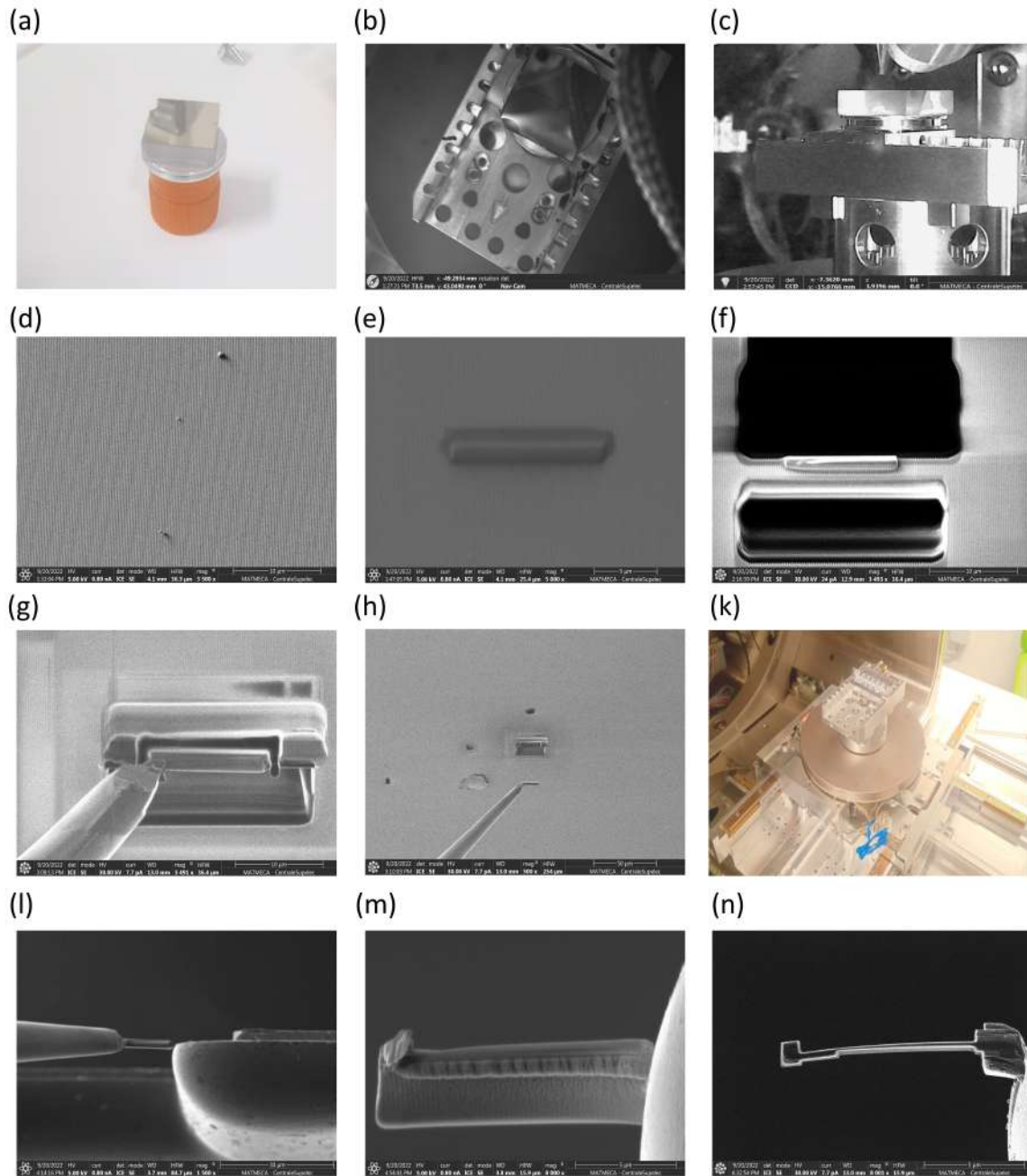


Figure 3.20: Photograph of different processes of Scanning electron microscopy to prepare the sample for transmission electron microscopy measurement.

within the sample, furnishing valuable insights into its composition.

### 3.1.5.4 Focused Ion Beam preparation for TEM

First, the samples designated for cutting are coated with a protective layer of platinum to safeguard the surface. Following that, the sample undergoes precise refinement into a thin section using a FIB-SEM within a vacuum cham-



ber. The main objective of the FIB-SEM is to prepare a cross-section of the sample and attach it to a sample holder resembling the one depicted in Fig.C.1. Subsequently, this prepared sample is inserted into the TEM for further measurements.

The process of preparing the sample for TEM measurement involves the following steps:

1. The desired grating to be measured is affixed to a sample holder using carbon tape, extending to the thin film, in order to mitigate charge effects, as depicted in Fig. 3.20(a).
2. Inserting the grating into the SEM and adjusting its position, as depicted from two different viewpoints in Fig.3.20(b-c).
3. Visualizing the grating grooves using SEM, as shown in Figure 3.20(d). The cross-section is oriented perpendicular to the grating grooves to observe the evolution of multilayers on the grooves for TEM measurements.
4. Performing platinum deposition using the organometallic gas injector integrated into the vacuum preparation chamber of the Focused Ion Beam (FIB) system. This involves scanning a rectangular area on the sample's surface with an electron or ion beam while injecting organometallic gas. The interaction between the beam and platinum precursor gas molecules leads to decomposition and subsequent deposition of platinum within the scanned area, as depicted in Fig.3.20(e). For Al/Mo/SiC samples, the first deposition involves a thin layer of platinum using organometallic gas of 5 kV accelerated electron beam with an incident electronic current of  $\approx 1.6$  nA. The desired thickness is approximately 500 nm. Subsequently, a second, thicker layer is deposited on top of the first layer using a 30 kV accelerated ion beam with an ion current of 0.23 nA or 80 pA.
5. Etching around a rectangular area on the sample's surface, as demonstrated in Fig.3.20(f).
6. Attaching the rectangular area on the sample's surface to the tip, as shown in Fig.3.20(g). Platinum is deposited over both the tip and the rectangular area.
7. Removing the tip with the attached rectangular area from the gratings sample, as depicted in Fig.3.20(h).
8. Extracting the gratings sample from the SEM, as shown in Fig.3.20(k). The gratings sample is no longer needed at this stage.
9. The procedure for attaching the rectangular area on the sample's surface to the TEM sample holder is shown in Fig.3.20(i). This involves depositing platinum on the cross-section between the TEM sample holder and the rectangular area on the sample's surface, as well as etching the cross-section between the tip and the rectangular area.
10. Figure 3.20(m) illustrates the successful attachment of the rectangular area on the sample's surface to the TEM sample holder.
11. The final step is to etch the rectangular area on the sample's surface, which is attached to the TEM sample holder, to thin down the TEM-prepared sample as much as shown in Fig.3.20(n).

## 3.2 SIMULATIONS TOOLS

### 3.2.1 Fresnel Equations Multilayer

For analyzing the measurements obtained from the synchrotron and XRR, we employed the IMD software [84]. This software enables the simulation of multilayer coatings using optical constants from tabulated data found in the CXRO database [2]. Additionally, it offers the ability to define a material by specifying its chemical composition and density via atomic diffusion factors. The IMD software further facilitates the modeling of layer behavior at the interface and allows for the estimation of interdiffusion/roughness between two layers.

The IMD software employed in this thesis served dual purposes: fitting and optimization.

#### 3.2.1.1 Optimization by IMD

Specifically, for the optimization aspect, a genetic algorithm was utilized, incorporating a figure-of-merit (FOM) function as defined in the equation.3.5.

$$FOM = \frac{\sum_{i=1}^{N_{target}} W[i] \times |R[i] - R_{target}[i]|^n}{\sum_{i=1}^{N_{target}} W[i]} \quad (3.5)$$

In the equation, the variables  $n$ ,  $N_{target}$ , and  $W[i]$  correspond to the exponent, the count of iterations for the multilayer optimization, and the respective weighting factors for each point. Specifically,  $R_{target}[i]$  is calculated as  $1/W[i]$ , and the expression for  $R_{target}$  is formulated as a function of the independent variable.

For equation 3.5, it is common practice to increase the number of iterations and set a typical value of 16 for  $n$ .

To ensure the prevention of diffusion, guarantee the presence of this layer during the deposition process, and maintain the stability of the multilayers, a minimum thickness of 2 nm was implemented for all materials in the optimization process.

For example, during the optimization procedure for multilayers which will be deposited over a specific grating designed for a central wavelength of 19nm, the parameters were configured to achieve a maximum reflectivity of 0.4 within the wavelength range of  $\lambda = 17$  nm to  $\lambda = 21$  nm. However, it was determined that the reflectivity target should be set to zero for wavelengths greater than 22 nm and wavelengths lower than 16 nm, and the number of multilayer periods was set at  $N = 6$  as illustrated in Fig.3.21(a).

Furthermore, 100 data points were allocated within the range of  $\lambda = 17$  nm to  $\lambda = 21$  nm in order to achieve the desired target. However, for wavelengths exceeding 22 nm and wavelengths below 16 nm, only 10 data points were assigned. This indicates that the emphasis in the optimization process is primarily placed on targeting a reflectivity of 0.4, rather than reducing the curve to zero at the edges.

In the context of aperiodic multilayer design, the optimization procedure deviates from the considerations of periodic design. Consequently, the objective was to attain a reflectivity of 0.3 within the wavelength range of  $\lambda = 17$

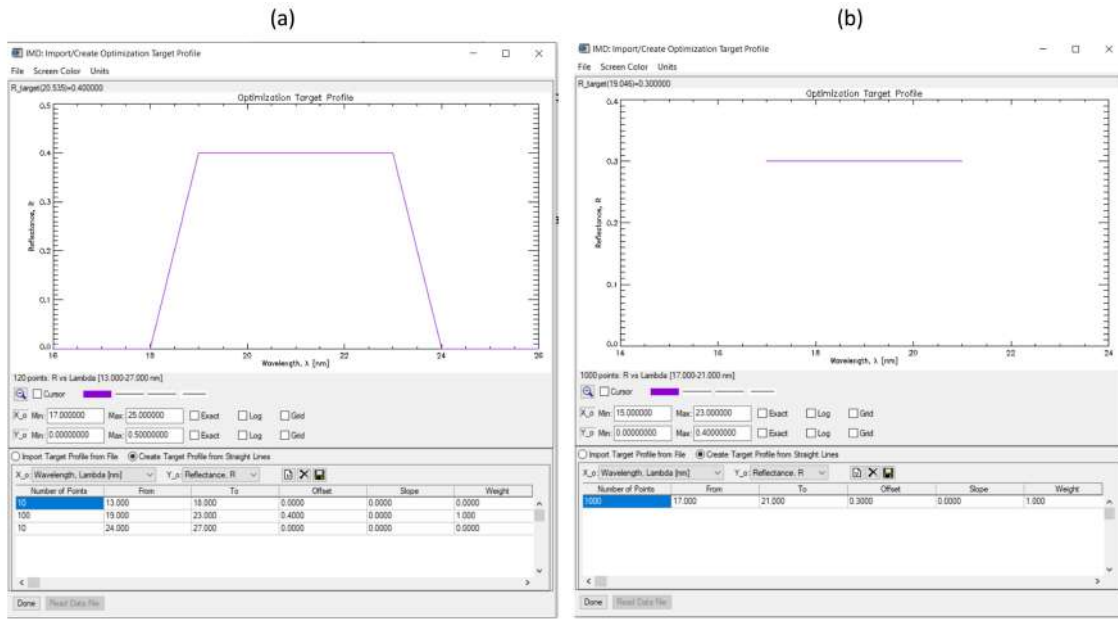


Figure 3.21: The optimization criteria differ for (a) periodic multilayers, and (b) aperiodic multilayers.

nm to  $\lambda = 21$  nm. Moreover, the requirement of zero reflectivity at the edges was omitted, as depicted in Fig.3.21(b). An attempt was made with 1000 data points to achieve a reflectivity of 0.3.

### 3.2.1.2 Fitting by IMD

For the fitting process, two approaches were utilized: genetic algorithm and manual fitting.

The genetic algorithm, implemented through the FOM equation.3.5, proved highly effective in fitting the roughness during reflectance characterization as a function of grazing angle or energy. Additionally, it played a crucial role in extracting information pertaining to density, layer thickness, and roughness using the effective medium approximation method.

In the case of manual fitting, it is typically employed for reflectance characterization as a function of grazing angle. For instance, when depositing thin films of materials like Al, Mo, or SiC onto a flat Si substrate, the characterization is conducted using GIXR. Through manual fitting of the GIXR data obtained, we estimate the relationship between the thickness of the thin film and the deposition rate of the same thin film. As illustrated in Fig.3.22(a), there is a notable agreement between the fitting and measured data for SiC, providing an example of a successful alignment.

In addition, manual fitting was utilized to determine the period thickness of the deposited periodic multilayer. This involved fixing the thicknesses of Al and Mo based on the estimated deposition rate from Fig.3.22(b). Meanwhile, the thickness of SiC was manually adjusted until a satisfactory agreement was achieved between the measured data obtained from GIXR and the fitted data obtained from IMD.

In our detailed exploration of fitting roughness, our final model embraces a consistent substrate roughness of

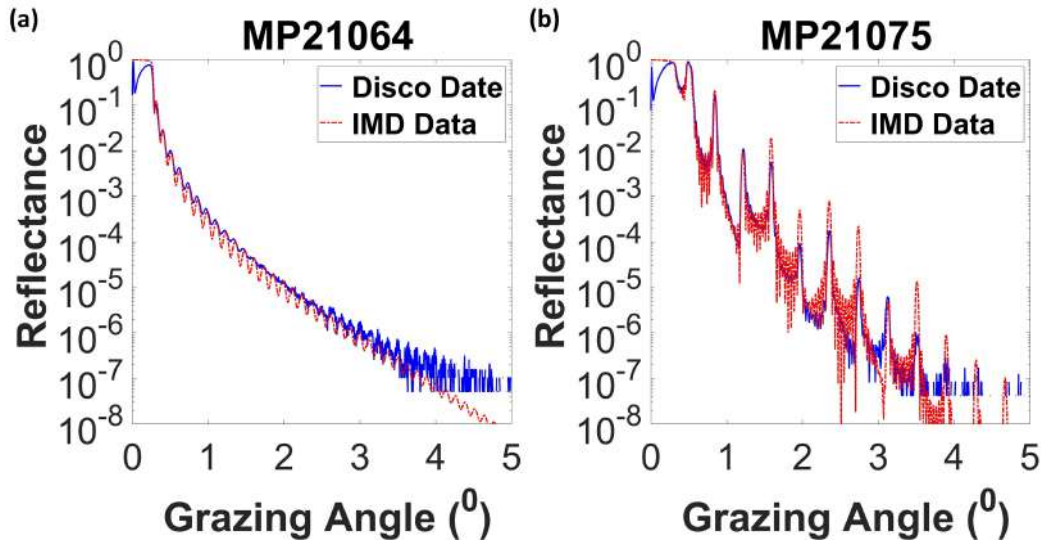


Figure 3.22: The data obtained includes fitted data using IMD and measured data obtained through GIXR for the following scenarios: (a) a thin film of SiC deposited on a flat Si substrate, and (b) 10-period of Al/Mo/SiC deposited on a flat Si substrate.

0.35 nm. Moreover, we assigned a singular, specific value to all the roughness values between layers, aligning with the values obtained from the genetic algorithm fitting using IMD software. This meticulous approach guarantees simplicity and uniformity across our final model.

### 3.2.1.3 Simulation by custom MATLAB code

It is noteworthy that a custom MATLAB code has been developed for simulating a multilayer on a flat substrate, resembling IMD. This approach simplifies the extraction of the polarization factor. Additionally, this method has been utilized to simulate the variations in multilayer reflectance with respect to the incident angle of the beam.

## 3.2.2 Rigorous Coupled-Wave Analysis (RCWA)

RCWA is a semi-analytical formulation derived from Maxwell's equations in Fourier space. Situated within the domain of computational electromagnetics, it serves as a valuable technique for investigating diffraction effects arising from a variety of planar gratings. These gratings are situated between two separate media and feature grooves with a diverse array of orientations, encompassing both slanted and unslanted configurations in relation to the grating's surface.

While there are alternative computational methods, such as the finite difference time domain (FDTD) and finite element method (FEM), the RCWA provides a similar level of accuracy to these previous methods. Notably, RCWA stands out with its unique capability to decrease computation time while maintaining this accuracy.

Figure 3.23(a) illustrates a schematic of a grating with a trapezoidal profile, excluding any multilayer components. It consists of a grating depth ( $d$ ), a trapeze angle ( $\alpha$ ), and top and bottom bases. The fill factor ( $f.f$ ) for the trape-

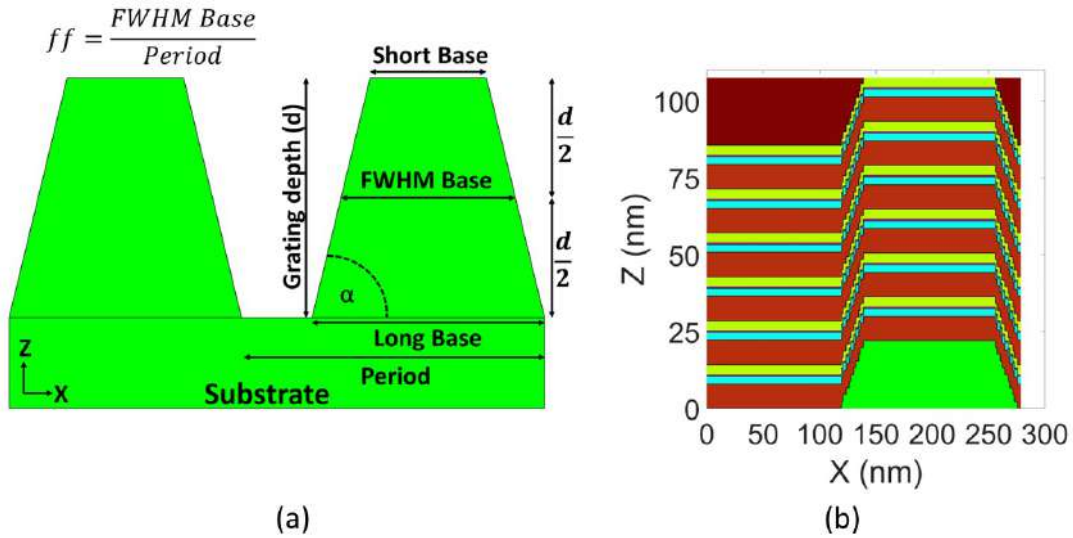


Figure 3.23: schematic diagram of (a) the trapezoidal grating profile before deposition and (b) the multilayer coating ( $N=6$ ) deposited on the trapezoidal grating.

zoidal grating is defined as the ratio of the full width at half maximum (FWHM) base to the period ( $P$ ). To investigate the diffraction efficiency of multilayers over trapezoidal or lamellar ( $\alpha=90^\circ$ ) gratings, as depicted in Fig.3.23(b), we simulated multilayer gratings using a custom MATLAB code based on RCWA (RETICOLO software [83]). Interfacial roughness was not considered in these simulations. The trapezoidal profile was approximated by dividing the depth into 10 layers of equal thickness, following previous literature [85]. Moreover, the width of each sub-layer linearly decreased from the bottom to the top of the groove, as shown in Fig. 3.23(b). The simulation model assumes a perfect replication of the initial grating profile after the multilayer deposition. Specifically, the model assumes that the  $\alpha$  values remain constant at both the grating surface and the multilayer surface and that the deposited layers have the same thickness on the slope, top, and bottom parts of the grating.

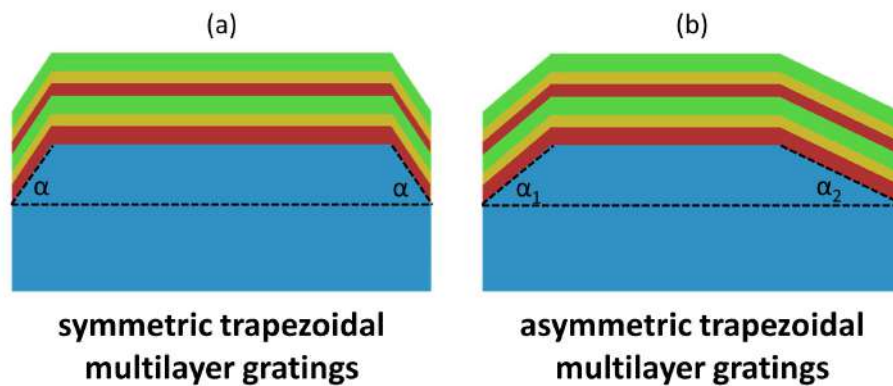


Figure 3.24: Schematic diagram illustrating the structure of multilayer trapezoidal gratings with periodic multilayers ( $N = 2$ ) in both symmetric (a) and asymmetric (b) configurations.

Typically, we manually adjust the parameter  $d$ , whereas the parameters  $\alpha$  and  $f.f$  (FWHM) are computed by averaging their values from the AFM profile after deposition. Parameter  $P$  is obtained from Zeiss' description of the grating substrate, which is validated by examining the AFM profile before deposition.

In certain instances, particularly when modeling multilayer gratings in a conical position, we would like to draw attention to a specific consideration. We have made a modification to the grating structure, transitioning from a symmetric trapezoidal shape to an asymmetric trapezoidal shape as shown in Fig.3.24. Specifically, in the case of a symmetric trapezoidal grating, the angle  $\alpha$  is uniform from both the right and left sides of the trapezoid. However, in the case of an asymmetric trapezoidal grating, the angle  $\alpha$  differs between the left and right sides of the trapezoid. As a result, we have assigned distinct slope angles to the asymmetric trapezoidal shape, denoted as  $\alpha_1$  and  $\alpha_2$ .

### 3.2.3 Materials optical constants.

The optical constants were determined relative to the references cited in [2; 86; 87; 88].

Table 3.4: Diverse material optical densities and their optical constants at  $\lambda = 0.154$  nm. [2].

Material	Density (g/cm <sup>3</sup> )	$\delta$ ( $\lambda=0.154$ nm)	$\beta$ ( $\lambda=0.154$ nm)
SiC	3.22	1.05e-05	1.76e-07
Mo	10.22	2.89e-05	1.91e-06
Al	2.7	8.55e-06	1.58e-07
SiO <sub>2</sub>	2.2	7.19e-06	9.40e-08
Si	2.33	0.999	1.72e-07

Table 3.4 presents the densities and optical constant values employed for modeling multilayers on silicon substrates or silica gratings in this thesis for the purpose of GIXR spectra analysis.

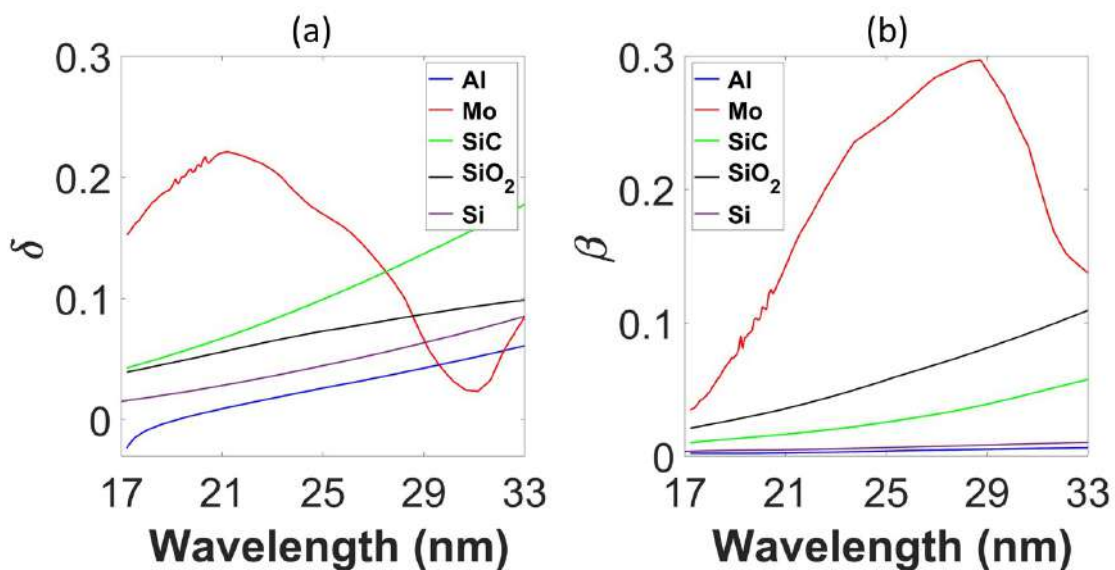


Figure 3.25: optical index of different materials in the EUV [2] (a)  $\delta$ , and (b)  $\beta$ .

Silicon carbide (SiC) thin films are commonly used in the construction of EUV/X multilayer mirrors for space-related purposes. Additionally, SiC demonstrates high reflectivity beyond a wavelength of 50 nm, making it an effective choice for single thin-film reflective coatings. The value tables of SiC indices are depicted in Fig. 3.25.

Molybdenum combined with silicon has frequently been employed in multilayer structures due to its excellent performance in the EUV spectral range. The utilization of Mo/Si periodic mirrors has demonstrated their effectiveness and durability in equipping on-board EUV telescopes like SOHO/EIT [89], STEREO/EUVI [90], SUVI/GOES, and SDO/AIA [91]. These mirrors enable the detection of iron and helium emission lines from various regions of the solar atmosphere.

Despite the wide range of applications, discrepancies still exist among various tables of molybdenum (Mo) optical indices, which significantly impact simulations (Fig. 3.25). These variations become noticeable from 30 nm for the  $\beta$  absorption coefficient and even earlier, starting at 21 nm for the  $\delta$  coefficient.

Aluminum serves as a central material in all the developments discussed in these studies. It holds crucial importance for transmission filters and multilayer mirror coatings used in space missions that explore EUV. In Fig. 3.25, significant discrepancies are observed, particularly in the vicinity of the  $L_{2,3}$  absorption threshold around 17nm.

Typically, oxygen atoms are predominantly present at the surface of the Si substrate (which was not deoxidized prior to deposition) and the surface of the top multilayer (representing the previously mentioned top  $\text{SiO}_x$  layer). Consequently, the values of  $\text{SiO}_2$  indices are presented in Fig. 3.25.

### 3.3 Methodology used to develop EUV multilayer gratings.

In this section, we explored the integration and correlation of simulation tools like IMD software and RCWA homemade Matlab code with experimental techniques such as magnetron sputtering deposition, along with experimental characterizations including GIXR, EUV metrology, AFM, and TEM, as depicted in Fig.3.26. The connection between these tools and techniques plays a crucial role in generating an accurate model for multilayer gratings.

- To commence, the Al/Mo/SiC multilayers with  $N=6$  are initially optimized on a flat  $\text{SiO}_2$  substrate without considering interfacial roughness. This optimization process involves employing a genetic algorithm to target maximum reflectance within a specific wavelength range, such as 25 nm to 29 nm or 17 nm to 21 nm, under normal incidence. Afterward, the Al/Mo/SiC multilayers' optimized thickness values are utilized as input for the homemade RCWA code MATLAB. This is done in conjunction with grating parameters provided by Zeiss and AFM to confirm the EUV efficiency of the multilayer gratings under normal spectra.
- The deposition of the Al/Mo/SiC multilayers was carried out using the Plassys MP800 magnetron sputtering machine. Firstly, To control the thickness of layers in the multilayer structure, the deposition process was monitored using metrology involving the magnetron sputtering deposition machine and grazing x-ray reflec-

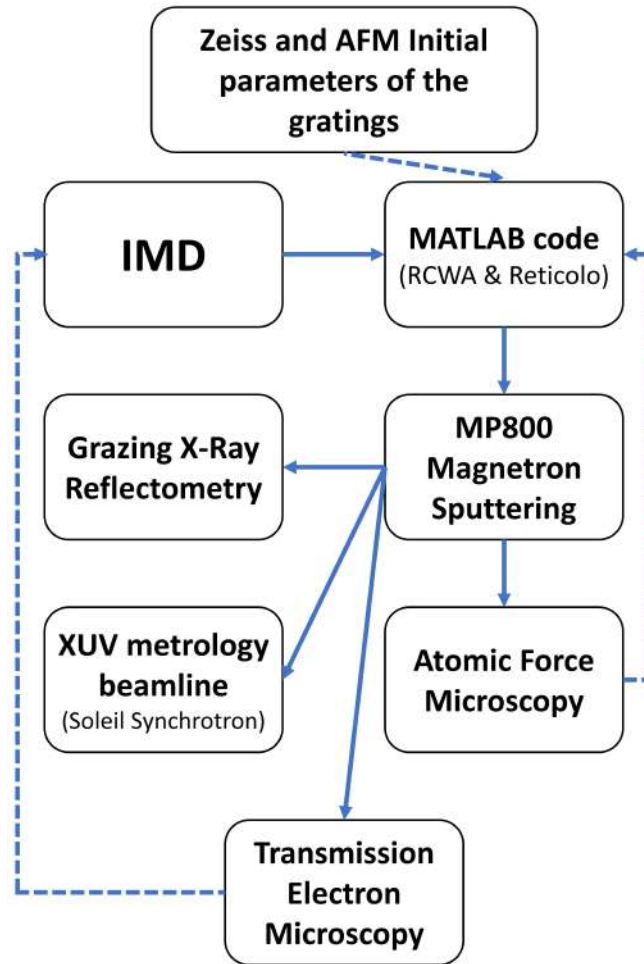


Figure 3.26: Simulation and Experimental strategy for multilayer gratings.

tometry. Each layer of SiC, Mo, and Al was individually deposited on three separate flat silicon substrates. By manually fitting the GIXR characteristics of each sample using IMD software, we were able to estimate the thickness of the deposited layers, as shown in Fig.3.22(a). Equation.3.6 describes the relationship between the thickness of the deposited layer and the constant 'a,' which represents the thickness of a deposited layer for one scan in one second. Normally, we assume the constant 'b' to be zero, where 'v' and 's<sub>n</sub>' represent the scan velocity and the number of scans, respectively.

$$T = a \left( \frac{s_n}{v} \right) + b \quad (3.6)$$

Hence, utilizing equation 3.6, we can determine initially the constant 'a.'

- Typically, when depositing different layers, the constant 'a' deviate from the initially computed value. To address this, we perform multiple depositions of the Al/Mo/SiC multilayer, while keeping all deposition parameters fixed except for either the scan velocity or scan number of one specific material. We manually fit the GIXR characteristics of this layer using IMD software, while maintaining the thickness of the other layers constant,



until achieving agreement, as illustrated in Fig.3.22(b). The presence of an oxidation layer is not considered in this step, and our focus lies on matching Bragg peaks and the critical angle. Through several deposition runs, we obtain different values of the constant 'a' for each material. By averaging these values, we determine the constant 'a' for each material, enabling us to deposit the desired thickness for each layer within the target period of the multilayer structure. This achievement is accomplished by adjusting and regulating the velocity and number of scans for each layer during the deposition process, taking into consideration the respective limitations.

- We deposit the target periodic ( $N = 10$ ) and aperiodic Al/Mo/SiC multilayers on flat Si substrates. We verify the quality of the deposition by fitting the GIXR characteristics using IMD software. These samples serve as references for the subsequent analysis of the multilayer structures. Following that, we proceed to deposit the multilayers onto  $SiO_2$  grating substrates. The detailed deposition script specifically designed for the periodic multilayer on  $SiO_2$  grating substrates can be found in the appendix.D.
- The profiles of the gratings were examined using AFM both before and after the deposition process in order to compare the changes in profile caused by the deposition.
- In the GIXR characteristics, the measurements are conducted for grazing angles, ranging from  $0^\circ$  to  $10^\circ$  for periodic multilayers on Si substrate. However, for multilayers on  $SiO_2$  gratings and aperiodic multilayers on Si substrates, the range is limited from  $0^\circ$  to  $6^\circ$  due to the use of a diaphragm.
- By aligning the model with GIXR measurements, we are able to estimate the roughness and relative thicknesses of materials for multilayers on Si substrate.
- In the case of multilayers on  $SiO_2$  grating substrates, the critical angle and positions of the Bragg peaks are influenced by various grating parameters, including grating depth, fill factor, the angle between grating grooves and incident X-ray beam, as well as the multilayer parameters. The adjustment of the model to match the experimental measurements for grating samples has been performed using the RCWA (RETICOLO) software.
- The multilayer samples on flat Si and grating  $SiO_2$  substrates underwent characterization at the EUV metrology beamline at Soleil synchrotron to obtain normal spectra (wavelength-reflectance at EUV range). By employing various simulation tools such as IMD and RCWA, a model was developed that demonstrated good agreement with both normal and angular spectra (GIXR measurements). This model allows us to estimate the relative thickness and roughness of the multilayers, as well as assess the presence of oxidation and interface layers.
- We employ TEM EDX to evaluate diffusion effects, assess roughness, and estimate the relative thickness of the material layers in the multilayer on Si substrate. Additionally, we examine the evolution of the multilayer on the grating's grooves using EDX analysis. Through this analysis, we have gained confidence in identifying the presence of an oxidation layer and the absence of an interface layer within the multilayer structure.
- In the final stage, By achieving a satisfactory agreement between the model for both normal and angular re-

flectance spectra obtained from IMD, along with TEM EDX analysis of the multilayer structure on Si substrate, we gain the ability to analyze various parameters related to deposition quality and interlayer roughness. Furthermore, by utilizing parameters estimated from AFM and TEM for the multilayers deposited on  $SiO_2$  substrates, including the pre-deposition groove shape, groove slope, groove fill factor, and groove periodicity, we successfully fit an RCWA model for the normal spectra of the multilayer gratings in the EUV range. Lastly, we enhance the RCWA model for the multilayer gratings by incorporating the Debye-Waller factor, which takes into account the effects of surface roughness.

### **3.4 Summary.**

In this chapter, the tools utilized for depositing, characterizing, and simulating the multilayer on the gratings were demonstrated. The criteria employed for measuring the grating for XRR or metrology beam line at Soleil synchrotron were showcased. Examples were presented to illustrate the analysis of AFM data in order to obtain more accurate results. The process of measuring the multilayer grating with TEM to extract EDX and classical TEM images was also demonstrated. Lastly, the combination of simulation and experimental techniques to develop the analysis of EUV multilayer gratings was showcased.



## Chapter 4

# Study of The Grating Substrates

In this chapter, the different grating substrates provided by Zeiss Company were analysed using various characterization tools such as atomic force microscopy (AFM) and x-ray reflectometry (GIXR) before the deposition. AFM provided insightful information about the grating, including the roughness at the bottom and top of the grooves, the shape of the grooves, the height of the grooves, and the slope of the grooves. The AFM parameters were compared with the Zeiss report for the grating. GIXR was employed to measure the changes in reflectivity with grazing angles for all sets of gratings in classical and conical configurations. Subsequently, the absolute depth of the grooves was estimated using the effective medium approximation through IMD software. Additionally, the RCWA method was utilized to model grating characteristics prior to the deposition. Finally, several studies were conducted to analyze the effect and sensitivity of grating parameter factors on two the wavelength with both angular and spectral characterization .

### 4.1 The Gratings (from Zeiss Report).

We asked The Zeiss Company to manufacture high-density lamellar silica gratings with varying groove depths of 22nm, 16nm, and 5nm (Fig.4.1). The gratings should have a high line density  $\geq 3600$  l/mm. This work is part of the ongoing effort to enhance the multilayer grating technology for the Solar-C mission, as described in the reference by [77]. These applications specifically aim to achieve high groove densities to maximize the instrument's spectral resolution.

#### 4.1.1 Fabrication process and Characterization.

The Zeiss Company has provided a report describing the steps involved in the fabrication process of the gratings.

1. The spin-coating photoresist on  $65 \times 65 \times 6 \text{mm}^3$  fused silica blanks.

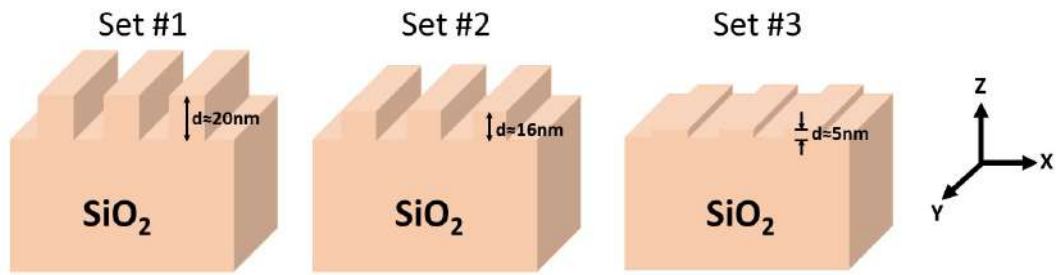


Figure 4.1: Schematic diagram for the gratings of different groove depths.

Table 4.1: Zeiss's description of the grating before deposition.

	Grating Set#1	Grating Set#2	Grating Set#3
Material	fused silica	fused silica	fused silica
substrate dimensions [mm]	20×20×6	20×20×6	20×20×6
roughness (nm RMS of grating blank)	0.17	< 0.2	< 0.2
Depth of groves [nm]	21±2	15.3±3%	5±5%
Density [L/mm]	3600 ±1	4000 ±<0.025%	4000 ±<0.025%

2. Holographic exposure employing a reference grating for alignment - all gratings manufactured by that setup will share the same line density of  $3600 \pm 1$  L/mm (set#1), and 4000 L/mm (set#2, and set#3); planarity of the waves was better than  $\lambda/20$
3. Etching by ion beam (IBE).
4. Cleaning in O<sub>2</sub>-plasma
5. Characterization of the grating and the etching results by AFM and white light source
6. Dicing of one successfully etched  $65 \times 65 \text{mm}^2$  into three  $20 \times 20 \text{mm}^2$  gratings (see Fig.4.2).
7. Cleaning and final inspection - see the results in Table.4.1.



Figure 4.2: Photograph of the final gratings of the second batch with dimensions  $20 \times 20 \times 6 \text{ mm}^3$  after the fabrication process by Zeiss.

Table 4.2: schematic diagram of set#1.

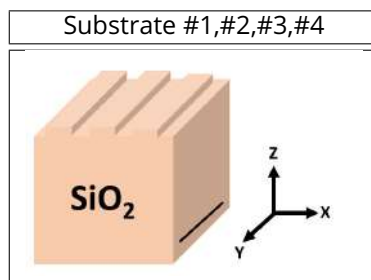
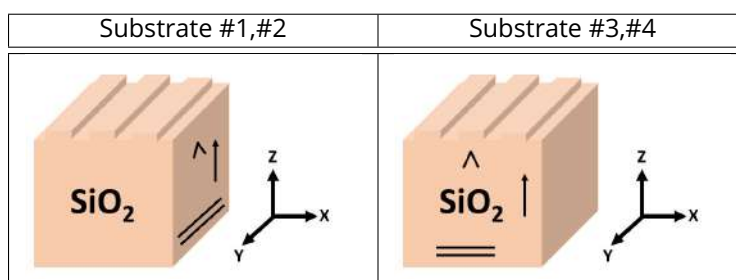


Table 4.3: schematic diagram of set#2 and set#3.



## 4.2 Atomic Force Microscopy measurements

The AFM tool has been utilized to verify the data provided by Zeiss, including parameters such as roughness, surface profile shape, groove height, fill factor of the grooves, and periodicity of the grating. A good knowledge of these parameters are essential to simulate and optimize.

### 4.2.1 Mechanical layout

Tables 4.2, and 4.3 display the grating configurations for set#1, set#2, and set#3, respectively. The diagrammatic representations in these tables indicate the location of the grooves on the grating with respect to the Zeiss mark. The horizontal lines and the upward-pointing arrow represent the markings made by Zeiss for the purpose of aiding in locating the orientation of the grooves and groove surfaces on the silica substrate. Regarding the "^" symbol, we utilized a diamond pen within our clean room environment because the markings on gratings set#2 and set#3 could be readily eliminated using acetone.

Drawing a schematic for the Zeiss mark on the grating was crucial due to the need to place the deposition mask in a perpendicular to the grooves. Additionally, it was important for aligning the metrology beamline measurements. It is worth mentioning that in certain grating instances, the position of the mark on the Zeiss report did not align properly with the grating lines. Therefore, the confirmation of atomic force microscopy (AFM) was required.

## 4.2.2 Measurements parameters

Figure 4.3(a) depicts a schematic diagram of the grating profile, which takes the form of a trapezoid characterized by parameters such as height,  $X_{part}$ , and  $\alpha$  (slope trapezoid angle). In Fig.4.3(b), the positions of two regions for experimental atomic force microscopy (AFM) measurements are indicated. Notably, the X-Part can be computed using the following equation:

$$\tan(\alpha) = \frac{\text{Grating Depth}}{X_{Part}} \quad (4.1)$$

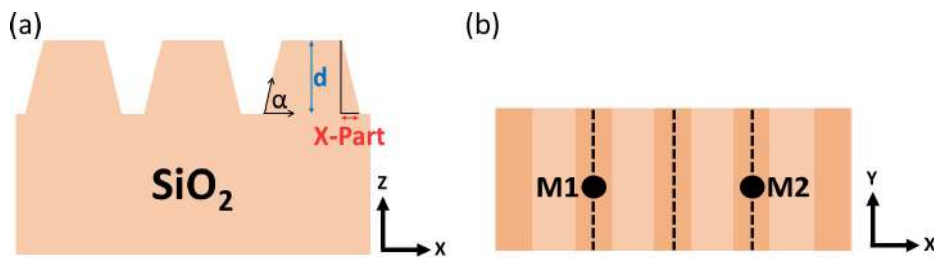


Figure 4.3: Schematic diagram of (a) the grating (b) the positions of points on the top of the grating.

Figure.4.4 illustrates the alignment of grating samples for AFM measurements. It is worth noting that the grating samples were maintained at a temperature of 23-24 C° during the AFM measurements.

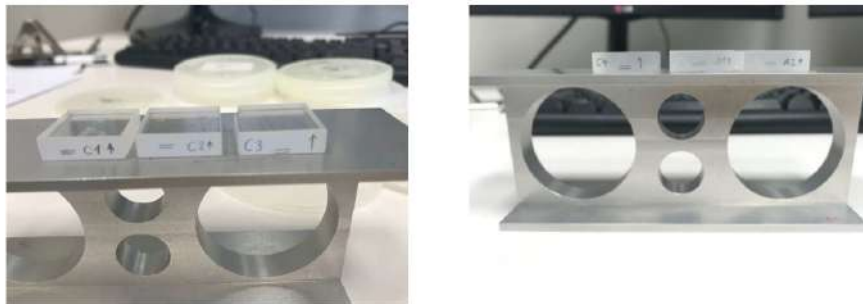


Figure 4.4: Photograph of the preparation of the gratings for AFM measurements.

## 4.2.3 AFM surface morphology and profile.

Figure 4.5, Figure 4.6, and Figure 4.7 display the AFM surface morphology of the trapezoidal grating substrate before the deposition of the samples. The images are captured using an AFM tip in non-contact mode, with a field of view of  $2\mu\text{m} \times 2\mu\text{m}$ . It is clearly observed from these figures that the grating grooves exhibit an inclined pattern, indicating misalignment of the grating pattern.

#### **4.2.3.1 AFM analysis for surface morphology.**

It can be observed from Fig.4.5 that the six AFM surface morphologies for set #1 exhibit similarities among each other. In contrast, for set #2 and set #3, the six AFM surface morphologies do not exhibit similarities among each other, as depicted in Fig.4.6 and Fig. 4.7.

#### **4.2.3.2 AFM analysis for surface profiles.**

The analysis of Fig.4.8 reveals that the six grating profiles within set #1 demonstrate consistent characteristics in terms of depth, fill factor, and trapezoidal shape. However, a notable distinction arises when examining set #2 and set #3, as illustrated in Fig.4.9 and Fig.4.10, where the six grating profiles exhibit significant variations in depth, fill factor, and trapezoidal shape.

#### **4.2.3.3 AFM analysis for all the sets of the gratings.**

In this section, the analysis of the data is performed using the surface morphology and grating profile data obtained from AFM measurements before the deposition process. The subsequent subsections (4.2.3.3.1, 4.2.3.3.2, 4.2.3.3.3, 4.2.3.3.4, and 4.2.3.3.5) are elucidated based on the information depicted in Fig. 4.8, Fig. 4.9, and Fig. 4.10.

##### **4.2.3.3.1 Roughness**

Figure.4.11, and Figure.4.12 display the roughness values calculated from the AFM data for all the grating samples, representing both the top and bottom of the grooves pattern. The results indicate that for set#1 and set#3, the roughness values remain consistently low, measuring below 0.5 nm. This suggests that the surface smoothness of these samples is relatively stable. However, in the case of set#2, certain samples exhibit a noticeably higher roughness exceeding 0.5 nm. This variation in roughness indicates that the surface characteristics of set#2 samples are less uniform compared to the other sets.

##### **4.2.3.3.2 grating depth (d)**

Figure 4.13 depicts the height of the three sets of gratings as reported by Zeiss. It is observed that the average height for set#1 is approximately 22 nm, for set#2 is around 16 nm, and for set#3 is about 5 nm. These results indicate variations in the height among the different grating sets.

##### **4.2.3.3.3 Slope angle ( $\alpha$ )**

Figure 4.14 illustrates the average slope angle ( $\alpha$ ) calculated from the AFM profiles of the three sets of gratings. The  $\alpha$  calculations were performed using Fig.4.8, Fig.4.9, and Fig.4.10, where there were approximately six trapezoidal grating profiles for each grating profile. The slope was measured for both sides of each trapezoidal grating



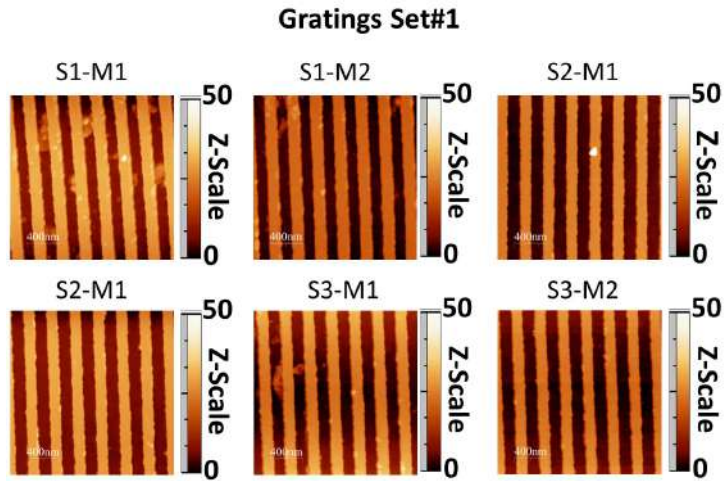


Figure 4.5: The  $2\mu\text{m} \times 2\mu\text{m}$  AFM surface morphology at different substrates and different positions of the trapezoidal grating without multilayers for set#1.

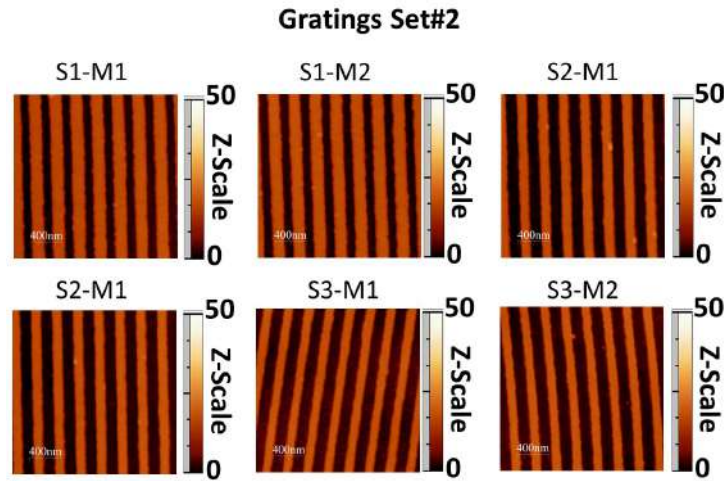


Figure 4.6: The  $2\mu\text{m} \times 2\mu\text{m}$  AFM surface morphology at different substrates and different positions of the trapezoidal grating without multilayers for set#2.

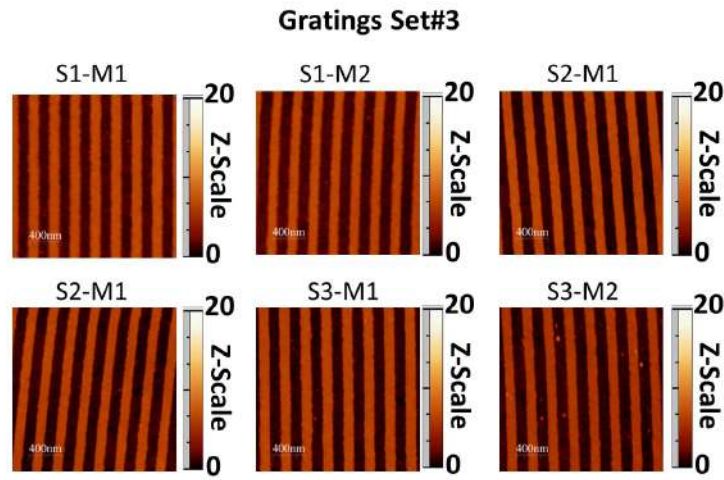


Figure 4.7: The  $2\mu\text{m} \times 2\mu\text{m}$  AFM surface morphology at different substrates and different positions of the trapezoidal grating without multilayers for set#3.

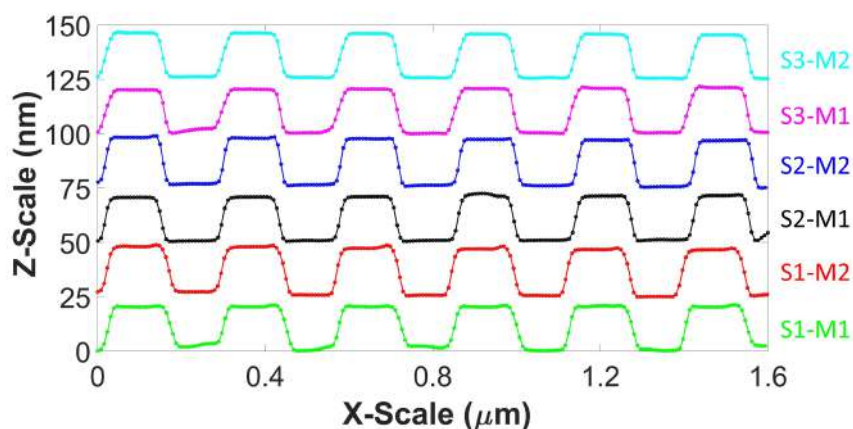


Figure 4.8: AFM groove profiles at different substrates and different positions of the trapezoidal grating without multilayers for set#1.

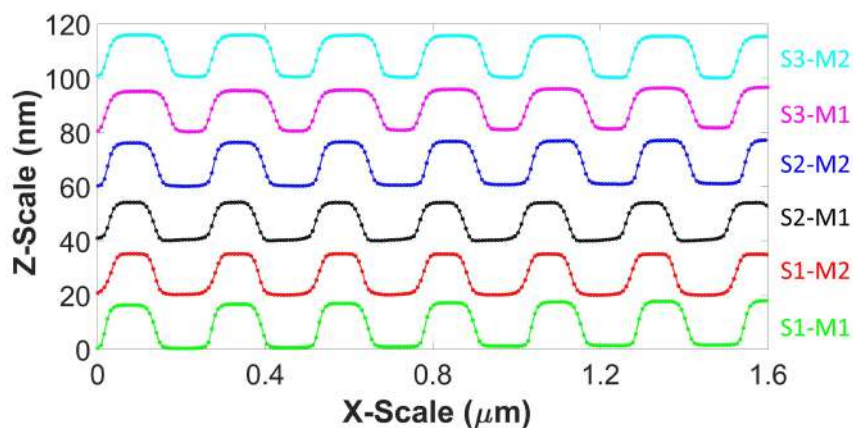


Figure 4.9: AFM groove profiles at different substrates and different positions of the trapezoidal grating without multilayers for set#2.

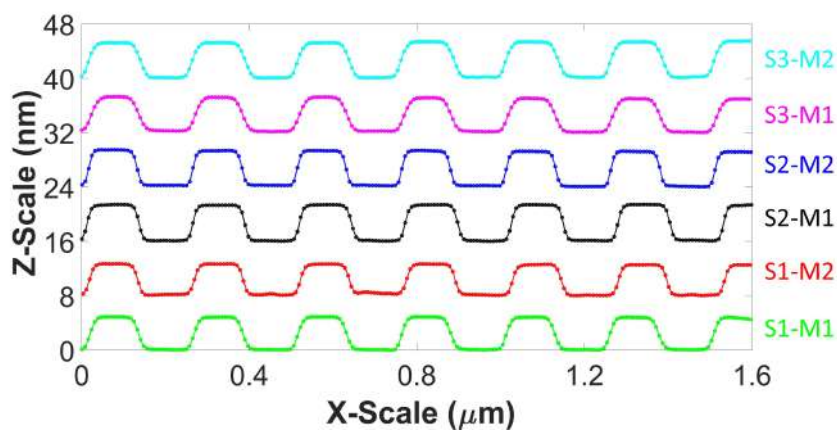


Figure 4.10: AFM groove profiles at different substrates and different positions of the trapezoidal grating without multilayers for set#3.

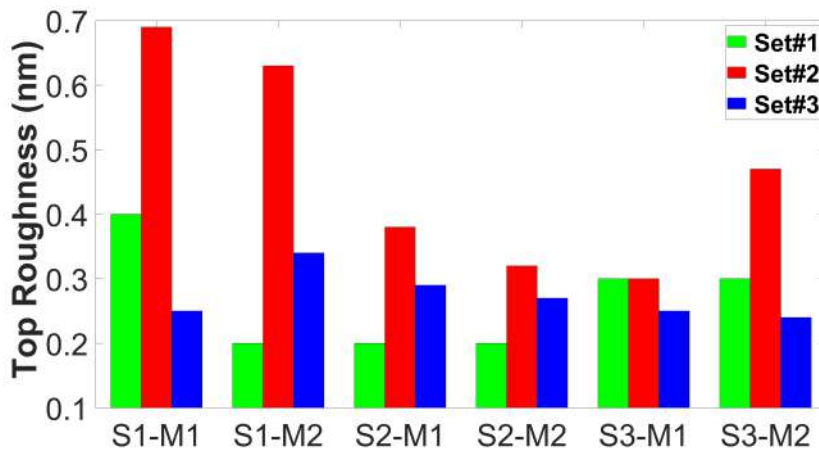


Figure 4.11: A bar chart displaying the fluctuations in roughness observed on the upper surface of the grating substrate.

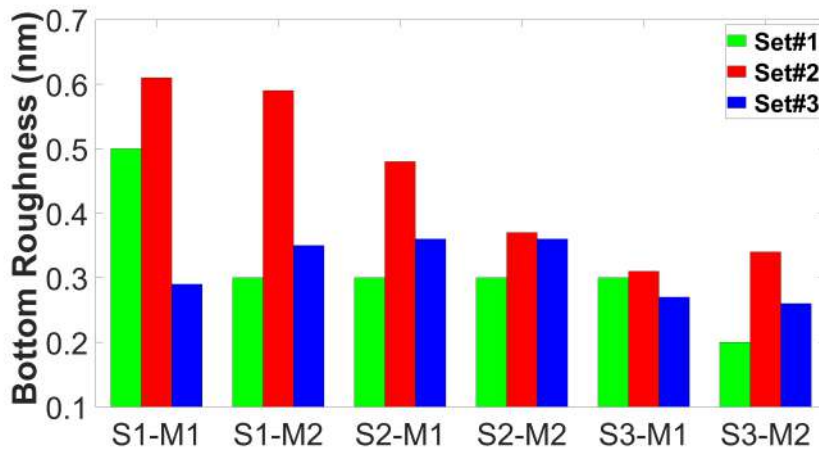


Figure 4.12: A bar chart depicting the fluctuation in roughness on the bottom surface of the grating substrate.

profile. Thus, the data shown in the bar chart Fig.4.14 represents the average of 12 slope trapezoidal grating profiles.

It is observed that the average  $\alpha$  for set#1 is approximately  $47^\circ$ , indicating a relatively steep slope angle. On the other hand, set#2 has an average  $\alpha$  of around  $21^\circ$ , suggesting a less inclined surface compared to set#1. Notably, set#3 exhibits an average  $\alpha$  of approximately  $10^\circ$ , indicating a relatively flat surface in this set. These results indicate variations in the slope angles among the different grating sets, with set#3 showing the least pronounced slopes.

#### 4.2.3.3.4 fill factor ( $f.f$ ) .

Figure 4.15 displays the average full-width half maximum (FWHM) fill factors ( $f.f$ ) for all sets of gratings. It can be observed that the average FWHM fill factors for all sets fall within the range of 0.4 to 0.6. This indicates that the grating profiles in all sets are rather symmetrical ( $f.f \approx 0.5$ ), with variations within this range among the different sets.

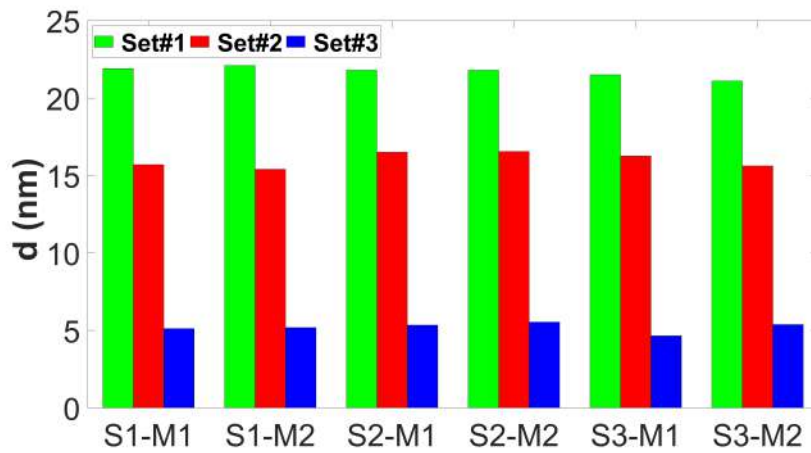


Figure 4.13: Bar chart depicting the fluctuation in grating depth across the grating substrate

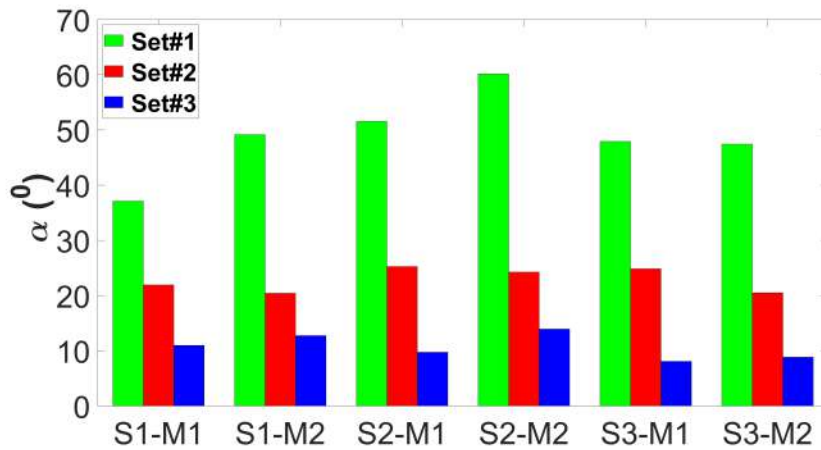


Figure 4.14: A bar chart illustrating the changes in the slope of the trapezoidal shape of the grating across the substrate.

#### 4.2.3.3.5 $X_{part}$

Figure.4.16 illustrates the computed  $X_{part}$  in accordance with Equation.4.1. It is evident that in set#3,  $X_{part}$  exhibits the highest value compared to the other sets.

#### 4.2.3.4 AFM conclusion

Table 4.4 summarizes the average parameters derived from the analysis conducted in the Subsection.4.2.3.3.

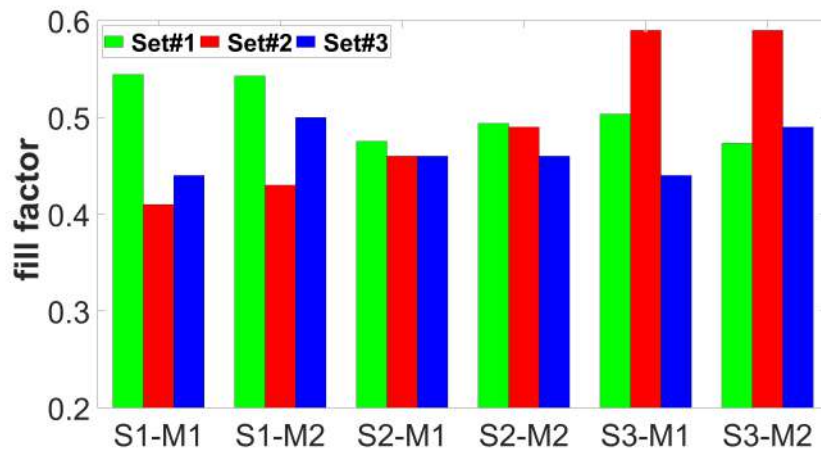


Figure 4.15: An illustrated bar chart showcasing the variations in grating fill factor (FWHM) observed across the grating substrate.

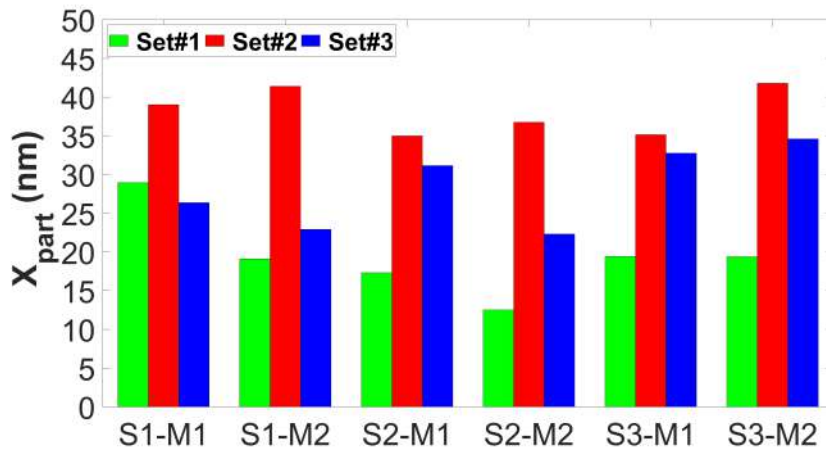
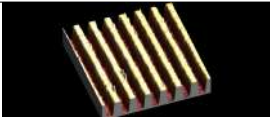
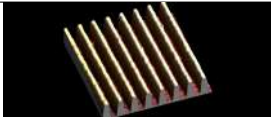
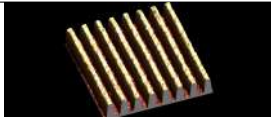


Figure 4.16: A visually represented bar chart displaying the observed variations in  $X_{part}$  grating across the substrate.

Table 4.4: Average gratings parameters.

	Set #1	Set #2	Set #3
AFM 3D Image			
height	22 nm	16.1 nm	5.2 nm
Top Roughness (nm)	0.2-0.4	0.3-0.69	0.2-0.34
Bottom Roughness (nm)	0.2-0.5	0.48-0.83	0.24-0.36
$\alpha$ ( $^{\circ}$ )	47.1	28	11.9
$X_{part}$ (nm)	19.45	38.17	28.35



### 4.3 X ray reflectivity analysis.

#### 4.3.1 GIXR measurements of the grating substrates.

Figure.4.17 depicts the GIXR data for different sets of gratings in both classical and conical configurations. Notably, when measuring set #2 and set #3, a diaphragm was utilized to limit the X-ray beam on the grating. As a result, the flux in these measurements was lower compared to set #1. In the GIXR setup, the grating alignment was manually adjusted with respect to the Zeiss mark, as evident from Figures.4.5, 4.6 and 4.7, where the grating grooves were observed to be inclined rather than perfectly vertical or horizontal. This indicates that the positioning of the classical or conical configurations was not ideal for this type of measurement. The dashed circles in Fig.4.17 highlight the sensitivity of groove alignment in GIXR characterization for grating set #1 and set #2. Intriguingly, there was no discernible difference in GIXR characterization between the classical and conical configurations for grating set #3. This can be attributed to the grooves of set #3 having a depth of approximately 5nm and a small slope angle of around 10 degrees, resulting in the grating set #3 closely resembling a flat substrate. Therefore, it has been determined that the modeling of GIXR characterization will focus specifically on the classical configuration.

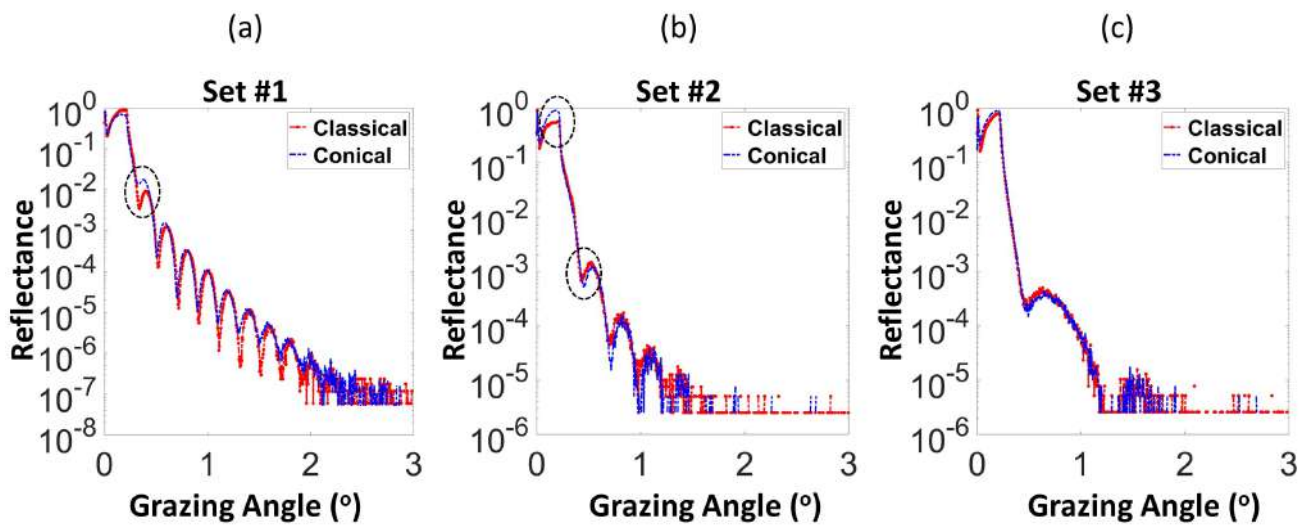


Figure 4.17: GIXR measurements for gratings (a) Set#1 substrate#1, (b) Set#2 substrate#4, and (c) Set#3 substrate#4 in classical, and conical configurations.

#### 4.3.2 Grating Models.

Optically characterizing grating patterns on substrates can be challenging due to the thin layer thickness of the discontinuous film, resulting in a weak optical signal and a low signal-to-noise ratio [92]. To overcome this challenge, one approach is to use the effective medium approximation (EMA) for optical characterization [93]. The EMA allows for averaging the density of the solid pattern and the spaces between the patterns, enabling the extraction of nu-

merical information about the cross-sectional pattern profile from the density profile obtained through Specular X-ray reflectivity. Figure 4.18.(a) illustrates an example of the density profile obtained from SXR and the resulting cross-sectional pattern profile.

This section outlines the methodology employed for the characterization of the optical properties of grating patterns on substrates. The characterization involved a combination of experimental measurements and optimized modeling using MATLAB software [94] with the RCWA method [95]. The RCWA method utilizes numerical solutions of Maxwell's equations to simulate the behavior of the grating pattern on the substrate. In addition, IMD software [84] was utilized to numerically solve the Fresnel equation and provide quantitative information regarding the EMA.

Figure 4.18.(a) depicts a lamellar grating, which consists of parameters such as the grating depth ( $d$ ), the width of the grating ( $W$ ), and the fill factor ( $f.f$ ) at full-width half maximum (FWHM).

Figure 4.18.(b) showcases the effective medium approximation (EMA) layer, which has a certain thickness ( $T$ ) and density ( $\rho$ ). The EMA layer represents an averaged density profile that combines the solid pattern and the spaces between the patterns.

Finally, Figure 4.18.(c) displays the RCWA model, which shares the same parameters as the lamellar grating. In addition to simulating a lamellar grating, the RCWA model can also replicate a trapezoidal grating by introducing an angle ( $\alpha$ ).

The desired lamellar shape is typically achieved when the profile is symmetrical ( $f.f$ ) = 0.5, resulting in a density ratio of the grating layer ( $\rho_{grating}$ ) to the substrate density ( $\rho_{substrate}$ ) of approximately 0.5.

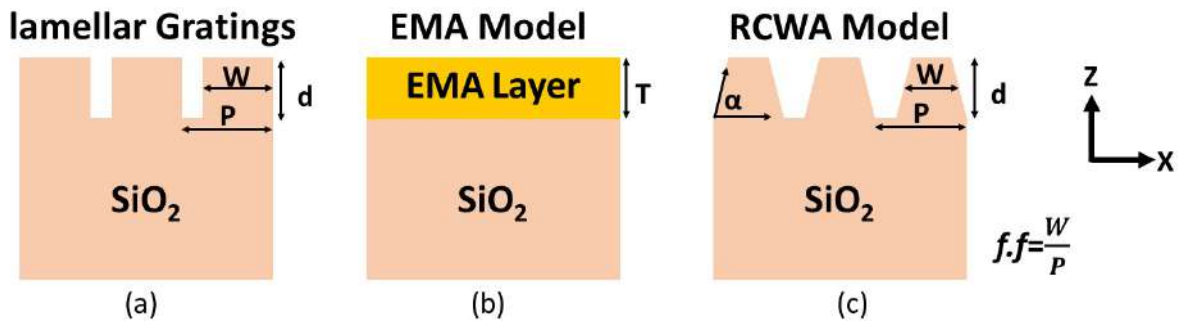


Figure 4.18: The schematic illustrates three physical structures (a) lamellar gratings, (b) the EMA model, and the RCWA model.

Figures 4.19, 4.20, and 4.21 show the EMA models derived from X-ray measurements of three distinct sets of gratings substrates. The parameters used for EMA model are given in Table.4.5.

Table 4.5: The thickness ( $T$ ) and density ( $\rho$ ) of the effective layer obtained by the EMA model.

	Gratings Set#1	Gratings Set#2	Gratings Set#3
$T$ (nm)	22.00	16.11	5.33
$\rho_{EMA}$ (g/cm <sup>3</sup> )	0.835	0.750	0.900

In the RCWA model, we set the grating depth equal to the thickness obtained from the EMA model. The value of

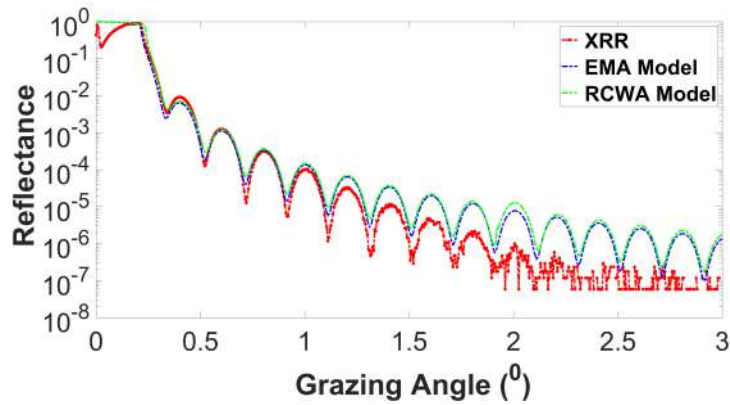


Figure 4.19: EMA model for GIXR measurements for gratings Set#1 substrate#1 in classical position.

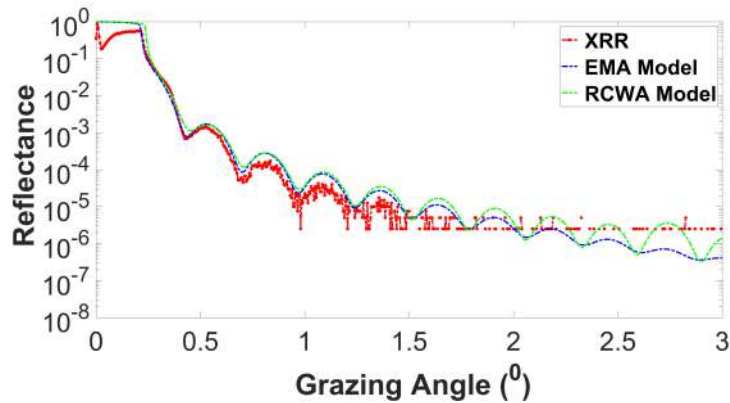


Figure 4.20: EMA model for GIXR measurements for gratings Set#2 substrate#4 in classical position.

$f.f$  is approximately determined by the ratio of  $\rho_{EMA}$  to  $\rho_{SiO_2}$ . However, we adjust the parameter  $\alpha$  to align with the limitations imposed by the AFM measurements. Table 4.6 presents the listed values for the grating depth,  $f.f$ , and  $\alpha$ .

Table 4.6: The grating depth ( $d$ ), grating slope ( $\alpha$ ), and fill factor ( $f.f$ ) of the effective layer obtained by the RCWA model.

	Gratings Set#1	Gratings Set#2	Gratings Set#3
Depth (nm)	22.00	16.10	5.40
$\alpha$ ( $^\circ$ )	47	30	9
$f.f$	0.4	0.341	0.41

In summary, the use of both EMA and RCWA models provides a means to determine almost actual grating parameters. The grating depth calculated by the RCWA model corresponds to the height of the EMA layer estimated by the EMA model.



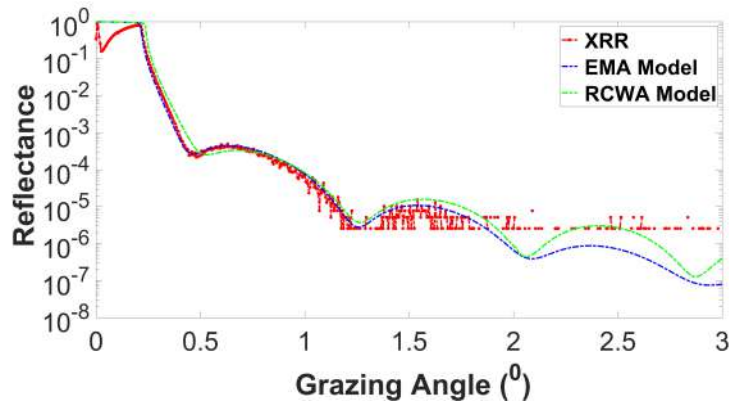


Figure 4.21: EMA model for GIXR measurements for gratings Set#3 substrate#4 in classical position.

## 4.4 Effect of grating parameters on EUV efficiency

In this section, we will conduct a detailed analysis of the grating's impact on EUV characteristics. Our focus will be on investigating how the presence of the grating influences the EUV domain. By studying these effects, we aim to gain valuable insights into the grating's behavior and performance in EUV applications. In this section, the grating parameters will be employed based on Table 4.7, except for the variables under investigation.

Table 4.7: The grating parameters.

Parameter	Value
$\omega$	0° (classical positions)
$\theta$	5°
$P$	250nm
$d$	21nm
$\alpha$	90° (lamellar gratings)
$f.f$ (FWHM)	0.5
Substrate	$SiO_2$

We examined the periodicity ranging from 1000 l/mm to 5000 l/mm in relation to the parameters listed in Table.4.7. Our findings revealed that this periodicity led to a slight change in +1<sup>st</sup>-order efficiency. In accordance with the grating equation.2.16, a decrease in groove density per line (resulting in an increased grating period) suggests that working with +2<sup>nd</sup>-order efficiency would be more favorable.

### 4.4.1 Grating depth's influence.

Figure.4.22 displays a simulation of the transverse electric (TE) efficiency of the 0<sup>th</sup> and +1<sup>st</sup> diffraction orders as a function of grating depth. This simulation specifically focuses on a lamellar grating without a multilayer, at an incident angle of  $\theta = 5^\circ$ . The simulation was conducted on a silica lamellar grating substrate with a fill factor of 0.5, a periodicity of 250nm, and a wavelength of 20 nm. The plot reveals an interesting relationship between the 0<sup>th</sup> and +1<sup>st</sup> orders: as the efficiency of the 0<sup>th</sup> order decreases, the efficiency of the +1<sup>st</sup> order increases, and vice versa.

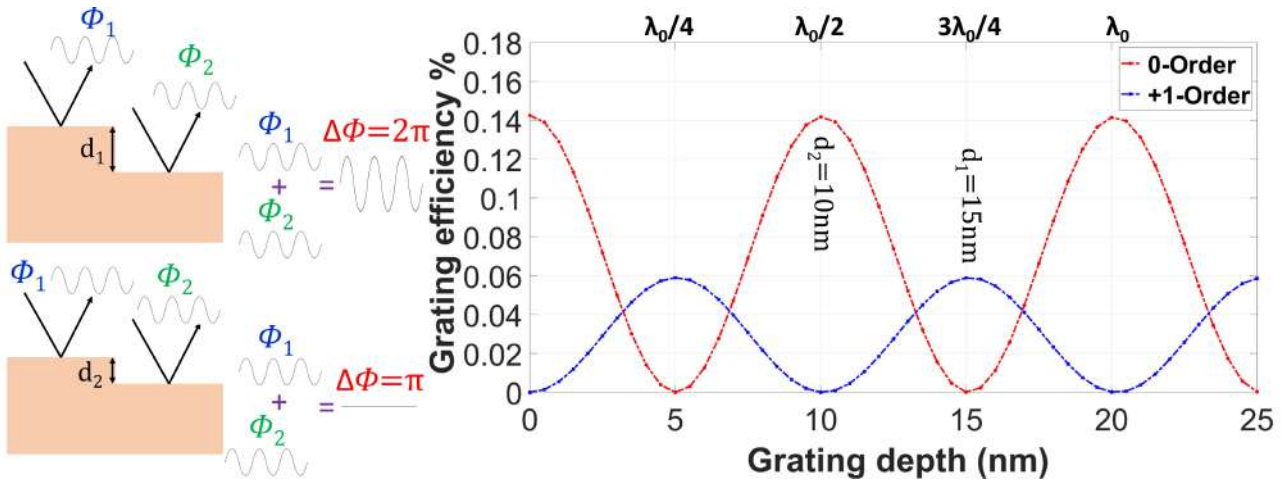


Figure 4.22: RCWA simulation for grating depth as a function of grating efficiency for gratings without multilayers.

This observation signifies that there is an inverse relationship in terms of the efficiency between the  $0^{th}$  and  $+1^{st}$  orders. The fluctuations in efficiency, ranging from maximum to minimum, can be attributed to the constructive and destructive interference of photons occurring between the grooves of the gratings.

This requirement imposes a constraint on the depth of the grooves. The maximum efficiency for the  $1^{st}$  order (and minimum for the  $0^{th}$  order) is achieved at normal incidence when the groove depth is approximately  $\lambda/4$  modulo  $3\lambda/4$ , where  $\lambda$  is the wavelength of light. For example, for a wavelength of 20 nm, the groove depth should be around 5 nm, 15 nm, 25 nm, and so on. Conversely, at a depth of 10 nm (approximately  $\lambda/2$ ), the efficiency is minimum for the  $1^{st}$  order and maximum for the  $0^{th}$  order. These findings highlight the importance of selecting the appropriate groove depth to achieve the desired efficiency for specific diffraction orders in optical gratings.

Figure 4.23 illustrates the efficiency of the  $+1^{st}$  diffraction order of a grating, represented by a color bar, as a function of depth and wavelength. This simulation assumes a lamellar grating with a fill factor ( $f.f.$ ) of 0.5, an angle ( $\alpha$ ) of  $90^\circ$ , a periodicity ( $P$ ) of 250 nm, an incidence angle ( $\theta$ ) of  $5^\circ$ , and a substrate material of silicon. The color intensity in the plot indicates the efficiency of the  $+1^{st}$  order diffraction at different depths and wavelengths.

The highest efficiencies indicated by the warmer colors in the plot correspond to regions where the grating depth matches the interference condition, resulting in a higher intensity of the  $+1^{st}$  order diffraction. On the other hand, the dark areas represent regions where the grating depth does not fulfill the interference condition, leading to a lower intensity of the  $+1^{st}$  order diffraction.

The depth of the grooves in a grating has a significant impact on the efficiency of the desired diffraction orders. The goal of the study is to achieve optimal efficiency for the  $+1^{st}$  diffraction orders while minimizing the efficiency for the  $0^{th}$  order. To achieve this efficiency ratio, it is important to ensure that the light reflected from the surface of the grating (i.e., the grooves) constructively interferes with the light reflected from the regions between the grooves (furrows) for the desired order.

From Fig.4.23, it can be observed that the multilayer structure should be adjusted in the depth of the grating

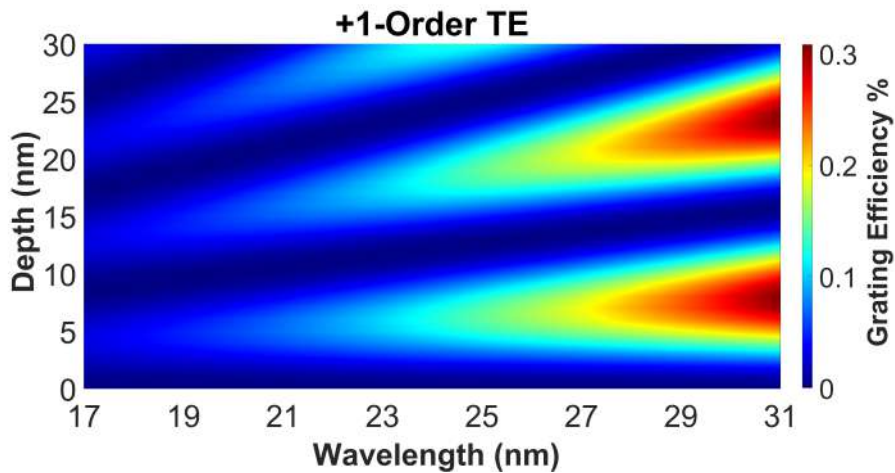


Figure 4.23: RCWA simulation for transverse electric grating efficiency +1<sup>st</sup> order as a function of wavelength and depth for lamellar gratings substrate.

grooves to maximize the efficiency of the +1<sup>st</sup> order while minimizing the efficiency of the 0<sup>th</sup> order. As a result, Table.4.8 demonstrates the determination of a specific range of wavelengths for which the multilayer will be optimized. This optimization aims to enhance the reflectance and consequently improve the efficiency within this particular wavelength range.

Table 4.8: The choice of a wavelength range depends on the depth of grating grooves.

	Gratings Set#1	Gratings Set#2	Gratings Set#3
grating grooves height (nm)	22	16.1	5.4
wavelength range (nm)	25-29	19-23	17-21

#### 4.4.2 Grating fill factor effect.

Figure 4.24 illustrates the efficiency of the +1<sup>st</sup> order in the color bar as a function of the fill factor and wavelength, without the presence of multilayer. The parameters used for the simulation include the grating depth (d) of 21 nm, the angle ( $\alpha$ ) of 90° (corresponding to a lamellar grating), the period (P) of 250 nm, the incidence angle ( $\theta$ ) of 5°, and the substrate material as silicon.

From the plot, it can be observed that the intensity of the +1<sup>st</sup> order is highest around a fill factor (*f.f.*) of 0.5, and it decreases as the fill factor deviates further away from 0.5. This indicates that the fill factor of the grating plays a crucial role in controlling the efficiency of the +1<sup>st</sup> order.

These results emphasize the importance of carefully selecting and controlling the fill factor of the grating to optimize the efficiency of the desired diffraction orders, particularly the +1<sup>st</sup> order.

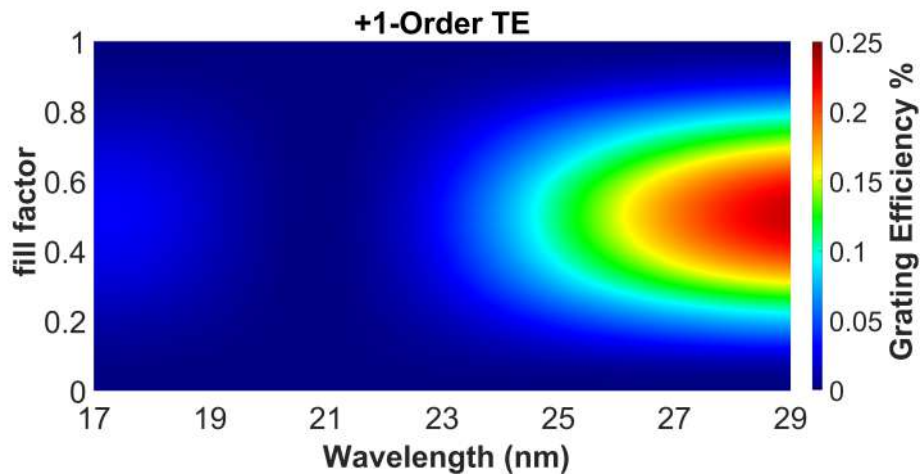


Figure 4.24: RCWA simulation for wavelength as a function of grating efficiency and fill factor for a lamellar grating substrate.

#### 4.4.3 Grating slope impact.

Figure 4.25 illustrates the efficiency of the +1<sup>st</sup> order in the color bar as a function of the grating slope ( $\alpha$ ) and wavelength, without the presence of multilayers. The parameters used for the simulation include the grating depth ( $d$ ) of 21 nm, a fill factor ( $f.f.$ ) of 0.5, a period ( $P$ ) of 250 nm, an incidence angle ( $\theta$ ) of  $5^\circ$ , and the substrate material as silicon.

From the plot, it can be observed that the intensity of the +1<sup>st</sup> order decreases as the grating slope ( $\alpha$ ) decreases or as it transitions from a lamellar grating shape to a trapezoidal grating shape. This indicates that the efficiency of the +1<sup>st</sup> order is negatively affected by imperfections in the manufacture of the grating.

These results emphasize the importance of precise control over the grating slope during the manufacturing process to optimize the efficiency of the desired diffraction orders, particularly the +1<sup>st</sup> order. Higher grating slope values tend to result in higher efficiencies, while lower grating slope values lead to reduced efficiencies.

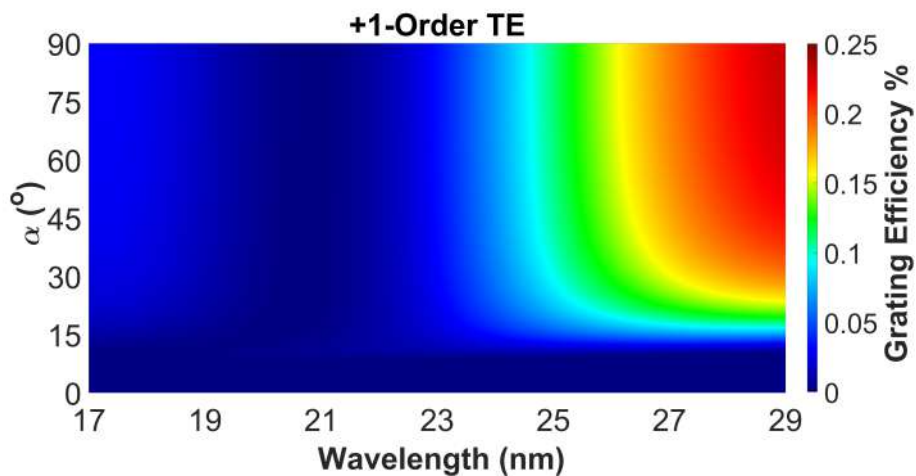


Figure 4.25: RCWA simulation for wavelength as a function of grating efficiency and alpha for gratings substrate.

#### 4.4.4 The grating groove alignment's consequence.

Figures 4.26 and 4.27 depict the efficiency of the  $+1^{st}$  order grating (in the color bar) as a function of the grating rotation angle ( $\omega$ ) and wavelength, without the presence of multilayers.

From the plots, it can be observed that the intensity of the  $+1^{st}$  order varies as the grating rotation angle ( $\omega$ ) changes. Interestingly, after reaching the conical position at  $\omega=90^\circ$ , the bright intensity of the  $+1^{st}$  order is inverted and corresponds to the  $-1^{st}$  order. This behavior can be seen in both Figure 4.26 and Figure 4.27.

These findings highlight the dependence of the diffraction efficiency on the alignment of the grating grooves to the incident beam. The inversion of the  $+1^{st}$  order and the appearance of the  $-1^{st}$  order after the conical position demonstrate the complex nature of the diffraction process and the influence of the grating geometry on the resulting diffraction patterns.

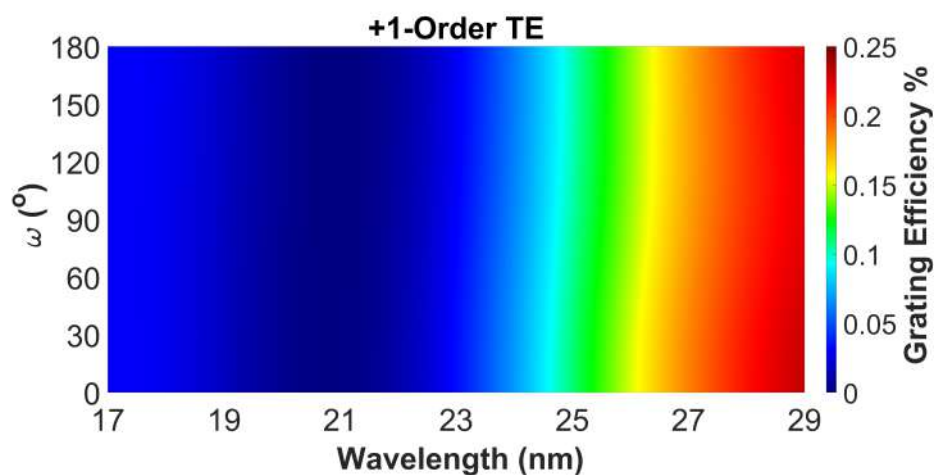


Figure 4.26: RCWA simulation for wavelength as a function of grating efficiency (+1-order) and omega for lamellar gratings substrate.

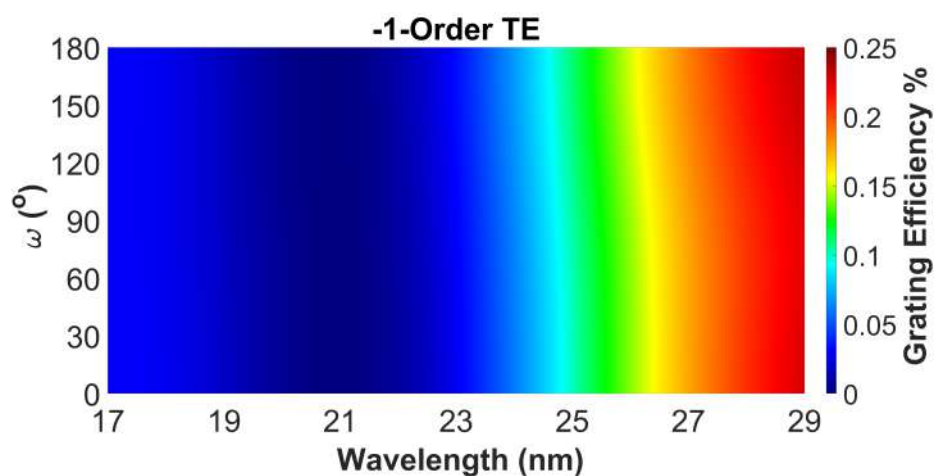


Figure 4.27: RCWA simulation for wavelength as a function of grating efficiency (-1-order) and omega for lamellar gratings substrate.

## 4.5 Effect of the grating parameters on x-ray angular reflectance spectra.

In this section, we will analyze the effect of the grating on X-ray characteristics individually. We will examine how the presence of the grating influences various X-ray properties and phenomena. By studying these effects, we can gain insights into the behavior and performance of the grating in X-ray applications. In this section, the grating parameters will be utilized according to Table.5.1, excluding the variables that are the subject of investigation.

Table 4.9: The grating parameters.

Parameter	Value
$\omega$	0° (classical positions)
$\lambda$	0.154nm
$P$	250nm
$d$	21nm
$\alpha$	90° (lamellar gratings)
$f.f$ (FWHM)	0.5
Substrate	$SiO_2$

### 4.5.1 The effect of the grating depth.

Figure.4.28 illustrates the impact of varying the grating depth on X-ray reflectance as a function of grazing angle. The reflectance is displayed logarithmically in a color bar. This figure reveals that different grating depths exhibit distinct X-ray reflectance characteristics. Each depth value corresponds to a unique reflectance profile, allowing for the possibility of extracting the average grating depth from X-ray measurements at a specific wavelength ( $\lambda=0.154$  nm) as shown in section.4.3.2. This analysis provides valuable information about the grating structure and can aid in the determination and characterization of grating parameters for X-ray applications.

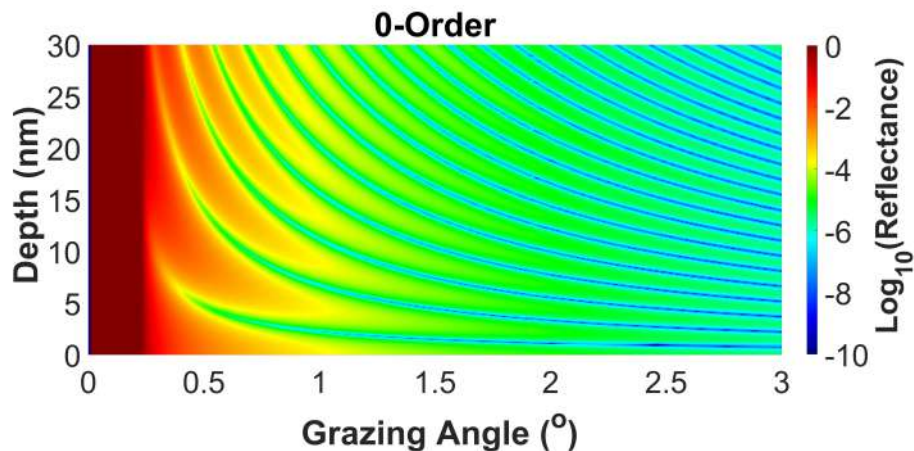


Figure 4.28: RCWA simulation for grazing angle as a function of reflectance logarithm and depth for lamellar gratings substrate.



### 4.5.2 The effect of the grating fill factor.

Figure.4.29 illustrates the impact of varying the fill factor of the grating on the change in grazing angle with reflectance, as determined by RCWA simulation. The figure reveals that the reflectance profile exhibits a critical angle slightly varying between  $0.2^\circ$  and  $0.4^\circ$ , and the position of this peak depends on the fill factor of the grating. Specifically, the intensity of the Kiessig fringes are interference patterns, which correspond to the constructive interference of X-rays, is at its maximum when the fill factor of the grating is 0.5. This finding highlights the importance of the fill factor in determining the optimal reflection properties of the grating for X-ray applications.

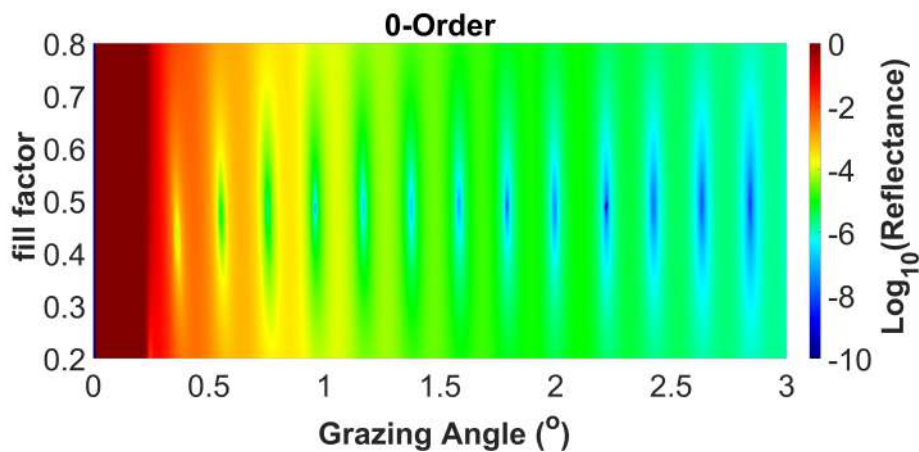


Figure 4.29: RCWA simulation for grazing angle as a function of reflectance logarithm and fill factor for lamellar gratings substrate.

### 4.5.3 The effect of the grating slope.

In Fig.4.30, the influence of changing the grating slope ( $\alpha$ ) on the grazing angle and reflectance logarithm is demonstrated. As the grating slope ( $\alpha$ ) decreases, there is a noticeable reduction in the reflectance amplitude of the Kiessig fringes or interference patterns. This observation highlights the correlation between the grating slope and the intensity of the reflected X-rays, indicating that adjusting the grating slope can effectively control the performance and efficiency of the grating in X-ray applications.

### 4.5.4 The effect of grooves grating alignment.

In Fig.4.31, the impact of changing the  $\omega$  angle on the relationship between the grazing angle and reflectance is depicted. The RCWA simulation reveals a Kiessig fringes or interference patterns shift occurring between  $\omega=90^\circ$  and either  $\omega=80^\circ$  or  $\omega=100^\circ$ . This observation suggests that the classical and conical positions exhibit distinct responses in X-ray characterization, and the precise position of the Kiessig fringes or interference patterns can be influenced by the X-ray characterization technique employed.

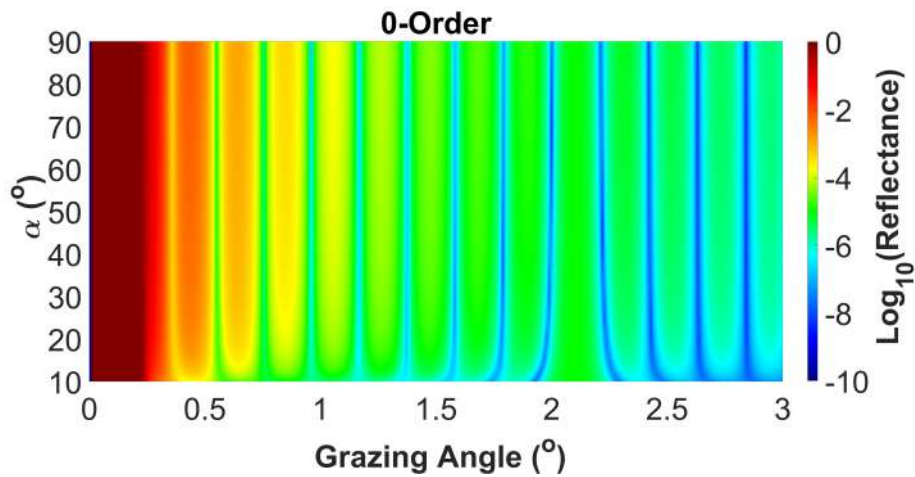


Figure 4.30: RCWA simulation for grazing angle as a function of reflectance logarithm and alpha for gratings substrate.

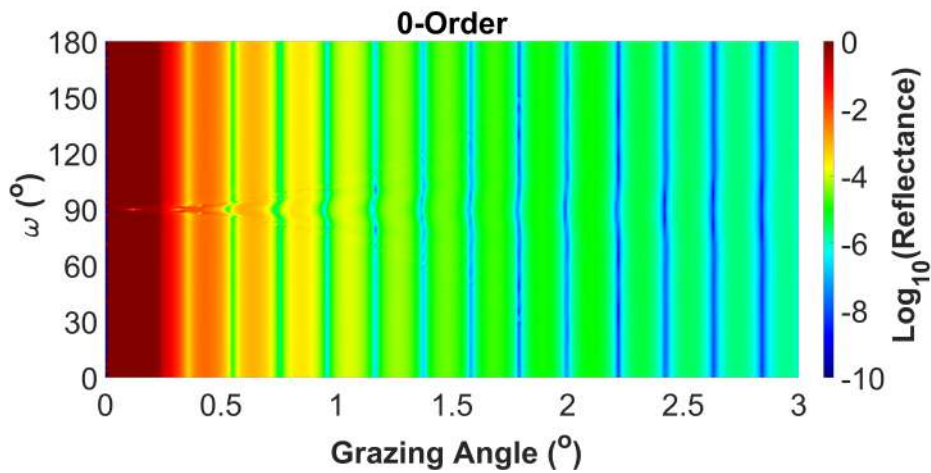


Figure 4.31: RCWA simulation for grazing angle as a function of reflectance logarithm and  $\omega$  for lamellar gratings substrate.

## 4.6 Summary.

To summarize this chapter, we examined the characterization of gratings provided by Zeiss Company and AFM at Synchrotron SOLEIL. We conducted a comparison of various grating parameters using a bar chart, which revealed similarities within one group of gratings and differences among the other groups. Additionally, we analyzed the grating's angular spectra and identified distinct characteristics between classical and conical positions. Subsequently, we employed two separate models to extract the absolute parameters of the gratings based on their angular spectra. Furthermore, we investigated the impact of different grating parameters on grating efficiency, considering both the specular and angular spectra aspects.





## Chapter 5

# Study of the interference coating

In this chapter, We focused on the study and optimization of periodic and aperiodic multilayer coatings using IMD software. The choice of materials and precise designs for the multilayers were based on existing literature and the optical constants (refractive index and optical coefficient) available within the wavelength range of 17–31 nm. The advantages of the materials combination Al/Mo/SiC, which was selected for the coating process, are demonstrated. The interest in aperiodic multilayers is also highlighted.

Multilayers were optimized for specific ranges of wavelengths that depended on the depth of the grating's grooves (see Chapter.4). Simulations were conducted on the multilayer coating applied to the flat silica substrate, including the analysis of reflectance variation with incidence angle and wavelength, the sensitivity of the multilayer, the effect of adding a cap layer, simulation of different numbers of multilayer periods, and their impact on maximum reflectance and bandwidth.

Next, the optimized multilayer was deposited on the flat silicon substrates and characterized using various tools such as transmission electron microscopy, and specular and angular reflectance measurements. The results provided in this chapter have been utilized as a reference for facilitating the analysis of multilayer gratings in the subsequent chapter.

### 5.1 Choosing optical materials

Several material combinations have been proposed with experimental EUV near-normal incidence reflectance higher than 50%, including Mo/Si [96] Mo/Be [39], Sc/Si [97], Mg/Sc/SiC [41], Al/Mo/SiC [17] and Al/Sc/SiC [43].

In previous literature, [42], the multilayer composed of Al and SiC materials shows interesting results in EUV applications in the range of 17-35nm. On one hand, as illustrated in Fig.2.2, it has been observed that the attenuation length for Mo is shorter compared to Al. This implies that the absorption coefficient for Al is lower than that of Mo, which presents a favorable advantage for utilizing Al instead of Mo within the wavelength range of 17-35 nm. In

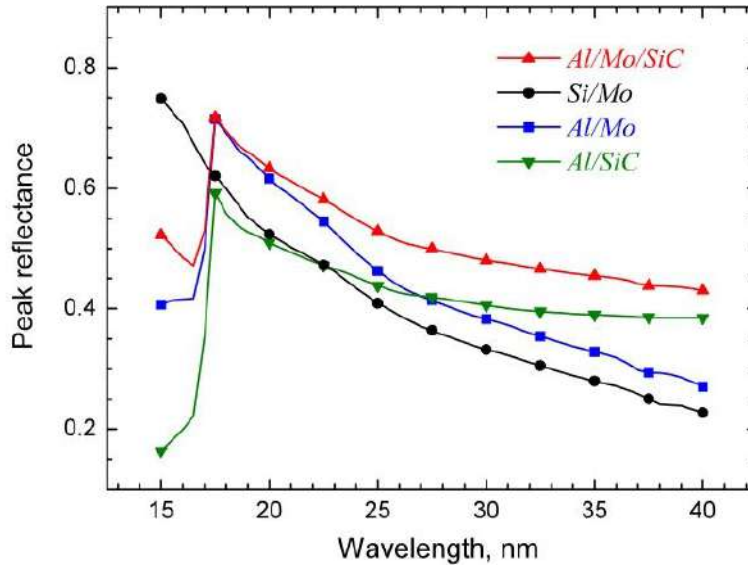


Figure 5.1: Theoretical calculated maximum reflectance of Si/Mo, Al/Mo, Al/SiC, and Al/Mo/SiC multilayer structures under normal incidence, spanning wavelengths from 15 to 40 nm. These calculations assume ideal structures (no surface roughness) comprising 50 periods. [17].

the previous literature [98], the authors investigated three distinct compositions of multilayer structures, namely Al/SiC, Al/W/SiC, and Al/Mo/SiC. In the case of Al/SiC, the analysis of GIXR data revealed significantly high roughness values for both Al and SiC layers. However, the introduction of an additional layer such as tungsten (W) or Mo led to a considerable reduction in roughness values. Hence, it is recommended to incorporate a thin layer of Mo to reduce roughness and improve the optical performance [42], particularly within the wavelength range of 17-35 nm. In addition, The combination of Al/Mo/SiC has been developed in our group for the solar orbital mission (see Section.2.6.2) as illustrated in Fig.5.1 and Fig.5.2.

To gain insights into the underlying physics behind the enhancement of multilayer reflectance depicted in Fig.5.1, Seely et al.[12; 19] employed a Si/Mo composition, where Si served as the spacer layer and Mo as the absorber layer. Substituting Si with Al resulted in an observed increase in reflectance, primarily attributed to a lower values of  $\beta$  and  $\delta$  for Al within the wavelength range of 17-33 nm, as illustrated in Fig.3.25(b) (Chapter 3).

Upon replacing the Mo absorber layer with SiC, the outcomes demonstrated that the Al/Mo composition exhibited higher reflectance for wavelengths below  $\approx 22.5$  nm. However, beyond this threshold, the Al/SiC configuration demonstrated significantly superior reflectance. This behavior can be attributed to the optical constant  $\delta$ , as illustrated in Fig. 3.25(a). It is important to note that the refractive index ( $n$ ) is related to  $\delta$  as  $n = 1 - \delta$ , and reflectance is calculated as the ratio between the difference in refractive indices and the sum of refractive indices.

Meltchakov et al.[17] conducted theoretical studies on various periodic multilayer compositions with  $N = 50$  layers, including Si/Mo, Al/Mo, and Al/SiC, while neglecting the consideration of interfacial roughness. Meltchakov et al. compared the peak reflectance of these compositions to that of Al/Mo/SiC, as illustrated in Fig. 5.1, under normal incidence. Each data point on the y-axis in Fig. 5.1 represents the peak efficiency achieved after optimizing the

## Al/Mo/SiC experimental results

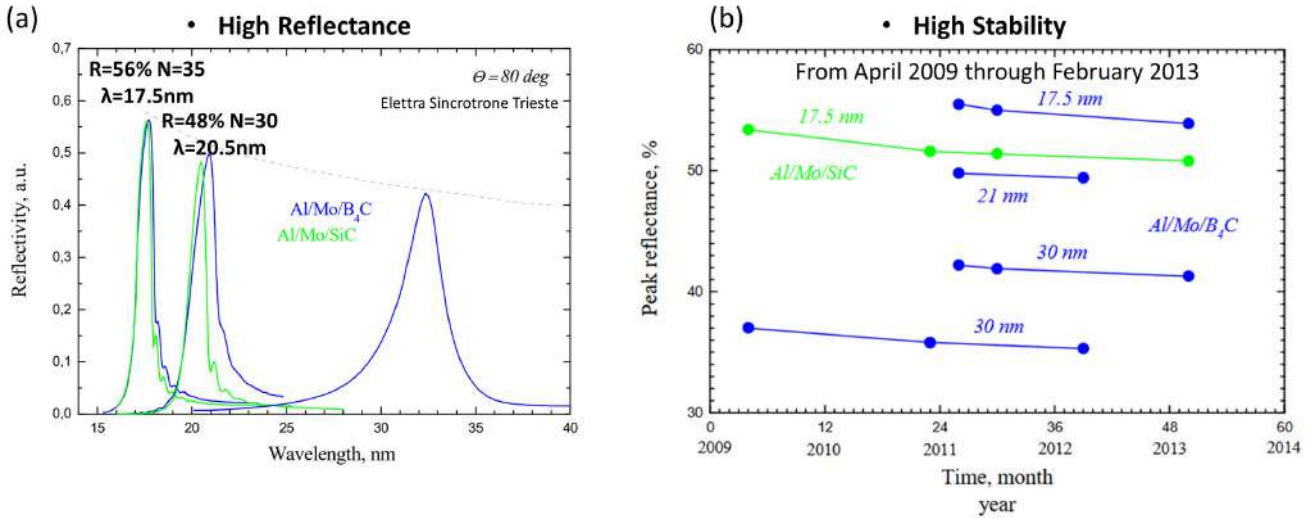


Figure 5.2: The EUV peak reflectances of certain Al/Mo/SiC and Al/Mo/B<sub>4</sub>C multilayers were assessed based on (a) their ability to achieve a high peak reflectance and (b) their capacity to maintain high stability throughout the period from April 2009 to February 2013. [18].

thickness of the multilayer materials at the corresponding central wavelength on the x-axis. Remarkably, despite the absence of roughness considerations between the materials, the composition of Al/Mo/SiC demonstrates superior performance in the wavelength range from 17 nm to 40 nm.

The composition of Al/Mo/SiC has demonstrated a remarkable peak reflectance of 56% at a wavelength of 17.5nm and 48% at 20.5nm when utilized in a periodic multilayer structure, as illustrated in Fig. 5.2(a) [18]. The estimated range for the interfacial roughness between Al/Mo/SiC falls between 0.3nm and 0.7nm. Meltchakov et al. [18] conducted an experimental investigation into the stability of a multilayer composition composed of Al/Mo/SiC, which was designed for a wavelength of 17.5 nm (depicted by the green curve). The deposited multilayer was subjected to EUV spectroscopy at various time intervals spanning from April 2009 to February 2013, as illustrated in Fig. 5.2(b). The findings reveal a slight decrease in the peak reflectance; nevertheless, the results suggest the enduring stability of this multilayer configuration.

In addition, The advantage of utilizing three-material multilayers becomes more significant as the wavelength moves away from the absorption edge, where material absorption increases, as observed in previous research [17].

## 5.2 From broadband to very broadband.

Until now, only a limited number of studies have focused on achieving EUV multilayer gratings with broadband efficiency. Prior research has shown that aperiodic multilayer structures can provide effective broadband reflectance in the EUV spectral range [99; 100; 101]. Yang et al. [45] conducted a theoretical investigation on blazed gratings

Table 5.1: Different multilayer designs.

Material	Design	Results	Reference
B4C/Mo/Si	Periodic		[102]
B4C/Mo/Si	Biperiodic		[102]
B4C/Mo/Si	Aperiodic		[99]

using aperiodic multilayer designs, covering the spectral range of 17–25 nm. By simulating different combinations of multilayer materials, they discovered the potential for optimizing diffraction efficiency across a wide spectral range through aperiodic multilayer coatings [45].

By referring to Table.5.1, we can observe the reflectance spectra of distinct multilayer designs in the case of B4C/Mo/SiC combination. In the case of periodic designs, the peak reflectance is high but the bandwidth is relatively low. Conversely, aperiodic designs demonstrate a broader bandwidth while maintaining a reasonable level of reflectance.

The biperiodic multilayer structure is a combination of two periodic multilayers. It exhibits a broader bandwidth compared to periodic structures but a narrower bandwidth compared to aperiodic structures.

It is worth mentioning that in the figures listed in Table 5.1, the dotted lines depict the measured reflectivity of multilayer samples, while the dashed or solid lines represent the theoretical modeling of these multilayer samples.

Hence, The Al/Mo/SiC multilayers will be optimized in periodic and aperiodic designs, where the optimization is done normally using genetic algorithm (see section.3.2.1.1).

The wavelength range chosen for the optimization process using IMD software will align with Table.4.8 in chapter.4, as our objective in the upcoming chapter.6 is to maximize the +1-order diffraction and minimize the 0-order diffraction for the multilayer gratings, as previously discussed in Section 4.4.1.

### **5.3 Multilayer optimization.**

An alternative approach to expanding the bandpass of a multilayer coating is to use a periodic stack with fewer periods. However, experimental data on multilayer gratings with a low number of periods or aperiodic multilayers are lacking. Previous findings indicate that the initial surface profile of lamellar gratings assumes a trapezoidal shape, and the angle of the trapezoid has a negative impact on efficiency [85]. Furthermore, the deposition of the multilayer coating tends to modify the profile, resulting in the smoothing of high-frequency components, as observed in the case of blazed gratings [65; 62]. By utilizing multilayers with a reduced number of periods, it may be possible to mitigate these smoothing effects and offer an alternative solution for achieving broadband efficiency in gratings.

It is worth noting that the optimization process was carried out using a silica substrate, which coincides with the material used for the gratings in the subsequent chapter. However, the flat substrates available in our laboratory consist of silicon. Therefore, the study of multilayer reflectance spectra in this chapter will be based on a silicon substrate.

The optimization process typically involved using a 6-period multilayer for the three structured designs of the gratings in this study. Additionally, different aperiodic multilayer designs were optimized for each set of gratings. In the following subsections, a 12-layer aperiodic multilayer design (Design 1) was optimized for Set 1 of the gratings, while Designs 2 and 3, composed of 18 and 24 layers respectively, were optimized for Set 2 of the gratings. Similarly, for Set 3 of the gratings, two aperiodic multilayers (Designs 4 and 5) composed of 18 and 24 layers respectively, were optimized.

For each multilayer structure designed for each set of the gratings, there will be a figure and table comparing the periodic design with  $N=6$  to the aperiodic designs in terms of maximum reflectance and wide bandwidth. It is important to note that in this chapter, the bandwidth is calculated as the difference between the two wavelengths corresponding to  $1/\sqrt{2}$  of the maximum reflectance [103].

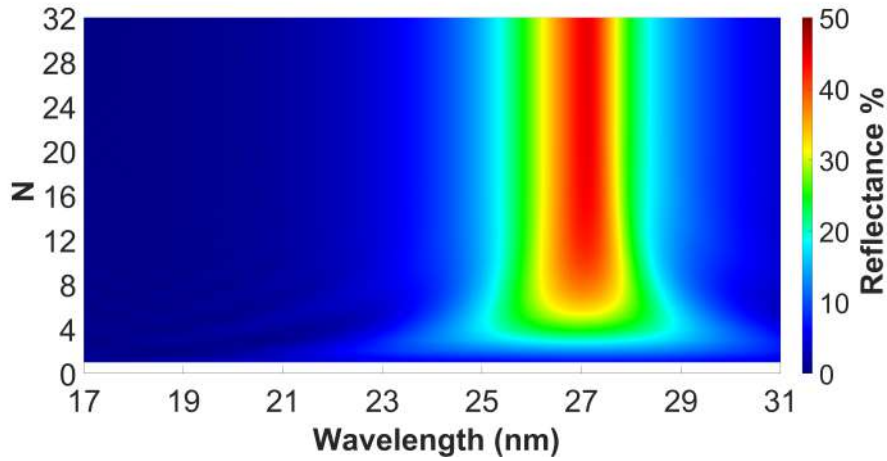


Figure 5.3: TE simulated reflectance of the optimized periodic Al/Mo/SiC multilayer as a function of wavelength and the number of periods ( $N$ ) at  $\theta = 5^\circ$  for set#1.

Table 5.2: Layer thickness and interfacial roughness for the optimized periodic Al/Mo/SiC for set#1 on the  $\text{SiO}_2$  substrate.

Material	Thickness (nm)	Interface	Roughness (nm)
Top Oxide layer	0.0	Top surface	0.0
SiC	3.69	Oxide-on-SiC and Al-on-SiC	0.0
Mo	2.68	SiC-on-Mo	0.0
Al	8.00	Mo-on-Al	0.0
$\text{SiO}_2$ Substrate	$\infty$	Al-on- $\text{SiO}_2$ substrate	0.0

### 5.3.1 Periodic multilayer for set#1.

The optimization process involved fine-tuning the three layers (Al/Mo/a-SiC) with a period  $N = 6$  on a Si substrate within the wavelength range of  $\lambda = 25\text{nm}$  to  $\lambda = 29\text{nm}$ , aiming to maximize the reflection around the central wavelength of  $\lambda = 27\text{nm}$ . The information provided in Table 5.2 signifies the optimized thickness of individual materials. In the optimization process, it is assumed that there is an absence of interfacial roughness between the layers. In Figure.5.3, it can be observed that as the number of multilayer periods increases, the Bragg peak becomes narrower until  $N = 14$ , leading to a decrease in peak bandwidth. After  $N = 14$ , the Bragg peak remains constant. Regarding the reflectivity at  $\lambda = 27\text{nm}$ , an increase in the number of multilayers results in a linear improvement followed by saturation. Conversely, for  $\lambda = 25\text{nm}$  and  $\lambda = 29\text{nm}$ , an increase in the number of multilayer periods leads to a slight improvement in reflectivity, followed by a slight decrease, after which it approximately stabilizes. In other words, as the number of periods increases from 2 to 16, the full width at half maximum (FWHM) of the peak decreases, while the peak reflectance increases. Since the dependence of optimal thicknesses on the number of periods ( $N$ ) was found to be small, we deposited different small numbers of periods for the gratings, which will be detailed in the next chapter.

Furthermore, investigating the impact of the angle of incidence on the reflectance of the multilayer coating was of particular interest. It was observed that the maximum peak shifted from  $\lambda=27\text{nm}$  under normal incidence to

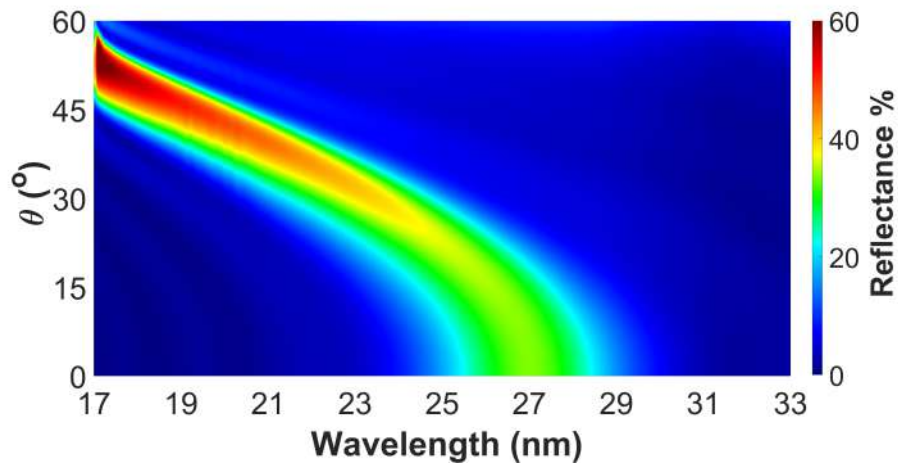


Figure 5.4: TE simulated reflectance of the optimized periodic Al/Mo/SiC multilayer  $N=6$  as a function of wavelength and incidence ( $\theta$ ) for set#1.

Table 5.3: Comparison of maximum reflectance and broadband for periodic ( $N = 6$ ) and aperiodic (Design 1) multilayer designs for Set#1

	Periodic (N=6)	Aperiodic Design 1
Maximum Reflectance	32.99%	22.96%
Broadband	2.59nm	5.09nm

$\lambda=19\text{nm}$  at an angle of  $\theta=45^\circ$ , as depicted in Fig.5.4. This finding holds the potential for conducting measurements of the multilayer coating at two different incidence angles, thereby enhancing the accuracy of the analysis.

### 5.3.2 Aperiodic multilayer for set#1.

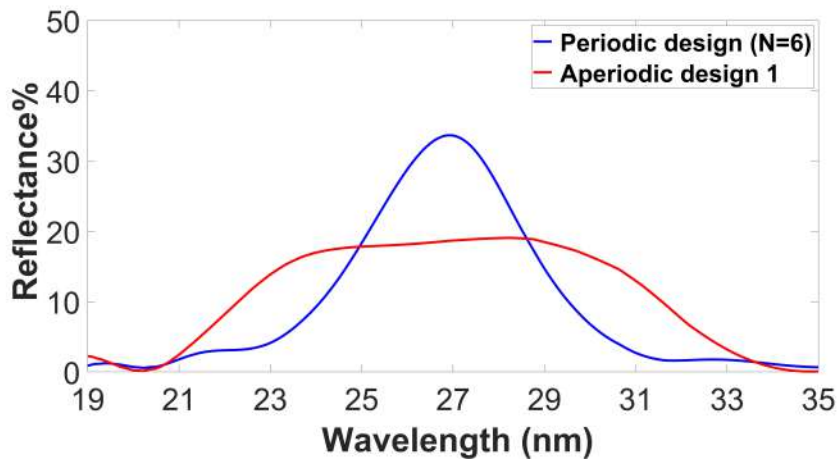


Figure 5.5: The simulated reflectance of the optimized aperiodic (12-layers) and periodic ( $N = 6$ ) Al/Mo/SiC multilayers as a function of wavelength at  $\theta= 5^\circ$ .

In the aperiodic coating design, the thicknesses of the 12 layers ranged between 3 and 11 nm. The detailed structure of the aperiodic design can be found in appendix Table.B.2. Figure Fig.5.5 presents the simulated reflectance spectra



Table 5.4: Layer thicknesses and interfacial roughness for the optimized periodic Al/Mo/SiC structure for Set#2 on the SiO<sub>2</sub> substrate.

Material	Thickness (nm)	Interface	Roughness (nm)
Top Oxide layer	0.0	Top surface	0.0
SiC	1.99	Oxide-on-SiC and Al-on-SiC	0.0
Mo	4.33	SiC-on-Mo	0.0
Al	3.84	Mo-on-Al	0.0
SiO <sub>2</sub> Substrate	∞	Al-on- SiO <sub>2</sub> substrate	0.0

at a 5° angle of incidence for the periodic multilayer as a function of wavelength. By disregarding roughness considerations, the optimization of aperiodic design 1 (Table.5.3) yielded a peak reflectance of 19.07% and a bandwidth of 8.0nm. Furthermore, the optimized periodic design with N=6 was included in this Fig.5.5 for comparison.

### 5.3.3 Periodic multilayer for set#3.

The optimization process aimed to maximize reflection at the central wavelength of 19nm by fine-tuning the three layers (Al/Mo/a-SiC) with a period of N=6 on a Si substrate, within the wavelength range of 17nm to 21nm. Fig.5.6 demonstrates a similar observation to Fig.5.3, considering the parameters specified in Table.5.4.

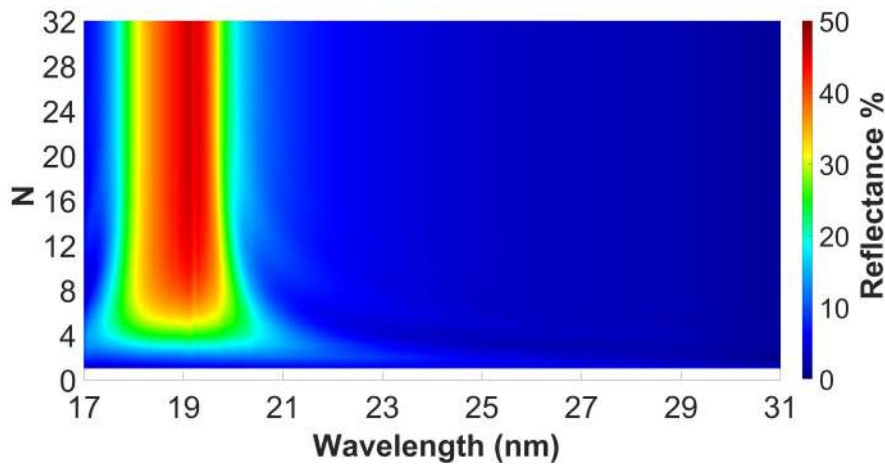


Figure 5.6: TE simulated reflectance of the optimized periodic Al/Mo/SiC multilayer as a function of wavelength and the number of periods (N) at  $\theta = 5^\circ$  for set#3.

The impact of the angle of incidence on the reflectance of the multilayer coating was examined. It was observed that the maximum peak, initially occurring at  $\lambda = 19\text{nm}$  under normal incidence, shifted towards the Al edge at an angle of approximately  $\theta = 30^\circ$ , as shown in Figure 5.7. This shift highlights the difficulty in measuring the multilayer coating at different incidence angles.

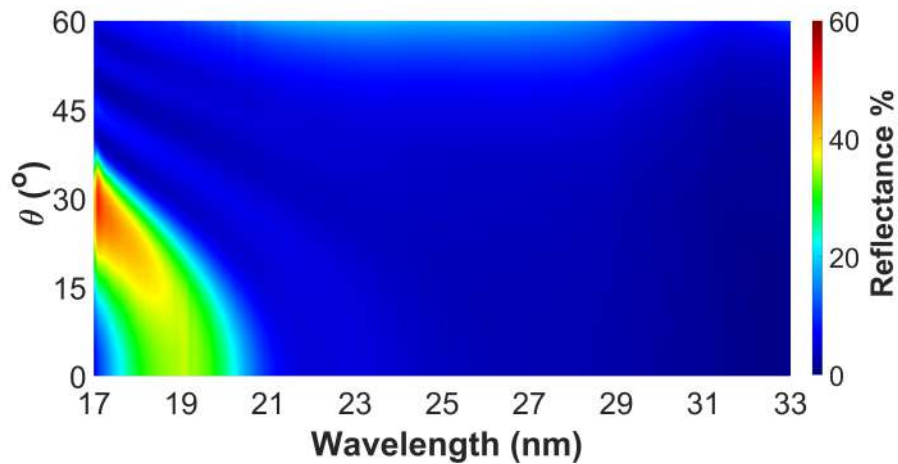


Figure 5.7: TE simulated reflectance of the optimized periodic Al/Mo/SiC multilayer  $N=6$  as a function of wavelength and incidence ( $\theta$ ) for set#3.

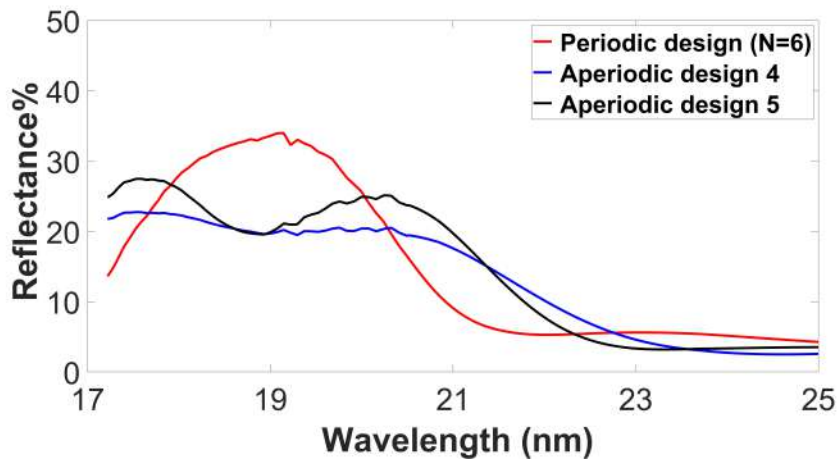


Figure 5.8: The reflectance simulation results are presented in this caption, showcasing the optimized performance of two aperiodic designs with 18 and 24 layers, along with the periodic ( $N = 6$ ) Al/Mo/SiC multilayers. The reflectance is plotted as a function of wavelength at an incidence angle of  $\theta= 5^\circ$ .

Table 5.5: Comparison of maximum reflectance and broadband for periodic ( $N = 6$ ), aperiodic Design 4, and aperiodic Design 5 of multilayer designs for Set#3

	Periodic (N=6)	Aperiodic Design 4	Aperiodic Design 5
Maximum Reflectance	33.98%	22.75%	27.48%
Broadband	2.33nm	4.00nm	3.81nm

### 5.3.4 Aperiodic multilayer for set#3.

Aperiodic design 4 and aperiodic design 5 (Table.B.4) exhibit maximum reflectance values of 22.75% and 27.48%, respectively. A bandwidth of 4.00nm was obtained for aperiodic design 4, while aperiodic design 5 achieved a bandwidth of 3.81nm as indicated in Table.5.5.

Table 5.6: Layer thickness and interfacial roughness for the optimized periodic Al/Mo/SiC for Set#2 on the SiO<sub>2</sub> substrate.

Material	Thickness (nm)	Interface	Roughness (nm)
Top Oxide layer	0.0	Top surface	0.0
SiC	1.99	Oxide-on-SiC and Al-on-SiC	0.0
Mo	4.37	SiC-on-Mo	0.0
Al	5.01	Mo-on-Al	0.0
SiO <sub>2</sub> Substrate	∞	Al-on- SiO <sub>2</sub> substrate	0.0

### 5.3.5 Periodic multilayer for set#2.

The findings in this section exhibit close resemblance to the results obtained for the multilayer coating of Set 2 in subsection 2. However, a slight shift of 2nm was implemented to optimize within the wavelength range of 19nm to 23nm, employing N=6 multilayer periods on a Si substrate, with the aim of maximizing reflectance at the central wavelength of 21nm. The results depicting the variation of reflectance with multilayer periods and wavelength, as well as the reflectance variation with incidence angle and wavelength, can be found in Appendix Figure C.2 and Figure C.3, respectively. The optimized thickness parameters are detailed in Table 5.6.

### 5.3.6 Aperiodic multilayer for set#2.

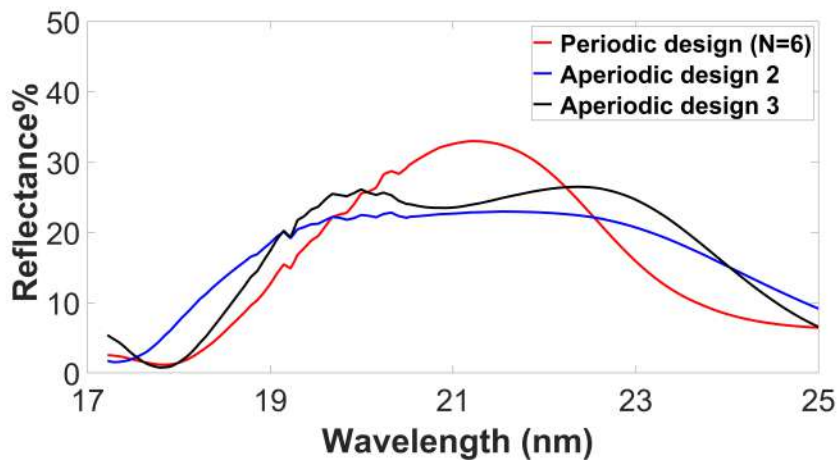


Figure 5.9: The reflectance simulations of the optimized periodic ( $N = 6$ ) Al/Mo/SiC multilayers and two aperiodic designs (consisting of 18 layers and 24 layers) are presented as a function of wavelength at an incidence angle of  $\theta = 5^\circ$ .

The aperiodic design 2, and aperiodic design 3 (Table.B.3) show maximum reflectance of 22.96%, and 26.47 respectively. 5.09 nm and 4.62 nm are the bandwidth obtained for aperiodic design 2, and aperiodic design 3 respectively.

Table 5.7: Comparison of maximum reflectance and broadband for periodic ( $N = 6$ ), aperiodic Design 2, and aperiodic Design 3 of multilayer designs for Set#2

	Periodic (N=6)	Aperiodic Design 2	Aperiodic Design 3
Maximum Reflectance	32.99%	22.96%	26.47%
Broadband	2.59nm	5.09nm	4.62nm

## 5.4 Multilayer sensitivity to the thickness changes.

The aim of this study is to investigate a common occurrence during multilayer deposition, where the actual thickness of deposited layers often deviates slightly from the target thickness due to factors like interdiffusion or surface roughness. Our goal is to demonstrate how altering the thickness of a single layer affects peak reflectance and bandwidth while maintaining a constant multilayer period as discussed in the subsection.5.4.1. Another effect to consider is increasing the thickness of the top layer as a protective measure for the multilayer structure, which we discussed in subsection.5.4.2.

### 5.4.1 Sensitivity of the ML periodic design.

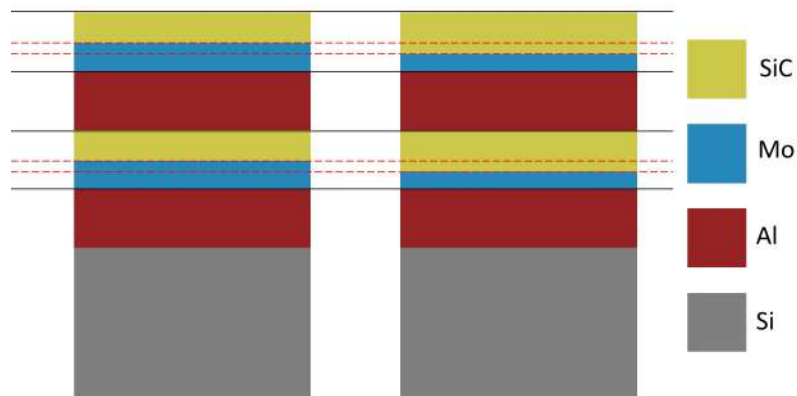


Figure 5.10: The schematic of 2 periods Al/Mo/SiC multilayers on a Si substrate illustrates the relative thickness variation between the Mo and SiC layers, while the thickness of the Al layer remains constant.

The phenomenon investigated in this section is commonly referred to as the gamma effect in multilayers. However, the gamma effect can only occur when there are exactly two different material layers in the multilayer composition. In our case, the multilayer is composed of three different layers: Al, Mo, and SiC. Therefore, to conduct this study, we will select two materials and maintain a constant thickness for the third layer. We have chosen to keep the thickness of Al constant while varying the thickness between Mo and SiC. This decision was made based on the expectation of interdiffusion between these two materials. Throughout the study, the period thickness remains unchanged.

In this study, the thickness of the SiC layers will be reduced by 0.2nm, 0.4nm, 0.6nm, 0.8nm, and 1nm (see Fig.5.10), while simultaneously increasing the thickness of the Mo layers by the same amount to maintain the overall thickness of the multilayer period. The objective of this analysis is to examine the sensitivity's impact on the maximum reflectivity and broadband width.

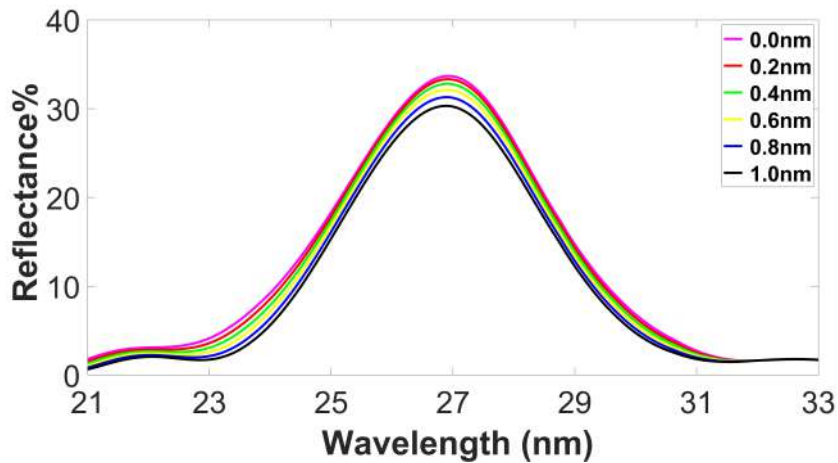


Figure 5.11: Relative thickness changes between SiC and Mo of TE simulated reflectance of optimized periodic Al/Mo/SiC multilayer design for Set#1 as a function of wavelength at  $\theta = 5^\circ$ .

Observing Fig.5.11, it becomes evident that the thickness of the SiC layer has a detrimental effect on the reflectance of the multilayer coating. The maximum reflectivity and broadband width are diminished from 33.68% and 2.73nm, respectively, to 30.31% and 2.67nm.

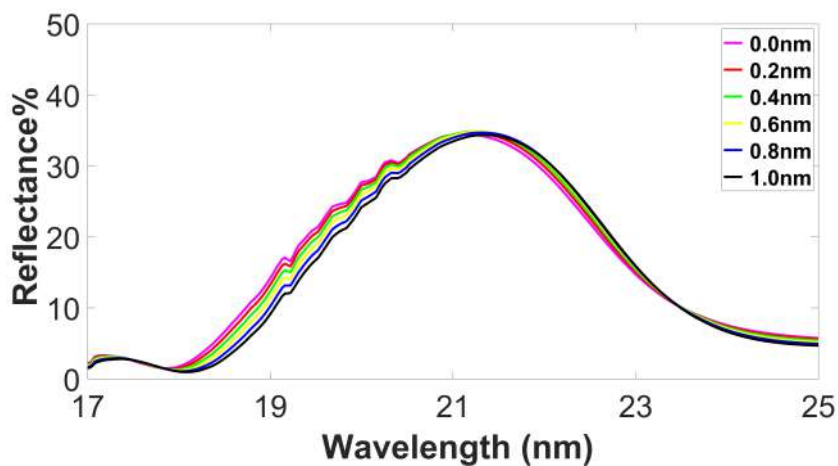


Figure 5.12: Relative thickness changes between SiC and Mo of TE simulated reflectance of optimized periodic Al/Mo/SiC multilayer design for set#2 as a function of wavelength at  $\theta = 5^\circ$ .

In Fig.5.12, the sensitivity analysis of the multilayer coating results in a slight shift of the peak towards longer wavelengths. Additionally, there is a notable reduction in the bandwidth from 2.63nm to 2.50nm. However, the decrease in maximum reflectance is relatively insignificant, declining from 34.44% to 34.35%.

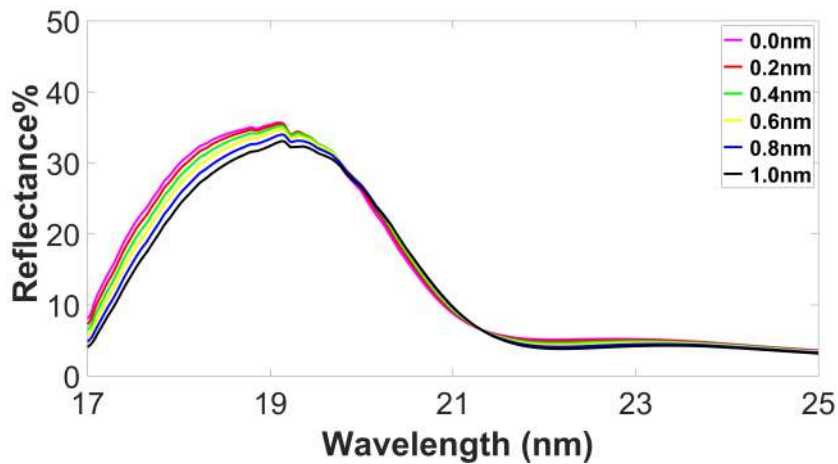


Figure 5.13: The relative thickness changes between SiC and Mo of TE simulated reflectance of the optimized periodic Al/Mo/SiC multilayer design for Set #3 as a function of wavelength at  $\theta = 5^\circ$ .

Regarding Fig.5.13, the sensitivity analysis leads to a decrease in both bandwidth and maximum reflectance. The bandwidth diminishes from 2.29nm to 2.22nm, while the maximum reflectance declines from 35.67% to 33.08%.

#### 5.4.2 Effect of adding a cap of SiC.

According to previous research by [17], it has been demonstrated that the SiC capping layers, with a thickness of approximately 3 nm, effectively safeguard periodic multilayer designs and ensure excellent temporal stability for Al-based multilayers.

The study was conducted on the multilayer structure of Set#2 and Set#3 gratings due to the optimized SiC thickness being 1.99nm, as indicated in Table.5.6 and Table.5.4. However, the capping layer was found to be unnecessary for the multilayer structure of Set#1 gratings, as the optimized SiC thickness was 3.69nm, as shown in Table.5.2.

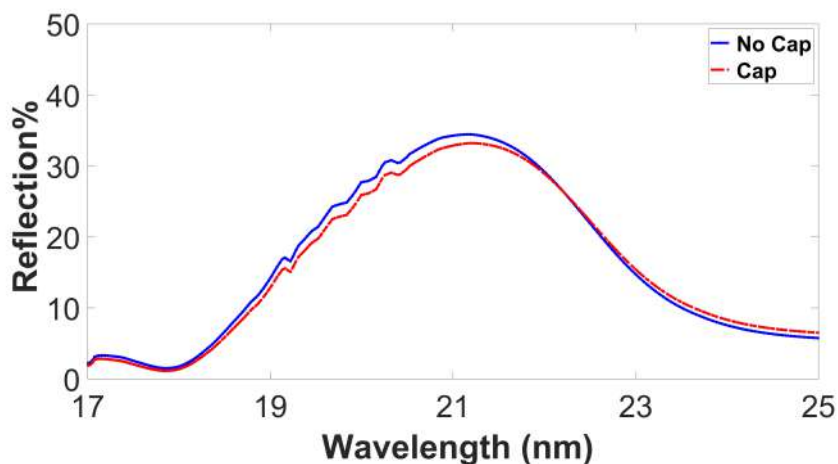


Figure 5.14: TE simulated reflectance variation due to adding SiC cap layer at the top of optimized multilayers for ML Set#2 at  $\theta = 5^\circ$ .

In Set#2 (Fig.5.14), the maximum reflectance and bandwidth experience a slight decrease, with values from 34.44% and 2.63 nm to 33.21% and 2.55 nm, respectively.

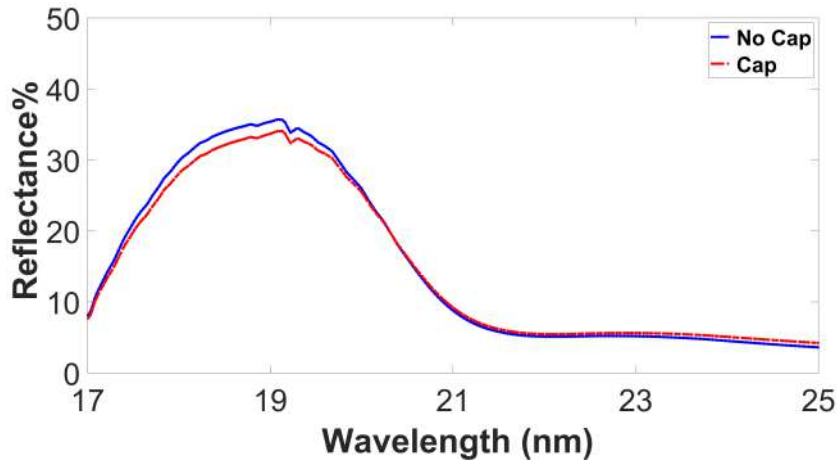


Figure 5.15: TE simulated reflectance variation due to adding SiC cap layer at the top of optimized multilayers for ML Set#3 at  $\theta = 5^\circ$ .

In Set#3 (Figure 5.15), the maximum reflectance experiences a decrease, reducing from 35.67% to 34.04%. However, the bandwidth almost remains unchanged.

## 5.5 Characterization multilayers deposition on a silicon substrate.

Two different multilayer designs of Al/Mo/SiC were deposited on flat Si substrates to investigate the thickness of the layers and the presence of interfacial defects such as interdiffusion and roughness. The first sample, labeled MP20065, corresponds to a periodic Al/Mo/SiC design with 10 periods ( $N=10$ ), while the second sample, labeled MP20070, corresponds to an aperiodic design consisting of 12 layers.

It is expected that the top surface of the SiC layer undergoes oxidation when the sample is exposed to air. Previous research utilized x-ray photoelectron spectroscopy to analyze Al/Mo/SiC multilayers and identified the presence of approximately 1.6 nm of  $\text{SiO}_x$  on the top surface of the SiC layer [42].

Figure.5.16(a) displays a high-angle annular dark-field (HAADF) STEM image of sample MP20065, where the bright lines represent high-density Mo layers, while the dark lines represent low-density Al and SiC layers. Distinguishing between Al and SiC layers in Fig.5.16(a) is challenging due to their similar densities. In Fig.5.16(b), the EDX-STEM analysis of Fig.5.16(a) is presented. EDX enables the identification of specific atom locations, and in Fig.5.16(b), images corresponding to different atoms (Al, Mo, Si, C, O, and Pt) are plotted. The top image in Fig.5.16(b) represents the sum of the images corresponding to Al, Mo, Si, and Pt. The presence of three distinct layers in each of the 10 periods of the coating can be clearly observed. Vertical lines indicating the interface positions between Al, Mo, and SiC layers, as used in x-ray and EUV models (refer to Fig.5.17 and Table.5.8), are also shown in Fig.5.16(b). The



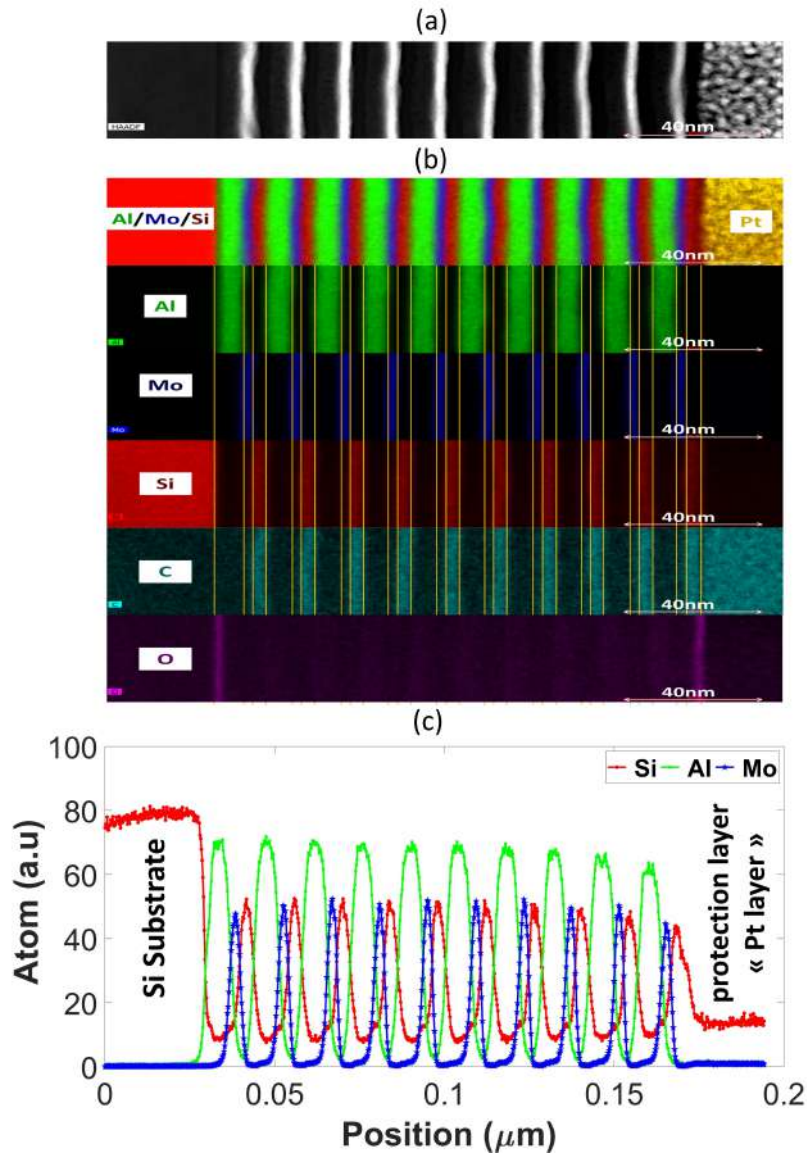


Figure 5.16: TEM analyses of sample MP20065: (a) HAADF (b) EDX images and (c) profile of the atom concentration, in arbitrary units (a.u.), as a function of the position.

respective thicknesses of these layers are 7.72 nm, 2.74 nm, and 3.91 nm.

Due to significant contamination in the cross-section sample which is around 100 nm thickness, images corresponding to C and O atoms were not included in the top image. However, it can be observed that C atoms appear at the same positions as Si atoms, while O atoms are located at the surface of the Si substrate (which was not de-oxidized before deposition) and the surface of the top SiC layer (corresponding to the previously mentioned  $\text{SiO}_x$  layer). Finally, in Fig.5.16(c), atomic profiles for Al, Mo, and Si atoms are plotted. Both Fig.5.16(b) and Fig.5.16(c) demonstrate that interdiffusion occurs between the layers, particularly at the Mo-on-Al and Al-on-SiC interfaces.

It is important to note that the observed difference in signal behavior, where some signals (such as Mo in Fig.5.16c) go to zero while others (such as Si and Al in Fig.5.16c) do not, is inherent to the technique itself. When electrons



Table 5.8: Layer thickness and interfacial roughness used to model the periodic Al/Mo/SiC coating (sample MP20065) on Si substrate.

Material	Thickness (nm)	Interface	Roughness (nm)
Top Oxide layer	1.40	Top surface	0.30
SiC	3.91	Oxide-on-SiC and Al-on-SiC	0.60
Mo	2.74	SiC-on-Mo	0.30
Al	7.72	Mo-on-Al	0.70
Si Substrate	$\infty$	Al-on- Si substrate	0.35

interact with matter, they generate X-rays within the small region probed by the electron beam (a few picometers). These X-rays are emitted in all directions. If their energy is sufficiently high, they can interact with other materials and produce new X-rays with lower energy. All X-rays are ultimately detected by the detector, and the signal is attributed to the position of the electron probe.

In this specific case, Mo can emit X-rays at high energy (such as K alpha at 17.441 keV), while Al and Si have K alpha at 1.486 and 1.739 keV, respectively. Consequently, X-rays generated by Mo can potentially ionize a Si or Al atom in a different location within the material. Since our intention was to analyze the entire deposition stack, we selected a relatively thick area (approximately 100 nm) to enhance the statistical probability of observing this phenomenon and to increase the intensity of the beam.

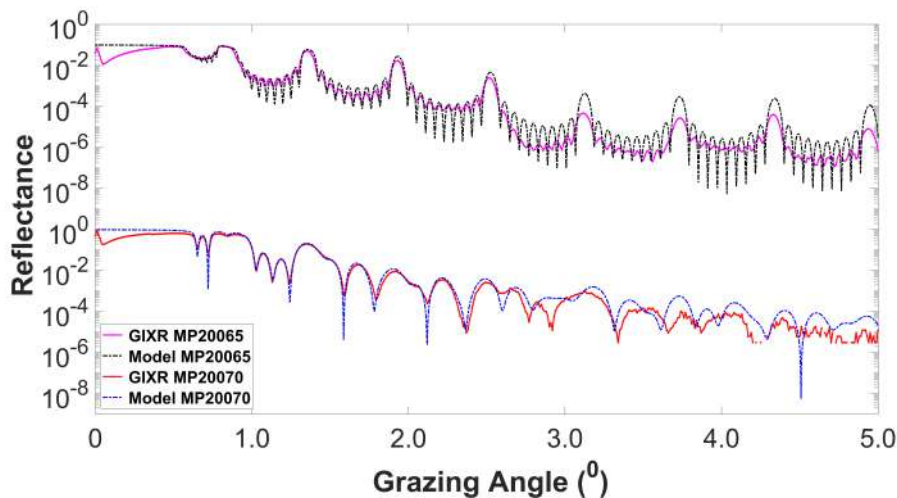


Figure 5.17: GIXR measured and fitted curves at  $\lambda=0.154$  nm for the 10-periods Al/Mo/SiC multilayer (sample MP20065) and the 12 layers aperiodic Al/Mo/SiC multilayer (sample MP20070).

Figure.5.17 illustrates the GIXR analysis conducted on samples MP20065 and MP20070. This type of measurement is valuable for extracting structural parameters of the coating, such as period thickness and interfacial roughness. Additionally, the optimized models that were fitted to the GIXR and SXR experimental data are plotted in Fig.5.17, Fig.5.18, and Fig.5.19. The details of the periodic and aperiodic models can be found in Table.5.8, Table.5.9, and Table.B.2 respectively. The total thickness of the periodic and aperiodic models, excluding the oxidation layers, matches the targeted multilayer thickness values (143.7 nm and 64.44 nm, respectively).

In the case of the periodic multilayer (sample MP20065), Fig.5.17 demonstrates a good agreement between the measured data and the model. The Bragg peaks are well-defined up to the 8<sup>th</sup> order, indicating the high periodicity of the structure and the quality of the interfaces. The periodic multilayer model incorporates interfacial roughness values ranging from 0.3 nm to 0.7 nm at different interfaces (refer to Table.5.8). These roughness values are consistent with the observations in Fig.5.16(c).

On the other hand, extracting precise thickness values from the fitting of the twelve-layer aperiodic model is more challenging due to the absence of well-defined interference peaks and a larger number of parameters. However, by combining GIXR and SXR data, a model was proposed that fits the GIXR data well for grazing incidence angles up to 5°. It should be noted that the individual layer thicknesses were kept equal to the ranged values, and the interfacial roughness values are within the same range as those in the periodic model.

Roughness is a parameter that can help address discrepancies in the intensity of high-order Bragg peaks for periodic multilayers. However, in the case of aperiodic multilayers, it is necessary to analyze each layer individually, considering both the thickness and interfacial roughness of each layer.

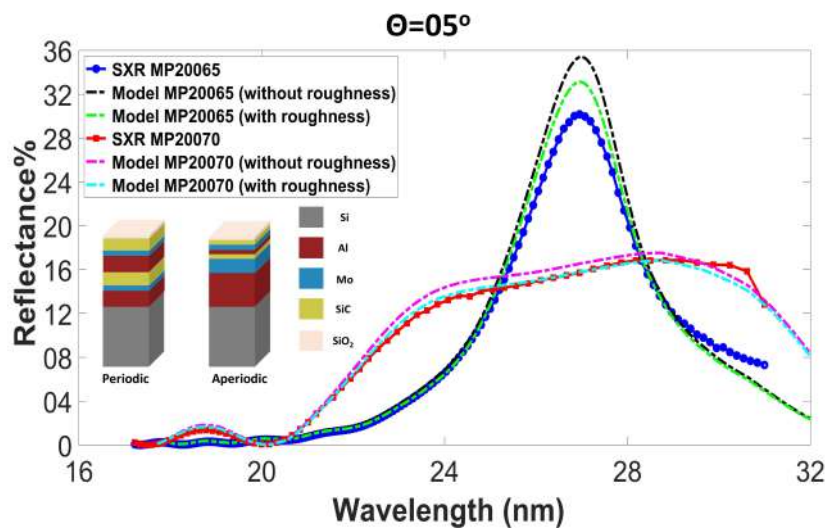


Figure 5.18: Reflectance of SXR measured and fitted spectra at  $\theta=5^\circ$  for the 10-periods Al/Mo/SiC multilayer (sample MP20065) and the 12 layers aperiodic Al/Mo/SiC multilayer (sample MP20070).

Subsequently, samples MP20065 and MP20070 were measured at an angle of  $\theta=45^\circ$  using the Metrology beam-line at the SOLEIL synchrotron to further refine the two models. At this angle, the impact of the polarization factor on the peak reflectance is maximized due to its proximity to the Brewster angle. The best-fitting results were achieved with a polarization factor of 0.96, indicating that 96% of the incident light was TE-polarized. Fig.5.19 and C.5 demonstrate the excellent agreement between the fitted models and the measured data for both samples, confirming the accuracy of the refined models.

Table 5.9: Interfacial roughness used to model the aperiodic Al/Mo/SiC coating (sample MP20070) on Si substrate.

Interface	Roughness (nm)
Top surface	0.45
Oxide-on-SiC and Al-on-SiC	0.55
SiC-on-Mo	0.30
Mo-on-Al	0.70
Al-on- Si substrate	0.35

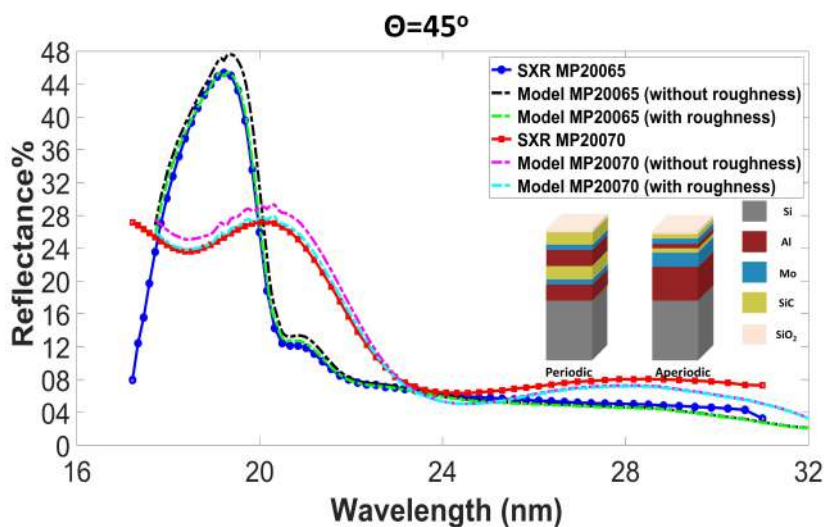


Figure 5.19: Reflectance of SXR measured and fitted spectra at  $\theta=45^\circ$  for the 10-periods Al/Mo/SiC multilayer (sample MP20065) and the 12 layers aperiodic Al/Mo/SiC multilayer (sample MP20070).

In addition, Fig.5.18 and Fig.5.19 include plots of simulated spectra using models without interfacial roughness, with all other simulation parameters remaining the same as in the previous models for both the periodic and aperiodic structures. In these simulations, the interfacial roughness values are set to 0 nm. As expected, the impact of roughness is more pronounced at near-normal incidence ( $\theta=5^\circ$ ) compared to  $45^\circ$ . Moreover, Fig.5.17 illustrates that the peak reflectance of the periodic model is more significantly affected by roughness compared to the reflectance of the aperiodic model.

In conclusion, the optimized periodic and aperiodic multilayer models, incorporating a top oxide layer and interfacial roughness values ranging from 0.3 nm to 0.7 nm, provide satisfactory results. These models enable accurate fitting of GIXR data (as depicted in Fig.5.17), as well as SXR data at two different incidence angles (as shown in Fig.5.18 and 5.19). The models successfully capture the structural parameters and reflectance characteristics of the coated samples.

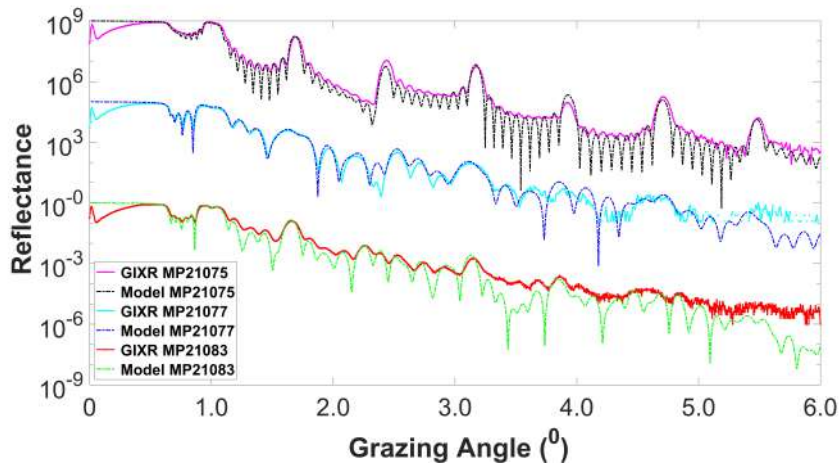


Figure 5.20: The measured and fitted curves for the 10-period Al/Mo/SiC multilayer (sample MP21074), the 18-layer aperiodic Al/Mo/SiC multilayer (sample MP21077), and the 24-layer aperiodic Al/Mo/SiC multilayer (sample MP21083) at GIXR at  $\lambda=0.154\text{nm}$

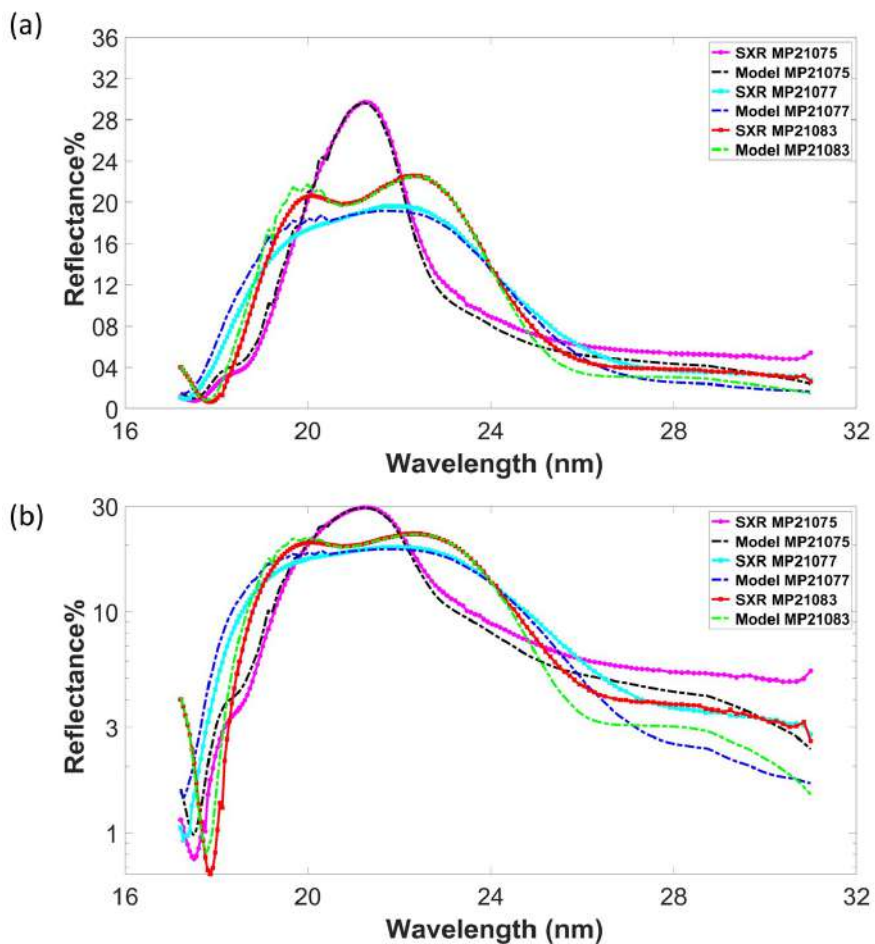


Figure 5.21: The measured and fitted curves for the 10-period Al/Mo/SiC multilayer (sample MP21075), the 18-layer aperiodic Al/Mo/SiC multilayer (sample MP21077), and the 24-layer aperiodic Al/Mo/SiC multilayer (sample MP21083) for SXR at  $\theta=5^\circ$  (a) reflectance-wavelength, and (b) reflectance logarithme-wavelength.

Table 5.10: Layer thickness and interfacial roughness were used to model the periodic Al/Mo/SiC coating (sample MP20075) on Si substrate.

Material	Thickness (nm)	Interface	Roughness (nm)
Top Oxide layer	0.50	Top surface	0.30
SiC	1.99	Oxide-on-SiC and Al-on-SiC	0.30
Mo	4.37	SiC-on-Mo	0.60
Al	5.01	Mo-on-Al	0.70
Si Substrate	$\infty$	Al-on- Si substrate	0.35

To evaluate the quality of the multilayer structures intended for use in grating Set#2, three test samples were deposited on a flat silicon substrate: a 10-period periodic multilayer, an 18-layer aperiodic multilayer, and a 24-layer aperiodic multilayer. These samples were characterized using GIXR and SXR measurements, as shown in Fig.5.20 and Fig.5.21. The measured data have then been modeled using IMD. The three sample models demonstrate good agreement with the measured data.

The parameters for the 10-period periodic multilayer (MP21075) are provided in Table.5.10. Additionally, there is a SiC cap layer with a thickness of 0.99 nm at the top of the SiC layers. For the 18-layer (MP21077) and 24-layer (MP21083) aperiodic multilayers, the material thicknesses used in the models are taken from Table.B.3. The thickness of the top oxide layer used to model MP21076 and MP21082 was 0.6 nm and 0.9 nm, respectively. The roughness values obtained, as presented in Table.5.10, have been applied to model all the samples: MP21075, MP21077, and MP21083.

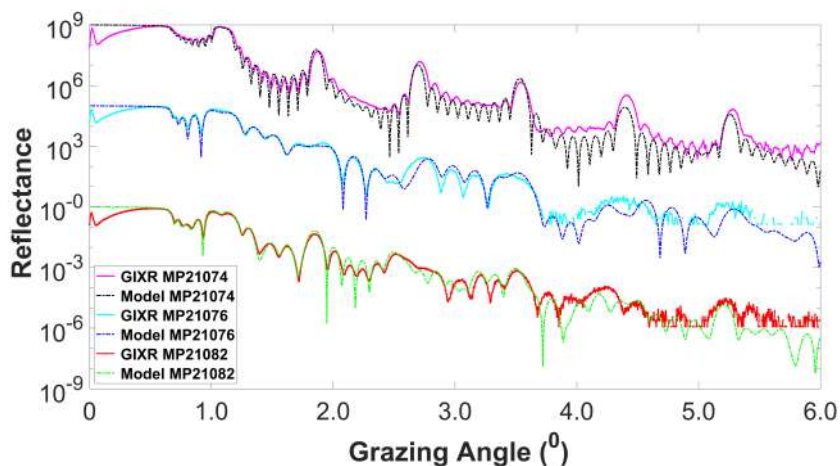


Figure 5.22: The measured and fitted curves for the 10-period Al/Mo/SiC multilayer (sample MP21074), the 18-layer aperiodic Al/Mo/SiC multilayer (sample MP21076), and the 24-layer aperiodic Al/Mo/SiC multilayer (sample MP21082) at GIXR at  $\lambda=0.154\text{nm}$

In a similar manner, a set of 10 periodic multilayers, 18-layer aperiodic multilayers, and 24-layer aperiodic multilayers were deposited on a test flat silicon substrate to evaluate the multilayer structures for grating Set#3. These samples were characterized using GIXR and SXR techniques and subsequently modeled using IMD, as illustrated in Fig.5.22 and Fig.5.23. The parameters employed by IMD to fit the 10 periodic multilayers (MP21074) are presented

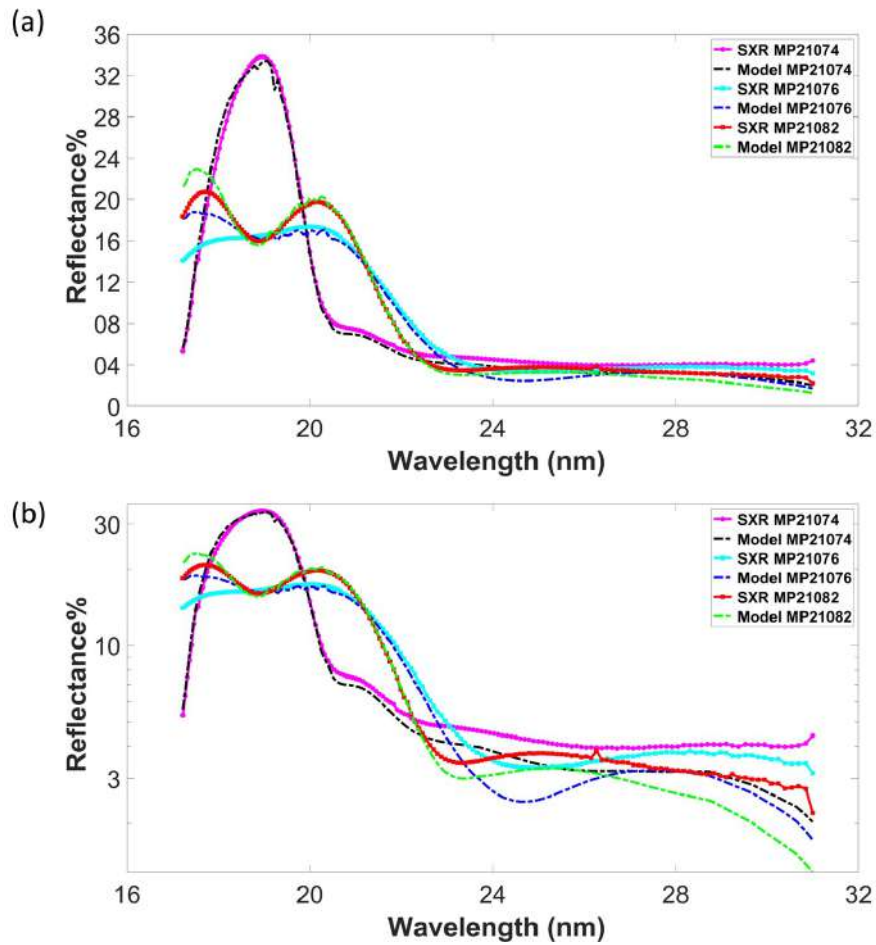


Figure 5.23: The measured and fitted curves for the 10-period Al/Mo/SiC multilayer (sample MP21074), the 18-layer aperiodic Al/Mo/SiC multilayer (sample MP21076), and the 24-layer aperiodic Al/Mo/SiC multilayer (sample MP21082) for SXR at  $\theta=5^\circ$  (a) reflectance-wavelength, and (b) reflectance logarithm-wavelength.

Table 5.11: Layer thickness and interfacial roughness were used to model the periodic Al/Mo/SiC coating (sample MP20074) on Si substrate.

Material	Thickness (nm)	Interface	Roughness (nm)
Top Oxide layer	0.50	Top surface	0.30
SiC	1.99	Oxide-on-SiC and Al-on-SiC	0.30
Mo	4.33	SiC-on-Mo	0.60
Al	3.84	Mo-on-Al	0.70
Si Substrate	$\infty$	Al-on- Si substrate	0.35

in Table.5.11. For the 18-layer (MP21076) and 24-layer (MP21082) aperiodic multilayers, the material thicknesses utilized by IMD for modeling are listed in Table.B.4. The oxide layer thicknesses used to model MP21076 and MP21082 are 0.8 nm and 0.7 nm, respectively. The roughness values in Table 5.11 remained unchanged compared to Table 5.10.



## 5.6 Final multilayers for the deposition process.

In this section, we demonstrate the selected designs that will be deposited in Chapter.6 on the gratings. We took special care in choosing periodic designs with a lower number of multilayer periods, which are below the saturation point presented in Fig.5.3, Fig.5.6, and Fig.C.3. These selected multilayer periods should exhibit different peak reflectance and broad bandwidth. The aperiodic designs, composed of 12 layers, 18 layers, and 24 layers, can be compared to periodic multilayer designs of  $N = 4$ ,  $N = 6$ , and  $N = 8$ , respectively, which have the same number of layers.

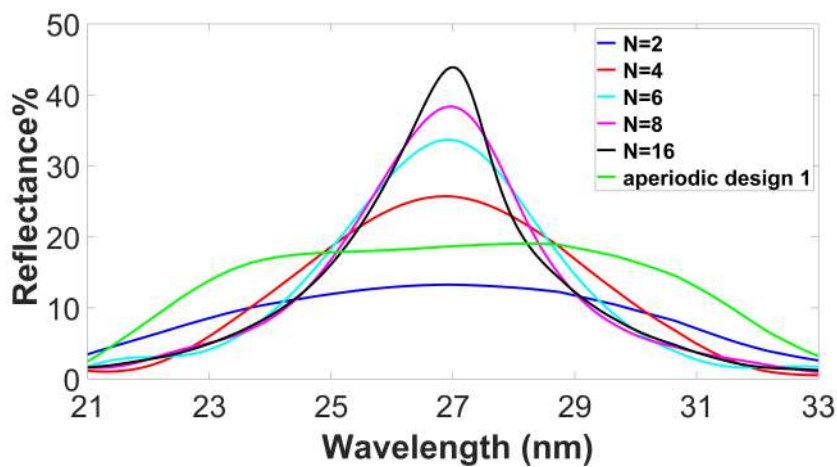


Figure 5.24: Simulated reflectance of optimized periodic Al/Mo/SiC multilayer with different numbers of periods and aperiodic Al/Mo/SiC multilayer as a function of wavelength for ML Set#1 at  $\theta = 5^\circ$ .

Figure.5.24 illustrates the reflectance spectra at a  $5^\circ$  angle of incidence for the chosen periodic multilayers ( $N = 2, 4, 6, 8,$  and  $16$ ) intended for deposition on the gratings Set#1. This plot serves to demonstrate that the appropriate number of periods can be selected based on the desired spectral bandwidth for a specific application. Additionally, the reflectance of the aperiodic multilayer (consisting of 12 layers) is included in the plot for comparison. Despite the optimization wavelength band being constrained to 25-29 nm, the aperiodic multilayer design exhibits significant efficiency within the range of 22 nm to 32 nm. This clearly indicates that employing an aperiodic coating allows for achieving higher reflectance across a broader spectral range, in comparison to a periodic coating with  $N = 4$ .

Similarly, Fig.5.25 and Fig.5.26 depict the reflectance spectra at a  $5^\circ$  angle of incidence for the selected periodic multilayers ( $N = 4, 6, 8,$  and  $10$ ) chosen for deposition on gratings Set#2 and Set#3, respectively. The reflectance of the aperiodic multilayers with 18 and 24 layers is also included in the plots for comparison. Likewise, this indicates that employing an aperiodic coating allows for achieving higher reflectance over a broader spectral range in comparison to a periodic coating with  $N = 6$  and  $N = 8$ .

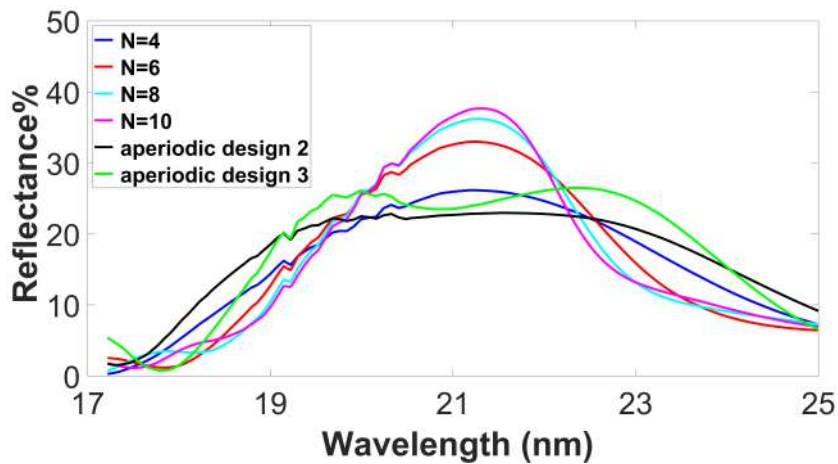


Figure 5.25: Simulated reflectance of optimized periodic Al/Mo/SiC multilayer with different numbers of periods and aperiodic Al/Mo/SiC multilayer as a function of wavelength for ML Set#2 at  $\theta = 5^\circ$ .

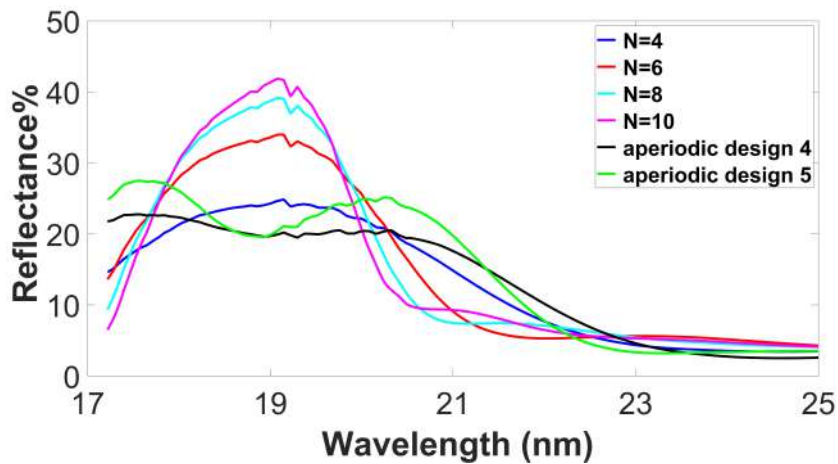


Figure 5.26: Simulated reflectance of optimized periodic Al/Mo/SiC multilayer with different numbers of periods and aperiodic Al/Mo/SiC multilayer as a function of wavelength for ML Set#3 at  $\theta = 5^\circ$ .

## 5.7 summary.

In summary, this chapter demonstrates the advantages of utilizing a multilayer composition of Al/Mo/SiC in the coating process. We highlight the benefits of employing aperiodic multilayers, which provide broad bandwidth with good efficiency. Furthermore, we optimize the multilayers specifically for a range of wavelengths that correspond to the depth of the grating's grooves for the three sets presented in Chapter.4.

To investigate the performance of the multilayers on a flat silica substrate, we conduct various simulations. These simulations include analyzing the reflectance variation concerning the incidence angle and wavelength, evaluating the sensitivity of the multilayer, studying the effect of adding a cap layer, simulating different numbers of multilayer periods, and assessing their impact on maximum reflectance and bandwidth.

Subsequently, we proceed with the deposition process on flat silicon substrates. The deposited samples were



characterized using different tools such as transmission electron microscopy, and specular and angular reflectance measurements. By thoroughly analyzing these data, we extract valuable information regarding roughness/diffusion, the presence of an oxide layer, and the absence of an interface layer. These findings serve as a reference and facilitate the analysis of multilayer gratings in the upcoming chapter.

## Chapter 6

# Investigating the Impact of Multilayer Deposition on High-Density Silica Gratings

In this chapter, we conducted both simulation and experimental investigations on the influence of multilayer deposition on gratings. We utilized the RCWA model to explore the correlation between the optimized multilayer parameters from Chapter.5 and the grating parameters from Chapter.4. Specifically, we examined how variations in grating parameters such as fill factor, grating slope, and grating depth affect the diffraction efficiency of the +1-order. Additionally, we characterized the multilayer gratings after deposition using characterization tools like AFM, TEM, and a metrology beamline which measure the efficiency of the +1-order. The evolution of the multilayer gratings was studied for three different sets of gratings which vary in groove depth and density.

Furthermore, we utilized the RCWA model to simulate the measured +1-order grating efficiency by incorporating parameters derived from AFM profiles. The model was enhanced by integrating the Debye-Waller equation to accurately represent surface roughness. Lastly, we compared the efficiency of our +1-order results for both periodic and aperiodic multilayers with the findings from previous studies conducted for the Solar B mission.

### 6.1 Multilayer on the gratings : state of the art.

Lamellar gratings have been successfully developed as a means to achieve high-resolution EUV spectrometers. For the EUV spectrometer aboard the Solar-B mission, two different periodic Mo/Si multilayer coatings were modeled and deposited on lamellar gratings. These gratings were designed to diffract light at a near-normal incidence within specific wavelength bands: 17–21 nm and 25–29 nm, respectively. The study conducted by [48] demonstrated grating efficiencies ranging between 8% and 12% at the central wavelength. However, maintaining high efficiency across the

desired wavelength band proved challenging due to the narrow bandpass of the multilayer reflectance spectra.

An application of periodic Mo/Si multilayer gratings has been observed in a sounding rocket high-resolution spectrometer experiment described in [12]. The measured diffraction efficiency at near-normal incidence was approximately 10% at a wavelength of 23 nm. Similarly, [104] reported similar efficiencies around 13 nm for Mo/Si multilayer gratings under a 45° incidence angle.

In contrast, blazed gratings offer higher diffraction efficiencies; however, fabricating them with a high groove density on curved substrates, such as toroidal or ellipsoidal grating substrates required for EUV spectro-imaging applications, is extremely challenging. Specifically, Voronov et al. have achieved exceptional diffraction efficiencies using multilayer blazed gratings. They achieved an efficiency of nearly 40% for the first order with an Al/Zr multilayer grating having a groove density of 10,000 lines per millimeter (l/mm) ([105]), and 50% for the second order with a Mo/Si multilayer grating having a groove density of 2525 l/mm ([62]). Unfortunately, the technology employed to produce these high-groove-density blazed gratings is not compatible with curved surface substrates.

Until now, only a limited number of studies have addressed the development of EUV multilayer gratings with broadband efficiency. Previous work has demonstrated that aperiodic multilayer structures can offer efficient broadband reflectance in the EUV spectral range [61]. In a theoretical study conducted by Yang et al. [63], aperiodic multilayer designs on a blazed grating were proposed for operation within the 17–25 nm spectral range. Their simulations, using various combinations of multilayer materials, indicated that it is possible to optimize diffraction efficiency over a wide spectral range by employing aperiodic multilayer coatings.

Another approach to enhancing the bandpass of a multilayer coating is to utilize a periodic stack with a reduced number of periods. However, experimental data for multilayer gratings with a low number of periods have not yet been reported.

Previous research, as highlighted in Gao et al.'s review [64], has revealed that the initial surface profile of a lamellar grating tends to exhibit a trapezoidal shape, and even a slight deviation in the angle of the trapezoid can negatively impact the grating efficiency. Additionally, when a multilayer coating is deposited onto the grating, it typically modifies the surface profile. Specifically, studies on blazed gratings, such as those conducted by Kleineberg et al. [105] and Voronov et al. [62], have reported a smoothing effect on the high-frequency components of the profile as the number of periods in the multilayer coating increases.

## **6.2 Multilayer on the gratings : simulations .**

Although one-dimensional multilayer structures have high efficiencies and find extensive applications, they have a drawback of limited spectral resolution, typically characterized by  $\lambda/\Delta\lambda < 50$  in the EUV range. To overcome this limitation, researchers have proposed two-dimensional multilayer gratings as an alternative approach. These gratings combine the principles of multilayer interferences and grating diffraction, resulting in significantly higher spectral

resolution ( $\lambda/\Delta\lambda > 1000$ ) while maintaining good efficiency. This concept was introduced in the works of [47; 48].

A diffraction multilayer grating possesses various geometric parameters that define its characteristics. These parameters include the number of grooves, groove depth, transverse period, and the evolution of the multilayer structure. When light interacts with a periodic grating, it scatters preferentially in specific directions, which are referred to as diffraction orders. The behavior of light is governed by the principles of grating diffraction (See Sub-section.2.4 and Section.4.4). The zeroth order corresponds to specular reflection, and it is desirable to minimize the energy in this order to enhance a higher diffraction order, typically  $\pm 1$  or  $\pm 2$ , depending on the specific application's requirements.

### 6.2.1 Influence of depth and wavelength on periodic multilayer grating efficiency orders.

In the initial stage, the optimized multilayer thicknesses presented in Table.5.2 were simulated on grating Set#1. The simulation parameters included a fill factor ( $f.f$ ) value of 0.5, a lamellar grating type, and an angle  $\theta$  of  $5^\circ$ . Figure 6.1 depicts the variations in grating depth, wavelength, and reflectance (indicated by the color bar) for the +1 order. It can be observed from Figure 6.1 that the +1 order exhibits maximum efficiency at a grating depth of 5 nm & 21 nm, with a wavelength range of 25 nm to 29 nm.

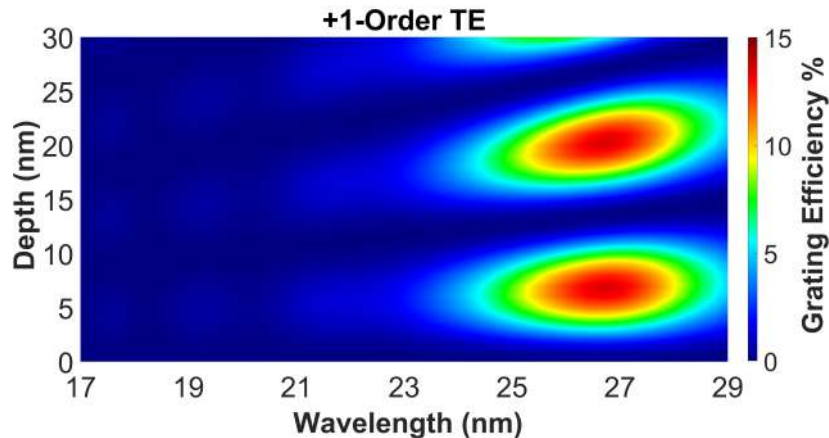


Figure 6.1: +1-Order simulation for wavelength as a function of grating efficiency and grating depth for multilayers on lamellar gratings with  $N = 6$  periods multilayers for gratings set#1.

In contrast, it has been noted that the efficiency of the zero order exhibits its peak value at approximately 15 nm grating depth and 26 nm wavelength within the given wavelength range (refer to Figure C.6 in the appendix). It should be highlighted that the peak efficiency at 27 nm, with a grating depth of 21 nm, is approximately half of the reflectance of the multilayer (refer to Fig.5.3 in Chapter.5). This indicates that the majority of photon flux is diffracted in the +1 and -1 orders, aligning with expectations. This observation serves as confirmation that the multilayer coating has been effectively optimized for this specific grating depth.

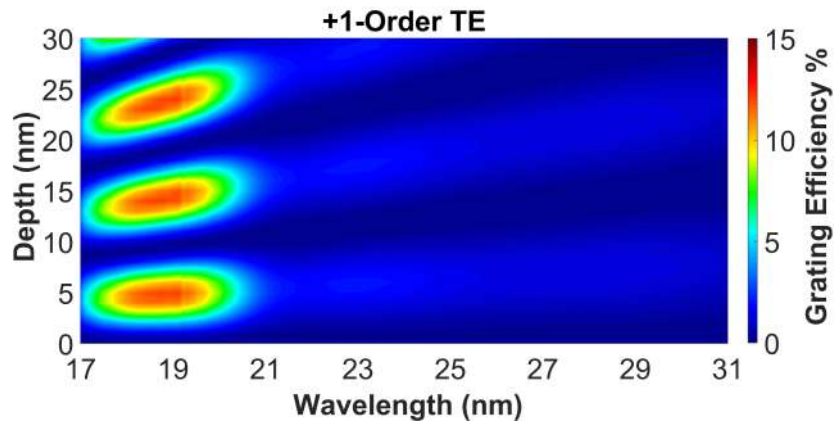


Figure 6.2: +1-Order simulation for wavelength as a function of grating efficiency and grating depth for multilayers on lamellar gratings with  $N = 6$  periods multilayers for gratings set#3.

In the subsequent investigation, we conducted simulations to assess the efficiency of multilayer gratings using Set#3, employing periodic multilayer materials (Al/Mo/SiC) with a total of  $N = 6$  layers. The optimization process utilized IMD to achieve the most favorable broadband reflectance within the wavelength range of 17-21 nm (refer to Fig.5.6 and Table.5.4 in Chapter.5). The optimized thickness values obtained were 3.84 nm, 4.33 nm, and 1.99 nm for Al, Mo, and SiC, respectively. To safeguard the multilayer structure from oxidation, a cap layer consisting of 1 nm SiC was selected and added to the multilayer layer.

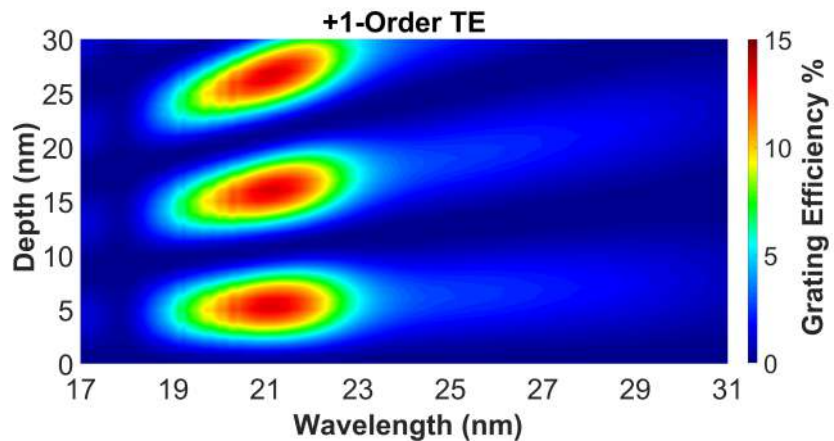


Figure 6.3: +1-Order simulation for wavelength as a function of grating efficiency and grating depth for multilayers on lamellar gratings with  $N = 6$  periods multilayers for gratings set#2.

To verify the performance of the optimized multilayer thickness, RCWA simulations were conducted, as illustrated in Figure 6.2. The simulation parameters used were  $N = 6$ , grating period  $P = 250$  nm, and a FWHM ( $f.f.$ ) value of 0.5. Figure 6.2 shows the efficiency of the +1 order as a function of depth and wavelength. The results indicate that grating Set#3 (with a depth of approximately 5 nm) exhibits good broadband efficiency. However, the groove depth of grating Set#2, which is approximately 16 nm, does not align with the central wavelength of the second peak efficiency at 19 nm. Consequently, it was decided to re-optimize the multilayer thickness for grating Set#2 by shifting

the target wavelength by 2 nm, aiming to achieve the highest broadband reflectance within the wavelength range of 19-23 nm. The revised thickness values of the multilayers were determined to be 5.01 nm, 4.37 nm, and 1.99 nm for Al, Mo, and SiC (refer to Table.5.6 in Chapter.5).

As a result, it was determined that incorporating a 1 nm protection layer of SiC would be suitable for the new re-optimization. Figure 6.2 has been re-plotted as Fig.6.3, considering the newly optimized multilayer thicknesses as indicated in the table, while keeping the other parameters unchanged. In Figure 6.3, it can be observed that the revised multilayer thicknesses exhibit high broadband efficiency for the +1 order in grating Set#2 within the wavelength range of 19 nm to 23 nm.

## 6.2.2 Effect of depth and fill factor on periodic and aperiodic multilayers gratings

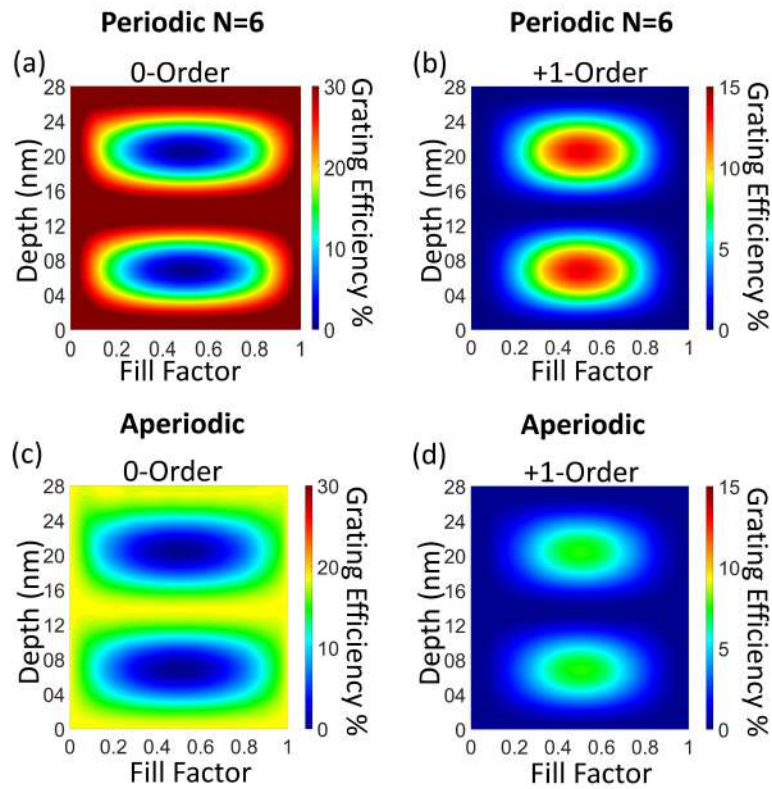


Figure 6.4: Calculated 0-order (a) and +1-order (b) grating efficiency in transverse electric mode at  $\lambda=27\text{nm}$  as a function of fill factor and grating depth. The parameters for the simulation are  $\theta=5^\circ$ ,  $N = 6$ ,  $\alpha=90^\circ$  (lamellar), and  $P=277.8 \text{ nm}$ . The grating efficiency for the aperiodic multilayer with the same grating parameters is plotted in (c) 0-order and (d) +1-order.

Figure 6.4 presents RCWA simulations of a grating coated with a periodic Al/Mo/SiC multilayer ( $N = 6$ ). The simulations focus on the fill factor-dependent transverse electric (TE) efficiency for the 0 and +1 diffraction orders at different grating depths. The remaining simulation parameters are kept constant:  $\theta = 5^\circ$ ,  $N = 6$ ,  $\alpha = 90^\circ$  (lamellar configuration),  $\lambda = 27 \text{ nm}$ , and  $P = 277.78 \text{ nm}$  (correspond to grating set#1).

In Figure 6.4(a) and 6.4(b), it can be observed that the 0-order and +1-order efficiencies exhibit opposite behaviors as the depth varies. A maximum efficiency in the +1 order corresponds to a minimum efficiency in the 0 order. This behavior is in accordance with theoretical expectations, where the 1st order efficiency is optimized when the depth is equal to half (or three halves) of the multilayer period and the profile is symmetric ( $f.f = 0.5$ ). These conditions satisfy the phase and amplitude requirements to suppress the 0-order.

Figure 6.4(b) also demonstrates that there is a significant tolerance for the fill factor parameter. For fill factors ranging from 0.45 to 0.55, the efficiency of the grating's +1 order is reduced by less than 0.4% relative to a fill factor of 0.5. Furthermore, this simulation confirms that the multilayer design is optimal for a depth in the range of 20 to 21 nm, which matches the measured depth of our grating samples.

For the simulations of the 0-order (Figure 6.4(c)) and +1-order (Figure 6.4(d)), an aperiodic multilayer design was employed, using the multilayer thicknesses provided in Table 5.2. These calculations exhibit similar characteristics to the case of a periodic multilayer but with lower efficiency. Additionally, they affirm that our aperiodic design is suitable for the groove depth of our gratings.

### 6.2.3 Impact of depth and grating slope on periodic and aperiodic multilayer gratings

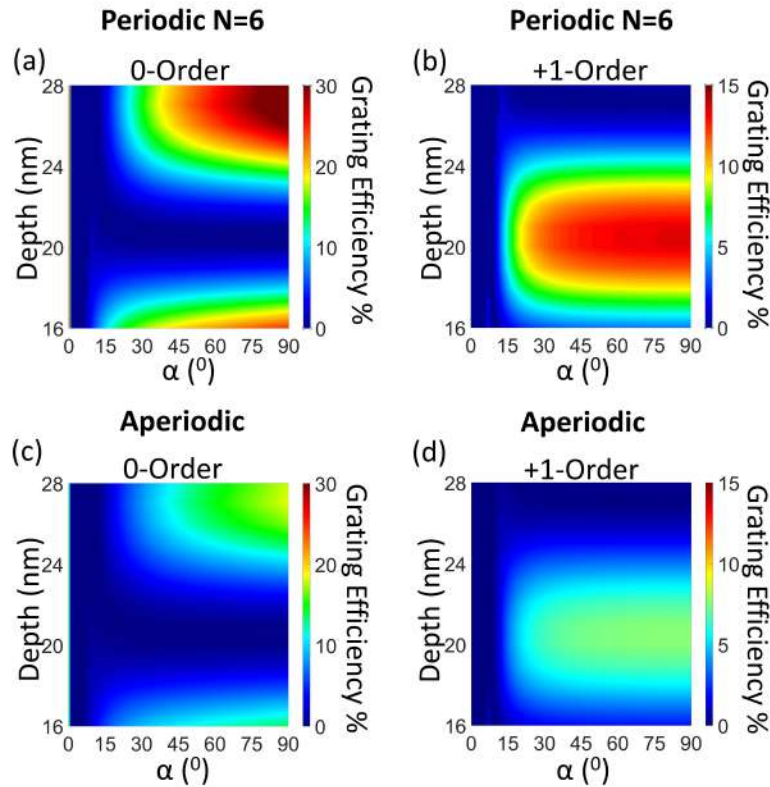


Figure 6.5: Calculated 0-order (a) and +1-order (b) grating efficiency in transverse electric mode at  $\lambda=27\text{nm}$  as a function of  $\alpha$  and grating depth. The parameters for the simulation are  $\theta=5^\circ$ ,  $N = 6$ ,  $f.f=0.5$ , and  $P=277.8\text{nm}$ . The grating efficiency for the aperiodic multilayer with the same grating parameters is plotted in (c) 0-order and (d) +1-order.

Figures 6.5(a) and 6.5(b) display the TE efficiency of the 0-order and +1-order as a function of  $\alpha$  and grating depth ( $d$ ). The simulations are conducted with fixed parameters:  $\theta = 5^\circ$ ,  $N = 6$ , FWHM  $f.f = 0.5$ ,  $\lambda = 27$  nm, and  $P = 277.78$  nm.

The results clearly demonstrate that the efficiencies of the 0-order and +1-order are maximized when  $\alpha = 90^\circ$  (lamellar shape) and decrease as  $\alpha$  decreases (trapezoidal shape). This implies that, when operating under near-normal incidence, the slope of the trapezoidal profile can be considered as a fabrication imperfection that affects the grating's efficiency. For instance, at  $d = 21$  nm, the +1-order efficiency is reduced from 13.38% at  $\alpha = 90^\circ$  to 12.68% at  $\alpha = 45^\circ$ . However, this dependence on  $\alpha$  is no longer significant when the grating operates at angles far from normal incidence. Liu et al. simulated EUV gratings under grazing incidence (gold-coated grating working under total reflection) and reported that the effect of  $\alpha$  on the efficiency is not significant for  $\alpha$  in the range of  $35^\circ - 90^\circ$  [80].

In the case of our multilayer grating at  $45^\circ$  incidence ( $\theta = 45^\circ$ ) for  $\lambda = 18$  nm, simulations reveal that the +1-order efficiency reaches a maximum of 24.49% at  $\alpha = 70^\circ$  and slightly decreases for higher  $\alpha$  values, reaching 24.37% at  $\alpha = 90^\circ$  (lamellar shape). This effect can be attributed to the shadowing effect, which alters the amplitude condition required to nullify the 0-order. Figure 6.5(c) and 6.5(d) depict the grating efficiencies of the 0-order and +1-order, respectively, in the case of an aperiodic multilayer. The overall behavior remains similar to the previous case (periodic multilayer) but with lower peak efficiencies. Interestingly, the effect of  $\alpha$  on the +1-order efficiency is less pronounced. For example, at  $d = 20.5$  nm, the +1-order efficiency is reduced from 7.69% at  $\alpha = 90^\circ$  to 7.33% at  $\alpha = 45^\circ$ .

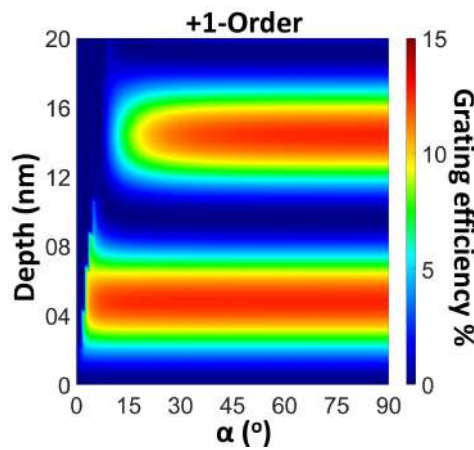


Figure 6.6: TE +1-order grating efficiency calculated at  $\lambda=19$ nm as a function of  $\alpha$  and grating depth. The simulation parameters used are  $\theta=5^\circ$ ,  $N=6$ ,  $f.f=0.5$ , and  $P=250$ nm.

In Fig.6.6, we employed the multilayer parameters described in Table.5.11 of Chapter.5. The simulation was conducted using a multilayer period of  $N = 6$ . The specific wavelengths chosen for the simulation were 19nm, with a grating periodicity of 250nm (corresponding to gratings set#2 and set#3) and FWHM  $f.f$  of 0.5. The results reveal that the peak efficiency of the +1 order at a groove depth of approximately 5nm remains nearly constant when varying  $\alpha$  from  $90^\circ$  (lamellar) to a very low  $\alpha$  of approximately  $5^\circ$  (almost flat substrate). However, for  $d \approx 14$ nm, the



peak efficiency gradually decreases from  $90^\circ$  to around  $15^\circ$  and then diminishes entirely for  $\alpha$  values less than  $15^\circ$ . These findings highlight the interesting characteristics of gratings in Set.#3, particularly in relation to the anticipated challenge of coating the gratings, where the deposition process can alter the slope, as indicated in the TEM figures in the previous literature [72; 62].

## 6.3 Multilayer on the gratings: experimental results

The discussion regarding the material purity for the deposition can be found in Section 3.1.1.2. The appendix includes Tables D.1, D.2, and D.3, where the deposition parameters for each grating set are provided.

For grating Set#1 ( $d \approx 22$  nm,  $P = 277.78$  nm,  $\alpha \approx 47.1^\circ$ ), periodic multilayers were deposited with  $N = 2, 4, 6, 8,$  and  $16$ , while for grating Set#2 ( $d \approx 16.1$  nm,  $P = 250$  nm,  $\alpha \approx 28^\circ$ ) and Set#3 ( $d \approx 5.2$  nm,  $P = 250$  nm,  $\alpha \approx 11.9^\circ$ ), periodic multilayers with  $N = 4, 6, 8,$  and  $10$  were deposited. Additionally, aperiodic multilayers consisting of  $12$  layers were deposited for grating Set#1, while grating Set#2 and Set#3 were deposited with  $18$  and  $24$  layers, respectively.

This section includes a demonstration of the surface profile evolution, as discussed in the respective subsection, utilizing AFM and TEM results. Another subsection focuses on the characterization and modeling of multilayer gratings, specifically using a symmetric multilayer trapezoidal model with an emphasis on modeling the +1 order. The analysis presented in this subsection is thoroughly discussed.

### 6.3.1 Surface profile evolution

Before examining the AFM profiles of the gratings both before and after the depositions, it is important to consider certain factors.

- Firstly, it should be noted that grating set #1 with a density of  $3600$  l/mm is less dense than grating sets #2 and #3, which have a density of  $4000$  l/mm.
- Secondly, grating set #2 exhibits a higher level of roughness when compared to grating sets #1 and #3.
- Additionally, the ratio of multilayer thickness to grating height was approximately  $0.7$  for both grating set #1 and set #3; however, this ratio was approximately  $2$  for grating set #2.

The grating samples Set#1 were characterized using AFM before and after the deposition of the multilayers to analyze the evolution of the surface profile with the number of deposited periods. An example of the grating Set#1 surface morphology before the deposition is shown in Fig.6.7(a). The average grating Set#1 parameters before deposition, including the depth of the groove ( $d$ ), FWHM fill factor ( $f.f$ ), and the slope of the groove ( $\alpha$ ), were computed

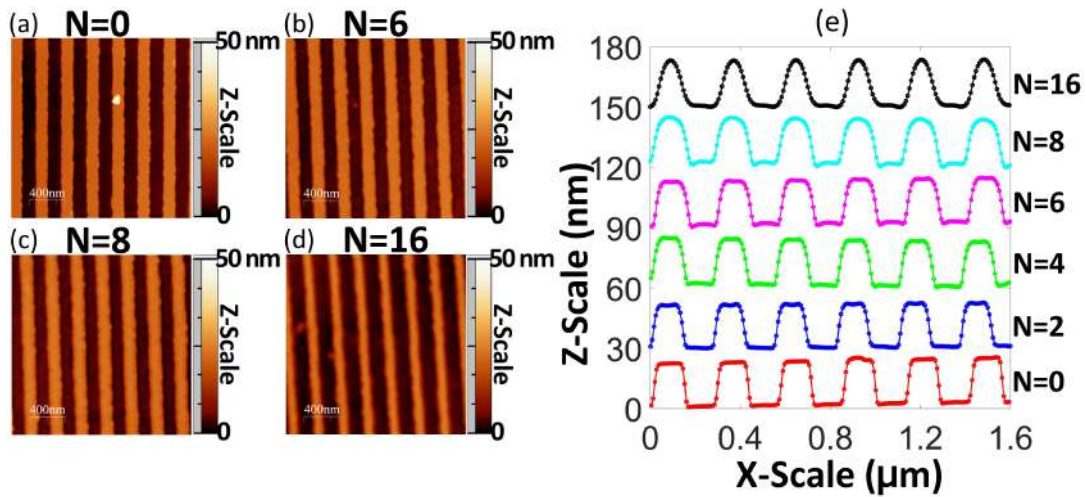


Figure 6.7: The  $2\mu\text{m} \times 2\mu\text{m}$  AFM surface morphology of trapezoidal grating substrate Set#1 before deposition (a), and after deposition of Al/Mo/SiC multilayer with (b)  $N = 6$ , (c)  $N = 8$ , (d)  $N = 16$ . (e) Average groove profiles as a function of the number of periods; every profile is shifted by 30nm in the Z-Scale.  $N = 0$  corresponds to the measurement  $N = 6$  before deposition.

Table 6.1: RMS roughness of the surface assessed by AFM before and after deposition for multilayer grating Set#1.

	$N = 2$	$N = 4$	$N = 6$	$N = 8$	$N = 16$	aperiodic (12 Layers)	average
Top before deposition (nm)	0.4	0.2	0.2	0.2	0.2	0.2	0.23
Top after deposition (nm)	0.5	0.4	0.4	0.4	0.4	0.4	0.42
Bottom before deposition (nm)	0.5	0.3	0.3	0.3	0.3	0.2	0.32
Bottom after deposition (nm)	0.5	0.5	0.5	0.5	0.4	0.4	0.47

from profiles measured on all samples. The average values were found to be 22 nm, 0.51, and  $48.9^\circ$ , respectively, which are consistent with the values reported by Zeiss (see Chapter.4 for more details).

Fig.6.7(b-d) presents the grating surface morphology after deposition for  $N = 6, 8$ , and 16 multilayer periods, respectively. Fig.6.7(e) shows the average surface profile evolution with the number of periods. Each profile is obtained by averaging the entire image along the groove direction, and each profile is shifted by 30 nm in the Z-scale from the previous one. It is noteworthy that the surface shape remains trapezoidal up to  $N = 6$ , and then the top parts of the trapezoid start to curve at  $N = 8$ , gradually transitioning to a top sinusoidal shape as  $N$  increases. AFM analyses also reveal that the depth after multilayer deposition remains nearly equal to the initial depth of the grating as  $N$  increases up to sixteen. This suggests that the deposition rate on the bottom and top parts of the trapezoid is similar.

Table.6.1 presents the surface roughness values of the grating before and after deposition. The average Root Mean Square (RMS) roughness before deposition is 0.23 nm on the top parts and 0.32 nm on the bottom parts. This slight difference in roughness may be attributed to the groove etching process. After deposition, the average RMS roughness increases to 0.42 nm and 0.47 nm for the top and bottom parts, respectively. These results indicate that the roughness at both the top and bottom parts of the grating slightly increases after deposition, and these values

remain consistent regardless of the number of periods.

It is worth noting that the AFM roughness values after deposition are comparable to the average interfacial roughness used in the modeling of the Al/Mo/SiC multilayer, as shown in Tables.B.2, 5.8, and 5.9.

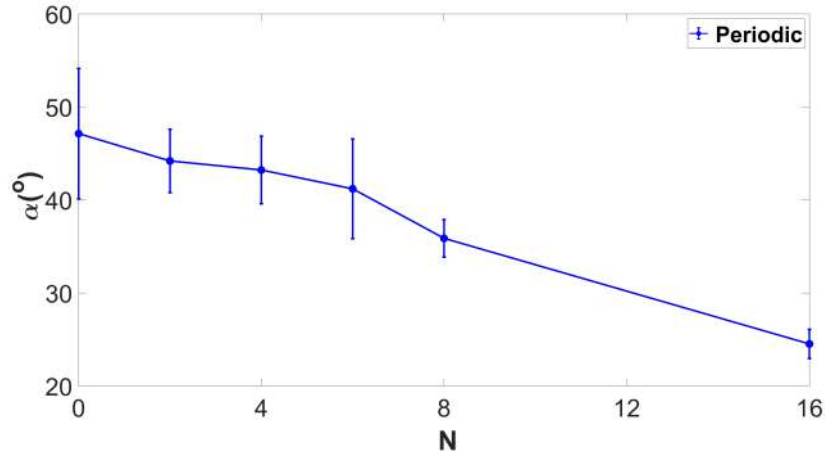


Figure 6.8: variation of the trapeze angle  $\alpha$  with the number of periods deposited on the grating Set#1.

The average values of  $\alpha$  calculated from the AFM profiles (Fig.6.7e) are plotted in Fig.6.8 as a function of the number of multilayer periods ( $N$ ). The error bars represent the standard deviation of the computed  $\alpha$  values. The value of  $\alpha$  before deposition for the trapezoidal grating ( $\approx 48.9^\circ$ ) was averaged across all grating substrates and is displayed at  $N = 0$ . One may notice that the error bar is most prominent when  $N = 0$ . This is because it has been computed based on all the grating profiles before deposition. The error bar at  $N = 0$  represents the dispersion of all calculated  $\alpha$  values derived from an averaged AFM groove profile obtained from different eight measurements conducted before the deposition of the multilayer on the grating's grooves.

Fig.6.8 demonstrates that  $\alpha$  decreases almost linearly as  $N$  increases. A similar trend in the evolution of  $\alpha$  has been reported previously for a trapezoidal grating coated with Mo/Si and analyzed by TEM [72]. Feng et al. observed that the grating shape remained trapezoidal after the deposition of 20 Mo/Si periods, and  $\alpha$  was slightly reduced. It is important to note that in their study, the initial grating depth ( $d \approx 6$  nm) and density (1800 l/mm) were much smaller compared to our case.

Alternatively, Voronov et al. reported a significant smoothing of the grating profile after the deposition of 20 Al/Zr periods on a blazed grating ( $d \approx 10$  nm) with a very high groove density (10,000 l/mm) [62]. They observed that the materials of the multilayer were redistributed on the surface of the blazed grating, with less thickness deposited in convex areas and more thickness in concave areas, as revealed by TEM analysis [62]. This phenomenon can qualitatively explain the evolution of  $\alpha$  presented in Fig.6.8. However, further studies would be needed to determine more precisely the influence of the initial grating parameters and the combination of multilayer materials on the evolution of the grating profile.

Concerning the grating with an aperiodic multilayer design, we observed a trapezoidal surface profile after deposition, characterized by an average  $\alpha$  value of  $28.70^\circ$  with a standard deviation of  $1.53^\circ$ . This value can be compared to the periodic design at  $N = 4$ , which has the same number of layers and a similar total thickness of 57.5 nm (compared to 64.8 nm for the aperiodic design, without considering the surface oxide layer).

The difference in profile shape between the periodic and aperiodic designs may be attributed to variations in individual material thicknesses. It is worth noting that the average  $\alpha$  value for the aperiodic multilayer grating is similar to the  $\alpha$  value obtained for a periodic multilayer with twice the number of layers ( $N = 8$ ).

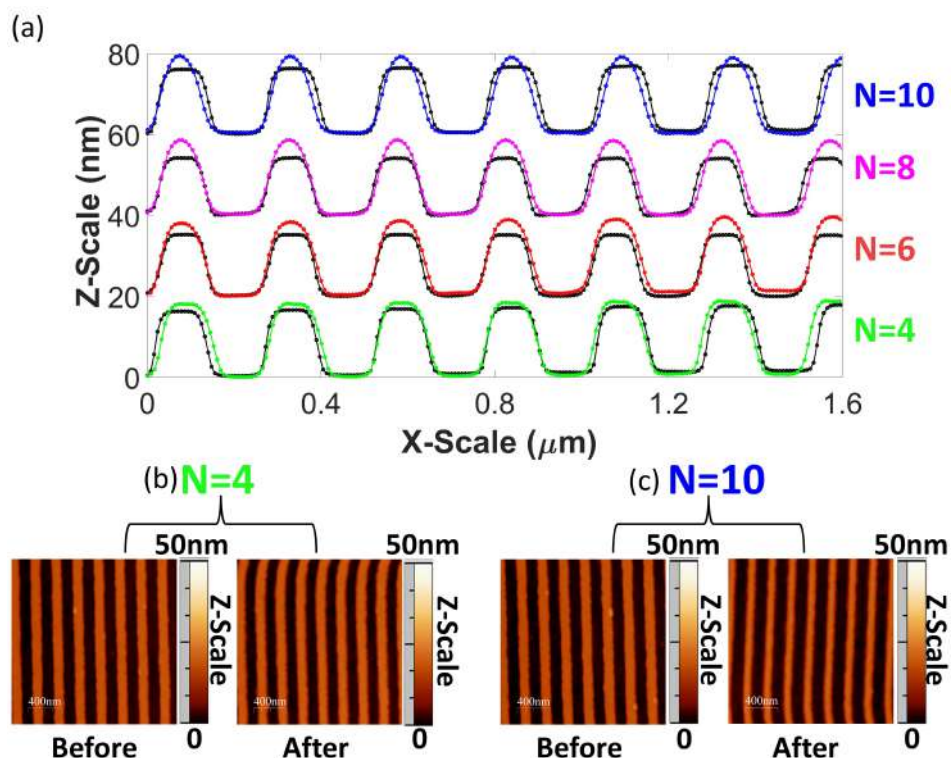


Figure 6.9: (a) Average groove profiles before (on black) and after (on colored) the deposition of Al/Mo/SiC for grating Set#2 as a function of the number of periods; every profile is shifted by 20.0nm in Z-Scale, and The  $2\mu\text{m} \times 2\mu\text{m}$  AFM surface morphology of trapezoidal grating substrate before, and after the deposition of Al/Mo/SiC multilayer with (b)  $N = 4$ , and (C)  $N = 10$ .

Table 6.2: RMS roughness of the surface before and after deposition measured by AFM for grating Set#2.

	Before deposition		After deposition	
	Top	Bottom	Top	Bottom
$N = 4$	0.30nm	0.30nm	0.89nm	0.56nm
$N = 6$	0.44nm	0.48nm	0.91nm	0.52nm
$N = 8$	0.65nm	0.83nm	1.15nm	0.60nm
$N = 10$	0.47nm	0.47nm	1.20nm	0.45nm
aperiodic design 2 (18 Layers)	0.32nm	0.37nm	0.53nm	0.40nm
aperiodic design 3 (24 Layers)	0.38nm	0.48nm	0.69nm	0.69nm
Average	0.43nm	0.49nm	0.90nm	0.54nm

Figure 6.9(a) illustrates the evolution of the grating profile before and after deposition for grating Set #2. In

Table 6.3: RMS roughness of the surface before and after deposition measured by AFM for grating Set#3.

	Before deposition		After deposition	
	Top	Bottom	Top	Bottom
$N = 4$	0.25nm	0.27nm	0.41nm	0.41nm
$N = 6$	0.22nm	0.36nm	0.34nm	0.35nm
$N = 8$	0.20nm	0.24nm	0.31nm	0.31nm
$N = 10$	0.24nm	0.26nm	0.44nm	0.44nm
aperiodic design 4 (18 Layers)	0.27nm	0.36nm	0.28nm	0.28nm
aperiodic design 5 (24 Layers)	0.29nm	0.36nm	0.27nm	0.27nm
Average	0.24nm	0.31 nm	0.34nm	0.34nm

Chapter.4, we have previously examined that the average parameters for grating Set#2 are approximately  $d \approx 16.1$  nm,  $P = 250$  nm, and  $\alpha \approx 28^\circ$ . The profiles after deposition exhibit a sinusoidal shape for all  $N$  values except for  $N = 4$ , which retains a trapezoidal profile. The AFM surface morphology of the grating before and after deposition for  $N = 4$  and  $N = 10$  is displayed in Figure 6.9(b) and Figure 6.9(c), respectively.

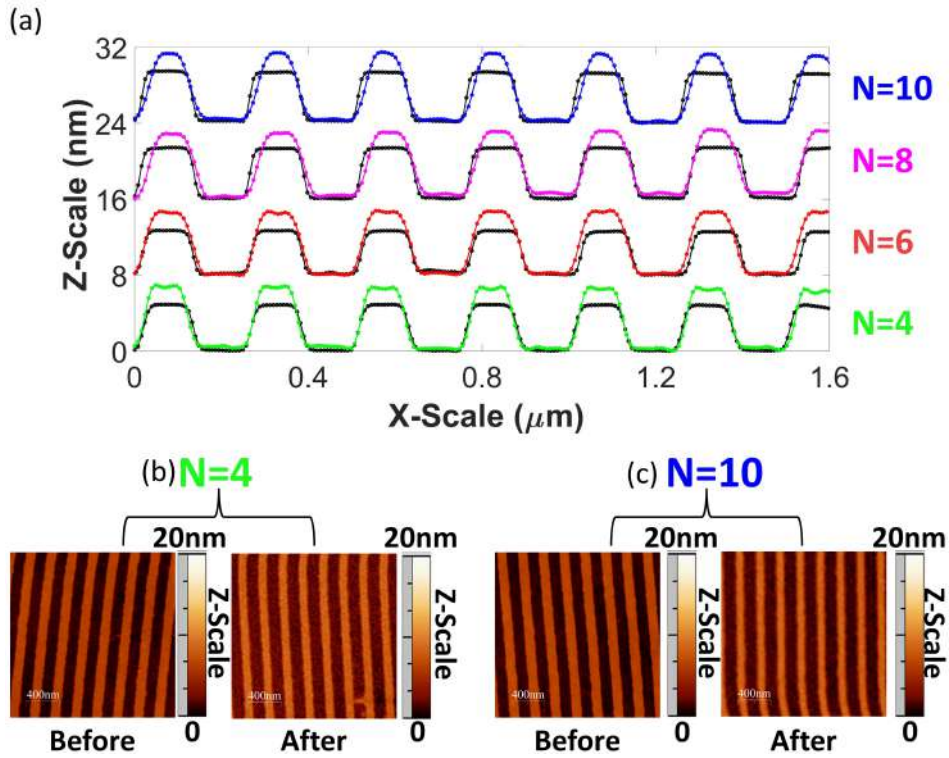


Figure 6.10: (a) Average groove profiles before (on black) and after (on colored) the deposition of Al/Mo/SiC for grating Set#3 as a function of the number of periods; every profile is shifted by 8.0nm in Z-Scale, and The  $2\mu\text{m} \times 2\mu\text{m}$  AFM surface morphology of trapezoidal grating substrate before, and after the deposition of Al/Mo/SiC multilayer with (b)  $N = 4$ , and (c)  $N = 10$ .

Figure 6.10(a) depicts the grating profiles of grating Set#3 before and after deposition. In Chapter.4, the average parameters for grating Set#3 were discussed, with values of approximately  $d \approx 5.2$  nm,  $P = 250$  nm, and  $\alpha \approx 11.9^\circ$ . It is evident that the profile after deposition maintains a trapezoidal shape for  $N = 4, 6$ , and  $8$ . However, for  $N = 10$ , the grating profile transitions towards a sinusoidal shape. Figure.6.10(b) and Figure 6.10(c) display the AFM surface



morphology before and after deposition for 4 and 6 periods, respectively.

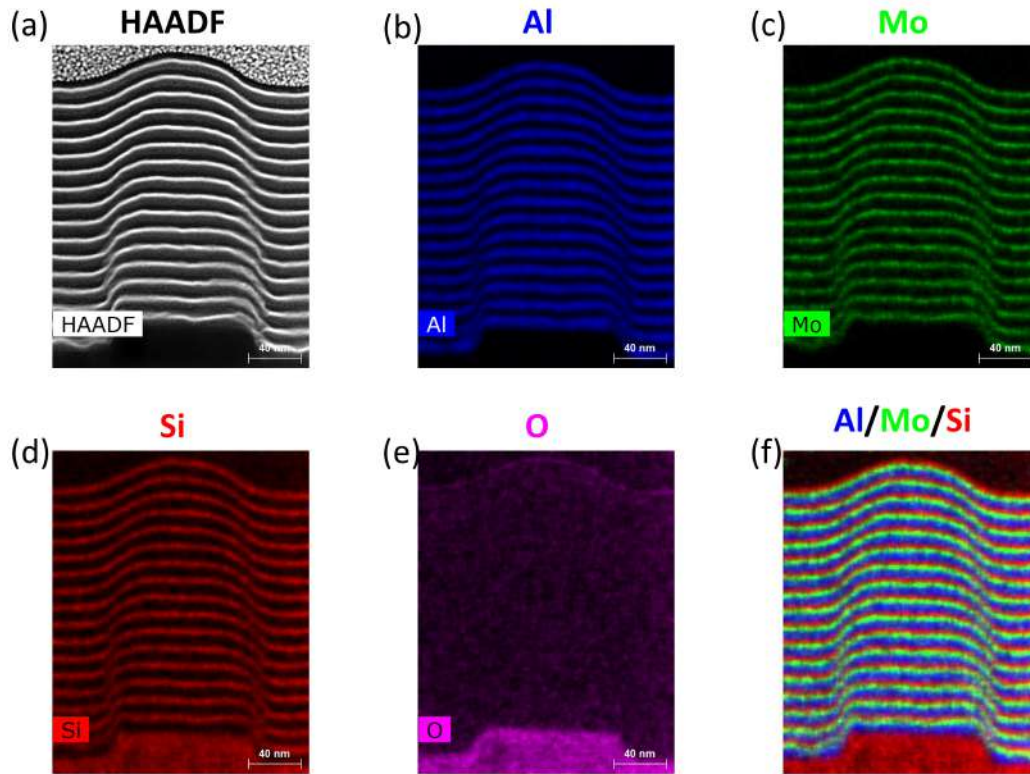


Figure 6.11: TEM analyses of periodic multilayer grating ( $N = 16$ ) for grating Set#1: (a) HAADF, and EDX images for (b) Al, (c) Mo, (d) Si, (e) O, and (f) Al/Mo/Si.

TEM analysis of the three grating sets yielded valuable insights into the multilayer formation, aligning with the AFM analysis findings. The HAADF images revealed that the bright lines corresponded to high-density Mo layers, while the dark lines represented low-density Al and SiC layers. These HAADF images visually confirmed the multilayer structure on the gratings.

In addition, EDX-STEM analysis was employed to individually identify the locations of specific atoms. This analysis allowed for separate visualization of the elements Al, Mo, Si, and O.

These TEM-HAADF and EDX-STEM images analysis provide a further understanding of the structural characteristics and elemental composition of the deposited multilayers.

Figure.6.11 presents HAADF and EDX-STEM images of the periodic Al/Mo/SiC multilayer gratings in Set#1 with  $N = 16$ . In Figure 6.11(a), it can be observed that the trapezoidal grating is asymmetric. Initially, at  $N = 1$ , the Al deposition appears well, but interdiffusion is evident between Mo and SiC. The grating profile maintains its trapezoidal shape from  $N = 1$  to  $N = 7$ . However, from  $N = 8$  to  $N = 10$ , the grating profile transitions to a rounded shape at the edges. At  $N = 11$ , the grating profile transforms into a top sinusoidal shape. The EDX-STEM images in Fig.6.11(b-f) demonstrate the quality of the deposition of the three materials without significant diffusion. Figure.6.11(e) reveals the presence of an oxidation layer at the top of the multilayers.

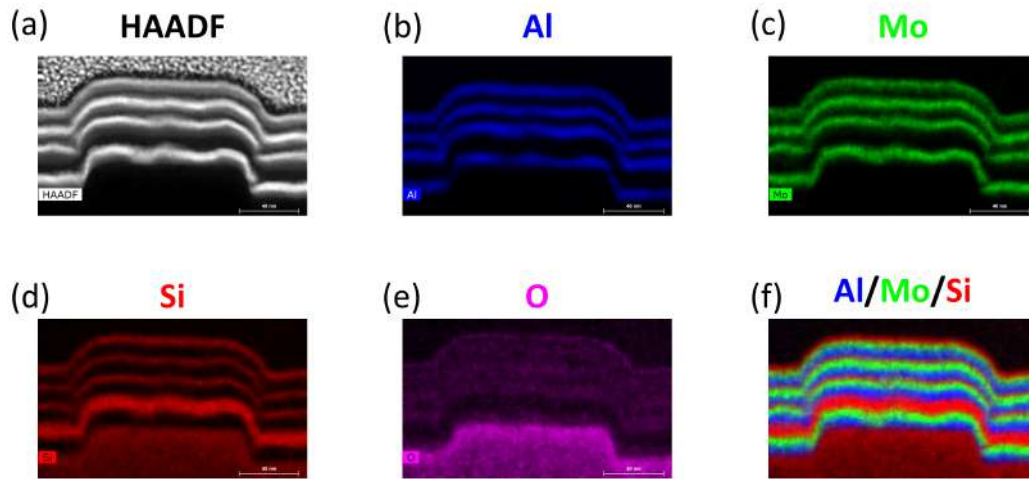


Figure 6.12: TEM analyses of periodic multilayer grating (12 layers) for grating Set#1: (a) HAADF, and EDX images for (b) Al, (c) Mo, (d) Si, (e) O, and (f) Al/Mo/Si.

Figure 6.12 illustrates HAADF and EDX-STEM images of the aperiodic Al/Mo/SiC multilayer gratings in Set#1 with 12 layers. The images clearly reveal the asymmetry of the trapezoidal grating. In Fig.6.12(b), a discontinuity is observed along the Al layer (layer-1). The target thickness for this layer is 4.99 nm, which is less than the target thickness of the Al layer (8 nm) in the periodic multilayer. Furthermore, in Figure 6.12(c,f), significant roughness is observed between the Al layer (layer-1) and the Mo layer (layer-2). This roughness also persists between the Mo layer (layer-2) and the SiC layer (layer-3). Although some roughness is present between the SiC layer (layer-3) and the Al layer (layer-4), it mostly disappears in the other layers from the top of the Al layer (layer-4) to the SiC layer (layer-12). Overall, the final aperiodic multilayer gratings still exhibit a trapezoidal shape profile.

Fig.6.13 showcases HAADF and EDX-STEM images of the periodic Al/Mo/SiC multilayer gratings in Set#2 with  $N = 10$ . In Fig.6.13(a), it is evident that the trapezoidal grating exhibits asymmetry. The trapezoidal shape is maintained from  $N = 1$  to  $N = 3$ . However, from  $N = 4$  to  $N = 5$ , the grating profile transitions to a rounded shape at the edges. At  $N = 6$ , the grating profile transforms into a top sinusoidal shape. Additionally, as  $N$  increases, the position of the top multilayer grating profile shifts to the right.

The EDX-STEM images in Figure 6.13(b-f) reveal that the Al, Mo, and SiC depositions appear well without any noticeable interdiffusion or roughness on the top, bottom, or right slope of the trapezoidal gratings. However, interdiffusion is observed on the left side of the slope between the three deposited materials. Furthermore, Fig.6.13(e) demonstrates the presence of an oxidation layer at the top of the multilayers.

Figure.6.14 showcases HAADF and EDX-STEM images of the periodic Al/Mo/SiC multilayer gratings in Set.#3 with  $N = 10$ . In Fig.6.14(a), it is evident that the trapezoidal grating exhibits clear asymmetry and is inclined towards the left. The trapezoidal shape is maintained from  $N = 1$  to  $N = 6$ . At  $N = 7$ , the grating profile transforms into a top sinusoidal shape.

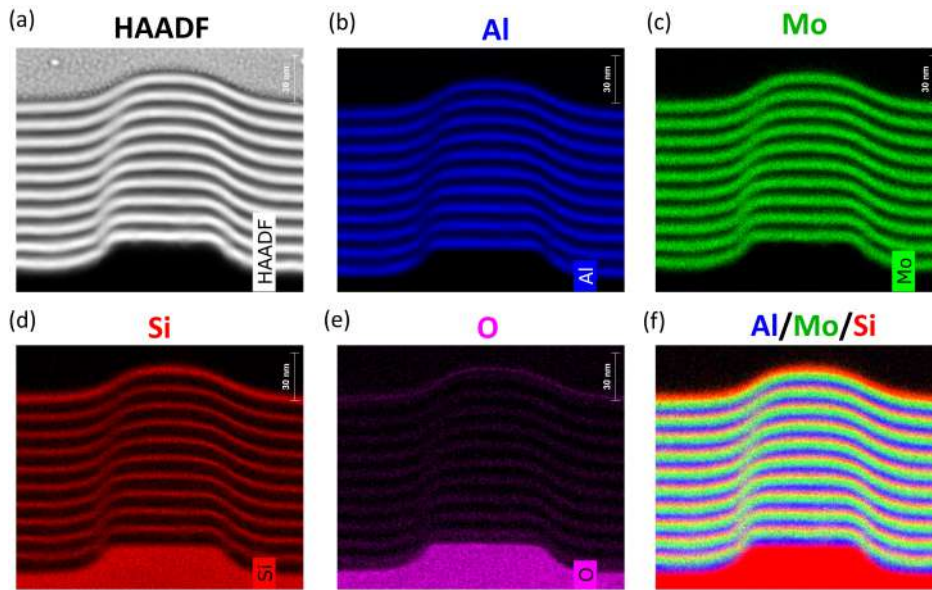


Figure 6.13: TEM analyses of periodic multilayer grating ( $N = 10$ ) for grating Set#2: (a) HAADF, and EDX images for (b) Al, (c) Mo, (d) Si, (e) O, and (f) Al/Mo/Si.

In Fig.6.14(b-f), the Al deposition appears to be well-preserved. However, significant roughness and interdiffusion are observed between the Mo and SiC layers. From  $N = 2$  to  $N = 10$ , minimal roughness or interdiffusion is observed on the top, bottom, and slope of the multilayer gratings.

1. No interface layer is observed between the deposited materials, indicating good interface quality at the atomic level.
2. The individual layers exhibit clear definitions on both the bottom and top of the grooves in all gratings. In most cases, they are also well-defined on the slope of the groove. However, for grating Set#2 (Fig.6.13), interdiffusion appears to occur on the left side, affecting the clarity of layer definition.
3. An oxide layer is present at the top of the multilayer grating, indicating surface oxidation during the deposition process.
4. The multilayer evolves from a trapezoidal shape to a sinusoidal shape towards the top, indicating a change in the growth mechanism, which is consistent with the AFM results.
5. The grating trapezoidal shape is asymmetric, suggesting non-uniform deposition or substrate effects.

### 6.3.2 Characterization and modeling

The +1-order diffraction efficiencies of the six different multilayer grating Set#1 samples were experimentally measured as a function of wavelength at the Soleil synchrotron. The measurement results are presented in Fig.6.15 and Fig.6.16, corresponding to an incidence angle of  $\theta = 5^\circ$  and  $\theta = 45^\circ$ , respectively. Additionally, to facilitate comparison and verification, the +1-order diffraction efficiencies of the samples were plotted in a logarithmic scale, as shown



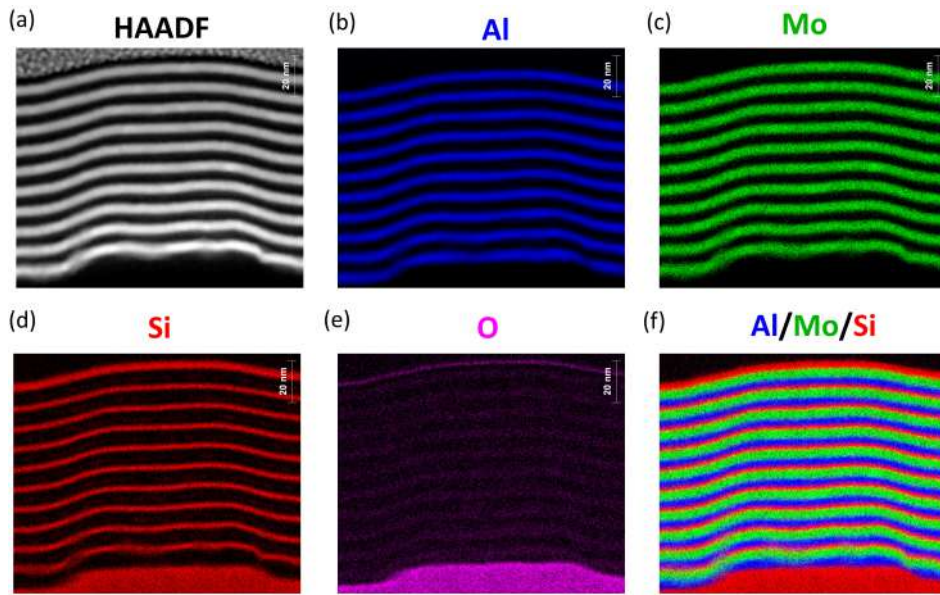


Figure 6.14: TEM analyses of periodic multilayer grating ( $N = 10$ ) for grating Set#3: (a) HAADF, and EDX images for (b) Al, (c) Mo, (d) Si, (e) O, and (f) Al/Mo/Si.

in appendix Fig.C.9 and appendix Fig.C.10. These figures provide insights into the spectral response and efficiency performance of the multilayer gratings under different experimental conditions.

Figures 6.15(a-c) and 6.16(a-c) illustrate the experimental diffraction peak efficiencies as a function of the number of periods for the multilayer grating samples. It can be observed that the peak efficiency increases and the peak narrows as the number of periods increases from 2 to 6. This trend is consistent with the evolution of the multilayer reflectance spectra as shown in Fig.6.17. However, for a higher number of periods ( $N = 8$  and 16), the experimental peak efficiency starts to decrease, as depicted in Fig.6.15(d,e) and Fig.6.16(d,e). This behavior deviates from the expected multilayer response depicted in Fig.6.17, suggesting that the evolution of the grating profile during deposition may be a contributing factor. Indeed, AFM measurements indicate that the surface profile remains trapezoidal up to  $N = 6$  and begins to deteriorate for  $N = 8$  periods and beyond.

RCWA simulations were conducted to model each sample using the same multilayer grating model for both incidence angles ( $\theta = 5^\circ$  and  $45^\circ$ ). The simulation results are presented in Fig.6.15 and Fig.6.16. Table.6.4 provides the grating parameters used for fitting the +1 order measurements. The layer thicknesses determined previously for the periodic and aperiodic multilayers (see Tables.B.2,5.8, and 5.9) were utilized, along with a 1.7 nm  $\text{SiO}_2$  layer as the top oxide layer for all grating models. The interfacial roughnesses were not included in the RCWA simulations. The polarization factor used in the simulations was determined from the measurements of the multilayer samples (96% s-polarization, as described previously in Section.3.1.4.5 in Chapter.3). It is important to note that the effective  $f.f$  reported in Table.6.4 was determined from AFM measurements, and the fitted  $\alpha$  values are approximately consistent with the  $\alpha$  values measured by AFM before deposition. This suggests that the diffraction efficiencies of the gratings are influenced by the pre-deposition grating profile.

## +1 Order @ $\theta=5^\circ$

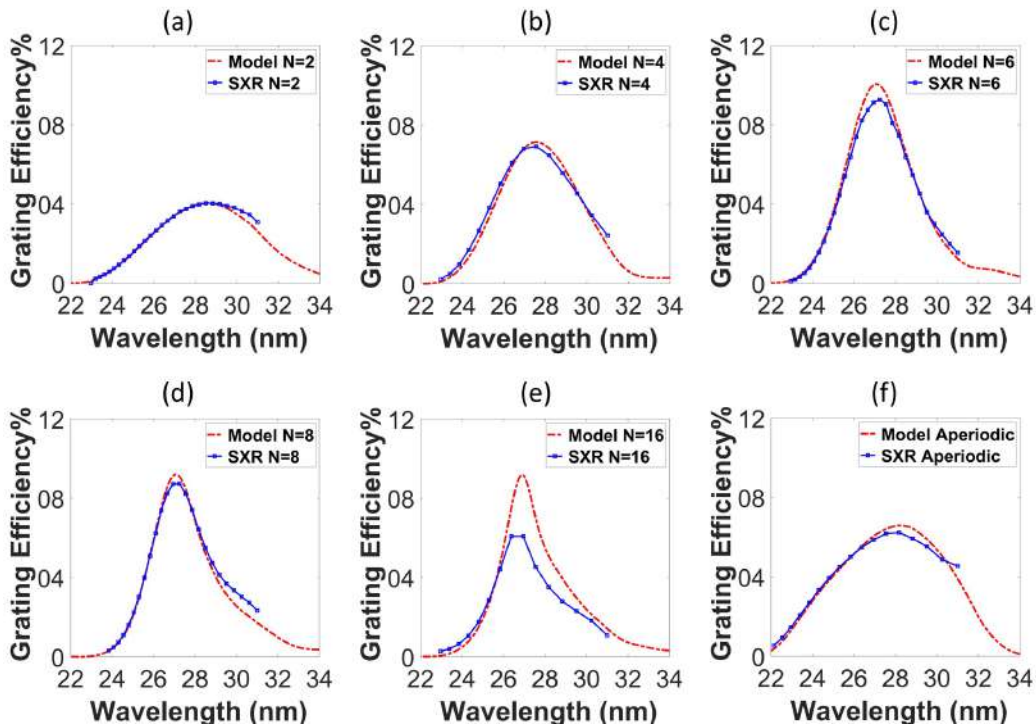


Figure 6.15: Measured and modeled +1 order diffraction efficiency of the multilayer gratings Set#1 at  $\theta=5^\circ$ : (a)  $N = 2$ , (b)  $N = 4$ , (c)  $N = 6$ , (d)  $N = 8$ , (e)  $N = 16$ , and (f) aperiodic.

As shown in Fig.6.15 and Fig.6.16, SXR measurements extend from the Al  $L_{2,3}$  absorption edge ( 17.2 nm) to 31 nm. For longer wavelength ( $\lambda>31\text{nm}$ ) the photon flux delivered by the beamline was too low to obtain reliable measurements. This wavelength range was sufficient to measure the peak efficiency for all samples, but the peak width was out of reach for some samples. Therefore, we used the simulation models shown in Fig.6.15 and Fig.6.16 to estimate the peak bandwidth. Figure 6.17 shows the evolution of the experimental peak efficiency and the bandwidth computed from the model as a function of the number of periods. It may be seen in Fig.6.17(a) and Fig.6.17(b) that the peak efficiency linearly increases up to  $N = 6$  and then starts decreasing, while the bandwidth reduces as the number of periods raises. These results clearly show that there exists an optimum number of periods ( $N = 6$  in this case) after which the efficiency does not improve anymore and the bandwidth continues to diminish. It also confirms experimentally that one can tune the number of periods to adjust the peak bandwidth to the desired value. Increasing the bandwidth (by reducing the number of periods) leads however to a lower peak efficiency (see Fig.6.17). The SXR measurements shown in Fig.6.15f and Fig.6.16f demonstrate however that it is possible to overcome this limitation by using an aperiodic multilayer design. We obtained a bandwidth of 5.1 nm with the aperiodic multilayer grating in near-normal incidence (Fig.6.15f) with a peak efficiency higher than 6%. As shown in Fig.6.17, this value of bandwidth is not attainable with a periodic design. It is worth noting that, despite the complexity of the multilayer design, the simulation models in the case of aperiodic multilayer agree very well with the experimental data at  $5^\circ$  and

### +1 Order @ $\theta=45^\circ$

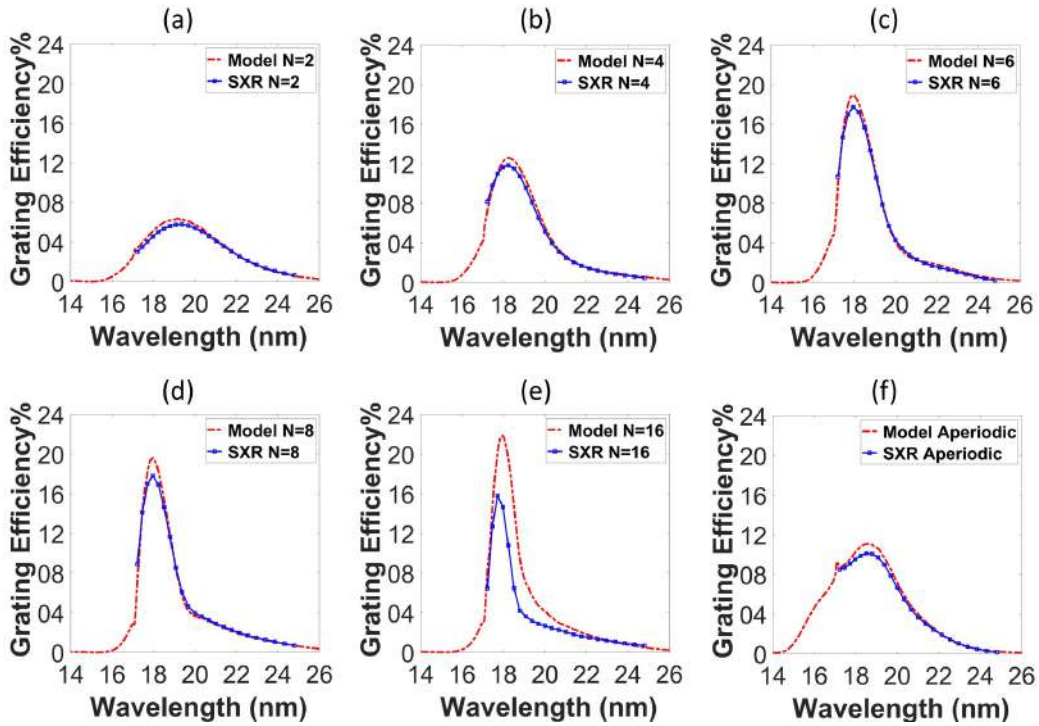


Figure 6.16: Measured and modeled +1 order diffraction efficiency of the multilayer gratings Set#1 at  $\theta=45^\circ$ : (a)  $N = 2$ , (b)  $N = 4$ , (c)  $N = 6$ , (d)  $N = 8$ , (e)  $N = 16$ , and (f) aperiodic.

$45^\circ$  (see Fig.6.15f and Fig.6.16f). Compared to previous literature [12; 19], this aperiodic multilayer grating provides a unique combination of peak efficiency and bandwidth.

The fitting results are shown in Fig.6.15 and Fig.6.16 exhibit good agreement between the model and the measured data for all samples, except for  $N = 16$ . It is worth noting that while the grating profile evolves with each period (as shown in Fig.6.7), the model with a constant average profile is sufficient to accurately simulate the diffraction efficiency as long as the profile remains trapezoidal. However, the significant discrepancies between the model and experimental data for  $N = 16$  (Fig.6.15e and Fig.6.16e) indicate that this simple model is no longer valid when the grating profile changes to sinusoidal patterns.

Table 6.4: Grating Set#1 parameters used to simulate +1 order efficiencies in Fig.6.15 and Fig.6.16.

	$N = 2$	$N = 4$	$N = 6$	$N = 8$	$N = 16$	aperiodic (12 Layers)
depth (nm)	22.4	22.3	21.8	22.7	22.5	21.2
$\alpha$ ( $^\circ$ )	42	42	49	41	41	43
effective ( $f.f$ )	0.45	0.47	0.49	0.49	0.39	0.48

The diffraction efficiencies of gratings Set#2 and Set#3 samples were measured at a near-normal incident angle of  $\theta = 5^\circ$ , as depicted in Fig. 6.18 and Fig. 6.19, respectively. Subsequently, the RCWA method was employed to model the diffraction using the grating parameters obtained from Table 6.5 for grating Set#2 and Table 6.6 for grating

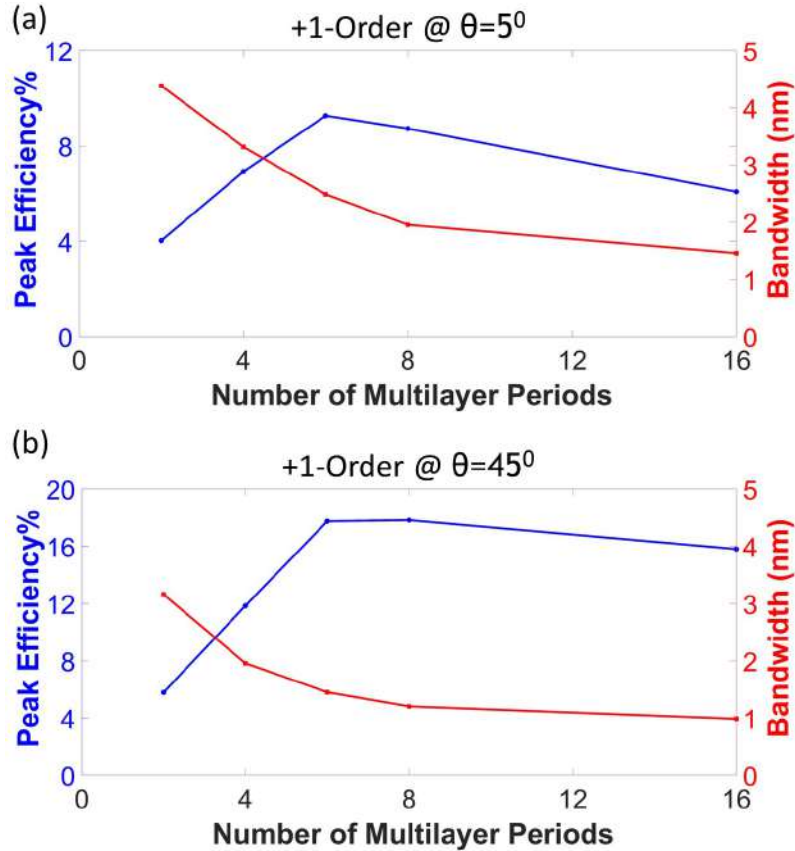


Figure 6.17: +1 order maximum efficiency and bandwidth for SXR at (a)  $\theta=5^\circ$  and (a)  $\theta=45^\circ$ .

Table 6.5: Grating Set#2 parameters used to simulate +1 order efficiencies in Fig.6.18.

	d (nm)	$\alpha$ ( $^\circ$ )	$f.f$ (FWHM)
$N = 4$	17.6	26.7	0.46
$N = 6$	17.6	25.1	0.43
$N = 8$	17.8	23.7	0.41
$N = 10$	18.0	23.6	0.36
aperiodic design 2	17.8	25.0	0.42
aperiodic design 3	17.0	23.4	0.42

Set#3. The thicknesses of the materials in the periodic deposition were obtained from Table 6.5 for grating Set #2 and Table 6.6 for grating Set#3. For the aperiodic designs, the multilayer thicknesses were obtained from Table.B.3 in the appendix for grating Set#2 and Table.B.4 in the appendix for grating Set#3, respectively. The thickness of the oxidation layers used in the RCWA models was set to 1.0 nm for all those cases.

It is important to note that the parameters  $\alpha$  and FWHM  $f.f$  in Table 6.5 and Table 6.6 represent average values computed from the grating profiles after deposition, as observed in Fig.6.18 and Fig.6.19, respectively. Additionally, the values of d were estimated from the RCWA model by adjusting the grating depth until a satisfactory agreement was achieved between the measured and simulated +1-order diffraction patterns. Moreover, the Debye-Waller roughness, as described by equation (6.1), was applied to the RCWA simulation of the +1-order diffraction,

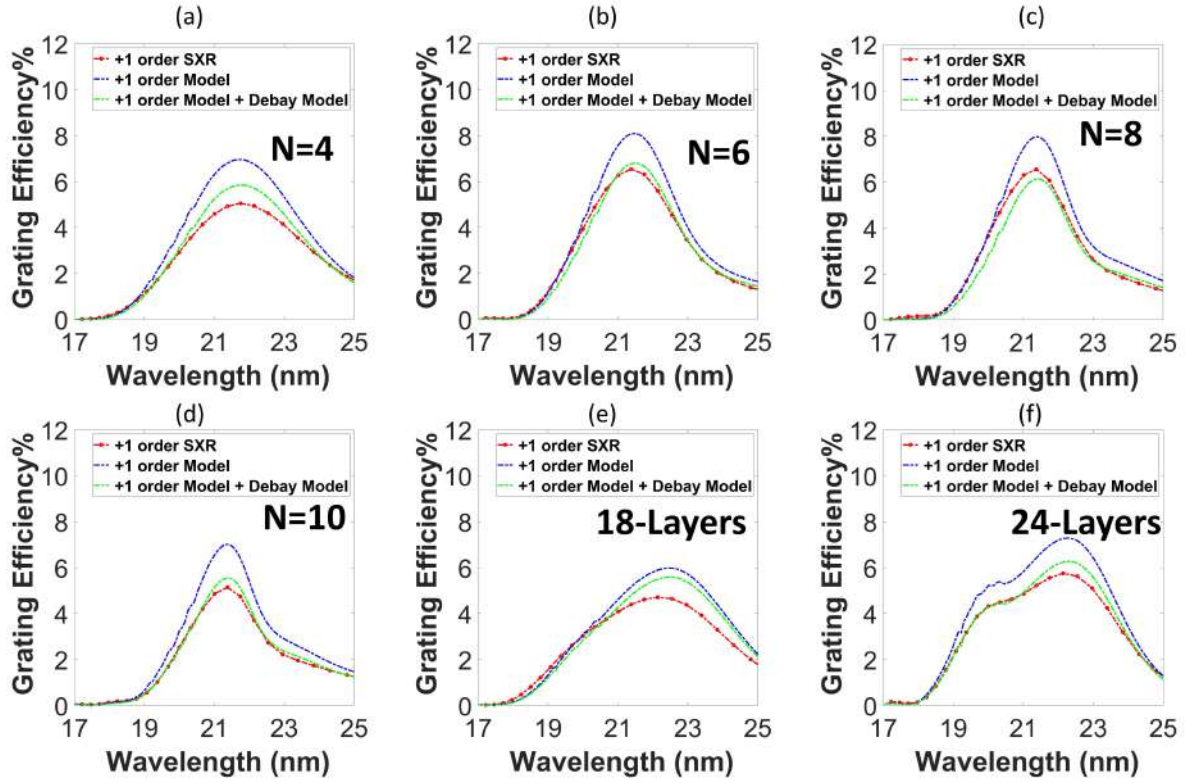


Figure 6.18: Measured and modeled +1 order diffraction efficiency of the multilayer grating set#2 at  $\theta=5^\circ$ : (a)  $N = 4$ , (b)  $N = 6$ , (c)  $N = 8$ , (d)  $N = 10$ , (e) 18-layers aperiodic, and (f) 24-layers aperiodic.

where  $\sigma_{DW}$  represents the roughness parameter.

$$E_{target} = E_0 \times \exp - \left[ \frac{4\pi \cos(\theta)\sigma_{DW}}{\lambda} \right]^2 \quad (6.1)$$

The  $\sigma_{DW}$  is the average roughness of the top and bottom of the grating after the deposition according to the tables in the appendix section. The Debye-Waller model shows small changes in the RCWA model.

In the case of periodic multilayers, as depicted in Fig.6.18(a-d) for multilayer gratings Set#2, the peak efficiency shows an increasing trend from  $N = 4$  to  $N = 6$ , followed by a decrease from  $N = 6$  to  $N = 10$ . As shown in Fig.6.9(a), the grating profile remains trapezoidal only at  $N = 4$ , transitioning to a sinusoidal shape from  $N=6$  to  $N=10$ . Conversely, aperiodic design 2 (18-layers) and design 3 (24-layers) exhibit wider bandwidth compared to periodic multilayers, as shown in Fig.6.18(e-f), respectively. Additionally, the Debye-Waller model enhances the RCWA model, aligning with the +1-order measurements and indicating the influence of roughness on +1-order diffraction. Table.6.5 displays the parameters utilized in the RCWA model, while Table.6.2 presents the parameters used to determine the average Debye-Waller factor for the roughness. Typically, this factor is computed by averaging the roughness values from the bottom and top of the grooves after deposition. The roughness values on the top and bottom of the grooves before deposition were retained for comparison.

In the context of periodic multilayers illustrated in Fig.6.19(a-d) for multilayer gratings Set#3, the peak efficiency



Table 6.6: Grating Set#3 parameters used to simulate +1 order efficiencies in Fig.6.19.

	d (nm)	$\alpha(^{\circ})$	$f.f$ (FWHM)
$N = 4$	7.2	12	0.4
$N = 6$	7.0	9.6	0.44
$N = 8$	7.2	9.1	0.44
$N = 10$	7.2	9.3	0.37
aperiodic design 4	6.2	9.0	0.38
aperiodic design 5	5.8	8.9	0.42

demonstrates an increase from  $N = 4$  to  $N = 8$ , followed by a decrease from  $N = 8$  to  $N = 10$ . Throughout this range (from  $N = 4$  to  $N = 10$ ), the grating profile maintains a trapezoidal shape, as depicted in Fig.6.10. However, at  $N = 10$ , a transition is observed, with the grating profile shifting from trapezoidal to sinusoidal. In contrast, aperiodic designs 4 (18-layers) and 5 (24-layers) exhibit wider bandwidth compared to the periodic multilayers, as shown in Fig.6.19(e-f). The DW model improves the RCWA model and aligns with the +1-order measurements. However, the enhancement achieved by the DW model is minimal this time, possibly due to the low roughness values measured by AFM (listed in Table.6.2). The deposition of multilayers on Set#3 leads to an increase in groove depth compared to the pre-deposition state, as observed in Fig.6.10. It is important to note that Set#3 gratings exhibit a low average groove depth of 5nm, a low  $\alpha$  value of 11.9 degrees, and a high groove periodicity of 250nm (see Table.4.4 in Chapter.4), resulting in a nearly flat surface appearance. The difference in groove depth measured by AFM before and after deposition can be attributed to the low depth and high groove density. Table.6.3 presents the parameters used to determine the average DW factor for the roughness.

Fig.6.20(a) and Fig.6.20(b) demonstrate the variations in peak efficiency and bandwidth with the number of multilayer periods for grating Set#2 and Set#3, respectively. The results indicate that the peak efficiency for both grating types increases from  $N=4$  to  $N=8$ , but starts to decrease at  $N=10$ , as depicted in Fig.6.20(a). In contrast, the bandwidth shows a linear reduction from  $N=4$  to  $N=10$ , as illustrated in Fig.6.20(b).

## 6.4 Three sets of multilayer gratings fulfilling Solar C mission requirements

### 6.4.1 Comparative Analysis with Previous Literature (Solar B mission)

In this subsection, we present a comparison of our obtained results for periodic and aperiodic designs across three sets of multilayer gratings with the previous work conducted for the Solar B mission. Reference [12] demonstrates the achieved efficiency of Mo/Si multilayer gratings for the Solar B mission within two specific wavelength ranges: 17-22nm and 25-29nm. Additionally, reference [19] provides a comprehensive description of the multilayer parameters used for the Solar B mission.

In Fig.6.21, we present a comparison of the measured grating efficiency for Set#1 at near-normal incidence, considering  $N = 4$ ,  $N = 6$ , and aperiodic coatings. To provide context, we have included experimental data from Seely

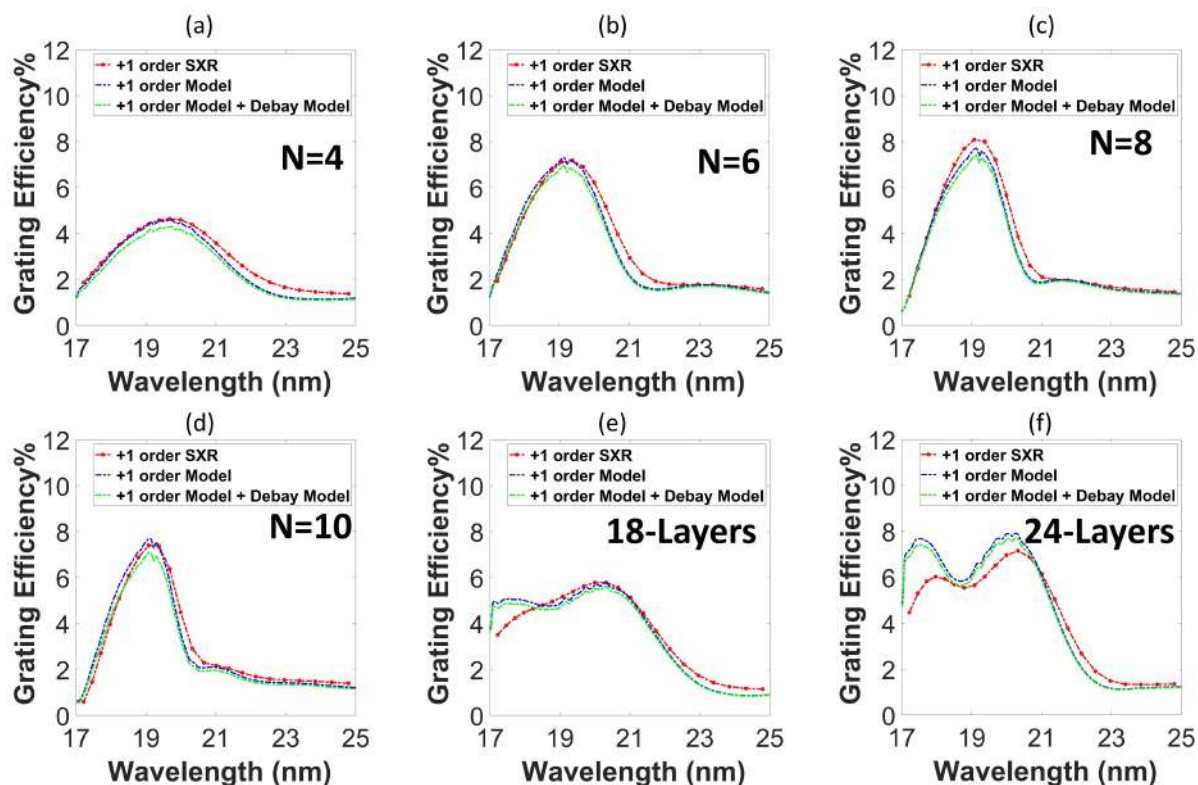


Figure 6.19: Measured and modeled +1 order diffraction efficiency of the multilayer grating set#3 at  $\theta=5^\circ$ : (a)  $N = 4$ , (b)  $N = 6$ , (c)  $N = 8$ , (d)  $N = 10$ , (e) 18-layers aperiodic, and (f) 24-layers aperiodic.

et al.[12], which corresponds to a Mo/Si multilayer grating with 20 periods. The results by Seely et al. demonstrate a peak efficiency of 7.88% at 27 nm with a bandwidth of 2.64 nm. Notably, the 6-period Al/Mo/SiC grating Set#1 exhibits higher efficiency within the range of 25.5 to 29 nm, reaching a peak of 9.27%. Moreover, we compare the measured data of the 12-layer aperiodic coating Set#1 with the periodic coating Set#1 at  $N = 4$ , which contains an equal number of layers. Both gratings demonstrate similar peak efficiency, but the aperiodic coating significantly enhances the bandwidth, reaching 5.10 nm compared to 3.32 nm for  $N = 4$ . Remarkably, the bandwidth achieved with the aperiodic multilayer grating in Set#1 is nearly double the previous results obtained by Seely et al. Our findings confirm the potential of aperiodic multilayer gratings in Set#1 as promising components for high-resolution EUV spectroscopy applications across a wide wavelength range.

In the wavelength range of 17-21nm, Seely et al.[12] achieved a peak efficiency of 8% with a bandwidth of 1.07nm, as shown in Fig.6.22. For grating Set#2, the 8-period Al/Mo/SiC design demonstrated a peak efficiency of 8.1% with a bandwidth of 1.76nm. Conversely, the Al/Mo/SiC aperiodic design 3 (consisting of 24 layers) achieved a wider bandwidth of 3.91nm while maintaining a high-efficiency plateau.

For grating Set#3, efficient performance was observed within the 19-23nm wavelength range. The 6-period multilayer exhibited a peak efficiency of 6.54% with a bandwidth of 2.22nm. The aperiodic design 5 (comprising 24 layers) achieved a broader bandwidth of 3.71nm with high band efficiency. These results obtained from aperiodic

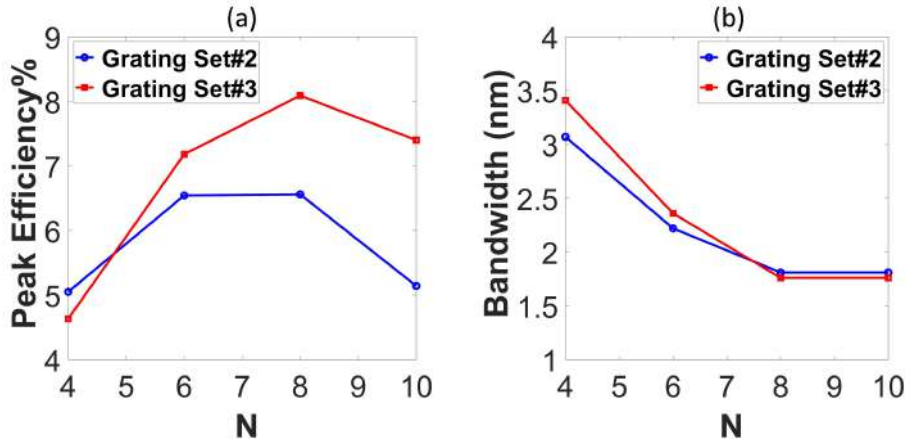


Figure 6.20: Parameters of +1 order achieved for grating Set#2 and Set#3 as a function of multilayer period  $N$  for SXR at near normal incidence ( $\theta = 5^\circ$ ): (a) Peak efficiency, and (b) Bandwidth.

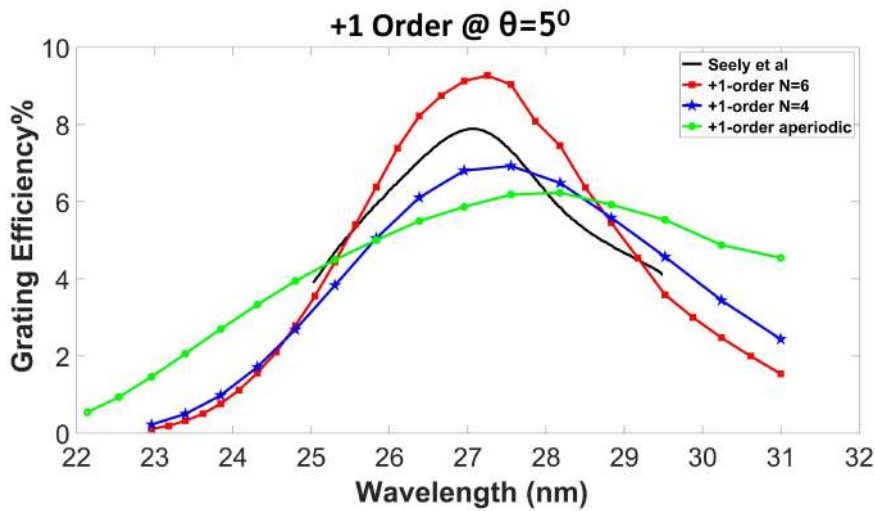


Figure 6.21: : +1 order efficiency measurement at  $\theta=5^\circ$  for the gratings for  $N=4$ ,  $N=6$ , and aperiodic coatings. Experimental data from Seely et al.[12; 19] are also plotted for comparison.

multilayers support the notion that they hold significant promise for applications in EUV spectroscopy.

## 6.4.2 Recommendations

The Solar C project aims to cover a wavelength range of 17.0-21.5 nm in the EUV spectrum, as discussed in reference [11]. For this purpose, gratings in Set#1 would be suitable if the incidence angle were  $45^\circ$ . To fulfill the project requirements, the depth of grooves in Set#2 should be reduced from approximately 16 nm to around 14 nm to align with the target wavelengths. Gratings in Set#3 are well-suited for meeting the project's specifications. We observed that roughness has a detrimental effect on the peak efficiency of the gratings. Although aperiodic multilayer gratings exhibit slightly lower peak efficiency compared to periodic multilayer gratings, they display intriguing results in terms of bandwidth. In some measurements, the bandwidth of aperiodic multilayer gratings was nearly double that of the



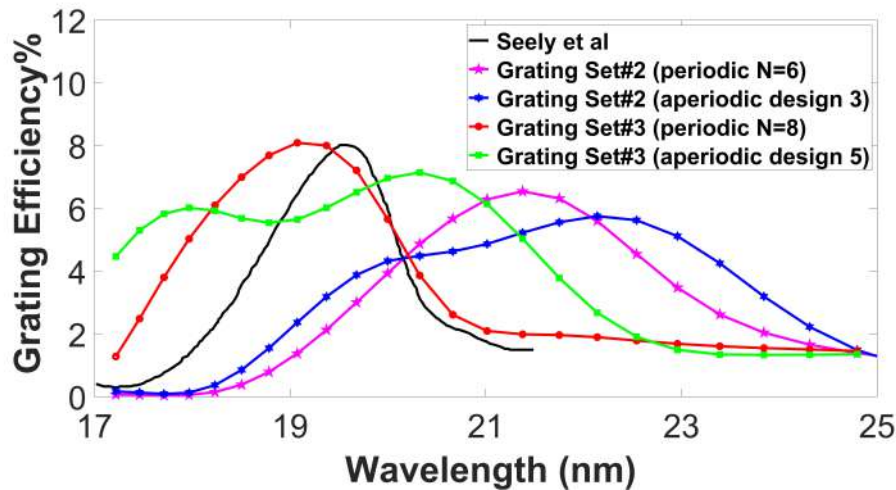


Figure 6.22: +1 order efficiency measurement at  $\theta=5^\circ$  for the grating set#2 for N=6, 24 layers of aperiodic coatings, and for the grating set#3 for N=8, 24 layers of aperiodic coatings. Experimental data from Seely et al.[12; 19] are also plotted for comparison.

corresponding periodic multilayer gratings with the same number of layers. Furthermore, we observed that the evolution of multilayer periods along the gratings (top, bottom, slope) leads to a change in the grating's profile from a trapezoidal shape to a top sinusoidal shape. This change negatively impacts peak efficiency. Therefore, we recommend depositing a lower number of periods. Additionally, our RCWA simulations revealed that as the depth of the grating's grooves decreases, the effect of changes in the deposited multilayer slope has a reduced impact on the peak efficiency.

## 6.5 Summary

In this chapter, we undertook an extensive analysis and investigation of the initial simulation results of multilayer gratings. We employed the grating parameters outlined in Chapter.4 and the multilayer parameters discussed in Chapter.5. Following this, we employed various techniques, such as angular and spectral efficiency measurements, transmission electron microscopy, and atomic force microscopy, to characterize the multilayer grating. We carefully documented the progression of the low period number of the deposited multilayer gratings by conducting a comparative analysis of the top profile gratings using atomic force microscopy before and after deposition. Additionally, we visualized the classical and energy-dispersive X-ray images obtained from transmission electron microscopy to further support our documentation. Our notable accomplishments encompassed the successful modeling of multilayer gratings and the enhancement of the model through the incorporation of the RCWA model with the Debye-Waller factor.

Considering the importance of this research in the context of the Solar C mission, we propose the adoption of multilayer gratings Set#3 instead of Set#2, as the changes in multilayer evolution on the groove shape have a

negligible impact on the efficiency of the gratings. Additionally, we recommend the utilization of aperiodic multilayer gratings instead of periodic ones, as they exhibit superior efficiency in terms of broader bandwidth coverage.



## Chapter 7

# Additional studies and observations for multilayer gratings

This chapter is not intended for applications related to Solar C; instead, it focuses on applications related to conical or classical diffraction of multilayer gratings, such as EUV beam splitters or EUV monochromators. The chapter highlights the benefits of angular spectra for conical diffraction multilayer gratings, demonstrating the potential to determine the absolute angle of groove alignment. In the preceding chapter.6, our focus was directed towards modeling solely the +1-order diffraction of multilayer gratings, specifically for the Solar C mission. However, in this current chapter, our interest lies in modeling different orders of diffraction, including 0-order and -1-order, to encompass all potential applications where multilayer gratings could be utilized. Furthermore, the position of conical multilayer gratings exhibits distinct characteristics in terms of the efficiency of the +1 order compared to classical multilayer gratings. It was observed that the asymmetric trapezoidal shape of the grating grooves has a negative impact on the amplitude of the diffracted -1 order in the EUV range at an incidence angle of 45 degrees.

In this Chapter, we present the modeling of data obtained from GIXR (Grazing Incidence X-ray Reflectivity) of the multilayer gratings. Furthermore, we measured the diffraction orders (+1, 0, and -1) for both periodic and aperiodic gratings within one set of the gratings. We were able to accurately model these measurements, revealing that the gratings exhibited the shape of asymmetrical trapezoidal gratings.

We have reached a consensus to implement all the measurements discussed in this chapter specifically for multilayer grating set #1. The reason behind this decision is the complexity associated with analyzing multilayer grating sets #2 and #3 in this chapter. In the previous chapter.6, AFM measurements have revealed that roughness and high-density grooves have a detrimental impact on the final grating profile, making the analysis somewhat intricate. Our primary focus is to investigate multilayer gratings for which the deposition of a small number of periods has minimal influence on both the groove shape and depth.

## 7.1 Angular Performance of Multilayer Gratings

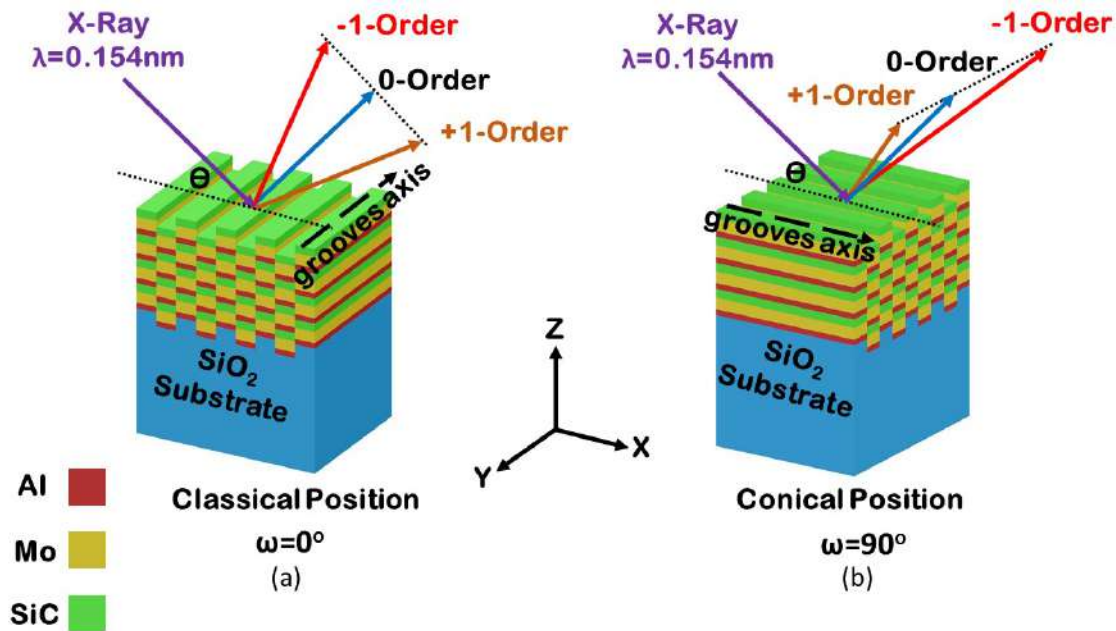


Figure 7.1: Schematic diagram for the gratings with periodic multilayers ( $N = 4$ ) at two different configurations, i.e., (a) classical and (b) conical.

Figure 7.1 shows a schematic diagram of Al/Mo/SiC multilayers deposited on gratings in two different configurations, i.e. the classical and the conical diffraction. Fig. 7.1(a) demonstrates the diffraction of X-ray radiation in a classical configuration, where the incident X-rays arrive perpendicular to the grating grooves resulting in the diffracted orders lying along an arc on the X-Z cone plane.

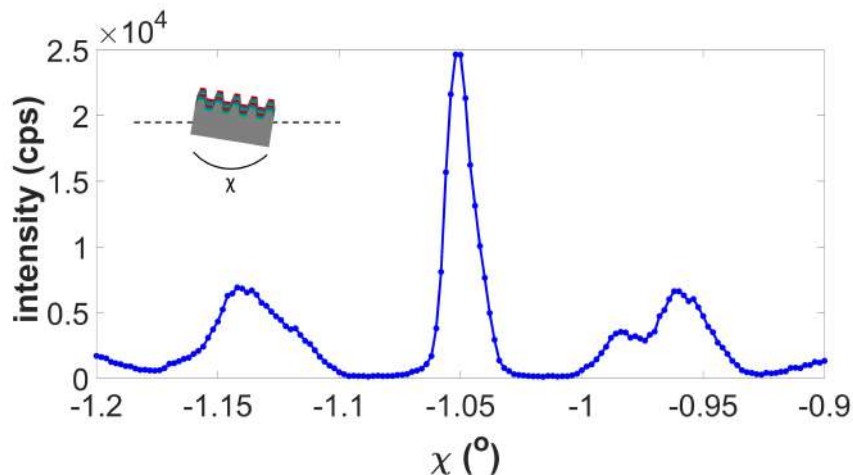


Figure 7.2: Alignment of the conical multilayer grating set#1 with  $N = 8$  layers using a rocking curve within the GIXR set up at an angle of  $\omega = 6^\circ$ .

While aligning the multilayer grating set#1 with  $N = 8$  layers in a conical position within the GIXR setup using a rotary stage at  $\omega = 6^\circ$  during the rocking curve step, it was observed that the detector captured three distinct diffrac-

tion orders, as illustrated in Fig.7.2. It is important to highlight that this phenomenon is observed exclusively with multilayer gratings in a conical position, whereas no detection of this kind occurs with multilayer gratings in the classical position. Therefore, it was interesting to analyze the diffraction angles of the 0<sup>th</sup>, +1<sup>st</sup>, and -1<sup>st</sup> orders as a function of the GIXR setup, as illustrated in Fig.7.3.

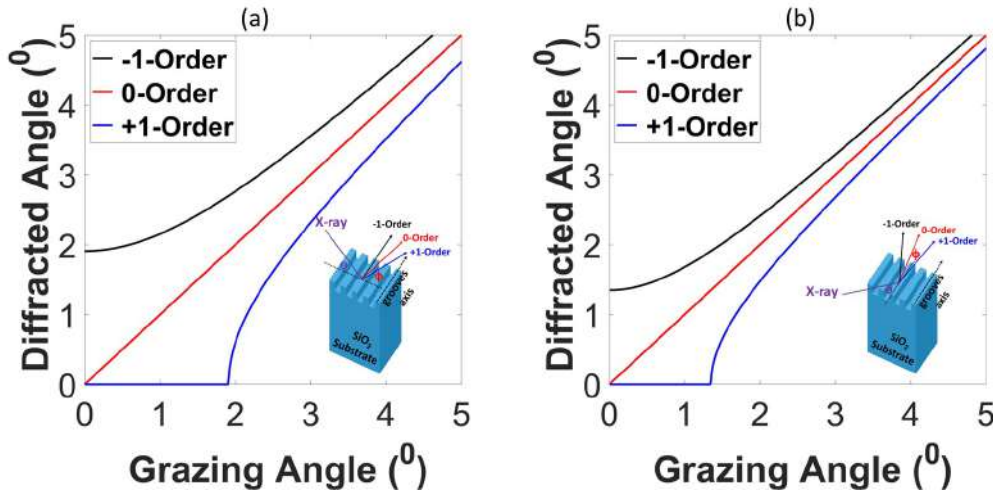


Figure 7.3: Estimation results of GIXR: Variation of diffraction angle for the 0<sup>th</sup>, +1<sup>st</sup>, and -1<sup>st</sup> orders with grazing angle for (a) classical configuration, and (b) conical configuration.

Normally, when an X-ray falls on the grooves of the gratings, it will be diffracted to 0,  $\pm 1$ , and  $\pm 2$  orders, etc. Figure.7.3(a) shows the diffraction angles  $\phi$  for +1, 0 and -1 orders according to the equation.2.16 in classical position, as a function of grazing angle  $\theta$  for a wavelength of  $\lambda=0.154$  nm and a grating periodicity of 277.7nm. Due to the spatial spreading of the different orders of diffraction the detector of the diffractometer employed in this work, mainly detects the 0-order, given that the detector is located approximately 300 mm away from the goniometer bearing the sampler holder and that there are two 0.1mm slits in front of it [106]. According to the equation.2.16, the detector reads only the 0-order. Therefore, for instance, as mentioned in the literature, in conical diffraction the non-adjusting groove axis with the incident beam will cause the asymmetric distribution of diffraction orders' magnitudes, something that can't be detected during the GIXR measurements. This can lead to an underestimation of the grating efficiencies.

In Fig.7.3(b), in the conical configuration, the X-rays arrive parallel to the grooves, and the light is diffracted in the incident plan Y-Z plane. The angle of diffraction  $\phi$  is given by the following eqn.2.16 for the classical position, however for the conical position it is computed by eqn.7.1.

$$\phi = \arcsin \left( \sqrt{\sin^2(\Theta) - \left(\frac{m\lambda}{p}\right)^2 - \left(\frac{2m\lambda \cos(\omega) \cos(\Theta)}{p}\right)^2} \right) \quad (7.1)$$

The variables  $\phi$ ,  $\Theta$ ,  $m$ ,  $\lambda$ ,  $P$ , and  $\omega$  correspond to the angle at which diffraction occurs, the angle at which the incident beam strikes the surface, the order of the diffraction pattern, the wavelength of the incident beam, the

periodicity of the gratings, and the angle between the plane of the incident beam and the alignment of the grating grooves, respectively.

The diffraction order results obtained in the conical position, as shown in Fig.7.3(b), indicate a significantly lower level of diffraction compared to the classical position depicted in Fig.7.3(a). This observation suggests that the detector in Disco may have the capability to detect measurements from two orders at a low grazing angle. This could potentially explain the presence of the anomalous detected peak, as indicated by the dashed circle in the conical GIXR measurements shown in the upcoming Fig.7.4(e-g).

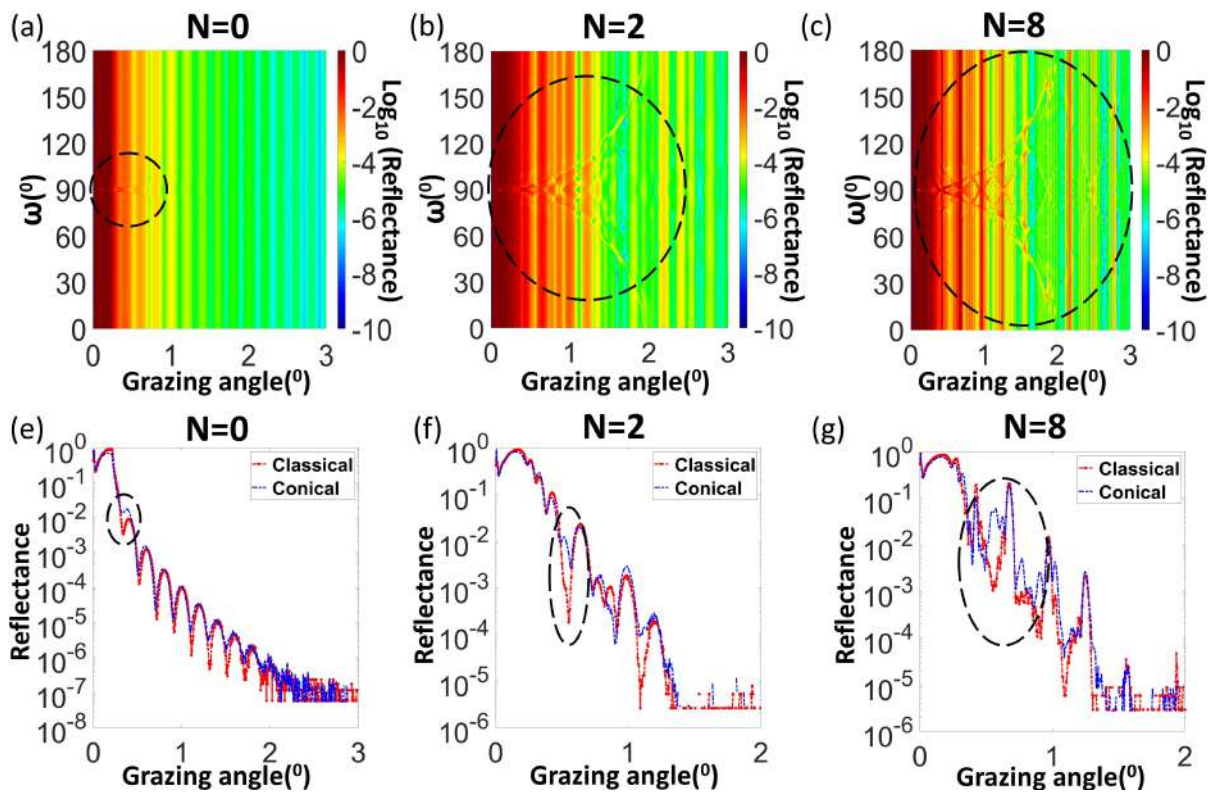


Figure 7.4: GIXR simulations and measurements for gratings Set#1. (a) GIXR simulation without multilayers ( $N = 0$ ), (b) and (c) GIXR simulations with periodic multilayers at  $N = 2$  and  $N = 8$ , respectively. (d) GIXR measurements without multilayers ( $N = 0$ ) in both conical and classical configurations, (e) and (f) GIXR measurements with multilayers at  $N = 2$  and  $N = 8$  in both conical and classical configurations, respectively.

Figures.7.4(a-c) depict the influence of varying the  $\omega$  angle (i.e., the angle between the incident X-ray and the normal to the grooves) on the grazing angle and the logarithm of reflectance, as indicated by the color bar. The simulations were conducted using the RCWA model with the parameters provided in Table.5.8 in Chapter.5 for the multilayer thickness parameters and Table.6.4 in Chapter.6 for the grating parameters. Interestingly, the RCWA simulations exhibit a shift in the Bragg peak between  $\omega = 90$  and ( $\omega = 80$  and  $\omega = 100$ ).

In Chapter.6, the TEM figure demonstrated the presence of distinct inclinations on the two sides of the grating grooves, leading to an asymmetric evolution of the multilayer behavior. However, achieving precise alignment between the simulated conical position and real-world conditions is challenging due to variations in surface deposition



rate, grating groove slope, and the top and bottom surfaces of the grating grooves.

Interestingly, the addition of multilayers to the grating proves to be beneficial in determining the optimal angle of conical position for  $N = 2$  (Fig.7.4(b)) and  $N = 8$  (Fig.7.4(c)), compared to the case of no multilayers ( $N = 0$ ) shown in Fig.7.4(a). This concept was further supported by GIXR measurements of  $N = 0$ ,  $N = 2$ , and  $N = 8$  at classical and conical positions (Fig.7.4(e), Fig.7.4(f), and Fig.7.4(g) respectively). Figures.7.4(e-g) demonstrate that the inclusion of multilayer with  $N = 2$  and  $N = 8$  leads to the formation of large, peculiar peaks in GIXR measurements for both classical and conical positions, as indicated by the dashed circles, in contrast to the case of  $N = 0$ .

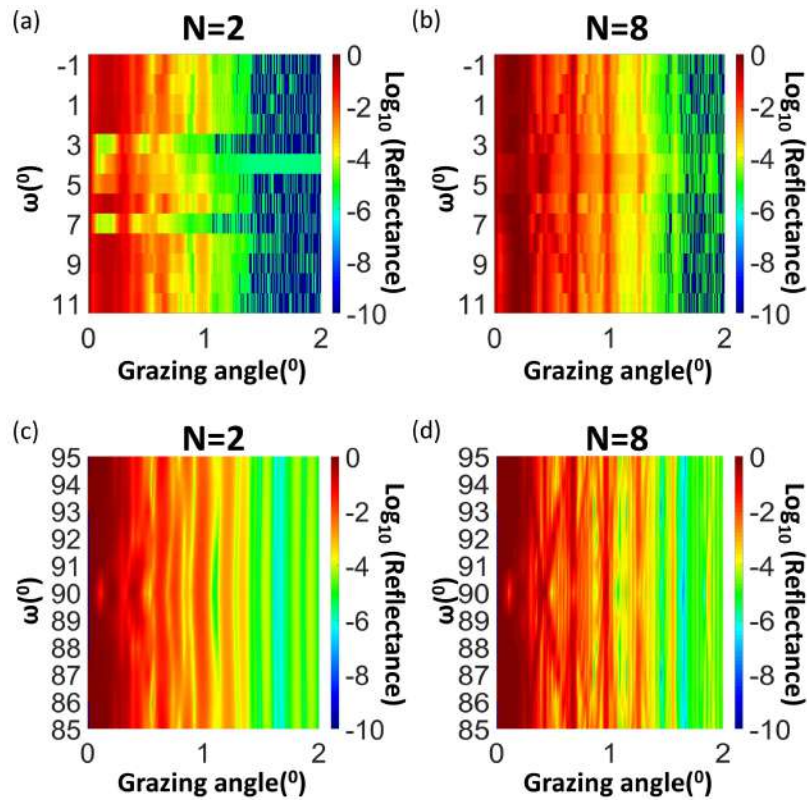


Figure 7.5: GIXR measurements using a rotation stage for different angles of  $\omega$  with grazing angle, and reflectance in the color bar for the behavior of multilayer gratings Set#1 with multilayer periods of (a)  $N = 2$  and (b)  $N = 8$ . Zoom-in GIXR simulations with periodic multilayers at (c)  $N = 2$  and (d)  $N = 8$

It should be mentioned that a diaphragm of 0.5 mm has been used in GIXR characterization for the multilayer grating whereas for the case of plane gratings, it has not been used any diaphragm. This was necessary to eliminate interference with the GIXR characteristics of the other side of the multilayer grating sample, where the diaphragm causes a loss of photons. It was interesting to characterize all the multilayer gratings to report the effect of the influence of the multilayer different periods on GIXR characteristics for periodic and aperiodic multilayer gratings.

Figure.7.5 exhibits GIXR measurements as a proof of concept with different angles of  $\omega$ . This was done by using a rotation stage to control the rotation of the gratings Set#1 and measure the angle  $\omega$  precisely. Figures.7.5(a), and 7.5(b) show the GIXR measurements for  $N = 2$ , and  $N = 8$  gratings Set#1 respectively.



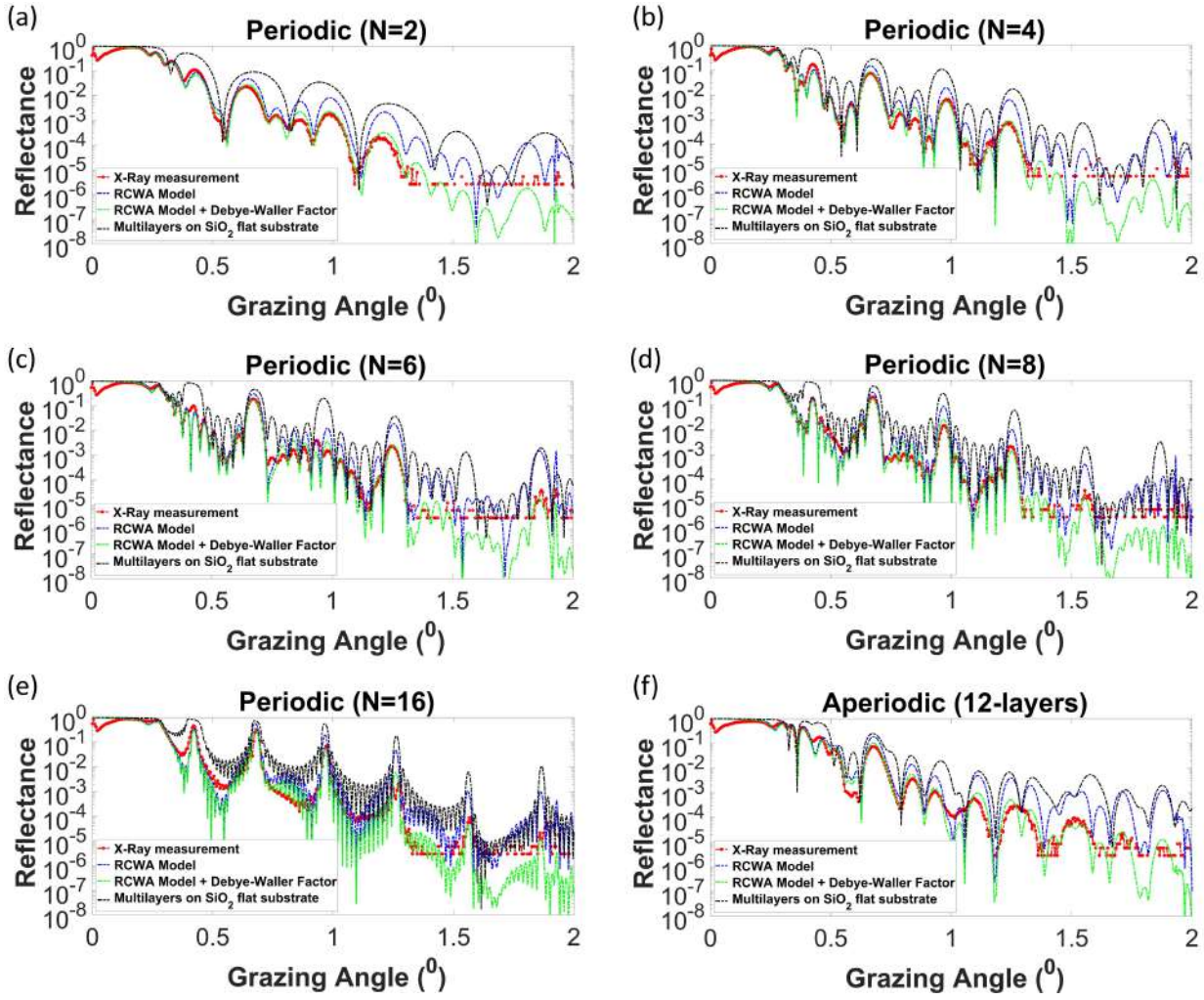


Figure 7.6: RCWA Model for GIXR measurements for multilayers on gratings set#1 (a) periodic ( $N = 2$ ), (b) periodic ( $N = 4$ ), (c) periodic ( $N = 6$ ), (d) periodic ( $N = 8$ ), (e) periodic ( $N = 16$ ) and (f) aperiodic (12 – layers).

The GIXR characterization for the multilayer gratings Set#1 is illustrated in Fig.7.6. A diaphragm was used in the measurements. The RCWA method was employed to model the GIXR measured data. The parameters of multilayer thickness ( $d$ ),  $\alpha$ , and  $f.f$  are shown in Table.6.4. These parameters have been verified in our previous Chapter.6. The RCWA model demonstrates good agreement with the simulation and measured data, particularly for the Bragg peak positions.

To compare the GIXR simulation of multilayer on  $\text{SiO}_2$  flat substrate with the GIXR simulation of multilayer on  $\text{SiO}_2$  grating substrate using the RCWA model, the GIXR simulation of multilayer on  $\text{SiO}_2$  flat substrate was added using IMD software. The GIXR measurements, which are the reflectance-grazing angle characteristics, are impacted by the multilayer period number and grating parameters.

It was observed that for  $N = 2$  in Fig.7.6 (a), there was no matching between the GIXR simulation of multilayer on  $\text{SiO}_2$  flat substrate and multilayer on  $\text{SiO}_2$  grating substrate. This indicates that the grating's parameters influenced the GIXR measurements at  $N = 2$ , whereas at  $N = 2$ , there was good agreement between the GIXR measurements

and the GIXR simulations using the RCWA model.

On the other hand, for  $N = 8$  in Fig.7.6(d) and  $N = 16$  in Fig.7.6(e), there was good matching between the GIXR simulation of multilayer on  $\text{SiO}_2$  flat substrate, multilayer on  $\text{SiO}_2$  grating substrate, and the GIXR measurements. This indicates that at high numbers of  $N$ , the GIXR measurements are influenced more by the multilayer parameters than the grating parameters.

Additionally, it is observed that the transition from a trapezoidal shape at  $N = 8$  to a top sinusoidal shape at  $N = 16$  has minimal impact on the angular measurements of GIXR, especially when taking into account the influence of the multilayer period at higher  $N$  values.

The aperiodic model in Fig.7.6(f) shows good agreement with the GIXR measurement. Additionally, the effect of roughness on the RCWA model was studied using the Debye-Waller equation.6.1. A roughness factor of 0.8 nm in the DW equation yielded good agreement between the RCWA model and the GIXR measurements.

## 7.2 Conical and Classical measurements at EUV

In this section, we aim to prove the asymmetry of three sets of gratings and its effect on multilayer evolution. We referred back to Chapter.6 and obtained the Transmission Electron Microscopy High-Angle Annular Dark Field (TEM HAADF) images for Set#1, Set#2, and Set#3, displayed in Fig.6.11(a), Fig.6.13(a), and Fig.6.14(a), respectively. To analyze the asymmetry, we plotted lines representing the slope for each  $N$ , which we measured using Fiji software [107], as depicted in Fig.7.7(a).

For the periodic multilayer grating Set#1 with  $N = 16$ , Fig.7.7(b) shows that the computed  $\alpha$  values exhibit extreme fluctuations on the left side. These fluctuations can be attributed to the presence of interdiffusion between layers in that region. On the contrary, the  $\alpha$  values on the right side demonstrate a normal decrease with only minimal fluctuations.

For the periodic multilayer grating Set#2 with  $N = 10$ , Fig.7.7(c) illustrates that the computed  $\alpha$  values exhibit minimal fluctuations on both the left and right sides. However, it is worth noting that the  $\alpha$  values at  $N = 0$  are not equal, displaying a difference of approximately 10 degrees. As  $N$  decreases, the  $\alpha$  computed values also decrease. Ultimately, at  $N = 10$ , the difference between the  $\alpha$  values from the left and right sides reaches about 15 degrees.

For the periodic multilayer grating Set#3 with  $N = 10$ , Fig.7.7(d) shows that the computed  $\alpha$  values exhibit minimal fluctuations on both the left and right sides. Nevertheless, it is important to mention that the  $\alpha$  values at  $N = 0$  are not equal, displaying a difference of approximately 15 degrees. As  $N$  decreases, the computed  $\alpha$  values also decrease. Eventually, at  $N = 10$ , the  $\alpha$  values become almost identical.

In the previous chapter (6), the TEM image analysis focused on zooming in on a single groove of the trapezoidal gratings in all sets. However, to confirm that this asymmetrical shape is not specific to just one groove but rather a general characteristic of all the grooves, we have presented Fig.7.8 which showcases a zoomed-out view of multiple

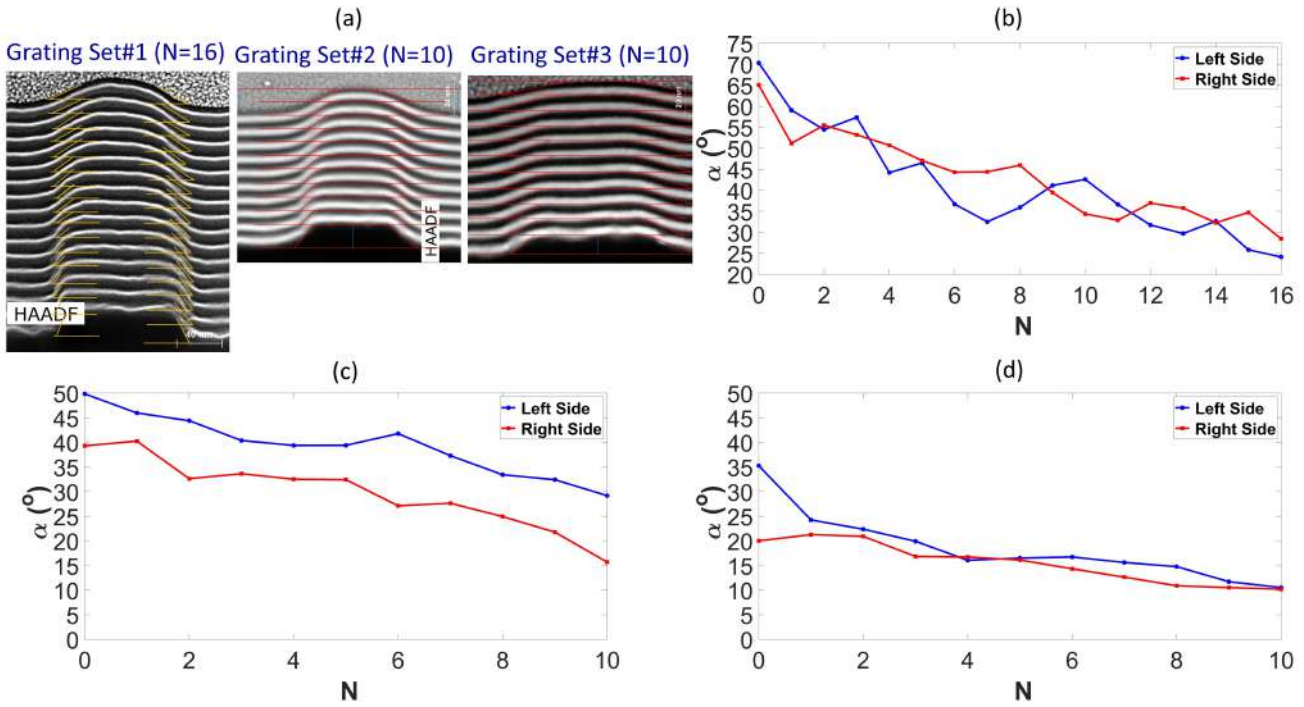


Figure 7.7: (a) TEM HAADF images of three sets of multilayer gratings, along with our estimation method used to compute the slope, (b) Slope calculation for each  $N$  in periodic multilayer (where  $N = 16$ ) of Grating Set #1, (c) Slope calculation for each  $N$  in periodic multilayer (where  $N = 10$ ) of Grating Set #2, and (d) Slope calculation for each  $N$  in periodic multilayer (where  $N = 10$ ) of Grating Set #3.

grooves ranging from 3 to 5. This analysis serves as a verification of our findings, demonstrating that all the grooves exhibit the asymmetrical shape of trapezoidal gratings.

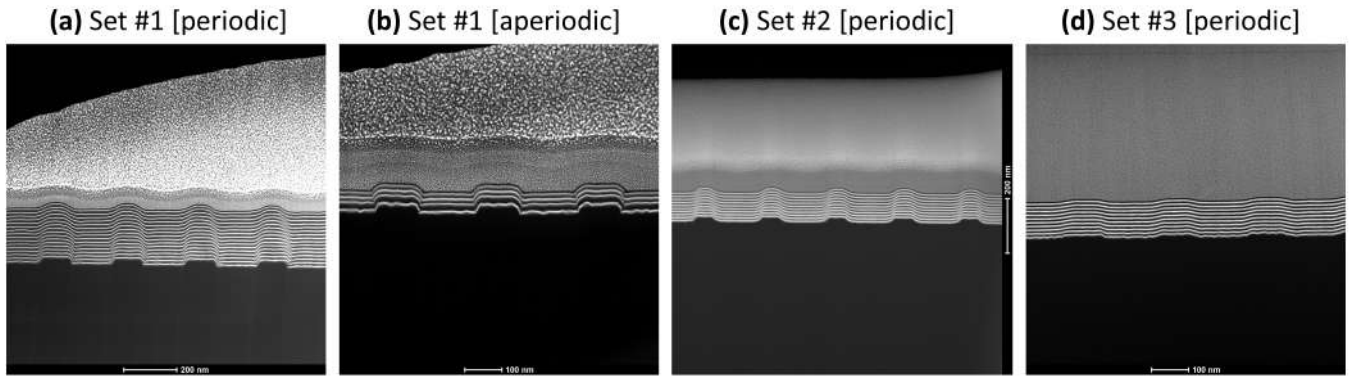


Figure 7.8: HAADF STEM images of different multilayer gratings: (a) Periodic Set#1 ( $N = 16$ ), (b) Aperiodic Set#1 (12 Layers), (c) Periodic Set#2 ( $N = 10$ ), and (d) Periodic Set#3 ( $N = 10$ ).

The measurement of gratings, both periodic ( $N = 6$ ) and aperiodic, and their order efficiencies at two different positions, classical and conical, was an intriguing endeavor. These measurements were conducted with incident angles of 45 degrees and varying wavelengths, as illustrated in Fig7.9. It is evident from the figure that the angles of the grooves relative to incident photons have a significant impact on the characteristics of the order efficiencies, resulting in shifted order peaks.

However, a discrepancy arose between the measured soft X-ray (SXR) data for the -1 order and the model of symmetric trapezoidal multilayer gratings, where we obtained that simulation of +1-order, -1-order are identical which is not in agreement with the measurements of +1-order and -1-order for both classical and conical position.

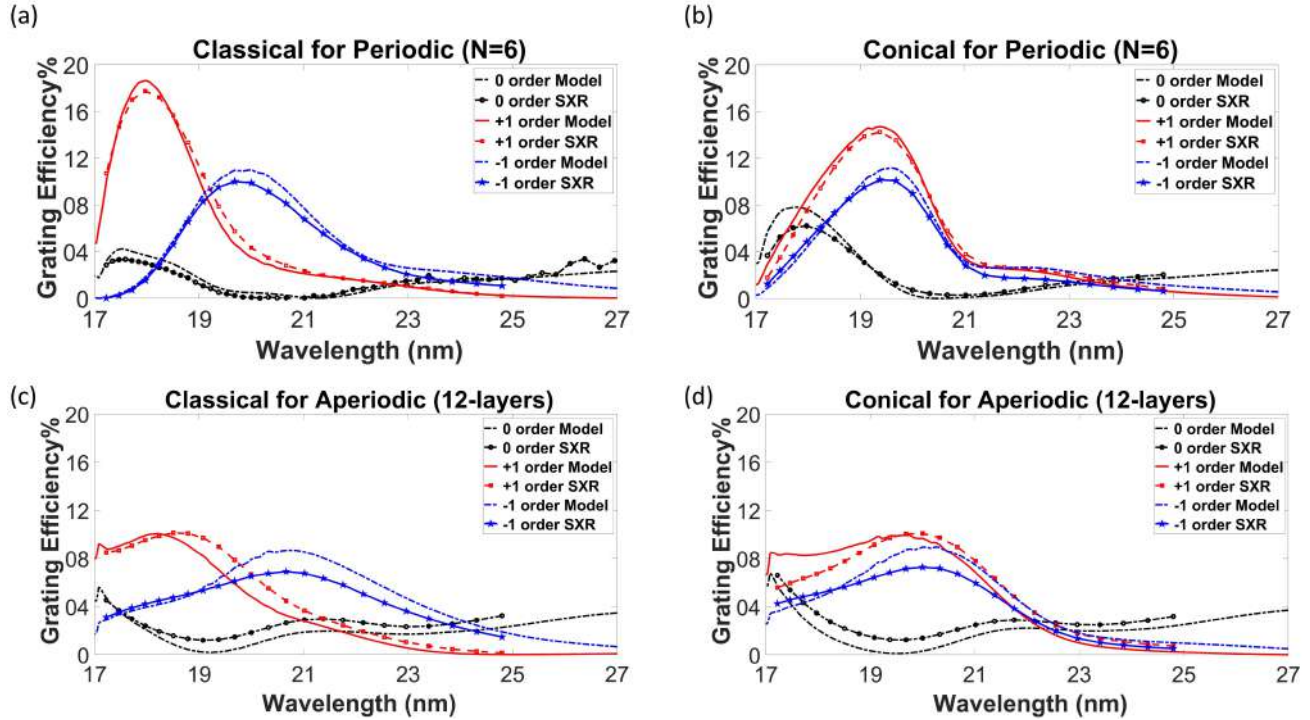


Figure 7.9: SXR measurements and models for periodic multilayer gratings Set#1 N=6 at (a) a classical position and (b) conical position, and for aperiodic multilayers gratings Set#1 at (c) classical position and (d) conical position.

To address this issue, a simulation code based on RCWA was developed, specifically designed to simulate multilayer gratings, including asymmetric trapezoidal structures depicted in Figure 3.24. These gratings possess two angles,  $\alpha_1$  and  $\alpha_2$ . The model parameters used are presented in Table.7.1, demonstrating a satisfactory agreement for the 0<sup>th</sup> and +1<sup>st</sup> orders in both periodic and aperiodic cases at the classical and conical positions, as illustrated in Figure.7.9.

Table 7.1: RCWA models parameters for modeling asymmetric trapezoidal multilayer grating.

Parameter	Periodic multilayer gratings	Aperiodic multilayer gratings
$d$ (nm)	22.2	21.2
$f.f$	0.51	0.48
$P$ (nm)	277.78	277.78
$\alpha_1$ (°)	49	43
$\alpha_2$ (°)	25	20

When examining a symmetric aperiodic multilayer grating, it is noteworthy that there is a marked enhancement in the agreement between measurements and simulations for the 0<sup>th</sup> and +1<sup>st</sup> orders. However, this improvement is not observed for the -1<sup>st</sup> order, where the discrepancy between measurements and simulations is amplified.



Conversely, in the case of a simulated asymmetric aperiodic multilayer grating, the disagreement between measurements and simulations is diminished for the  $-1^{st}$  order, while the agreement for the  $0^{th}$  and  $+1^{st}$  orders is diminished.

The remaining periodic multilayer grating configurations within grating set #1, namely those with  $N = 2$ ,  $N = 4$ ,  $N = 8$ , and  $N = 16$ , were solely subjected to measurements in the classical position, as illustrated in Appendix Fig. C.13.

We did not conduct measurements with an incident angle of  $5^\circ$  in the conical position for any of the grating sets. However, we made a deliberate decision to include in the appendix the measurements of zero orders for all three grating sets in the classical position: set #1 (refer to Fig.C.14), set #2 (refer to Fig.C.15), and set #3 (refer to Fig. C.16).

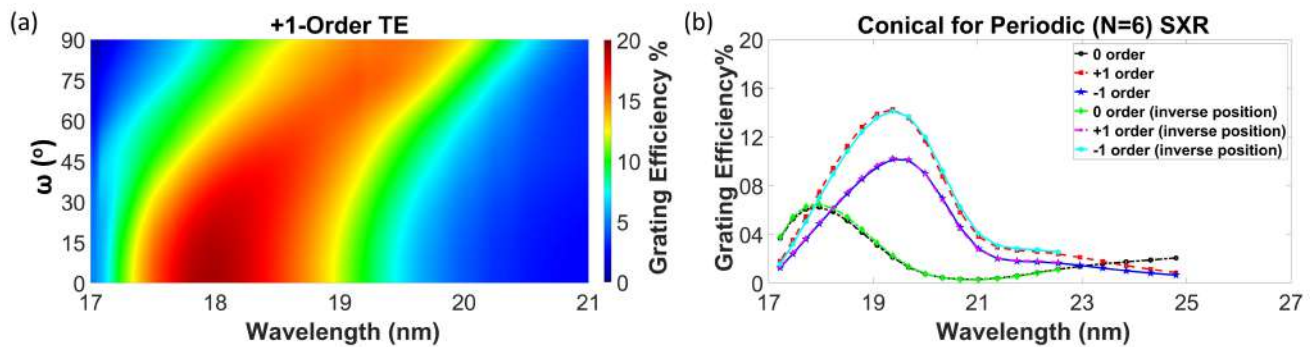


Figure 7.10: (a) +1-order simulation of the variation of  $\omega$  angle with wavelength, and efficiency for periodic  $N = 6$  at an incident angle  $45^\circ$ , and (b) SXR grating efficiencies measurements for conical position and inverse conical position (rotation  $180^\circ$ ).

Exploring the impact of changing the  $\omega$  angle on wavelength and grating efficiency through theoretical simulations is a captivating area of study. This effect is illustrated in Fig.7.10(a) for a periodic  $N = 6$  grating at an incident angle of  $45^\circ$ . Upon close examination of Fig.7.10(a), it becomes apparent that the alignment of the grooves relative to the incident SXR has the potential to induce a shift in the peak position towards specific wavelengths.

Furthermore, in the experimental measurements, a reversal in the position of the periodic  $N = 6$  grating with respect to the incident SXR by  $180^\circ$  has been observed. This reversal has led to a corresponding reversal in the measurements of the  $+1^{st}$  and  $-1^{st}$  orders, as depicted in Fig.7.10(b).

### 7.2.1 Multilayer gratings sensitivity to EUV

In grating Set#1 ( $N = 4$ ), we encountered a discrepancy between our RCWA model and SXR measurements for the +1-order, which led us to doubt the accuracy of the SXR measurements. To address this, we decided to conduct the measurements at three different points. In Fig. 7.11(a), we present a schematic of the top multilayer grating sample, with the points located at different positions along the y-axis.

From the measurements taken at near normal incidence ( $\theta = 5^\circ$ ), we observed interesting differences. As shown

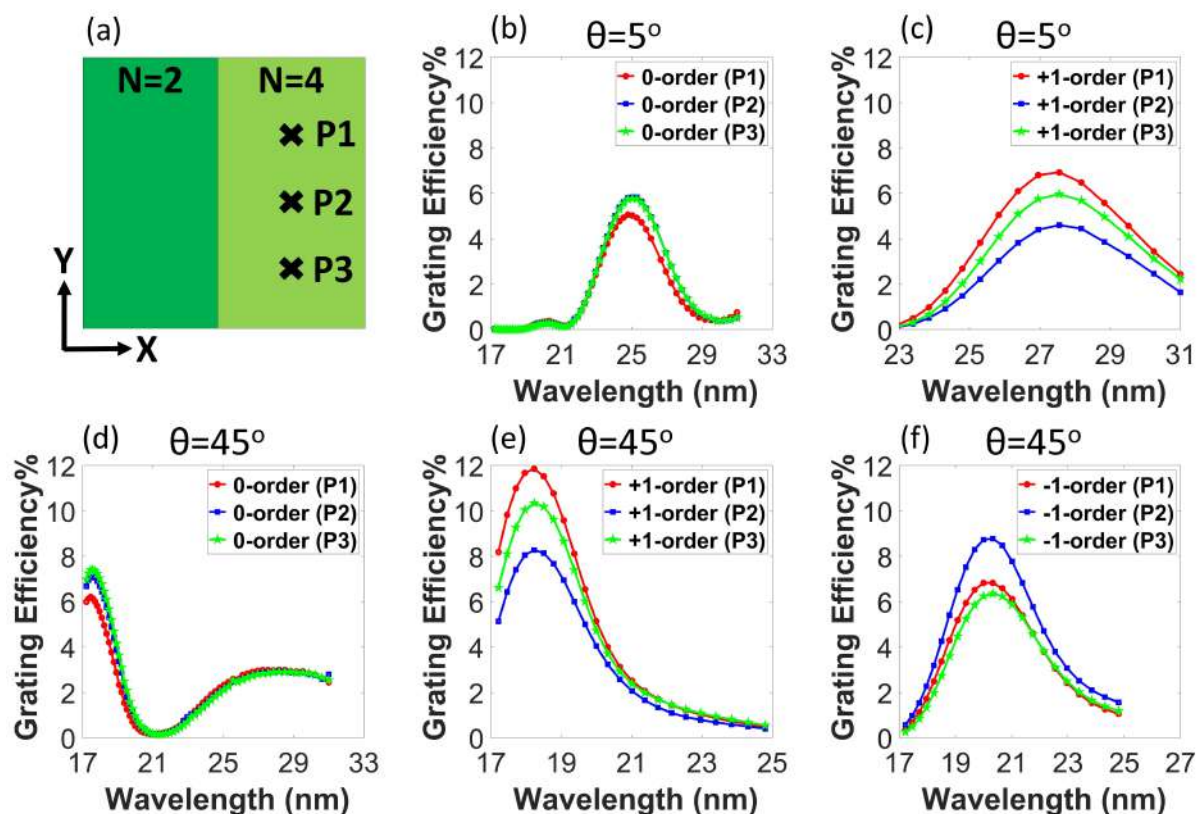


Figure 7.11: (a) Schematic diagram of the top x-y plan of the gratings showing the positions where the SXR beam interacts with multilayer gratings in classical position. (b) Three measurements of the 0-order at near-normal incidence ( $\theta = 5^\circ$ ). (c) Three measurements of the +1-order at near-normal incidence ( $\theta = 5^\circ$ ). (d) Three measurements of the 0-order at incidence ( $\theta = 45^\circ$ ). (e) Three measurements of the +1-order at incidence ( $\theta = 45^\circ$ ). (f) Three measurements of the +1-order at incidence ( $\theta = 45^\circ$ ).

in Fig. 7.11(b), the 0-order measurement at point  $P1$  was the lowest among the three points. In contrast, the +1-order measurement at  $P1$  was the highest, as shown in Fig. 7.11(c). At points  $P2$  and  $P3$ , the measurements of the 0-order were nearly identical in Fig. 7.11(b). However, the +1-order measurement at  $P3$  was higher than at  $P2$ . Unfortunately, we were unable to measure the -1 order at near normal incidence ( $\theta = 5^\circ$ ). As a result, we decided to conduct the same measurements at an incidence angle of ( $\theta = 45^\circ$ ).

As we conducted measurements at ( $\theta = 45^\circ$ ), we were able to observe and measure all three diffraction orders: 0-order, +1-order, and -1-order. For point  $P1$ , we found that the 0-order measurement was the lowest (Fig. 7.11(d)), the +1-order measurement was the maximum (Fig. 7.11(e)), and the -1-order measurement was of average intensity (Fig. 7.11(f)). On the other hand, for point  $P2$ , the 0-order measurement was of average intensity (Fig. 7.11(d)), the +1-order measurement was the minimum (Fig. 7.11(e)), and the -1-order measurement was the maximum (Fig. 7.11(f)). Lastly, at point  $P3$ , the 0-order measurement was the maximum (Fig. 7.11(d)), the +1-order measurement was of average intensity (Fig. 7.11(e)), and the -1-order measurement was the lowest (Fig. 7.11(f)).

The results indicate that the sensitivity of multilayer grating grooves can indeed impact the distribution of energy between different diffraction orders.

We would like to mention that we conducted experiments using custom silicon gratings to observe the evolution of different materials deposition, including Si/B<sub>4</sub>C, Mo/Si, and Si/Mo/B<sub>4</sub>C. Additionally, we employed different deposition machines such as ion beam sputtering and magnetron sputtering to examine their effects on the evolution of multilayer gratings. We utilized various characterization tools such as AFM and TEM to analyze the multilayer grating evolution. Our research objective was to model the profile evolution. Unfortunately, due to fabrication delays with the custom silicon gratings and technical issues with the machine, we were unable to conduct this research within the timeframe of this thesis. However, we performed some preliminary work related to this research, which we have included in the appendix.A.

### **7.3 Summary**

This chapter focused on the examination of angular efficiency in multilayer gratings, particularly through the utilization of GIXR measurements. We successfully developed models for the angular spectra of multilayer gratings in the classical position. Furthermore, we were able to determine the absolute angle value for groove alignments using angular spectra in the conical position. Additionally, we conducted measurements of conical diffraction at near-normal incidence. Lastly, we enhanced the modeling of both conical and classical multilayer gratings by incorporating asymmetric trapezoidal gratings.

# Chapter 8

## Conclusions and Future Work

### 8.1 Conclusions

The objective of this thesis was to optimize the designs of periodic and aperiodic *Al/Mo/SiC* multilayers in order to achieve broadband efficiency centered around a central wavelength of 19 nm. The optimized multilayer designs aimed to strike a balance between higher efficiency and a broader bandwidth, specifically for solar EUV spectro-imaging applications within the 22-32 nm wavelength range. The broadband efficiency of *Al/Mo/SiC* multilayers were optimized for 3 types of gratings with groove depths from 5 nm to 20 nm.

For grating Set#1, which its groove depth was around 22 nm, five periodic multilayers were created with varying numbers of periods (ranging from  $N = 2$  to  $N = 16$ ), along with an aperiodic multilayer composed of 12 layers. These multilayers were deposited on high-density 3600 l/mm trapezoidal grating substrates.

For grating Set#2 and Set#3, which their groove depths were around 16 nm and 5 nm respectively, four periodic multilayers were created with varying numbers of periods (ranging from  $N = 4$  to  $N = 10$ ), along with two aperiodic multilayers composed of 18 and 24 layers. These multilayers were deposited on high-density 4000 l/mm trapezoidal grating substrates.

Initially, all the periodic and aperiodic *Al/Mo/SiC* multilayers designs were deposited on flat *Si* substrates samples using magnetron sputtering. The deposited samples were then characterized using transmission electron microscopy (TEM), grazing incidence X-ray reflectometry (GIXR), and soft X-ray reflectometry (SXR). This combination of characterization techniques enabled the researchers to develop realistic models for both the periodic and aperiodic coatings.

Subsequently, all the grating substrate sets were analyzed using atomic force microscopy (AFM) before and after the deposition of the multilayers. This analysis aimed to determine how the initial profile evolved with the addition of the multilayer coating. The findings demonstrated that the slope of the trapezoidal shape decreased in an almost linear manner as the number of periods increased. Additionally, after a certain number of periods, the top profile



transitioned from a trapezoidal pattern to a sinusoidal pattern. This was also confirmed by the measurement of transmission electron microscopy, which was conducted on all multilayer grating substrate sets. Hence, the evolution of the multilayer grating surface profile has been successfully presented after multilayer deposition, depending on the groove depth and/or density.

In addition, we developed a model of the multilayer grating and utilized it for rigorous coupled wave analysis (RCWA) simulations. The simulations confirmed that an increase in the slope of the trapezoidal shape has a negative impact on the diffraction efficiency when the incidence angle is near-normal. However, in the case of oblique incidence ( $45^\circ$ ) for multilayer gratings Set#1, the influence of the slope on efficiency is significantly reduced.

Furthermore, for multilayer gratings Set#1, we conducted experimental measurements of the +1-order diffraction efficiency for both periodic and aperiodic multilayer gratings in the EUV range, considering two different incidence angles ( $5^\circ$  and  $45^\circ$ ). The measured data exhibited excellent agreement with the simulated diffraction efficiencies based on the trapezoidal profile models. The experimental results revealed that the peak efficiency increased until reaching a maximum at  $N = 6$  (number of periods), after which it started to decrease. This behavior can be attributed to the evolution of the surface profile, as determined by AFM, which deviates from the trapezoidal shape when  $N > 6$ .

Similarly, for multilayer gratings Set#2 and Set#3, we modeled +1-order diffraction efficiency for both periodic and aperiodic multilayer gratings in the EUV range, considering an incidence angle of  $5^\circ$ . The measured data exhibited good agreement with the simulated diffraction efficiencies based on the trapezoidal profile models. Therefore, we improved the fitting by introducing the Debye-Waller correction, which represents the roughness. The same observation was observed that as the profile shape of trapezoidal gratings changes to sinusoidal gratings, it negatively affects the +1-order peak efficiency.

Compared to previous studies, the 6 and 8 periods of period Al/Mo/SiC multilayer gratings exhibited higher efficiencies over a broader bandwidth for grating Set#1 and Set#3 respectively. Additionally, the aperiodic multilayer grating achieved an unprecedented broad bandwidth while maintaining reasonable efficiency. These findings pave the way for designing instruments with extended performance for EUV high-resolution spectrometry or spectro-imaging applications. Finally, we achieved a broadband efficiency with a significant improvement compared to the Solar-B mission results (see Fig.8.1).

When considering multilayer gratings Set#1, the Bragg peak undergoes a transition in its central wavelength from 27nm to 19nm as the incidence angle shifts from near-normal ( $5^\circ$ ) to  $45^\circ$ .

## 8.2 Future Work

We conducted an initial study involving the deposition of various compositions of multilayer materials on custom silicon gratings. Our objective was to investigate the impact of depositing the same multilayer structure on custom

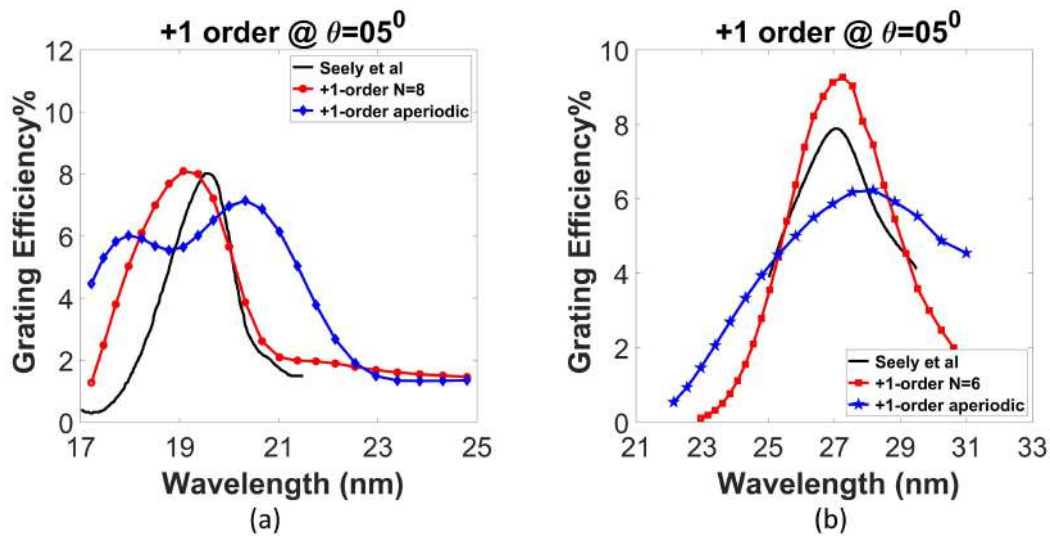


Figure 8.1: A comparison between our findings and the previous work on the Solar B mission, which focused on a 20-period Mo/Si multilayer presented by Seely [12]. Our study demonstrates improvements in (a) the +1-order measurements for the 8-periodic and 24-layer aperiodic Al/Mo/SiC multilayer of gratings set 3 at a central wavelength of 19 nm, and (b) the +1-order measurements for the 6-periodic and 12-layer aperiodic Al/Mo/SiC multilayer of gratings set 1 at a central wavelength of 27 nm.

silicon gratings using different deposition techniques, such as magnetron sputtering deposition and ion beam sputtering. Subsequently, we planned to characterize these depositions using AFM and TEM to analyze the evolution of the material on the grating's surface profile. This analysis aimed to provide insights into how the roughness and groove shape would influence the multilayer evolution.

Additionally, we attempted to model this evolution using a local curvature model. While the model successfully captured some aspects of the multilayer grating's evolution, it requires further improvement in terms of fill factor and roughness. We recommend continuing this work as it will contribute to a better understanding of how multilayers evolve on the profile of gratings.



## Appendix A

# Deposition on Custom Silicon Grating.

This part presents unfinished research pertaining to the thesis. Our objective was to investigate the evolution of multilayers using two distinct deposition techniques and various multilayer structures in materials. The main focus was on modeling the surface evolution of the profile multilayer gratings. Unfortunately, we encountered challenges that prevented us from completing this work within the designated timeframe of the thesis.

The primary hurdles were the unavailability of fabricated samples and breakdowns in some of the deposition machines, which impeded the execution of the research analysis. Despite these obstacles, we did manage to obtain some initial results related to this study, which we have chosen to showcase. However, it is important to note that there are still open questions that can only be addressed through continued research in this area.

It is crucial to emphasize that our primary objective in depositing the multilayer on these custom Si gratings is to visually observe the evolution of the multilayer on the grating's surface, rather than measuring it using an EUV metrology beamline.

### A.1 Etched Silicon Arrays Fabrication Process

All the process steps until mask removal are done using the PTC IOGS/Thales/X facilities.

1. A  $100 \times 100 \mu\text{m}$  surface array with 150 nm width and 300 nm period is realized through standard e-beam lithography and IBE etching processes which are detailed step by step below.
2. Two inches silicon wafers with 110 orientation and  $180 \mu\text{m}$  thickness are first cleaned with acetone followed by isopropanol and then dried with  $\text{N}_2$ .
3. Before the e-beam process, wafers are desiccated onto a hotplate at  $180^\circ\text{C}$ . AP300 adhesion promoter is first spin-coated (speed  $3000 \text{ t}\cdot\text{min}^{-1}$ , duration 30s), followed by a 150 nm PMMA A4 layer. Wafers are then baked on the hotplate at  $180^\circ\text{C}$  for 5 min. Return to room temperature is conducted for 5 min by putting the wafer

on a high thermal conducting plate.

4. Finally, a charge dispersing agent (Espace 300 Z from Showa Denko) is spun with the same speed/ time conditions and baked at 110°C for 1 min.
5. This last layer is very important to ensure good electron dispersion during e-beam writing.

In details,

- The grooves are written by conducting E-beam writing using an nB3 e-beam machine (NanoBeam Ltd) at 80 kV. The average dose utilized for writing these grooves is  $780 \mu\text{C}\cdot\text{cm}^{-2}$ .
- Patterns are finally developed using first deionized water and then a MIBK: ISO 1:3 solution (MIBK: Methyl Iso Butyl Ketone, ISO: isopropanol) during 55s (average time) followed by a rinsing step in isopropanol of 1min 15s.
- An array etching process is realized in a Plassys Ion Beam Etching machine with an  $\text{Ar}^+$  beam and a SIMS spectrometry in-situ analysis. The sample holder is maintained at a 5°C temperature and 20° angle to the ion beam. Etching energy is set to  $0.41 \text{ mA}\cdot\text{cm}^{-2}$  and etching time is fixed at 3 min for the first sample.
- Based on the AFM measurements, it has been observed that the groove depth deviates significantly from our initial expectations. This discrepancy can be attributed to the significant aspect ratio of the grooves and the noticeably slower etching rate of silicon ion beams within the grooves compared to the top surface of the array. To address this issue, a second etching run was performed on the samples. This second etching run was conducted without utilizing a mask, with a 0-degree etching angle, and lasted for one minute. All other conditions remained consistent with the first etching step.
- PMMA etching mask is then removed using  $\text{O}_2$  plasma for 10 min.

## A.2 Custom silicon gratings sample 1

The objective of using this particular sample was to conduct an initial test. We opted to utilize a deposition technique that had been previously employed for Zeiss silica gratings Set#1. This method involves a periodic multilayer design consisting of Al/Mo/SiC and utilizes the same deposition parameters as sample MP20065, which was achieved through magnetron sputtering deposition MP800 (refer to Section.5.6 for detailed information on MP20065). However, we introduced a modification by increasing the number of periods from 10 to 20.

### A.2.1 Characterization before deposition.

Figure.A.1 showcases the surface morphology and grating profile of custom silicon grating sample 1, as observed through Atomic Force Microscopy (AFM) in tapping mode. The measurements were performed using a Bruker

Dimension-ICON AFM machine, employing the ScanAsyst tool. Additionally, Table.A.1 provides the average parameters computed from Fig.A.1(b).

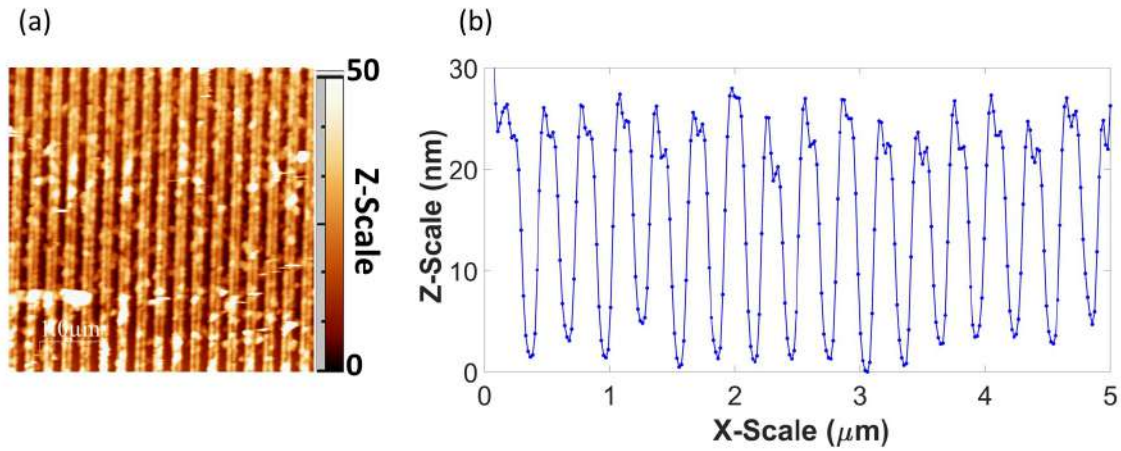


Figure A.1: (a) The  $5\mu\text{m} \times 5\mu\text{m}$  AFM surface morphology, and (b) the groove profiles after making rotation to the grooves to have a perpendicular alignment of the grooves.

Table A.1: The average grating parameters computed from Fig.A.1.(b).

average Parameter	numeric value
$f.f$ (FWHM)	0.57
$\alpha$ ( $^\circ$ )	19.53
grating grooves depth (nm)	$\leq 20$

### A.2.2 Initial deposition.

We performed the deposition of a 20-period multilayer using the thickness parameters obtained for Al, Mo, and SiC materials, as specified in Table 5.2. The aim was to maximize the broadband reflectance for wavelengths ranging from 25nm to 29nm, considering an incident angle of 5 degrees.

Table A.2: The proposed multilayers parameters for the gratings.

Parameter	numeric value
Number of periods	20
Materials	Al/Mo/SiC
Al thickness (nm)	8
Mo thickness (nm)	2.68
SiC thickness (nm)	3.69

### A.2.3 Characterization after deposition by X-ray reflectometry.

The deposition process was initiated on a flat Si substrate. To characterize this deposition, Grazing Incidence X-ray Reflectivity (GIXR) was employed. Additionally, the model described in Table.5.8 was used to simulate the deposition

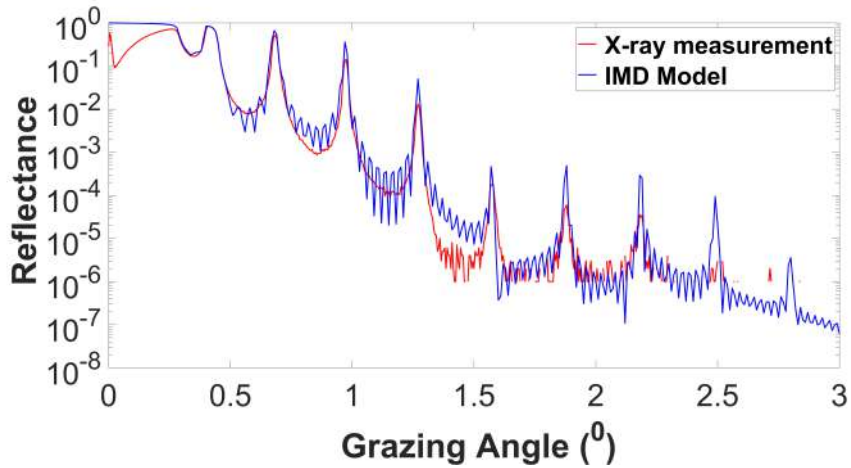


Figure A.2: GIXR measured and fitted curves at  $\lambda=0.154\text{nm}$  for the 20-periods Al/Mo/SiC multilayer (sample MP22055).

using IMD Software. The outcomes of this simulation can be observed in Table.A.3 and Fig.A.2.

Table A.3: Layer thickness and interfacial roughness for the analyzed periodic Al/Mo/SiC of  $N = 20$  on the Si substrate.

Material	Thickness (nm)	Interface	Roughness (nm)
Top Oxide layer	1.50	Top surface	0.450
SiC	3.810	Oxide-on-SiC and Al-on-SiC	0.700
Mo	2.740	SiC-on-Mo	0.700
Al	7.720	Mo-on-Al	0.700
Si Substrate	$\infty$	Al-on- Si substrate	0.350

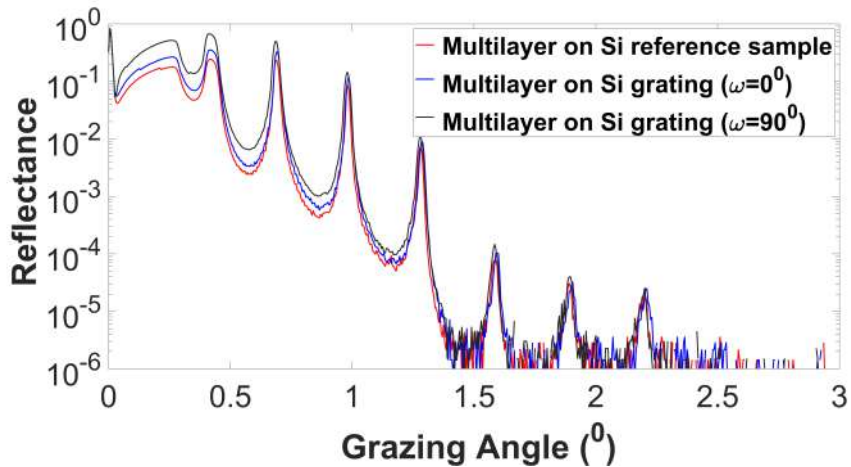


Figure A.3: GIXR measured for multilayer on Si reference sample (red line) multilayer on Si grating sample (blue line), and multilayer on Si grating sample after rotating it  $90^\circ$  with respect to  $\omega$  (black line) at  $\lambda=0.154\text{nm}$  for the 20-periods Al/Mo/SiC multilayer.

To provide further clarity regarding the impact of gratings on GIXR measurements, a comparison was conducted as depicted in Fig.A.3. The comparison involved multilayers deposited on a flat Si substrate, multilayers on a grating

substrate, and multilayers on a grating substrate with a 90-degree rotation to represent both classical and conical multilayer grating substrates. We observed a minor variation in the measurements, as illustrated in Fig.A.3.

#### A.2.4 Optical microscope.

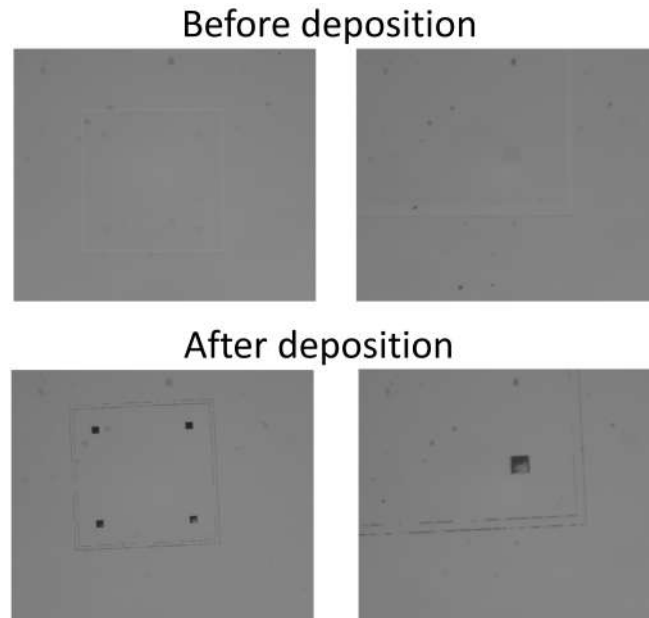


Figure A.4: Optical telescope photography for test grating sample before and after deposition.

The gratings are positioned within four small rectangles contained within a larger square, as depicted in Fig.A.4, which was captured using an optical microscope in our clean room. The optical microscope used is from Olympus System Model BH2.

#### A.2.5 Characterization after deposition by TEM.

The TEM images reveal a triangular hole positioned at the top of the grating structure. The grating itself assumes a trapezoidal shape, but Fig.A.5(d) demonstrates the existence of two edges at the upper portion of the trapezoidal grating. The TEM analysis of the multilayer structure evolution primarily investigates the changes occurring in the multilayer beneath the trapezoidal gratings. Additionally, TEM analysis examines the separate evolutions of two distinct multilayers on either side of the triangular hole located at the top of the trapezoidal gratings. Furthermore, the evolution of a multilayer positioned at the highest point of the triangular hole on the top of the trapezoidal gratings is also being studied.

In the evolution of multilayers at the bottom of the trapezoidal gratings, an interesting observation emerges, as illustrated in Fig.A.5(f). Despite the presence of a flat surface area between the two trapezoidal gratings at  $N = 0$ ,



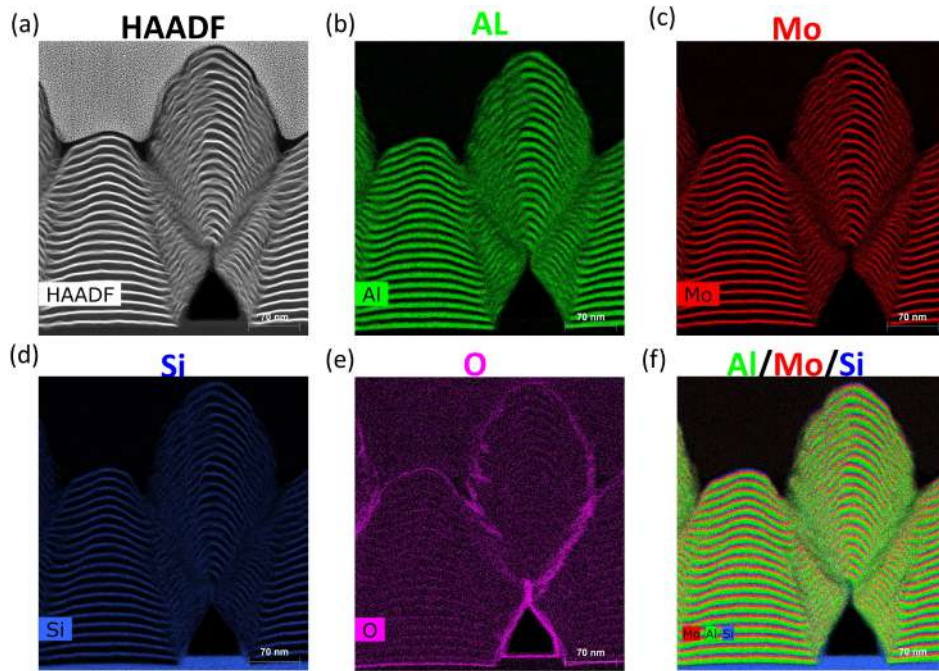


Figure A.5: TEM analyses of sample MP22055: (a) HAADF, and EDX images (b) Al, (c) Mo, (d) Si, (e) O, and (f) 20-periods three materials Al/Mo/Si.

the multilayer evolution in this region results in a non-flat final shape at the top when reaching  $N = 20$ . Interestingly, the deposition in this specific area reveals distinct layers without any interdiffusion, as shown in Fig.A.5(a-f).

Regarding the evolution of two different multilayers on each side of the triangular hole, it can be observed that there is evident interdiffusion between the deposited multilayers, as depicted in Fig.A.5(f). Furthermore, Fig.A.5(e) demonstrates a notable oxidation occurring predominantly on the right side of the multilayer evolution adjacent to the triangular hole.

The evolution of the multilayer at the highest point of the triangular hole is peculiar, as depicted in Fig.A.5(a-f). It begins at a single point and transitions into a top sinusoidal shape. Interestingly, interdiffusion has been observed from both the right and left sides of the top sinusoidal multilayer evolution. However, no interdiffusion has been observed at the center of the sinusoidal multilayer evolution. In addition, it is worth noting that the area surrounding the triangular hole exhibits a high degree of oxidation, as illustrated in Fig.A.5(e).

The development of the multilayer on the grating profile shown in Fig.A.5 exhibits some resemblance to the multilayer progression on the grating profile discussed in earlier research as depicted in Fig.A.6. In that previous study, the authors [20] elucidated that this evolution arises due to the amplification of roughness caused by the shadow. Additionally, we anticipate that there may have been imperfections in the fabrication process, specifically in fully removing unnecessary components. The two references [108; 109] have noted that imperfections significantly influence the development of the surfaces in multilayer systems.

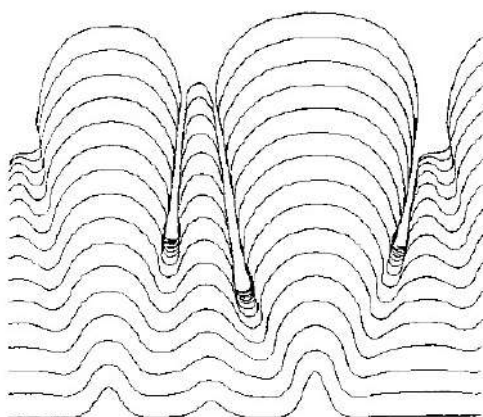


Figure A.6: surface profile growth model of multilayer grating [20].

### A.3 Custom silicon gratings sample 2

For this sample, our plan is to deposit three distinct compositions of multilayer materials on the same substrate. To achieve this, we will utilize a mask that allows deposition on one quarter of the sample. As a result, we will have three different depositions on three separate quarters of the sample, while one quarter will remain without deposition. This approach facilitates a comparative analysis using AFM to demonstrate the final surface profile of the three multilayer structures, as well as the surface profile of the reference quarter without deposition.

All AFM measurements will be conducted on the same day using the AFM NX 20 machine from Park System company at SOLEIL Synchrotron. Subsequently, the samples will undergo TEM analysis to visualize the evolution of the multilayer structure profile on the grating.

As demonstrated in Chapter.5, the composition of Al/Mo/B4C has exhibited notable efficiency and stability, as shown in Fig.5.2. In this section, we employed the same composition but made a substitution in the spacer material, replacing Al with Si.

At present, four grating samples have been manufactured. The plan is to deposit three distinct multilayer structures, namely Si/Mo/B4C, Mo/Si, and Si/B4C, using two different deposition techniques: ion beam sputtering and magnetron sputtering.

The reference [79] provides a comprehensive overview of the physical and operational principles of ion beam sputtering, which is available in our ISO6 cleanroom at Laboratoire Charles Fabry and has been used to deposit multilayers in this section.

#### A.3.1 Initial AFM Profile of Custom Silicon Gratings Sample 2

The surface morphology was analyzed using three different scans:  $2\mu\text{m} \times 2\mu\text{m}$ ,  $5\mu\text{m} \times 5\mu\text{m}$ , and  $10\mu\text{m} \times 10\mu\text{m}$ , employing the non-contact method, as depicted in Fig.A.7(a-c). Fig.A.7(d) illustrates the surface profile for the  $5\mu\text{m} \times$

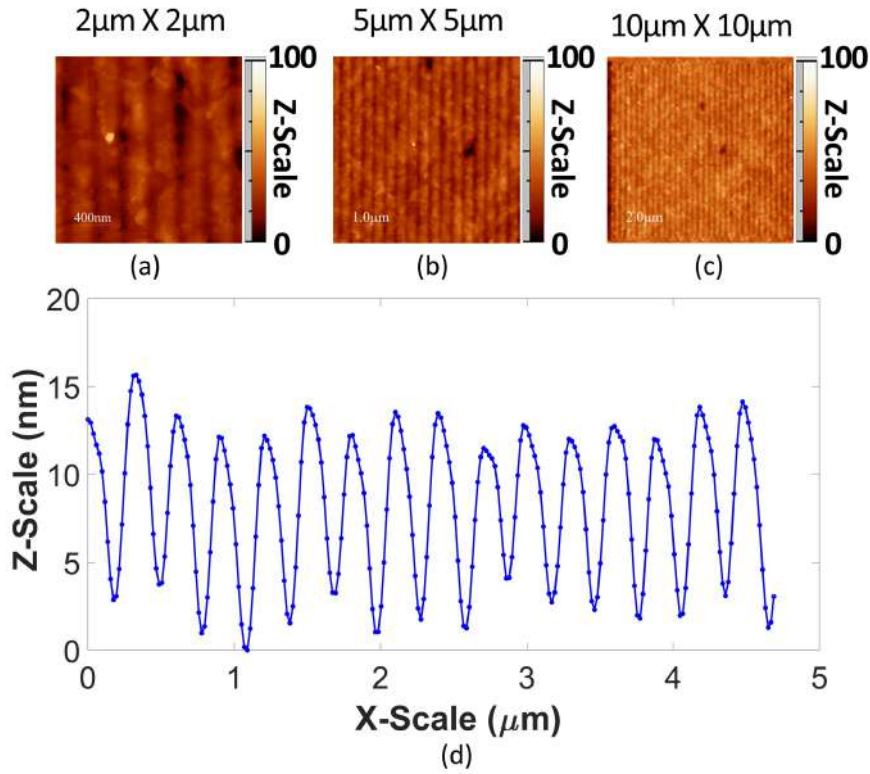


Figure A.7: Surface morphology of custom Si grating sample 2 at different scales: (a)  $2\mu m \times 2\mu m$ , (b)  $5\mu m \times 5\mu m$ , and (c)  $10\mu m \times 10\mu m$ . Additionally, (d) displays the groove profile of the sample at a scale of  $5\mu m \times 5\mu m$ .

$5\mu m$  scan, with variable groove depths ranging from 10-15 nm. Assuming an average groove depth of 12 nm for the gratings, as determined from the previous study in Fig.4.23, the groove depth aligns with a wavelength of 19 nm. Consequently, We conducted optimization on three multilayer structures to achieve a broadband high reflectance at a central wavelength of 19 nm.

### A.3.2 Optimized multilayer structure




The multilayer optimization process was carried out following the description provided in subsection.3.2.1.1. The resulting thickness of the material layers for each structure is documented in Table.A.4.

### A.3.3 Analysis of Multilayer on Custom Silicon Gratings Sample 2

After subjecting the three compositions with  $N = 10$  for Si/Mo/B4C, Mo/Si, and Si/B4C to ion beam sputtering, we observed that the deposition of the composition containing B4C failed due to mechanical stress. We then examined all three compositions using GIXR, as depicted in Fig.A.8.

In Fig.A.3, it is evident that the dominant influence on the spectra is attributed to the multilayer, as changing the substrate from a flat Si substrate to a Si grating substrate does not alter the positions of the Bragg peaks. Consequently, we conducted an analysis of the Mo/Si multilayer, as shown in Fig.A.8, using IMD software. The results of

Table A.4: Comparative of three distinct optimized multilayer structures, showcasing the layer thicknesses acquired through the optimization process.

Parameters	multilayer [Si/B4C]	multilayer [Mo/Si]	multilayer [Si/Mo/B4C]
Schematic			
Si Thickness	4.847 nm	4.788 nm	3.857 nm
B4C Thickness	4.692 nm	-	2.000 nm
Mo Thickness	-	4.878 nm	3.737 nm

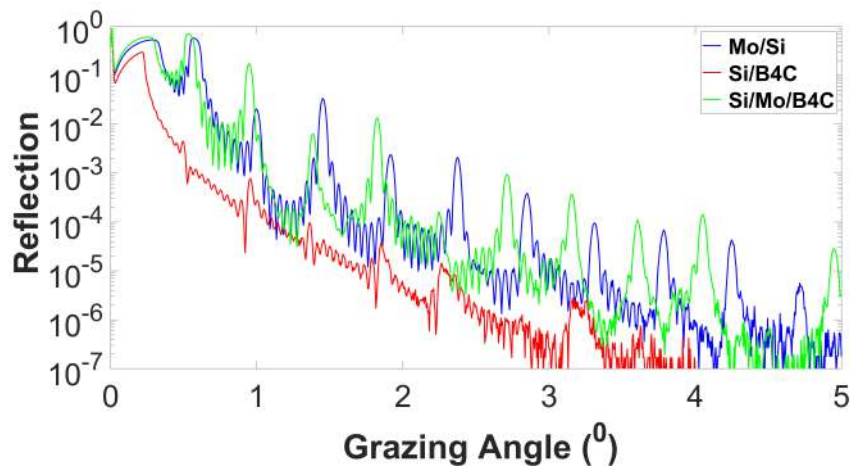


Figure A.8: GIXR measurements conducted on a Si grating sample with multilayer compositions of  $N = 10$ , including Si/Mo/B4C (green line), Mo/Si (blue line), and Si/B4C (red line).

Table A.5: Layer thickness and interfacial roughness for the analyzed periodic Mo/Si of  $N = 20$  on the Si substrate.

Material	Thickness (nm)	Interface	Roughness (nm)
a-Si	4.779	Oxide-on-a-Si and Mo-on-a-Si	0.500
Mo	4.591	a-Si-on-Mo	0.350
Si Substrate	$\infty$	Al-on- Si substrate	0.350

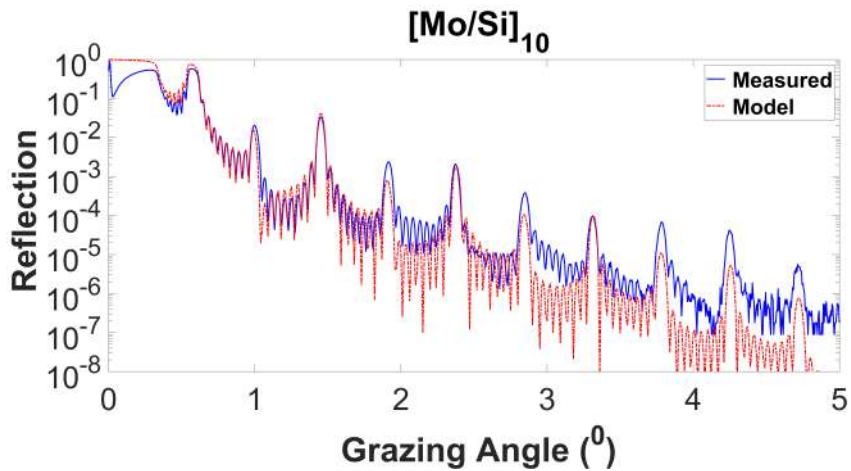


Figure A.9: GIXR measurements were performed on a Si grating sample containing multilayer Mo/Si compositions with  $N = 10$ . The data is presented as the measured results (blue line) and the corresponding modeled data (red dashed line).

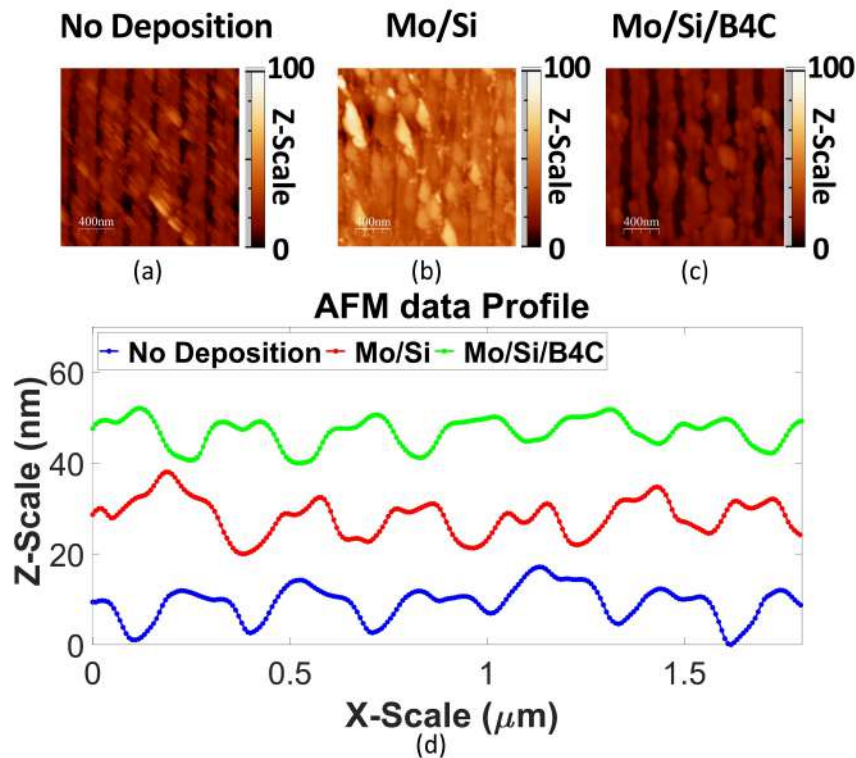


Figure A.10: Surface morphology of a custom Si grating sample 2 at different deposition stages: (a) without deposition, (b) after 10 periods of Mo/Si deposition, and (c) after 10 periods of Al/Mo/B4C deposition. Additionally, (d) presents the groove profile of the undeposited sample in blue, the profile after 10 periods of Mo/Si deposition in red with a Y-axis shift of 20 nm, and the profile after 10 periods of Mo/Si/B4C deposition in green with a Y-axis shift of 40 nm.

this analysis for the deposited Mo/Si with  $N = 10$  are presented in Table.A.5.

### A.3.4 AFM Profile of Custom Silicon Gratings Sample 2 Following Deposition

We deposited 10 periods of Mo/Si, Mo/Si/B4C on a test grating after cleaning it with acetone to prevent dust from accumulating in the grating grooves. On the same day, we conducted an examination of the grating profile using an AFM with a non-contact method. This examination included a part of the grating that had not undergone deposition, as well as two other parts of the grating that were coated with 10 periods of Mo/Si and Mo/Si/B4C, respectively, using the IBS deposition machine, as illustrated in Fig. A.10.

## A.4 Layer growth model

The modulation of the deposition rate is proportional to the local curvature.

$$\frac{\partial z}{\partial t} = v_0 + c \frac{\partial^2 z}{\partial x^2} \quad (\text{A.1})$$

In this context,  $z$  represents the position of the growth interface, while  $v_0$  denotes the average deposition rate.

Under the assumption that the growth interface profile can be expressed using its Fourier expansion.

$$z(x, t) = \sum_{n=-N}^N a_n(t) \exp(j \frac{2\pi n x}{p}) \quad (\text{A.2})$$

Then,

$$\frac{\partial}{\partial t} z(x, t) = \sum_{n=-N}^N \left( \frac{da_n(t)}{dt} \exp(j \frac{2\pi n x}{p}) \right) = v_0 - c \frac{4\pi^2}{p^2} \sum_{n=-N}^N n^2 a_n(t) \exp(j \frac{2\pi n x}{p}) \quad (\text{A.3})$$

$$a_0(t) = a_0(0) + v_0 t \quad (\text{A.4})$$

If  $n \neq 0$

$$\frac{da_n}{dt} = -kn^2 a_n \rightarrow a_n = a_n(0) \exp(-ktn^2) \quad (\text{A.5})$$

In Equation.A.5, it's worth noting that the damping factor  $k$  possesses a dimension that is inversely related to time. However, in our code calculations, we treat  $k$  as dimensionless, as we interpret it as a measure of how damping affects the deposition process. we make the assumption that  $k$  does not rely on the deposited material. Consequently,  $t$  can be interpreted as the average deposited thickness, allowing for straightforward computation of the composition at a given  $(x, z)$  coordinate.

To demonstrate the applicability of our profile evolution model for multilayer deposition, we utilized Set#1 gratings as a representative example. The initial profiles of the grating, obtained through AFM, are depicted by the blue



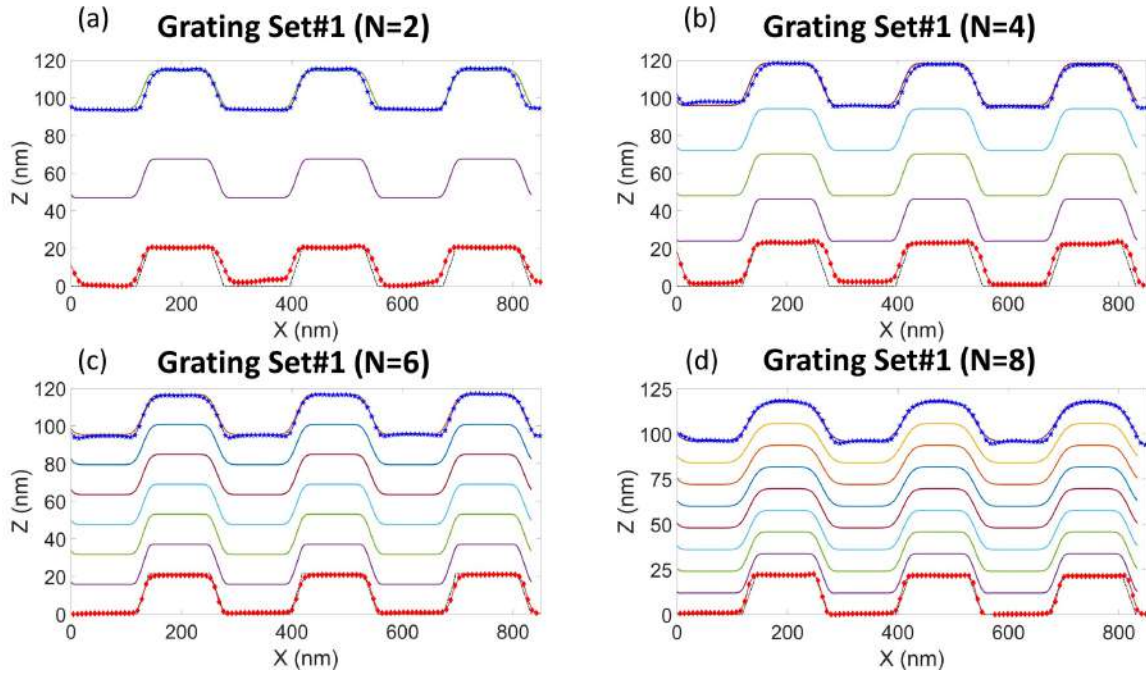


Figure A.11: Profile model of multilayer gratings from Set#1 shown for different numbers of periods: (a)  $N = 2$ , (b)  $N = 4$ , (c)  $N = 6$ , and (d)  $N = 8$ . The red dot curve represents the AFM profile of the grating before deposition, while the blue dot curve represents the AFM profile of the grating after deposition.

Table A.6: Multilayer Period and Corresponding Damping Parameters

Multilayer Period	Damping Factor/Period ( $\text{\AA}^{-1}$ )
$N = 2$	0.008
$N = 4$	0.005
$N = 6$	0.004
$N = 8$	0.008

and red curves in Fig.A.11, representing the pre-deposition and post-deposition states, respectively. Our results exhibit satisfactory agreement for  $N = 2$  to  $N = 8$ . However, due to limitations in capturing changes in the fill factor, we were unable to successfully model  $N = 16$  using this particular approach. In Table.A.6, we present the values of  $k$  that were employed to achieve a satisfactory alignment between the initial and final grating profiles with the AFM average profile.

In addition, despite the model's failure for  $N = 16$  attributed to the fill factor, we successfully obtained a top sinusoidal profile and a bottom flat profile for the final  $N = 16$  profile. This outcome aligns with the measured AFM profile average for  $N = 16$ . Consequently, the model serves as a valuable tool for comprehending the multilayer evolution of the grating profile.

## A.5 Summary

In this appendix, we conducted a comprehensive investigation into the evolution of various multilayer compositions on custom Si gratings. These custom Si gratings were meticulously crafted at Thales laboratories and underwent initial characterization through Atomic Force Microscopy (AFM) prior to the deposition process.

To explore the deposition process further, we employed two distinct deposition methods: ion beam sputtering and magnetron sputtering deposition. Specifically, we deposited 20 periods of Al/Mo/SiC on the custom Si gratings and subsequently examined them using Transmission Electron Microscopy (TEM) with Energy-Dispersive X-ray Spectroscopy (EDX). The results of this analysis revealed intriguing and somewhat unconventional behavior in the evolution of the multilayer structure.

In addition to the aforementioned investigation, we carried out deposition of 10 periods of multilayer compositions, including Mo/Si, Si/B<sub>4</sub>C, and Si/Mo/B<sub>4</sub>C, on Si custom gratings, employing ion beam sputtering as the deposition technique. We conducted both pre-deposition and post-deposition AFM characterizations of these multilayers. Notably, we observed a significant issue with multilayers containing B<sub>4</sub>C, which appeared to experience structural failure due to mechanical stress within the material.

Furthermore, we endeavored to develop a model that could elucidate the evolution of multilayers on these gratings. To construct this model, we utilized the AFM data acquired from the deposition process on gratings set#1. However, it is important to note that the model exhibited success in describing periodic structures within the range of  $N = 2$  to  $N = 8$ . Unfortunately, it proved inadequate when applied to  $N = 16$ . Therefore, it is evident that further refinement and enhancement of the model are necessary, particularly in addressing aspects such as fill factor evolution and depth variation.

This research serves as a valuable foundation for future investigations in this field, and we look forward to improving our understanding of these complex multilayer systems.





## Appendix B

### Appendix Tables

Table B.1: Comparison of DC and RF Magnetron Sputtering

	Direct Current (DC) magnetron sputtering	Radio Frequency (RF) magnetron sputtering
Power Supply	DC generates ionization and sputtering with an electric field	RF employs an alternating electric field
Plasma Generation	Relies on ionization of sputtering gas by high voltage	Relies on the high-frequency electric field for ionization of sputtering gas
Target Voltage	DC applies high negative voltage to accelerate ions for sputtering	RF operates at a lower voltage due to the alternating electric field
Plasma Density and Uniformity	DC achieves lower plasma density resulting in less uniform deposition	RF achieves higher plasma density resulting in more uniform deposition
Target Cooling	DC magnetron sputtering can cause significant heating of the target due to high voltage and power	RF magnetron sputtering generates less heat and is more suitable for temperature-sensitive materials
Applications	DC is used for deposition on conductive materials	RF is preferred for deposition on non-conductive or temperature-sensitive substrates

Table B.2: the model design thickness for aperiodic design for grating set#1.

-	Material	Design 1 -Thickness (nm)
Oxidation Layer	SiO <sub>2</sub>	-
Layer 1	SiC	3.94
Layer 2	Mo	3.87
Layer 3	Al	6.78
Layer 4	SiC	3.18
Layer 5	Mo	4.90
Layer 6	Al	6.50
Layer 7	SiC	3.40
Layer 8	Mo	3.81
Layer 9	Al	7.61
Layer 10	SiC	10.35
Layer 11	Mo	5.44
Layer 12	Al	4.99
Substrate	SiO <sub>2</sub>	∞

Table B.3: the model design thickness for aperiodic design for grating set#2.

-	Material	Design 2 -Thickness (nm)	Design 3 -Thickness (nm)
Oxidation Layer	SiO <sub>2</sub>	-	-
Layer 1	SiC	2.90	3.03
Layer 2	Mo	3.39	3.10
Layer 3	Al	5.64	5.86
Layer 4	SiC	2.01	2.03
Layer 5	Mo	4.23	4.01
Layer 6	Al	5.13	5.35
Layer 7	SiC	2.01	2.03
Layer 8	Mo	4.65	4.38
Layer 9	Al	4.87	5.12
Layer 10	SiC	2.01	2.03
Layer 11	Mo	4.52	4.56
Layer 12	Al	3.51	5.16
Layer 13	SiC	1.70	2.36
Layer 14	Mo	2.01	2.89
Layer 15	Al	3.53	3.57
Layer 16	SiC	1.50	1.08
Layer 17	Mo	5.52	2.45
Layer 18	Al	5.42	4.45
Layer 19	SiC	-	2.08
Layer 20	Mo	-	4.76
Layer 21	Al	-	4.66
Layer 22	SiC	-	2.21
Layer 23	Mo	-	4.76
Layer 24	Al	-	3.54
Substrate	SiO <sub>2</sub>	∞	∞

Table B.4: the model design thickness for aperiodic design for grating set#3.

-	Material	Design 4 -Thickness (nm)	Design 5 -Thickness (nm)
Oxidation Layer	SiO <sub>2</sub>	-	-
Layer 1	SiC	2.79	3.00
Layer 2	Mo	3.69	3.46
Layer 3	Al	4.30	4.42
Layer 4	SiC	1.99	2.01
Layer 5	Mo	4.15	4.07
Layer 6	Al	3.95	4.08
Layer 7	SiC	1.99	2.01
Layer 8	Mo	4.38	4.28
Layer 9	Al	3.79	3.92
Layer 10	SiC	2.00	2.01
Layer 11	Mo	4.56	4.46
Layer 12	Al	3.52	3.61
Layer 13	SiC	0.98	2.54
Layer 14	Mo	2.00	2.71
Layer 15	Al	3.51	3.51
Layer 16	SiC	0.53	0.53
Layer 17	Mo	4.63	2.18
Layer 18	Al	4.53	3.90
Layer 19	SiC	-	2.04
Layer 20	Mo	-	4.52
Layer 21	Al	-	3.66
Layer 22	SiC	-	2.58
Layer 23	Mo	-	2.00
Layer 24	Al	-	3.51
Substrate	SiO <sub>2</sub>	∞	∞

## Appendix C

### Appendix Figures

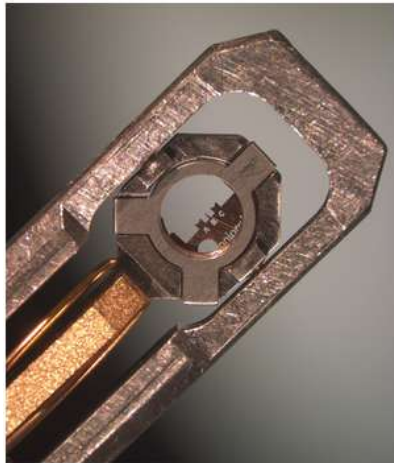


Figure C.1: Photography of TEM sample holder.

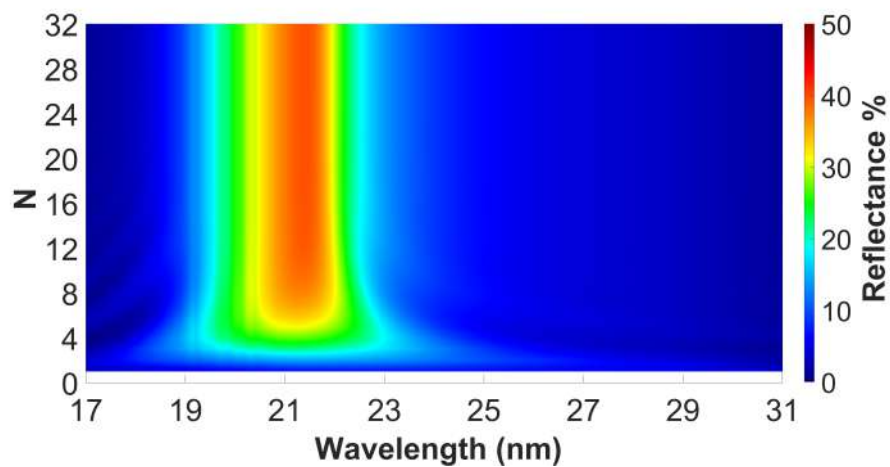


Figure C.2: TE simulated reflectance of the optimized periodic Al/Mo/SiC multilayer as a function of wavelength and the number of periods (N) at  $\theta = 5^\circ$  for set#2.

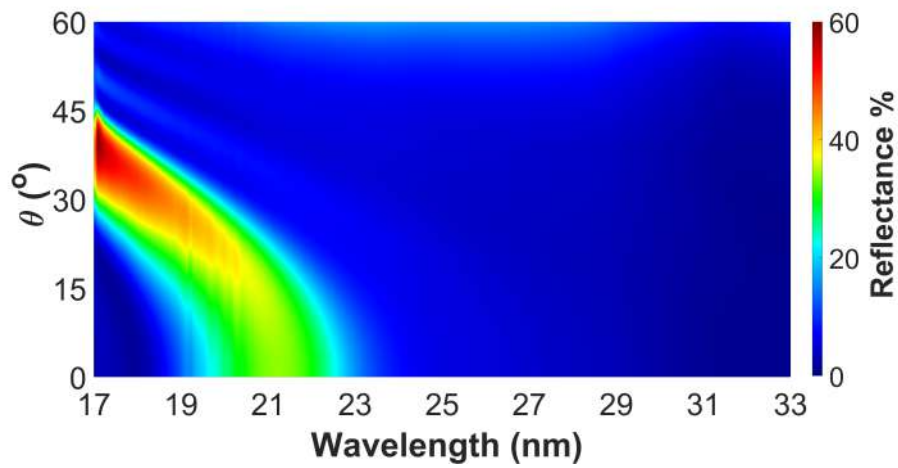


Figure C.3: TE simulated reflectance of the optimized periodic Al/Mo/SiC multilayer  $N=6$  as a function of wavelength and incidence ( $\theta$ ) for set#2.

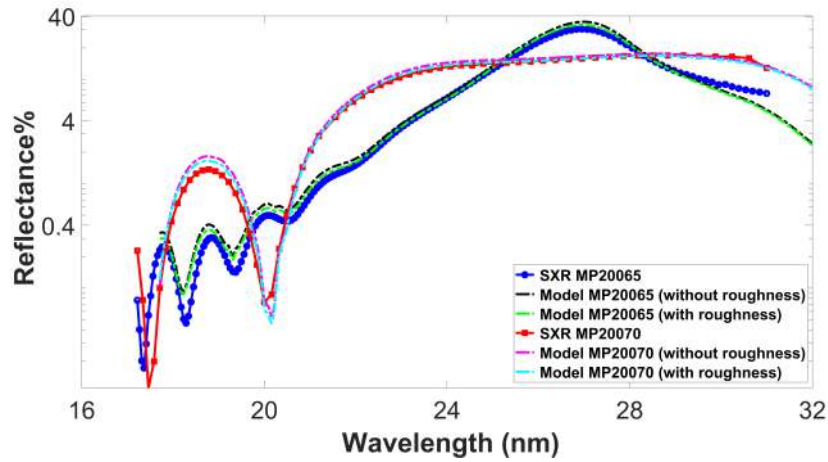


Figure C.4: Logarithmic reflectance of SXR measured and fitted spectra at  $\theta=5^\circ$  for the 10-periods Al/Mo/SiC multilayer (sample MP20065) and the 12 layers aperiodic Al/Mo/SiC multilayer (sample MP20070)

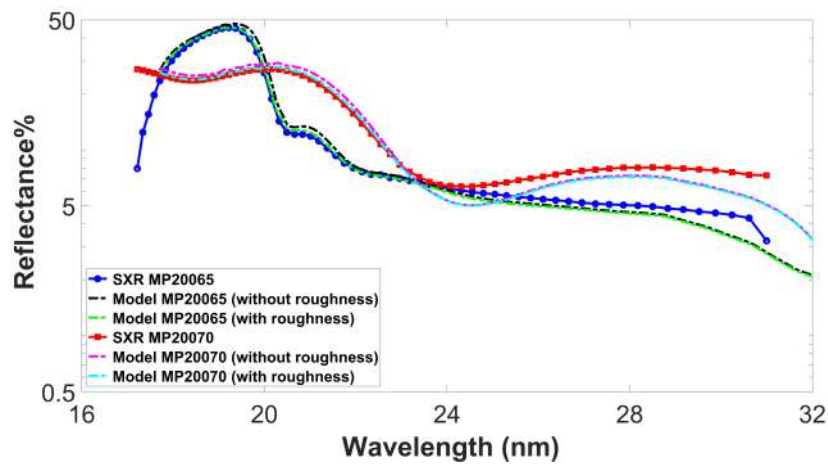


Figure C.5: Logarithmic reflectance of SXR measured and fitted spectra at  $\theta=45^\circ$  for the 10-periods Al/Mo/SiC multilayer (sample MP20065) and the 12 layers aperiodic Al/Mo/SiC multilayer (sample MP20070)

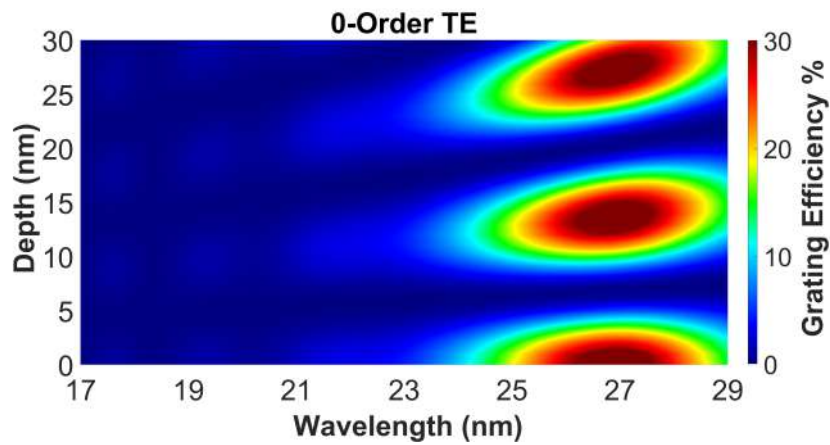


Figure C.6: 0-Order simulation for wavelength as a function of grating efficiency logarithm and grating depth for multilayers on lamellar gratings with N=6 periods multilayers for gratings set#1.

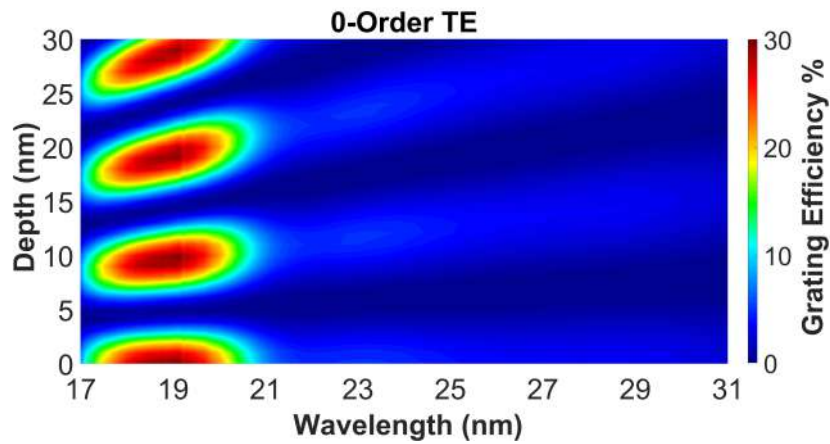


Figure C.7: 0-Order simulation for wavelength as a function of grating efficiency logarithm and grating depth for multilayers on lamellar gratings with N=6 periods multilayers for gratings set#3.

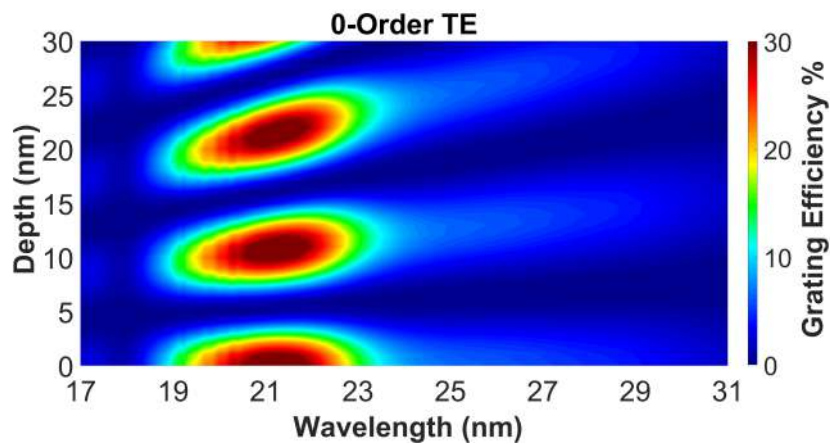


Figure C.8: 0-Order simulation for wavelength as a function of grating efficiency logarithm and grating depth for multilayers on lamellar gratings with N=6 periods multilayers for gratings set#2.



### +1 Order @ $\theta=5^\circ$

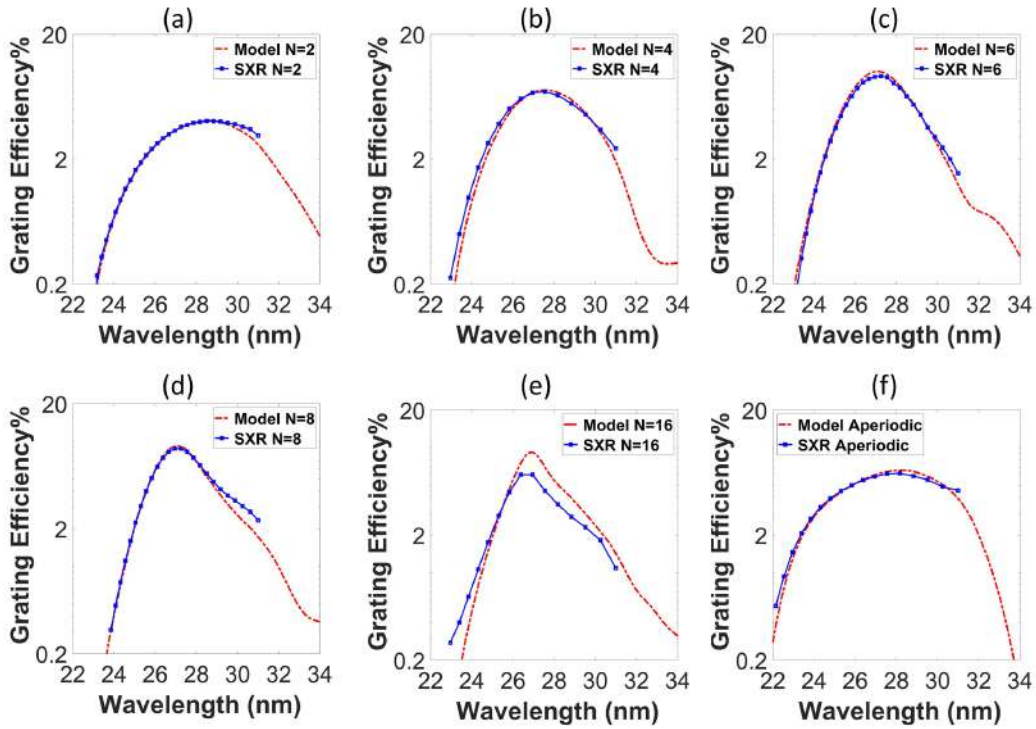


Figure C.9: Measured and modeled logarithm +1 order diffraction efficiency of the multilayer gratings at  $\theta=5^\circ$ : (a) N=2, (b) N=4, (c) N=6, (d) N=8, (e) N=16, and (f) aperiodic.

### +1 Order @ $\theta=45^\circ$

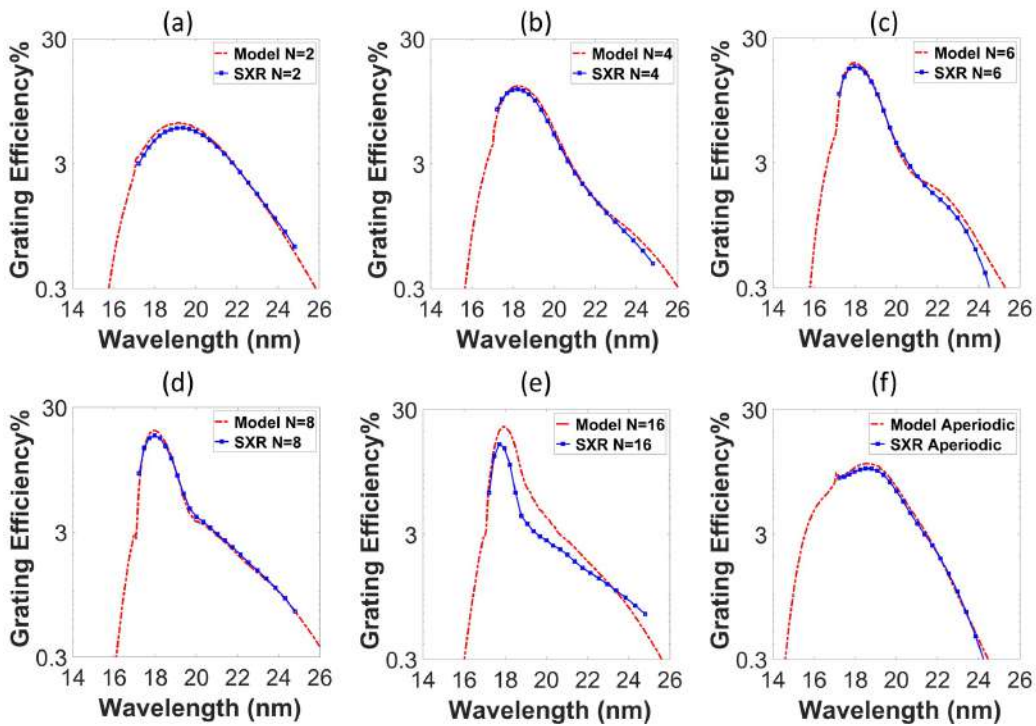


Figure C.10: Measured and modeled logarithm +1 order diffraction efficiency of the multilayer gratings at  $\theta=45^\circ$ : (a) N=2, (b) N=4, (c) N=6, (d) N=8, (e) N=16, and (f) aperiodic.

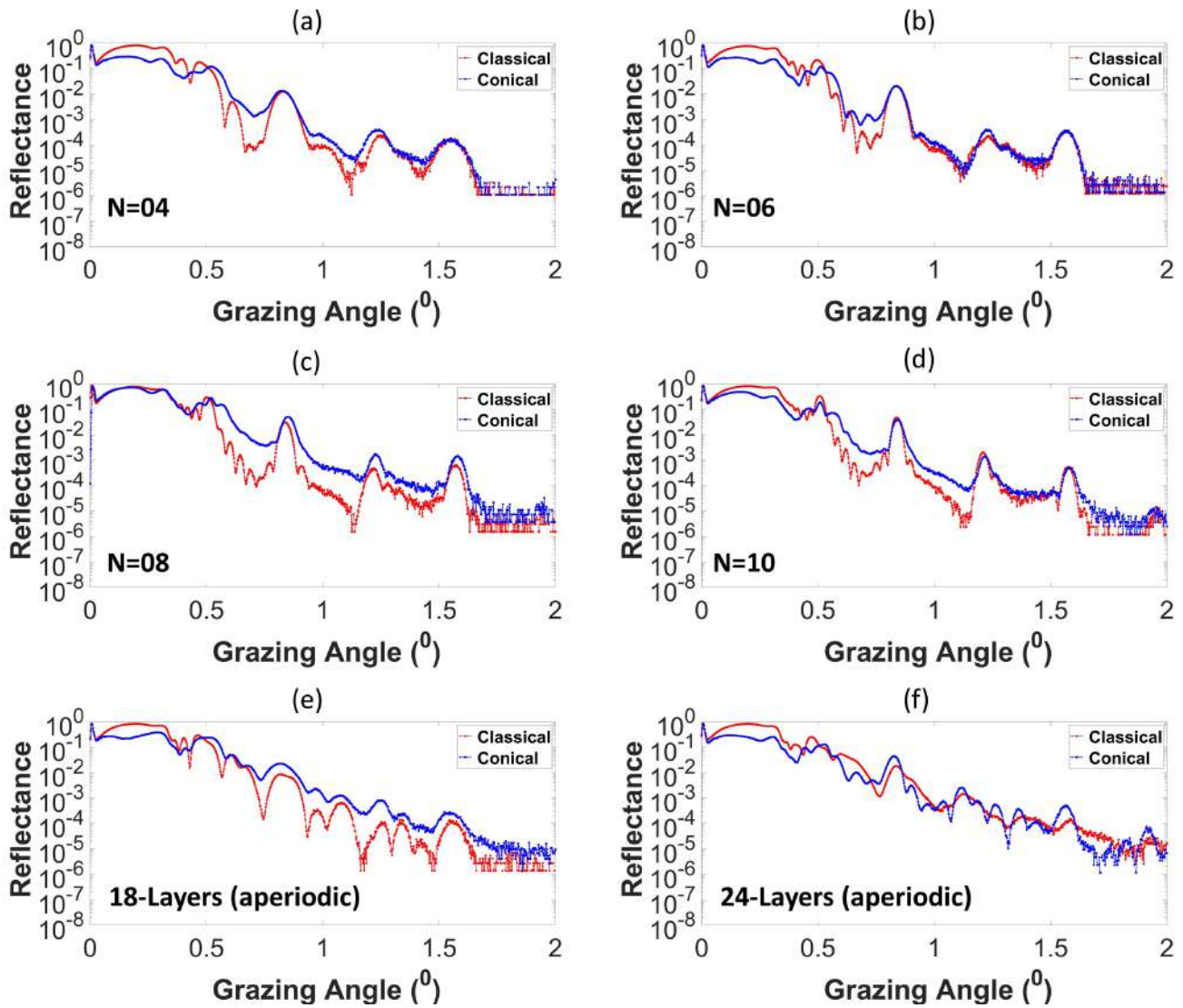


Figure C.11: Classical and Conical GIXR measurements for multilayers on gratings set#2 (a) periodic ( $N = 4$ ), (b) periodic ( $N = 6$ ), (c) periodic ( $N = 8$ ), (d) periodic ( $N = 10$ ), (e) aperiodic (18 – layers) and (f) aperiodic (24 – layers).

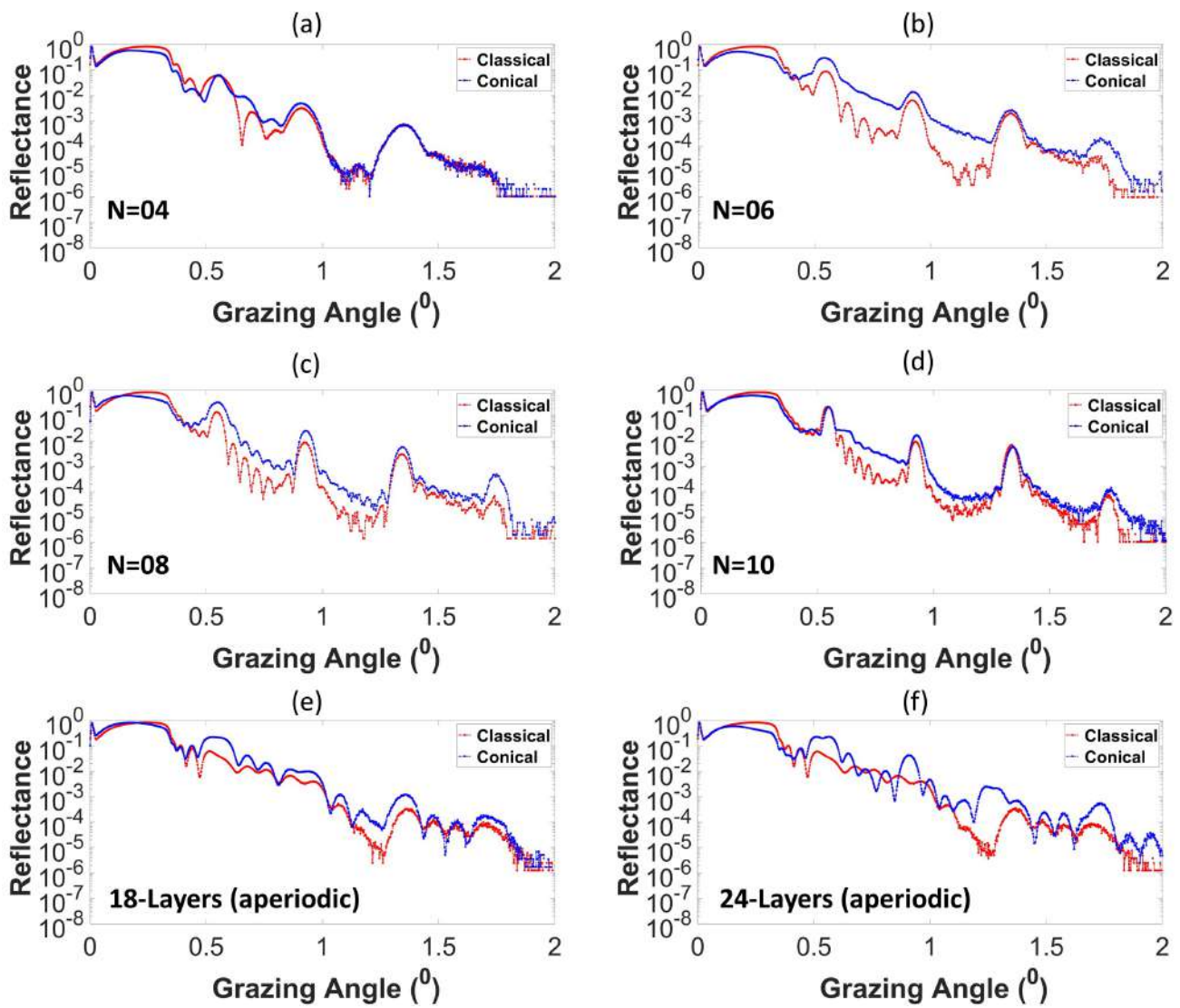


Figure C.12: Classical and Conical GIXR measurements for multilayers on gratings set#3 (a) periodic ( $N = 4$ ), (b) periodic ( $N = 6$ ), (c) periodic ( $N = 8$ ), (d) periodic ( $N = 10$ ), (e) aperiodic (18 – layers) and (f) aperiodic (24 – layers).

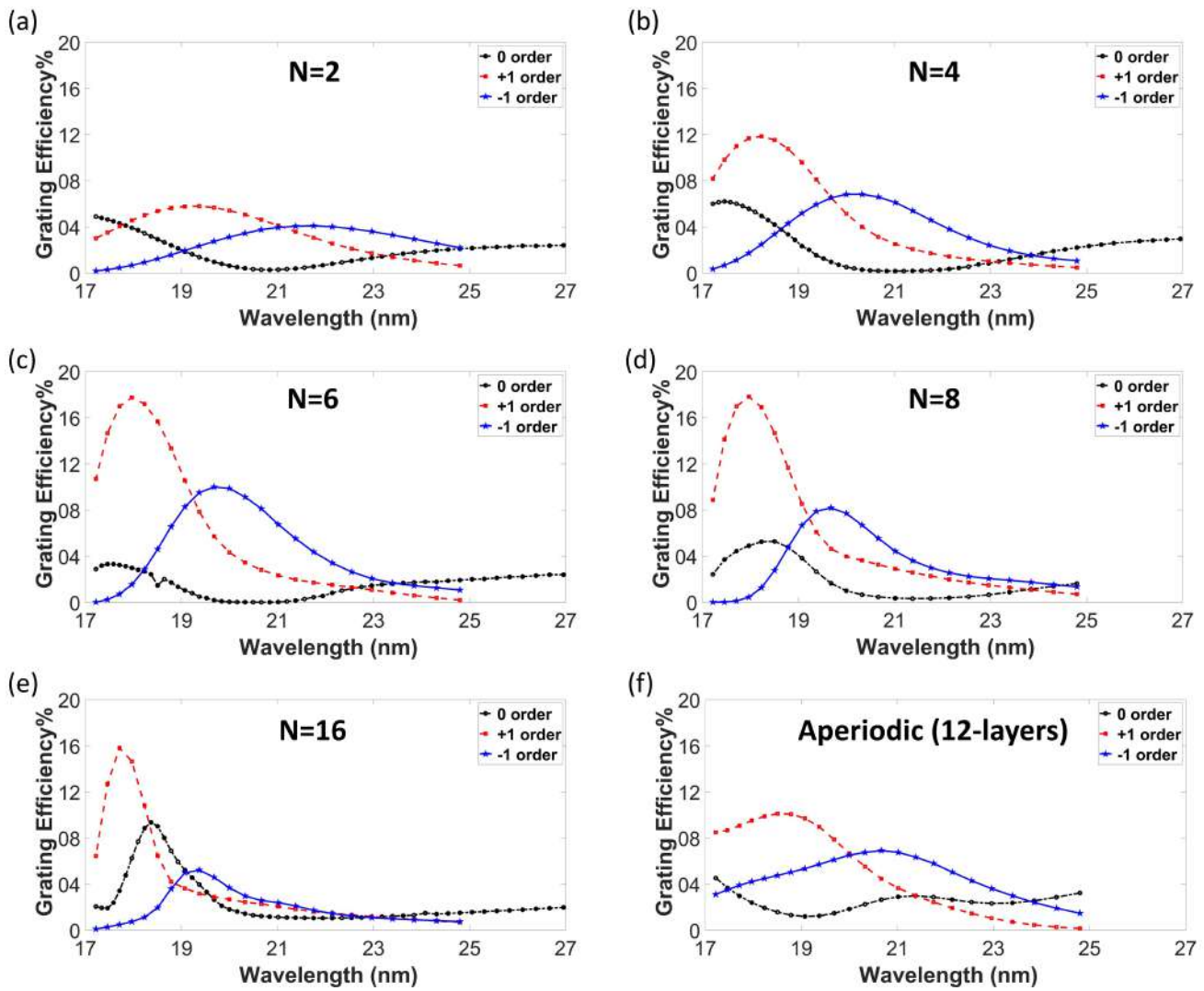


Figure C.13: Measured three orders results for all depositions at  $\theta=45^\circ$  for gratings set#1.

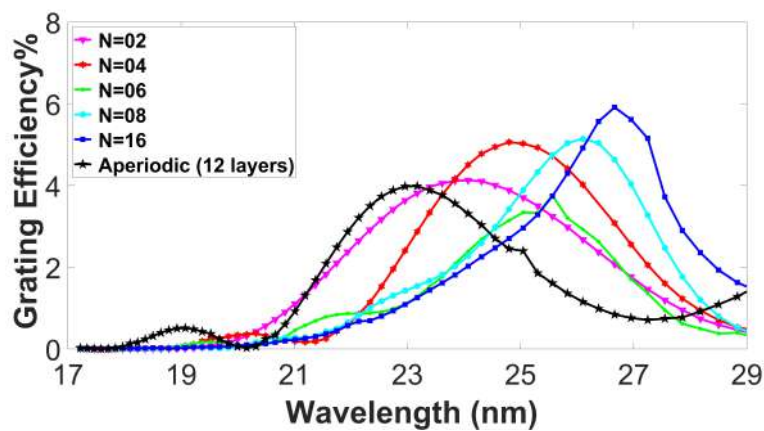


Figure C.14: Measured zero-order results for all depositions at  $\theta=5^\circ$  for gratings set#1.



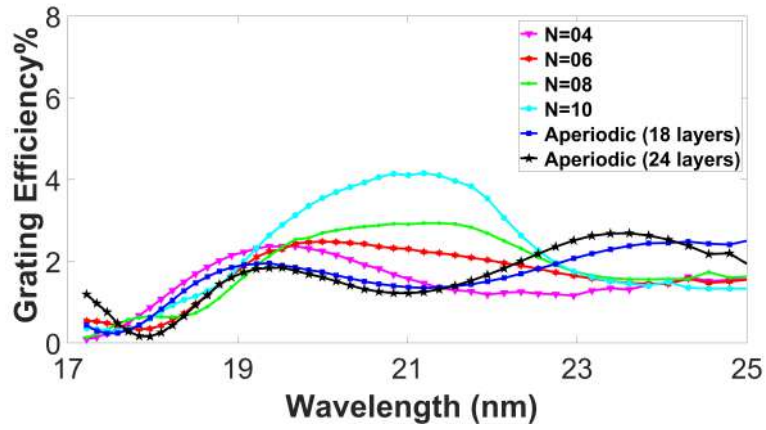


Figure C.15: Measured zero-order results for all depositions at  $\theta=5^\circ$  for gratings set#2.

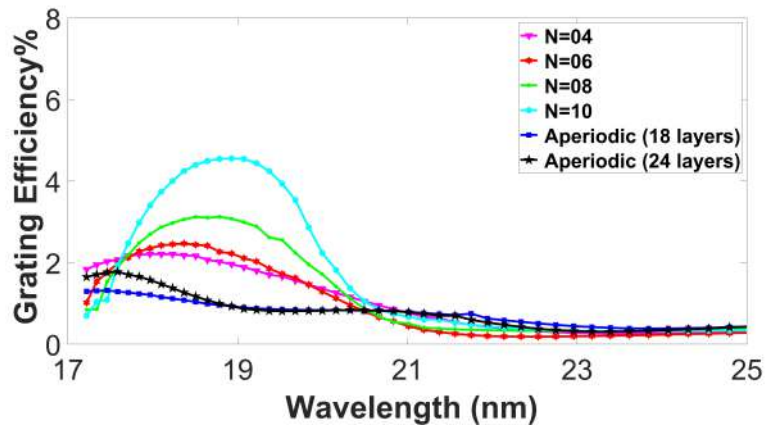


Figure C.16: Measured zero-order results for all depositions at  $\theta=5^\circ$  for gratings set#3.

## Appendix D

# Compendium of Deposition Specifications for Multilayer Coatings on Silica Gratings

Table D.1: Multilayer deposition by magnetron sputtering deposition on the grating set#1 samples.

Sample N	Date	Material	Gating Number	Period Number	N scans	Velocity
MP20066	08/10/2020	Al(Si)/Mo/SiC	Grating 1 (L)	2	SiC=3 Al(Si)=1 Mo=1	SiC=1.220/s Al(Si)=2.010/s Mo=0.510/s
MP20067	08/10/2020	Al(Si)/Mo/SiC	Grating 1 (R)	4	SiC=3 Al(Si)=1 Mo=1	SiC=1.220/s Al(Si)=2.010/s Mo=0.510/s
MP20068	09/10/2020	Al(Si)/Mo/SiC	Grating 2 (L)	6	SiC=3 Al(Si)=1 Mo=1	SiC=1.220/s Al(Si)=2.010/s Mo=0.510/s
MP20069	09/10/2020	Al(Si)/Mo/SiC	Grating 2 (R)	8	SiC=3 Al(Si)=1 Mo=1	SiC=1.220/s Al(Si)=2.010/s Mo=0.510/s
MP20071	14/10/2020	Al(Si)/Mo/SiC	Grating 3 (L)	16	SiC=3 Al(Si)=1 Mo=1	SiC=1.220/s Al(Si)=2.010/s Mo=0.510/s
MP20072	14/10/2020	Al(Si)/Mo/SiC	Grating 3 (R)	Aperiodic (12-layers)	NA	NA

Table D.2: Multilayer deposition by magnetron sputtering deposition on the grating set#2 samples.

Sample N	Date	Material	Gating Number	Period Number	N scans	Velocity
MP21091	08/10/2020	Al(Si)/Mo/SiC	Grating 1 (R)	Aperiodic (18-layers)	NA	NA
MP21090	08/10/2020	Al(Si)/Mo/SiC	Grating 1 (L)	Aperiodic (24-layers)	NA	NA
MP21068	08/10/2020	Al(Si)/Mo/SiC	Grating 2 (L)	4	SiC=1 Al(Si)=1 Mo=3	SiC=1.730/s Al(Si)=2.300/s Mo=0.750/s
MP21069	08/10/2020	Al(Si)/Mo/SiC	Grating 2 (R)	10	SiC=1 Al(Si)=1 Mo=3	SiC=1.730/s Al(Si)=2.300/s Mo=0.750/s
MP21086	08/10/2020	Al(Si)/Mo/SiC	Grating 3 (L)	6	SiC=1 Al(Si)=1 Mo=3	SiC=1.730/s Al(Si)=2.300/s Mo=0.750/s
MP21087	08/10/2020	Al(Si)/Mo/SiC	Grating 3 (R)	8	SiC=1 Al(Si)=1 Mo=3	SiC=1.730/s Al(Si)=2.300/s Mo=0.750/s

Table D.3: Multilayer deposition by magnetron sputtering deposition on the grating set#3 samples.

Sample N	Date	Material	Gating Number	Period Number	N scans	Velocity
MP21091	08/10/2020	Al(Si)/Mo/SiC	Grating 1 (R)	Aperiodic (18-layers)	NA	NA
MP21090	08/10/2020	Al(Si)/Mo/SiC	Grating 1 (L)	Aperiodic (24-layers)	NA	NA
MP21068	08/10/2020	Al(Si)/Mo/SiC	Grating 2 (L)	4	SiC=1 Al(Si)=1 Mo=3	SiC=1.730/s Al(Si)=3.000/s Mo=0.750/s
MP21069	08/10/2020	Al(Si)/Mo/SiC	Grating 2 (R)	10	SiC=1 Al(Si)=1 Mo=3	SiC=1.730/s Al(Si)=3.000/s Mo=0.750/s
MP21086	08/10/2020	Al(Si)/Mo/SiC	Grating 3 (L)	6	SiC=1 Al(Si)=1 Mo=3	SiC=1.730/s Al(Si)=3.000/s Mo=0.750/s
MP21087	08/10/2020	Al(Si)/Mo/SiC	Grating 3 (R)	8	SiC=1 Al(Si)=1 Mo=3	SiC=1.730/s Al(Si)=3.000/s Mo=0.750/s





# Bibliography

- [1] David Attwood. *Soft x-rays and extreme ultraviolet radiation: principles and applications*. Cambridge university press, 2000.
- [2] Cxro x-ray interactions with matter. [http://henke.lbl.gov/optical\\_constants/](http://henke.lbl.gov/optical_constants/). Accessed: 2021-07-01.
- [3] Armin Bayer, Frank Barkusky, Stefan Döring, Bernhard Flöter, Christian Peth, and Klaus Mann. Active beam control for the euv/xuv spectral range using an adaptive kirkpatrick-baez arrangement. In *Optical Design and Engineering III*, volume 7100, pages 483–495. SPIE, 2008.
- [4] Jennifer Rebellato. *Miroirs interférentiels efficaces dans l'extrême ultraviolet pour la physique solaire*. PhD thesis, Université Paris-Saclay, 2020.
- [5] All about diffraction gratings. <https://www.edmundoptics.eu/knowledge-center/application-notes/optics/all-about-diffraction-gratings/>. accessed Jul. 27, 2022.
- [6] Solar core. [https://en.wikipedia.org/wiki/Solar\\_core](https://en.wikipedia.org/wiki/Solar_core). accessed Jan. 19, 2022.
- [7] Thomas N Woods, Rachel Hock, Frank Eparvier, Andrew R Jones, Phillip C Chamberlin, James A Klimchuk, Leonid Didkovsky, Darrell Judge, John Mariska, Harry Warren, et al. New solar extreme-ultraviolet irradiance observations during flares. *The Astrophysical Journal*, 739(2):59, 2011.
- [8] Marie-Francoise Ravet, Françoise Bridou, Xueyan Zhang-Song, Arnaud Jerome, Franck Delmotte, Raymond Mercier, Marie Bougnet, Philippe Bouyries, and Jean-Pierre Delaboudiniere. Ion-beam-deposited mo/si multilayers for euv imaging applications in astrophysics. In *Advances in Optical Thin Films*, volume 5250, pages 99–108. SPIE, 2004.
- [9] Nasa scientific visualization studio. <https://svs.gsfc.nasa.gov/4496>. Accessed: 2023-06-14.
- [10] Esa - solar orbiter captures giant solar eruption. [https://www.esa.int/ESA\\_Multimedia/Images/2022/02/Solar\\_Orbiter\\_captures\\_giant\\_solar\\_eruption#.Yh-e3jnJ0iQ.link](https://www.esa.int/ESA_Multimedia/Images/2022/02/Solar_Orbiter_captures_giant_solar_eruption#.Yh-e3jnJ0iQ.link). accessed Jul. 28, 2022.

- [11] Toshifumi Shimizu, Shinsuke Imada, Tomoko Kawate, Yoshinori Suematsu, Hirohisa Hara, Toshihiro Tsuzuki, Yukio Katsukawa, Masahito Kubo, Ryoko Ishikawa, Tetsuya Watanabe, et al. The solar-c (euvs) mission: the latest status. In *Space Telescopes and Instrumentation 2020: Ultraviolet to Gamma Ray*, volume 11444, pages 113–119. SPIE, 2020.
- [12] John F Seely, Charles M Brown, David L Windt, Soizik Donguy, and Benjawan Kjornrattanawanich. Normal-incidence efficiencies of multilayer-coated laminar gratings for the extreme-ultraviolet imaging spectrometer on the solar-b mission. *Applied optics*, 43(7):1463–1471, 2004.
- [13] David José Pereira Coelho. *Fabrication of Gd<sub>5</sub>(Si<sub>1-x</sub>Ge<sub>x</sub>)<sub>4</sub> Nanoparticles by Femto and Nanosecond Pulsed Laser Ablation in Liquids*. PhD thesis, Universidade do Porto (Portugal), 2019.
- [14] Georg Schitter, Juergen Steininger, Friedjof CA Heuck, and Urs Staufer. Towards fast afm-based nanometrology and nanomanufacturing. *International Journal of Nanomanufacturing*, 8(5-6):392–418, 2012.
- [15] S Kaiser Ali, Umashankar Das, Yanjie Lu, Vijayanada Kundapur, and Tim May. Synchrotron radiation: Applications in diagnosis and treatment of malignant brain tumors. In *Diagnostic techniques and surgical management of brain tumors*. IntechOpen, 2011.
- [16] M Idir, S Brochet, A Delmotte, B Lagarde, P Mercere, T Moreno, F Polack, and M Thomasset. Le pôle de métrologie de soleil. In *Journal de Physique IV (Proceedings)*, volume 138, pages 265–274. EDP sciences, 2006.
- [17] Evgueni Meltchakov, Christophe Hecquet, Marc Roulliay, Sébastien De Rossi, Yves Ménesguen, Arnaud Jérôme, Françoise Bridou, Françoise Varniere, M-F Ravet-Krill, and Franck Delmotte. Development of al-based multilayer optics for euv. *Applied Physics A*, 98(1):111–117, 2010.
- [18] Evgueni Meltchakov, Sébastien De Rossi, Raymond Mercier, Françoise Varniere, Arnaud Jérôme, Frédéric Auchère, Xueyan Zhang, Marc Roulliay, and Franck Delmotte. Single and multi-channel al-based multilayer systems for space applications in euv range. In *Damage to VUV, EUV, and X-ray Optics IV; and EUV and X-ray Optics: Synergy between Laboratory and Space III*, volume 8777, pages 288–296. SPIE, 2013.
- [19] John F Seely. Multilayer grating for the extreme ultraviolet spectrometer (eis). In *X-Ray Optics, Instruments, and Missions IV*, volume 4138, pages 174–181. SPIE, 2000.
- [20] G Steven Bales, Robijn Bruinsma, Elliott A Eklund, RPU Karunasiri, Joseph Rudnick, and Andrew Zangwill. Growth and erosion of thin solid films. *Science*, 249(4966):264–268, 1990.
- [21] Qiushi Huang, Viacheslav Medvedev, Robbert van de Kruijs, Andrey Yakshin, Eric Louis, and Fred Bijkerk. Spectral tailoring of nanoscale euv and soft x-ray multilayer optics. *Applied physics reviews*, 4(1):011104, 2017.

- [22] Kenneth P Dere, Giulio Del Zanna, Peter R Young, Enrico Landi, and Ralph S Sutherland. Chianti—an atomic database for emission lines. xv. version 9, improvements for the x-ray satellite lines. *The Astrophysical Journal Supplement Series*, 241(2):22, 2019.
- [23] Wilhelm Conrad Röntgen. *Ueber eine neue Art von Strahlen*. Phys.-med. Gesellschaft, 1895.
- [24] Yuchun Tu. *Multilayer monochromators for EUV and X-ray optics and the interface characterization*. PhD thesis, Paris 6, 2015.
- [25] AEH Gaballah, P Nicolosi, Nadeem Ahmed, K Jimenez, G Pettinari, A Gerardino, and P Zuppella. Euv polarimetry for thin film and surface characterization and euv phase retarder reflector development. *Review of Scientific Instruments*, 89(1):015108, 2018.
- [26] JA Anna Selvan, Alan E Delahoy, Sheyu Guo, and Yuan-Min Li. A new light trapping tco for nc-si: H solar cells. *Solar energy materials and solar cells*, 90(18-19):3371–3376, 2006.
- [27] Taesoo D Lee and Abasifreke U Ebong. A review of thin film solar cell technologies and challenges. *Renewable and Sustainable Energy Reviews*, 70:1286–1297, 2017.
- [28] Jeronimo Buencuerpo, Luis E Munioz-Camuniez, Maria L Dotor, and Pablo A Postigo. Optical absorption enhancement in a hybrid system photonic crystal–thin substrate for photovoltaic applications. *Optics Express*, 20(104):A452–A464, 2012.
- [29] Detlev Ristau and Henrik Ehlers. Thin film optical coatings. In *Springer Handbook of Lasers and Optics*, pages 401–424. Springer, 2012.
- [30] Eberhard Spiller. *Soft X-ray optics*, volume 15. SPIE press, 1994.
- [31] Asim Jilani, Mohamed Shaaban Abdel-Wahab, and Ahmed Hosny Hammad. Advance deposition techniques for thin film and coating. *Modern Technologies for Creating the Thin-film Systems and Coatings*, 2(3):137–149, 2017.
- [32] Hendrik Anthony Kramers. La diffusion de la lumiere par les atomes. In *Atti Cong. Intern. Fisica (Transactions of Volta Centenary Congress) Como*, volume 2, pages 545–557, 1927.
- [33] BL Henke, P Lee, TJ Tanaka, RL Shimabukuro, and BK Fujikawa. Low-energy x-ray interaction coefficients: Photoabsorption, scattering, and reflection:  $E = 100\text{--}2000$  eV  $z = 1\text{--}94$ . *Atomic data and nuclear data tables*, 27(1):1–144, 1982.
- [34] Carlos F Bunge, Jose A Barrientos, and A Vivier Bunge. Roothaan-hartree-fock ground-state atomic wave functions: Slater-type orbital expansions and expectation values for  $z = 2\text{--}54$ . *Atomic data and nuclear data tables*, 53(1):113–162, 1993.

- [35] P Nicolosi. Euv multilayer optics: Design, development and metrology. *Short Wavelength Laboratory Sources*, pages 283–312, 2014.
- [36] LRB Elton and Daphne F Jackson. X-ray diffraction and the bragg law. *American Journal of Physics*, 34(11):1036–1038, 1966.
- [37] Alain J Corso and Maria G Pelizzo. Extreme ultraviolet multilayer nanostructures and their application to solar plasma observations: A review. *Journal of nanoscience and nanotechnology*, 19(1):532–545, 2019.
- [38] Catherine Burcklen, Tom Pardini, Jennifer Alameda, Jeff Robinson, Yuriy Platonov, Chris Walton, and Regina Soufli. Depth-graded mo/si multilayer coatings for hard x-rays. *Optics Express*, 27(5):7291–7306, 2019.
- [39] KM Skulina, CS Alford, RM Bionta, DM Makowiecki, EM Gullikson, R Soufli, JB Kortright, and JH Underwood. Molybdenum/beryllium multilayer mirrors for normal incidence in the extreme ultraviolet. *Applied Optics*, 34(19):3727–3730, 1995.
- [40] Annalisa D’Arco, Maria Antonietta Ferrara, Maurizio Indolfi, Vitaliano Tufano, and Luigi Sirleto. Implementation of stimulated raman scattering microscopy for single cell analysis. In *Nonlinear Optics and Applications X*, volume 10228, pages 132–139. SPIE, 2017.
- [41] Andrew Aquila, Farhad Salmassi, Yanwei Liu, and Eric M Gullikson. Tri-material multilayer coatings with high reflectivity and wide bandwidth for 25 to 50 nm extreme ultraviolet light. *Optics Express*, 17(24):22102–22107, 2009.
- [42] Min-Hui Hu, Karine Le Guen, Jean-Michel André, Philippe Jonnard, Evgueni Meltchakov, Franck Delmotte, and Anouk Galtayries. Structural properties of al/mo/sic multilayers with high reflectivity for extreme ultraviolet light. *Optics Express*, 18(19):20019–20028, 2010.
- [43] Jennifer Rebellato, Regina Soufli, Evgueni Meltchakov, Eric Gullikson, Sébastien de Rossi, and Franck Delmotte. High efficiency al/sc-based multilayer coatings in the euv wavelength range above 40 nanometers. *Optics Letters*, 45(4):869–872, 2020.
- [44] Diffraction efficiency - plymouth grating laboratory. <https://www.plymouthgrating.com/guidance/technical-notes/fundamentals/diffraction-efficiency/>. accessed Jul. 27, 2022.
- [45] Xiaowei Yang, Igor V Kozhevnikov, Qiushi Huang, Hongchang Wang, Kawal Sawhney, and Zhanshan Wang. Wideband multilayer gratings for the 17–25 nm spectral region. *Optics Express*, 24(13):15079–15092, 2016.
- [46] James E Harvey and Richard N Pfisterer. Understanding diffraction grating behavior: including conical diffraction and rayleigh anomalies from transmission gratings. *Optical Engineering*, 58(8):087105–087105, 2019.

- [47] W Jark. Enhancement of diffraction grating efficiencies in the soft x-ray region by a multilayer coating. *Optics communications*, 60(4):201–205, 1986.
- [48] Andrew M Hawryluk, Natale M Ceglio, Daniel G Stearns, K Danzmann, M Kuhne, P Muller, and B Wende. Soft x-ray beamsplitters and highly dispersive multilayer mirrors for use as soft x-ray laser cavity components. In *Multilayer Structures & Laboratory X-Ray Laser Research*, volume 688, pages 81–90. SPIE, 1987.
- [49] Ritva AM Keski-Kuha. Layered synthetic microstructure technology considerations for the extreme ultraviolet. *Applied optics*, 23(20):3534–3537, 1984.
- [50] Ian McNulty, Yipeng Feng, Sean P Frigo, and Timothy M Mooney. Multilayer spherical grating monochromator for 1-to 4-keV x rays. In *Gratings and Grating Monochromators for Synchrotron Radiation*, volume 3150, pages 195–204. SPIE, 1997.
- [51] JC Rife, TW Barbee Jr, WR Hunter, and RG Cruddace. Performance of a tungsten/carbon multilayer-coated, blazed grating from 150 to 1700 eV. *Physica Scripta*, 41(4):418, 1990.
- [52] Masato Koike, Masahiko Ishino, Takashi Imazono, Kazuo Sano, Hiroyuki Sasai, Masatoshi Hatayama, Hisataka Takenaka, Philip A Heimann, and Eric M Gullikson. Development of soft x-ray multilayer laminar-type plane gratings and varied-line-spacing spherical grating for flat-field spectrograph in the 1–8 keV region. *Spectrochimica Acta Part B: Atomic Spectroscopy*, 64(8):756–760, 2009.
- [53] Fadi Choueikani, Bruno Lagarde, Franck Delmotte, Michael Krumrey, Françoise Bridou, Muriel Thomasset, Evgueni Meltchakov, and François Polack. High-efficiency b 4 c/mo 2 c alternate multilayer grating for monochromators in the photon energy range from 0.7 to 3.4 keV. *Optics Letters*, 39(7):2141–2144, 2014.
- [54] B Lagarde, F Choueikani, B Capitanio, P Ohresser, E Meltchakov, Franck Delmotte, M Krumrey, and F Polack. High efficiency multilayer gratings for monochromators in the energy range from 500 eV to 2500 eV. In *Journal of Physics: Conference Series*, volume 425, page 152012. IOP Publishing, 2013.
- [55] Masahiko Ishino, Philip A Heimann, Hiroyuki Sasai, Masatoshi Hatayama, Hisataka Takenaka, Kazuo Sano, Eric M Gullikson, and Masato Koike. Development of multilayer laminar-type diffraction gratings to achieve high diffraction efficiencies in the 1-8 keV energy region. *Applied optics*, 45(26):6741–6745, 2006.
- [56] MP Kowalski, RG Cruddace, KF Heidemann, R Lenke, H Kierey, TW Barbee, and WR Hunter. Record high extreme-ultraviolet efficiency at near-normal incidence from a multilayer-coated polymer-overcoated blazed ion-etched holographic grating. *Optics Letters*, 29(24):2914–2916, 2004.
- [57] M Nevière. Multilayer coated gratings for x-ray diffraction: differential theory. *JOSA A*, 8(9):1468–1473, 1991.

- [58] MP Kowalski, JF Seely, WR Hunter, JC Rife, TW Barbee, GE Holland, CN Boyer, CM Brown, and RG Cruddace. Dual-waveband operation of a multilayer-coated diffraction grating in the soft x-ray range at near-normal incidence. *Applied optics*, 32(13):2422–2425, 1993.
- [59] Dmitriy L Voronov, Minseung Ahn, Eric H Anderson, Rossana Cambie, Chih-Hao Chang, Leonid I Goray, Eric M Gullikson, Ralf K Heilmann, Farhad Salmassi, Mark L Schattenburg, et al. High-efficiency multilayer blazed gratings for euv and soft x-rays: recent developments. *Advances in X-Ray/EUV Optics and Components V*, 7802:45–57, 2010.
- [60] AE Franke, ML Schattenburg, Eric M Gullikson, J Cottam, SM Kahn, and A Rasmussen. Super-smooth x-ray reflection grating fabrication. *Journal of Vacuum Science & Technology B: Microelectronics and Nanometer Structures Processing, Measurement, and Phenomena*, 15(6):2940–2945, 1997.
- [61] DL Voronov, EM Gullikson, F Salmassi, T Warwick, and HA Padmore. Enhancement of diffraction efficiency via higher-order operation of a multilayer blazed grating. *Optics letters*, 39(11):3157–3160, 2014.
- [62] DL Voronov, EH Anderson, Rossana Cambie, Stefano Cabrini, SD Dhuey, LI Goray, EM Gullikson, Farhad Salmassi, Tony Warwick, VV Yashchuk, et al. A 10,000 groove/mm multilayer coated grating for euv spectroscopy. *Optics Express*, 19(7):6320–6325, 2011.
- [63] F Siewert, B Löchel, J Buchheim, F Eggenstein, A Firsov, G Gwalt, O Kutz, St Lemke, B Nelles, I Rudolph, et al. Gratings for synchrotron and fel beamlines: a project for the manufacture of ultra-precise gratings at helmholtz zentrum berlin. *Journal of Synchrotron Radiation*, 25(1):91–99, 2018.
- [64] Jian Gao, Peng Chen, Lei Wu, Bingjun Yu, and Linmao Qian. A review on fabrication of blazed gratings. *Journal of Physics D: Applied Physics*, 54(31):313001, 2021.
- [65] DL Voronov, Erik H Anderson, Eric M Gullikson, Farhad Salmassi, Tony Warwick, Valeriy V Yashchuk, and Howard A Padmore. Ultra-high efficiency multilayer blazed gratings through deposition kinetic control. *Optics Letters*, 37(10):1628–1630, 2012.
- [66] Patrick P Naulleau, J Alexander Liddle, Erik H Anderson, Eric M Gullikson, Paul Mirkarimi, Farhad Salmassi, and Eberhard Spiller. Fabrication of high-efficiency multilayer-coated gratings for the euv regime using e-beam patterned substrates. *Optics communications*, 229(1-6):109–116, 2004.
- [67] Rabah Benbalagh, Jean-Michel André, Robert Barchewitz, Philippe Jonnard, Gwénaelle Julié, Laurent Mollard, Guy Rolland, Christian Rémond, Philippe Troussel, Rémy Marmoret, et al. Lamellar multilayer amplitude grating as soft-x-ray bragg monochromator. *Nuclear Instruments and Methods in Physics Research Section A: Accelerators, Spectrometers, Detectors and Associated Equipment*, 541(3):590–597, 2005.

- [68] Robert van der Meer, Igor Kozhevnikov, Balachander Krishnan, Jurriaan Huskens, Petra Hegeman, Christian Brons, Boris Vratzov, Bert Bastiaens, Klaus Boller, and Fred Bijkerk. Single-order operation of lamellar multilayer gratings in the soft x-ray spectral range. *AIP advances*, 3(1):012103, 2013.
- [69] Saša Bajt, Henry N Chapman, Andrew Aquila, and Eric Gullikson. High-efficiency x-ray gratings with asymmetric-cut multilayers. *JOSA A*, 29(3):216–230, 2012.
- [70] Mauro Prasciolu, Anton Haase, Frank Scholze, Henry N Chapman, and Saša Bajt. Extended asymmetric-cut multilayer x-ray gratings. *Optics express*, 23(12):15195–15204, 2015.
- [71] Shengnan He, Ying Liu, Jingtao Zhu, Haochuan Li, Qiushi Huang, Hongjun Zhou, Tonglin Huo, Zhanshan Wang, and Shaojun Fu. Sic/w/ir multilayer-coated grating for enhanced efficiency in 50–100 nm wavelength range in seya–namioka mount. *Optics letters*, 36(2):163–165, 2011.
- [72] Yufei Feng, Qiushi Huang, Yeqi Zhuang, Andrey Sokolov, Stephanie Lemke, Runze Qi, Zhong Zhang, and Zhanshan Wang. Mo/si lamellar multilayer gratings with high efficiency and enhanced resolution for the x-ray region of 1000–1700ev. *Optics Express*, 29(9):13416–13427, 2021.
- [73] V Domingo, Bernhard Fleck, and Al Poland. Soho: the solar and heliospheric observatory. *Space Science Reviews*, 72(1):81–84, 1995.
- [74] JP Wuelser, JR Lemen, TD Tarbell, CJ Wolfson, JC Cannon, and BA Carpenter. Telescopes and instrumentation for solar astrophysics, proc. spie, 2004.
- [75] Ali BenMoussa, IE Dammasch, J-F Hochedez, Udo Schühle, Silvio Koller, Yvan Stockman, Frank Scholze, M Richter, Udo Kroth, Christian Laubis, et al. Pre-flight calibration of Iyra, the solar vuv radiometer on board proba2. *Astronomy & Astrophysics*, 508(2):1085–1094, 2009.
- [76] Tomoko Kawate, Toshifumi Shimizu, Shinsuke Imada, Toshihiro Tsuzuki, Yukio Katsukawa, Hirohisa Hara, Yoshinori Suematsu, Kiyoshi Ichimoto, Harry Warren, Luca Teriaca, et al. Concept study of solar-c\_euvst optical design. In *UV, X-Ray, and Gamma-Ray Space Instrumentation for Astronomy XXI*, volume 11118, pages 400–408. SPIE, 2019.
- [77] Peter R Young. Future prospects for solar euv and soft x-ray spectroscopy missions. *Frontiers in Astronomy and Space Sciences*, 8:662790, 2021.
- [78] Julien Gautier, Franck Delmotte, Marc Roulliay, Françoise Bridou, Marie-Françoise Ravet, and Arnaud Jérôme. Study of normal incidence of three-component multilayer mirrors in the range 20–40 nm. *Applied optics*, 44(3):384–390, 2005.



- [79] Catherine Burcklen. *Microscope X dans la fenêtre de l'eau: conception, miroirs à revêtements multicouches et métrologie associée*. PhD thesis, Université Paris Saclay (COmUE), 2017.
- [80] Diffraction des rayons x e scattering | axs bruker - x-ray diffraction and elemental analysis | bruker. [://www.bruker.com/fr/products/x-ray-diffraction-and-elemental-analysis/x-ray-diffraction.html](http://www.bruker.com/fr/products/x-ray-diffraction-and-elemental-analysis/x-ray-diffraction.html).
- [81] X-ray reflectivity - wikipedia. [https://en.wikipedia.org/wiki/X-ray\\_reflectivity](https://en.wikipedia.org/wiki/X-ray_reflectivity). accessed Jun. 12, 2020.
- [82] Ignacio Horcas, Rs Fernández, JM Gomez-Rodriguez, JWSX Colchero, JWSXM Gómez-Herrero, and AM Baro. Wsxn: A software for scanning probe microscopy and a tool for nanotechnology. *Review of scientific instruments*, 78(1):013705, 2007.
- [83] Jean Paul Hugonin and Philippe Lalanne. Reticolo software for grating analysis. *arXiv preprint arXiv:2101.00901*, 2021.
- [84] David L Windt. Imd—software for modeling the optical properties of multilayer films. *Computers in physics*, 12(4):360–370, 1998.
- [85] Ying Liu, Hans-Jörg Fuchs, Zhengkun Liu, Huoyao Chen, Shengnan He, Shaojun Fu, Ernst-Bernhard Kley, and Andreas Tünnermann. Investigation on the properties of a laminar grating as a soft x-ray beam splitter. *Applied optics*, 49(23):4450–4459, 2010.
- [86] Burton L Henke, Eric M Gullikson, and John C Davis. X-ray interactions: photoabsorption, scattering, transmission, and reflection at  $e = 50\text{--}30,000$  ev,  $z = 1\text{--}92$ . *Atomic data and nuclear data tables*, 54(2):181–342, 1993.
- [87] Regina Soufli and Eric M Gullikson. Absolute photoabsorption measurements of molybdenum in the range 60–930 ev for optical constant determination. *Applied Optics*, 37(10):1713–1719, 1998.
- [88] Charles Tarrio, Richard N Watts, Thomas B Lucatorto, Jon M Slaughter, and Charles M Falco. Optical constants of in situ-deposited films of important extreme-ultraviolet multilayer mirror materials. *Applied optics*, 37(19):4100–4104, 1998.
- [89] F Clette, P Cugnon, and EL Van Dessel. J.-p. delaboudinière, ge artzner, j. brunaud, ah gabriel. *The SOHO Mission*, 162(1-2):291–312, 1995.
- [90] Jean-Pierre Wülser, James R Lemen, Theodore D Tarbell, C Jacob Wolfson, Joseph C Cannon, Brock A Carpenter, Dexter W Duncan, Glenn S Gradwohl, Syndie B Meyer, Augustus S Moore, et al. Euvi: the stereo-secchi extreme ultraviolet imager. In *Telescopes and instrumentation for solar astrophysics*, volume 5171, pages 111–122. SPIE, 2004.

- [91] James R Lemen, Alan M Title, David J Akin, Paul F Boerner, Catherine Chou, Jerry F Drake, Dexter W Duncan, Christopher G Edwards, Frank M Friedlaender, Gary F Heyman, et al. The atmospheric imaging assembly (aia) on the solar dynamics observatory (sdo). *Solar Physics*, 275:17–40, 2012.
- [92] Chuanwei Zhang, Shiyuan Liu, Tielin Shi, and Zirong Tang. Fitting-determined formulation of effective medium approximation for 3d trench structures in model-based infrared reflectometry. *JOSA A*, 28(2):263–271, 2011.
- [93] Bruggeman et al., “effective medium approximations - wikipedia,”. [https://en.wikipedia.org/wiki/Effective\\_medium\\_approximations](https://en.wikipedia.org/wiki/Effective_medium_approximations). Accessed: 2020-04-16.
- [94] “install the software - matlab simulink.”. [https://en.wikipedia.org/wiki/Effective\\_medium\\_approximations](https://en.wikipedia.org/wiki/Effective_medium_approximations). Accessed: 2020-01-03.
- [95] Nicolas Chateau and Jean-Paul Hugonin. Algorithm for the rigorous coupled-wave analysis of grating diffraction. *JOSA A*, 11(4):1321–1331, 1994.
- [96] Troy W Barbee, Stanley Mrowka, and Michael C Hettrick. Molybdenum-silicon multilayer mirrors for the extreme ultraviolet. *Applied Optics*, 24(6):883–886, 1985.
- [97] Sergiy A Yulin, Franz Schaefer, Torsten Feigl, and Norbert Kaiser. High-performance cr/sc multilayers for the soft x-ray range. In *Advances in Mirror Technology for X-Ray, EUV Lithography, Laser, and Other Applications*, volume 5193, pages 172–176. SPIE, 2004.
- [98] Philippe Jonnard, Karine Le Guen, M-H Hu, J-M André, Evgueni Meltchakov, Christophe Hecquet, Franck Delmotte, and Anouk Galtayries. Optical, chemical, and depth characterization of al/sic periodic multilayers. In *EUV and X-Ray Optics: Synergy between Laboratory and Space*, volume 7360, pages 211–219. SPIE, 2009.
- [99] Y Ménesguen, S De Rossi, E Meltchakov, and F Delmotte. Aperiodic multilayer mirrors for efficient broadband reflection in the extreme ultraviolet. *Applied Physics A*, 98:305–309, 2010.
- [100] AL Aquila, F Salmassi, F Dollar, Y Liu, and EM Gullikson. Developments in realistic design for aperiodic mo/si multilayer mirrors. *Optics express*, 14(21):10073–10078, 2006.
- [101] Michele Suman, Fabio Frassetto, Piergiorgio Nicolosi, and Maria-Guglielmina Pelizzo. Design of aperiodic multilayer structures for attosecond pulses in the extreme ultraviolet. *Applied optics*, 46(33):8159–8169, 2007.
- [102] Franck Delmotte, Julien Gautier, Marc Roulliay, Marie Françoise Ravet, Françoise Bridou, and Arnaud Jérôme. B4c/mo/si multilayers for 20–40 nm wavelengths: application to broadband mirrors. In *Advances in Optical Thin Films II*, volume 5963, pages 539–546. SPIE, 2005.
- [103] etcourse. <https://www.etcourse.com/news-blog/bandwidth-resonant-circuits>. Accessed: 2021-12-31.

- [104] Michael P Kowalski, Troy W Barbee, Klaus F Heidemann, Herbert Gursky, Jack C Rife, William R Hunter, Gilbert G Fritz, and Raymond G Cruddace. Efficiency calibration of the first multilayer-coated holographic ion-etched flight grating for a sounding rocket high-resolution spectrometer. *Applied optics*, 38(31):6487–6493, 1999.
- [105] U Kleineberg, H-J Stock, A Kloidt, K Osterried, D Menke, B Schmiedeskamp, Ulrich Heinzmann, D Fuchs, P Müller, F Scholze, et al. Mo/Si multilayer coated laminar phase and ruled blaze gratings for the soft x-ray region. *Journal of electron spectroscopy and related phenomena*, 80:389–392, 1996.
- [106] D8 discover | bruker. <https://www.bruker.com/en/products-and-solutions/diffractometers-and-scattering-systems/x-ray-diffractometers/d8-discover-family/d8-discover.html>. Accessed: 2022-10-20.
- [107] Johannes Schindelin, Ignacio Arganda-Carreras, Erwin Frise, Verena Kaynig, Mark Longair, Tobias Pietzsch, Stephan Preibisch, Curtis Rueden, Stephan Saalfeld, Benjamin Schmid, et al. Fiji: an open-source platform for biological-image analysis. *Nature methods*, 9(7):676–682, 2012.
- [108] Ted Liang, Erdem Ultanir, Guojing Zhang, Seh-Jin Park, Erik Anderson, Eric Gullikson, Patrick Naulleau, Farhad Salmassi, Paul Mirkarimi, Eberhard Spiller, et al. Growth and printability of multilayer phase defects on extreme ultraviolet mask blanks. *Journal of Vacuum Science & Technology B: Microelectronics and Nanometer Structures Processing, Measurement, and Phenomena*, 25(6):2098–2103, 2007.
- [109] Eric M Gullikson, Charles Cerjan, Dan G Stearns, Paul B Mirkarimi, and Don W Sweeney. Practical approach for modeling extreme ultraviolet lithography mask defects. *Journal of Vacuum Science & Technology B: Microelectronics and Nanometer Structures Processing, Measurement, and Phenomena*, 20(1):81–86, 2002.

**Titre:** Réseaux de diffraction multicouches efficaces sur une large bande passante dans l'extrême ultraviolet.

**Mots clés:** extrême ultraviolet- rayons X- films minces nanométriques- miroir interférentiel

**Résumé:** Récemment le développement de réseaux optiques multicouches à forte densité de traits a permis d'augmenter l'efficacité et la résolution spectrale dans le domaine spectral extrême ultraviolet (EUV) permettant la réalisation de spectromètres à ultra-haute résolution et des spectro-imageurs pour l'observation solaire. Cette thèse présente une étude expérimentale et de modélisation de réseaux multicouches EUV à haute densité de traits afin d'optimiser l'efficacité de diffraction dans une gamme de longueur d'onde s'étendant de 17nm à 30 nm. Ce travail se situe dans le cadre du développement du spectro-imageur EUV de la mission japonaise Solar-C. La technique de pulvérisation cathodique magnétron a été utilisée pour déposer des multicouches Al/Mo/SiC optimisées pour diverses plages de longueur d'onde sur des réseaux lamellaires ( 4000 traits/mm) avec des profondeurs comprises entre 5 et 20 nm. Tous les échantillons ont été caractérisés avant et après le dépôt des multicouches par microscopie à force atomique (AFM) et par réflectométrie de rayons X en incidence rasante (GIXR) à 8,05 keV. L'évolution du

profil de surface avec l'augmentation du nombre de couches déposées a été observée grâce aux mesures AFM, et confirmée par l'analyse de coupes transversales par microscopie électronique en transmission. L'efficacité de diffraction dans l'EUV des réseaux multicouches a été mesurée dans différents ordres sur rayonnement synchrotron (ligne de métrologie XUV du synchrotron SOLEIL). Les résultats obtenus sont en excellent accord avec les simulations numériques, obtenues par une analyse rigoureuse en ondes couplées (RCWA), qui incorporent les paramètres structuraux déterminés par AFM et GIXR. L'efficacité au premier ordre mesurée en incidence normale a atteint 8.1% sur la plage spectrale 17-21 nm ce qui est supérieure à l'efficacité du réseau utilisé dans la précédente mission Solar B. De plus, l'utilisation d'empilement multicouche aperiodique sur le réseau a montré des efficacités élevées sur une plage de longueur d'onde étendue. Ce travail ouvre la voie au développement d'instruments aux performances accrues pour la spectrométrie EUV à haute résolution ou les applications de spectro-imagerie.

**Title:** Multilayer diffraction gratings with broadband efficiency in the extreme ultraviolet.

**Keywords:** X-rays-extreme UV-Nanoscale multilayer mirror-Optical Interference Coating

**Abstract:** Recently, the development of high-density multilayer optical gratings has allowed for increased efficiency and spectral resolution in the extreme ultraviolet (EUV) spectral range, enabling the realization of ultra-high-resolution spectrometers and spectro-imagers for solar observation. This thesis presents an experimental and modeling study of high-density EUV multilayer gratings to optimize diffraction efficiency in a wavelength range from 17nm to 30nm. This work is part of the development of a EUV spectro-imager for the Japanese Solar-C mission. The magnetron sputtering technique was used to deposit Al/Mo/SiC multilayers optimized for various wavelength ranges on lamellar gratings ( 4000 lines/mm) with depths ranging from 5nm to 20nm. All samples were characterized before and after multilayer deposition using atomic force microscopy (AFM) and grazing incidence X-ray reflectometry (GIXR) at 8.05 keV. The evolution of the surface

profile with an increasing number of deposited layers was observed through AFM measurements and confirmed by cross-sectional analysis using transmission electron microscopy. The EUV diffraction efficiency of the multilayer gratings was measured in different orders using synchrotron radiation (XUV metrology beamline of the SOLEIL synchrotron). The obtained results are in excellent agreement with numerical simulations performed using rigorous coupled-wave analysis (RCWA), incorporating the structural parameters determined by AFM and GIXR. The measured first-order efficiency at normal incidence reached 8.1% in the spectral range of 17-21 nm, surpassing the efficiency of the grating used in the previous Solar B mission. Moreover, the use of aperiodic multilayer stacks on the grating demonstrated high efficiencies over an extended wavelength range. This work paves the way for the development of high-performance instruments for EUV spectroscopy with increased resolution or spectro-imaging applications.

